

Multidisciplinary Optimization of In-Flight Electro-Thermal Ice Protection Systems

A dissertation

submitted to the Department of Mechanical Engineering of

McGill University

in partial fulfilment of the requirements for the degree of

Doctor of Philosophy

© Copyright by Mahdi Pourbagian Barzi

All rights reserved.

December 2014

DEDICATION

To those who use science in good ways.

ACKNOWLEDGMENTS

After praising and thanking the Almighty, I would like to thank my family, especially my dear parents who have always supported me. I should thank my teachers, my friends, and all those who have helped me acquire worthwhile knowledge through my life. I should thank Professor Wagdi G. Habashi who supervised my Ph.D. study at McGill. During this period, I learned how to efficiently research, which I think is more important than research itself. I should also thank all those who provided me with valuable comments and ideas: my colleagues at the CFD Laboratory, the staff of Newmerical Technologies International, and those from GERAD, a multi-university research center. Finally, I should acknowledge the significant contribution of a McGill Engineering Doctoral Award (MEDA) in financially supporting my research work.

TABLE OF CONTENTS

DEDICATION	ii
ACKNOWLEDGMENTS	iii
TABLE OF CONTENTS.....	iv
NOMENCLATURE	vii
LIST OF TABLES	x
LIST OF FIGURES	xi
Chapter 1 INTRODUCTION	21
1.1 Background.....	21
1.1.1 In-Flight Icing	21
1.1.2 Adverse Aerodynamic Effects of Icing.....	23
1.1.3 Ice Protection Systems	25
1.1.4 Electro-Thermal IPS	28
1.2 Review of Literature	31
1.2.1 In-Flight Icing	31
1.2.2 Ice Protection Systems.....	32
1.2.3 Improvement of Thermal-Based IPS	35
1.3 Objectives and Outline.....	36
1.4 Discussion and Conclusions	37
Chapter 2 SIMULATION OF ELECTRO-THERMAL ANTI-ICING.....	39
2.1 In-Flight Icing Simulation	39
2.1.1 Framework	39
2.1.2 Numerical Test Case	43
2.2 IPS Simulation	46
2.3 Discussion and Conclusions	50
Chapter 3 ENERGY ANALYSIS OF ANTI-ICING	51
3.1 Calculation of the Minimum Energy Requirements of Anti-Icing.....	51
3.2 Influential Parameters on the Energy Requirements of Anti-Icing	57
3.3 Sensitivity Analysis of the Energy Requirements of Anti-Icing	58

3.3.1	Airspeed	58
3.3.2	Angle of Attack	63
3.3.3	Ambient Temperature	65
3.3.4	LWC and MVD	69
3.4	Discussion and Conclusions	74
Chapter 4	OPTIMIZATION OF IPS IN ANTI-ICING MODE	76
4.1	Overall Framework	76
4.2	Optimization Method	78
4.2.1	Poll Step	78
4.2.2	dynaTree Library	79
4.2.3	Statistical Relevance	79
4.2.4	Lack of Information	81
4.2.5	Surrogate-Based Search	83
4.3	Formulations of the Objective and Constraint Functions	84
4.4	Numerical Test Cases	91
4.4.1	Running-Wet Regime	93
4.4.1.1	Primary Optimization	93
4.4.1.2	Power Optimization	93
4.4.1.3	Optimization under Lack of Energy	99
4.4.1.4	Power-Extent Optimization	101
4.4.2	Evaporative Regime	104
4.4.2.1	Primary Optimization	104
4.4.2.2	Power Optimization	105
4.4.2.3	Optimization under Lack of Energy	112
4.4.2.4	Power-Extent Optimization	114
4.5	Discussion and Conclusions	118
Chapter 5	SURROGATE-BASED OPTIMIZATION	120
5.1	Background	120
5.2	Reduced Order Modeling	121
5.2.1	Proper Orthogonal Decomposition	121
5.2.2	Method of Snapshots	122

5.2.3 Kriging	124
5.3 Overall Optimization Framework	126
5.4 ROM-Based CHT	128
5.4.1 Design of Experiments	126
5.4.2 Surrogate Modeling	128
5.4.3 Improvement Strategies	129
5.4.3.1 Splitting	129
5.4.3.2 Scalarization	132
5.4.3.3 Localization	132
5.5 Numerical Test Cases	134
5.5.1 Running-Wet Regime	134
5.5.2 Evaporative Regime	139
5.6. Adaptive Surrogate-Based Optimization	149
5.7 Discussion and Conclusions	151
Chapter 6 IPS IN TRANSIENT DE-ICING MODE	152
6.1 Unsteady CHT Simulation of De-Icing System	152
6.2 Primary Modifications	154
6.3 Formulations of the Objective and Constraint Functions	159
6.4 Optimization Approach	165
6.5 Numerical Test Cases	166
6.6 An Addendum on the Aerodynamic Effects of Surface Heating	181
6.7 Discussion and Conclusions	182
Chapter 7 CLOSURE	184
REFERENCES	186

NOMENCLATURE

C_D	=	drag coefficient
C_p	=	pressure coefficient
c	=	constraint function
c_h	=	convective heat transfer coefficient
c_p	=	specific heat capacity
D	=	MADS mesh set
EI	=	expected improvement function
EFI	=	expected feasible improvement function
Fr	=	Froude number, $Fr = U_\infty / \sqrt{lg}$
f	=	objective function
H_r	=	relative humidity
h_f	=	water film height
h_{ice}	=	ice height
I	=	improvement function
K	=	inertia parameter, $K = \rho_w d^2 U_\infty / 18l\mu$
k	=	thermal conductivity
L	=	latent heat
\dot{m}''	=	mass transfer rate
P	=	probability of feasibility
P''	=	electric power density
P_s	=	surface pressure
P_v	=	saturation vapor pressure
\dot{Q}''	=	heat transfer rate
R	=	covariance (correlation) matrix
Re_d	=	droplets Reynolds number, $Re_d = \rho_w d U_\infty / \mu$

T_m	=	melting temperature
T_{rec}	=	recovery temperature
T_s	=	surface temperature
T_∞	=	ambient temperature
\mathbf{u}	=	velocity
\mathbf{x}	=	vector of design variables

Greek Letters

α	=	water volume fraction
β	=	water collection efficiency
γ	=	Kriging's mean term
Δ^m	=	mesh size parameter
Δ^p	=	poll size parameter
δ	=	Kriging's departure term
ε	=	solid emissivity
ζ	=	thermal diffusivity
\mathbf{K}	=	kernel
Λ	=	eigenvalue
μ	=	uncertainty in feasibility
ξ	=	eigenfunction
ρ	=	density
σ	=	Stefan-Boltzmann constant
ν	=	thermal penetration depth
Φ	=	probability density function
ϕ	=	POD base function
χ	=	design space
ω	=	POD base coefficient

Abbreviations

AoA	=	angle of attack
(DEFH) _{lo}	=	distance-end film height (lower surface)
(DEFH) _{up}	=	distance-end film height (upper surface)
EFH	=	end film height
FE	=	fully-evaporative
FIV	=	final ice volume
IPD	=	ice-pressure distance
ISI	=	ice shape irregularity
LWC	=	liquid water content
MADS	=	mesh adaptive direct search
MIG	=	maximum ice growth
MIT	=	maximum ice thickness
MST	=	maximum shell temperature
MVD	=	liquid water content
MWT	=	minimum wall temperature
RW	=	running-wet
TEE	=	total electric energy
TEP	=	total electric power
(TMWT) _c	=	target-minimum wall temperature (continuous)
(TMWT) _d	=	target-minimum wall temperature (discontinuous)
TWT	=	target wall temperature

LIST OF TABLES

Table 2.1: Flight and icing conditions.	44
Table 2.2: Material properties of the composite shell at the leading edge.....	47
Table 2.3: Flight and icing conditions.	48
Table 3.1: Flight and icing conditions.	55
Table 4.1: Formulations of the objective and constraint functions.....	85
Table 4.2: Flight-icing conditions.....	91
Table 4.3: Matrix of test cases for power optimization.	92
Table 4.4: Optimized total electric power values for different cases.....	103
Table 4.5: Optimized total electric power values for different cases.....	116
Table 5.1: Flight-icing conditions.....	128
Table 5.2: Three sample target data sets.	129
Table 5.3: Parameters of two adaptive test cases.....	149
Table 6.1: Flight-icing conditions.....	153
Table 6.2: Flight-icing conditions.....	154
Table 6.3: Formulation of the objective and constraint functions.	160
Table 6.4: Sample target data set.	165
Table 6.5: Different sets of objective and constraint functions.	167
Table 6.6: Matrix of test cases.	168

LIST OF FIGURES

Figure 1.1: Glaze ice (left) and rime ice (right) on wing (picture adapted from <i>New Scientist</i>).....	22
Figure 1.2: Time and accident percentage for different flight phases (data adapted from <i>Robert E. Breiling Associates</i>).....	23
Figure 1.3: Comparison of lift (left) and drag (right) coefficients of a clean (solid line) and iced (line with circles) airfoil for $Re = 7.5 \times 10^6$ and $Ma = 0.21$ (plots adapted from [3]).	24
Figure 1.4: Instantaneous schematic of a separation bubble flow field downstream of a horn ice shape (picture adapted from [4] and [5]).....	24
Figure 1.5: Distribution of primary occurrences due to aerodynamic, stability, control problems in the period 1978-2002 (data adapted from [6]).	25
Figure 1.6: distribution of primary occurrences related to aerodynamic, stability, control, based on the use of ice protection in the period 1978-2002 (data adapted from [6]).....	26
Figure 1.7: Surface temperature contour plots of a part of a wing hot-air anti-icing system (picture adapted from [7]).	26
Figure 1.8: Left: <i>Goodrich</i> ® pneumatic boots, before (top) and after (bottom) activation; Right: Effect of de-icing boot activation in presence of ice formation (picture adapted from [8]).....	27
Figure 1.9: Weeping wings (picture adapted from <i>TKS</i> ™).	28
Figure 1.10: Droplet motion on a surface with (left) and without (right) hydrophobic coating (picture adapted from <i>Optics Balzers</i>).	28
Figure 1.11: Evolution of electrical power needs (data adapted from [15]).	29
Figure 1.12: A conventional architecture with four different energy vectors (picture adapted from [15]).	30
Figure 1.13: Leading edge electro-thermal IPS (pictures adapted from <i>GKN</i> and <i>FMLC</i>).	30
Figure 1.14: Typical power level for electrical loads on an aircraft (data adapted from [79]).	37
Figure 2.1: General framework of in-flight icing simulation.....	40

Figure 2.2: Hybrid grid around the clean airfoil (left) and displaced grid around the iced airfoil (right).	44
Figure 2.3: Surface distributions of pressure coefficient for clean and iced airfoils.	45
Figure 2.4: Contour plots of turbulent viscosity for clean (left) and iced (right) airfoils.	45
Figure 2.5: Surface distributions of collection efficiency for clean and iced airfoils.	45
Figure 2.6: Comparison of ice shapes obtained by different methods.	46
Figure 2.7: Domains involved in the CHT procedure.	46
Figure 2.8: Schematic picture of the electro-thermal IPS.	47
Figure 2.9: Hybrid grid around the NACA0012 airfoil and structured grid inside the leading edge composite shell.	48
Figure 2.10: Comparison of the surface temperature distribution.	48
Figure 2.11: Heat flux (left) and heat transfer coefficient (right) distributions for different surface temperatures.	49
Figure 2.12: Comparison of the surface temperature distributions (left) and minimum and maximum solid shell temperature (right) obtained by different strategies.	50
Figure 3.1: Mass transfer mechanisms (left): 1:sublimation, 2:evaporation, 3:water impingement, 4:ice accretion; heat transfer mechanisms (right): 1:sublimation, 2:evaporation, 3:kinetic, 4:sensible, 5:convection, 6:irradiation, 7:fusion, 8:conduction.	52
Figure 3.2: Heat flux required by various heat transfer mechanisms for the running-wet (left) and fully-evaporative (right) regimes.	56
Figure 3.3: Total heat flux required for the running-wet and fully-evaporative regimes.	56
Figure 3.4: Appendix C envelopes, including intermittent and continuous maximum atmospheric icing conditions (left) and Appendix C envelopes converted to a distance-based format for MVD = 20 μm (right) (data adapted from [91]).	58
Figure 3.5: Total heat flux distributions required for the running-wet (left) and fully-evaporative (right) regimes at different airspeeds.	59
Figure 3.6: Water film height distribution for the running-wet regime at different airspeeds.	60
Figure 3.7: Overall variation of different heat transfer mechanisms for the running-wet (left) and fully-evaporative (right) regimes with respect to airspeed.	61
Figure 3.8: Sensitivity of impingement, evaporation, convection and total heat rate with respect to airspeed.	62
Figure 3.9: Sensitivity of the impingement mass rate with respect to airspeed.	62

Figure 3.10: Total heat flux distributions required for the running-wet (left) and fully- evaporative (right) regimes at different angles of attack.	63
Figure 3.11: Water film height distribution for the running-wet regime at different angles of attack.....	64
Figure 3.12: Overall variation of different heat transfer mechanisms for the running-wet (left) and fully-evaporative (right) regimes with respect to angle of attack.....	64
Figure 3.13: Sensitivity of impingement, evaporation, convection and total heat rate with respect to angle of attack.....	66
Figure 3.14: Sensitivity of the impingement mass rate with respect to angle of attack. ...	66
Figure 3.15: Total heat flux distributions required for the running-wet (left) and fully- evaporative (right) regimes at different ambient temperatures.	67
Figure 3.16: Water film height distribution for the running-wet regime at different ambient temperatures.	67
Figure 3.17: Sensitivity of the impingement mass rate with respect to ambient temperature.	68
Figure 3.18: Overall variation of different heat transfer mechanisms for the running-wet (left) and fully-evaporative (right) regimes with respect to ambient temperature.	69
Figure 3.19: Sensitivity of impingement, evaporation, convection and total heat rate with respect to the ambient temperature.	70
Figure 3.20: Sensitivity of the impingement mass rate with respect to the variables of Appendix C.	70
Figure 3.21: Sensitivity of the impingement heat rate for the running-wet (left) and fully- evaporative (right) regimes within the entire Appendix C.....	72
Figure 3.22: Sensitivity of the evaporation heat rate for the running-wet (left) and fully- evaporative (right) regimes within the entire Appendix C.....	73
Figure 3.23: Sensitivity of the convection heat rate for the running-wet (left) and fully- evaporative (right) regimes within the entire Appendix C.....	73
Figure 3.24: Sensitivity of the total heat rate for the running-wet (left) and fully- evaporative (right) regimes within the entire Appendix C.....	73
Figure 4.1: Schematic of the optimization process.	77
Figure 4.2: Mesh and poll size parameters.	79
Figure 4.3: dynaTree model on 24 data points in \mathbb{R} (picture adapted from [103]).	81
Figure 4.4: Probability of feasibility and uncertainty about feasibility (picture adapted from [103]).	82

Figure 4.5: Illustration of the function $TMWT$ for infeasible and feasible cases (S_i is the surface integration of temperature profile over infeasible parts and S_f is that over feasible parts).....	87
Figure 4.6: An infeasible case with net feasible output (S_i is the surface integration of temperature profile over infeasible parts and S_f is that over feasible parts).	88
Figure 4.7: Bad (left) and good (right) constraint formulations.....	89
Figure 4.8: Illustration of the function $DEFH$ for positive (a) and negative (b) values....	90
Figure 4.9: Pareto front (Case W-P).	93
Figure 4.10: Convergence history of the best feasible objective function and design variables values (Case W-I).	94
Figure 4.11: Optimized and experimental values of power densities (Case W-I).	95
Figure 4.12: Pressure (left) and velocity (right) contour plots (Case W-I).	95
Figure 4.13: Convergence history of the best feasible objective function (left) and constraint violation (right) values (Case W-II).	96
Figure 4.14: Convergence history of the objective function values (left) based on the best constraint violation values (right) (Case W-III).	97
Figure 4.15: Optimized values of power densities.	98
Figure 4.16: Profiles of three surface quantities at optimal states.	98
Figure 4.17: Convergence history of the objective function values (left) based on the best constraint violation values (right) (Case W-III).	99
Figure 4.18: Profiles of three surface quantities at optimal states (Case W-III).	99
Figure 4.19: Convergence history of the best feasible objective function values (Case W-LE).	100
Figure 4.20: Profiles of three surface quantities at optimal state (Case W-LE).	100
Figure 4.21: Schematic picture of the design variables.	101
Figure 4.22: Convergence history of the best feasible objective function values for Case W-I and Case W-II.	102
Figure 4.23: Convergence history of the objective function values (left) based on the best constraint violation values (right) (Case W-III).	103
Figure 4.24: Original and optimized heaters' extents of Case (HP-HE).	103
Figure 4.25: Optimized values of power densities.	104
Figure 4.26: Profiles of three surface quantities at optimal state (Case W-III).	104
Figure 4.27: Pareto front (Case E-P).	105

Figure 4.28: Convergence history of the best feasible objective function (left) and constraint violation (right) values (Case E-I).....	106
Figure 4.29: Optimized and experimental values of power densities (Case E-I).....	107
Figure 4.30: Optimized (left) and experimental (right) temperature contour plots inside the solid shell (Case E-I).....	107
Figure 4.31: Convergence history of the best feasible objective function (left) and constraints violation (right) values (Case E-II).....	108
Figure 4.32: Convergence history of the best feasible objective function (left) and constraints violation (right) values.....	109
Figure 4.33: Optimized power densities.	109
Figure 4.34: Profiles of two surface quantities at optimal state.....	110
Figure 4.35: Convergence history of the best feasible objective function (left) and constraints violation (right) values.....	111
Figure 4.36: Optimized power densities.	111
Figure 4.37: Convergence history of the best feasible objective function (left) and constraints violation (right) values.....	112
Figure 4.38: Convergence history of the best feasible objective function values (Case E-VI).....	113
Figure 4.39: Pareto front (Case E-LE).....	114
Figure 4.40: Profiles of three surface quantities at optimal state (Case E-LE).....	114
Figure 4.41: Convergence history of the best feasible objective function values (Case E-I).....	115
Figure 4.42: Convergence history of the best feasible objective function values (Case E-II).....	116
Figure 4.43: Convergence history of the best feasible objective function values (Case E-IV).....	116
Figure 4.44: Original heaters' extents.....	117
Figure 4.45: Optimized heaters' extents for Case E-II and Case E-IV.....	117
Figure 4.46: Optimized power densities (Case E-II).....	117
Figure 4.47: Optimized power densities (Case E-IV).....	118
Figure 4.48: Profiles of two surface quantities at optimal state.....	118
Figure 5.1: Overall framework of surrogate-based optimization.....	127
Figure 5.2: Profiles of three surface quantities for 60 snapshots.....	128

Figure 5.3: Profiles of three surface quantities for Target I, II and III, from top to bottom, respectively.	130
Figure 5.4: Schematic of the split ROM.	131
Figure 5.5: Profiles of three surface quantities for Target I, II and III, from top to bottom, respectively.	131
Figure 5.6: Relative error of different functions for vector and scalar ROMs for targets I, II and III.	133
Figure 5.7: Selection of snapshots in a 2D design space based on local number (left) and local distance (right).	134
Figure 5.8: Convergence history of the best feasible objective values (Case W-I).	135
Figure 5.9: Optimized power densities (Case-W-I).	136
Figure 5.10: Profiles of three surface quantities at optimal states (Case W-I).	136
Figure 5.11: Convergence history of the best feasible objective values (Case W-II).	137
Figure 5.12: Optimized power densities (Case-W-II).	137
Figure 5.13: Profiles of three surface quantities at optimal states (Case W-II).	137
Figure 5.14: Convergence history of the objective function values (left) based on the best constraint violation values (right) (Case W-III).	138
Figure 5.15: Optimized power densities (Case-W-III).	138
Figure 5.16: Profiles of three surface quantities at optimal states (Case W-III).	139
Figure 5.17: Convergence history of the best feasible objective function values (left) and constraint violation values (right) (Case E-I).	140
Figure 5.18: Optimized power densities (Case E-I).	141
Figure 5.19: Profiles of three surface quantities at optimal states (Case E-I).	141
Figure 5.20: Convergence history of the best feasible objective values (Case E-II).	141
Figure 5.21: Convergence history of the best feasible constraint violation values (Case E-II).	142
Figure 5.22: Optimized power densities (Case E-II).	142
Figure 5.23: Profiles of three surface quantities at optimal states (Case E-II).	142
Figure 5.24: Convergence history of the best feasible objective values (Case E-IV).	143
Figure 5.25: Convergence history of the best feasible constraint violation values (Case E-IV).	144
Figure 5.26: Optimized power densities (Case E-IV).	144
Figure 5.27: Profiles of three surface quantities at optimal states (Case E-IV).	144
Figure 5.28: Convergence history of the best feasible objective values (Case E-V).	145

Figure 5.29: Convergence history of the best feasible constraint violation values (Case E-V).	146
Figure 5.30: Optimized power densities (Case E-V).	146
Figure 5.31: Profiles of three surface quantities at optimal states (Case E-V).	147
Figure 5.32: Convergence history of the best feasible objective values (Case E-VII).	147
Figure 5.33: Optimized power densities (Case E-VII).	147
Figure 5.34: Convergence history of the best feasible constraint violation values (Case E-VII).	148
Figure 5.35: Profiles of three surface quantities at optimal states (Case E-VII).	148
Figure 5.36: Convergence history of the objective function values (left) based on the best constraint violation values (right) (Case E-II).	150
Figure 5.37: Profiles of three surface quantities at optimal states (Case E-I).	150
Figure 6.1: Heater cycling sequence pattern for validation test case (power densities shown in W/m^2).	153
Figure 6.2: Comparison of the temperature history underneath heater 3.	153
Figure 6.3: Heater cycling sequence pattern for the modification test case (power densities shown in W/m^2).	155
Figure 6.4: Profiles of three surface quantities at the moment of maximum ice thickness and at the end of the cycles for the modification test case.	155
Figure 6.5: Heater cycling sequence patterns for continuously (top) and cyclically (bottom) activated parting strip cases (power densities shown in $[W/m^2]$).	158
Figure 6.6: Profiles of three surface quantities at the moment of maximum ice thickness and at the end of the cycles for continuously activated parting strip.	158
Figure 6.7: Profiles of three surface quantities at the moment of maximum ice thickness and at the end of the cycles for cyclically activated parting strip.	159
Figure 6.8: Smooth (left) and irregular (right) ice shapes with the same maximum ice thickness at the same location.	162
Figure 6.9: Two sets of points with same data values, average and standard deviation, but with different data locations and differential standard deviation.	163
Figure 6.10: Variation of maximum lift of NACA 0012 airfoil with respect to the chord-wise location of protuberances with different heights (k/c); $Re = 3.1 \times 10^6$ (picture adapted from [157] and [17]).	164
Figure 6.11: Variation of maximum ice thickness as through time for 200 snapshots on the lower (left) and upper (right) surfaces of the wing.	166

Figure 6.12: Variation of maximum ice thickness through time for the target on the lower (left) and upper (right) surfaces of the wing.	166
Figure 6.13: Two types of cycling sequence patterns: Pattern A (top), Pattern B (bottom).	168
Figure 6.14: Convergence history of the best feasible objective function values for cases I-P-A and I-P-B.....	170
Figure 6.15: Power densities (W/m^2) and cycling sequence patterns for optimal solutions of Case I-P-A (top) and Case I-PT-A (bottom).....	171
Figure 6.16: Profiles of three surface quantities at the moment of maximum ice thickness and at the end of the cycles for Case I-P-A.....	171
Figure 6.17: Profiles of three surface quantities at the moment of maximum ice thickness and at the end of the cycles for Case I-PT-A.	172
Figure 6.18: Pareto fronts of cases with function set II.	173
Figure 6.19: Feasible Pareto fronts for cases with function set II.....	174
Figure 6.20: Optimal power densities (W/m^2) and cycling sequence pattern for Case II-P-A.....	175
Figure 6.21: Profiles of three surface quantities at the moment of maximum ice thickness and at the end of the cycles for Case II-P-A.	175
Figure 6.22: Pareto fronts of cases with function set III.	176
Figure 6.23: Feasible Pareto fronts for cases with function set III.	177
Figure 6.24: Optimal power densities (W/m^2) and cycling sequence pattern for Case III-P-A.	178
Figure 6.25: Profiles of three surface quantities at the moment of maximum ice thickness and at the end of the cycles for Case III-P-A.....	178
Figure 6.26: Pareto fronts of cases with function set IV.....	179
Figure 6.27: Feasible Pareto fronts for cases with function set IV.	180
Figure 6.28: Profiles of three surface quantities at the moment of maximum ice thickness and at the end of the cycles for Case IV-P-A.....	180
Figure 6.29: Pressure contour plot and locations of maximum ice thickness and minimum surface pressure.....	181
Figure 6.30: Pressure coefficient distribution and locations of maximum ice thickness and minimum pressure coefficient.....	181

ABSTRACT

The numerical multidisciplinary analysis and optimization of in-flight electro-thermal ice protection systems (IPS), in both anti-icing and de-icing modes, are presented by introducing general methodologies. The numerical simulation of the IPS is carried out by solving the conjugate heat transfer (CHT) problem between the fluid and solid domains. The sensitivity analysis of the energy requirements of anti-icing systems is performed with respect to different parameters, such as airspeed, angle of attack (AoA), ambient temperature, liquid water content and median volumetric diameter (MVD). For optimization, the goal is to reduce the power demand of the electro-thermal IPS, while ensuring a safe protection against icing. The design variables taken into account include power density, and the extent and activation time (in case of de-icing) of the electric heating blankets. Various constrained problem formulations for optimization in both the running-wet and evaporative regimes are presented. The formulations are carefully proposed from the physical and mathematical viewpoints; their performance is assessed by means of several numerical test cases to determine the most promising for each regime. The optimization is conducted using the mesh adaptive direct search (MADS) algorithm, which needs a large number of evaluations of the objective and constraint functions. This would be impractical as aero-icing flow simulations are computationally intensive and prohibitive, especially when coupled with conjugate heat transfer calculations, as for ice protection systems. Instead a surrogate-based optimization approach using reduced order modeling is proposed. In this approach, proper orthogonal decomposition (POD), in conjunction with Kriging, is used to replace the expensive CHT simulations. The results obtained show that the methodology is efficient and reliable in optimizing electro-thermal ice protection systems in particular, and thermal-based ones in general.

ABRÉGÉ

Cette thèse vise la simulation numérique, l'analyse et l'optimisation de systèmes électrothermiques d'antigivrage et de dégivrage.. La simulation numérique de tels systèmes nécessite la résolution d'un problème de transfert de chaleur dit conjugué (dit CHT), entre les domaines fluides et solides. Les besoins énergétiques du système sont analysés en fonction du flux d'air, de l'angle d'attaque, de la température ambiante, du contenu en eau liquide et du diamètre des gouttelettes surfondues. Le système est ensuite optimisé afin de réduire la consommation énergétique et la puissance électrothermique, tout en assurant une protection suffisante contre le givrage. Les variables d'optimisation prises en compte sont la puissance, le dimensionnement et le temps d'activation (dans le cas du dégivrage) des revêtements électrothermiques. Plusieurs formulations du problème d'optimisation sont proposées, à la fois pour le régime évaporation partielle (durant lequel une couche liquide se forme sur le bord d'attaque de l'aile) et pour le régime évaporation totale. Ces formulations sont analysées en détail du point de vue de la physique ainsi que du point de vue mathématique. Leur performance est évaluée lors d'essais numériques pour en déterminer les plus prometteuses. L'optimisation est réalisée par l'algorithme MADS qui nécessite un grand nombre d'évaluations de l'objectif et des contraintes. Ceci devient problématique en temps calcul, car les simulations air-givre couplées avec des calculs de transfert de chaleur conjugué (dits CHT) sont extrêmement coûteuses. Pour pallier à cette problématique, nous proposons une méthode d'optimisation basée sur des modèles d'ordre réduit. Dans cette méthode, une décomposition en composantes principales, couplée à une méthode de krigeage, vient remplacer les simulations CHT coûteuses. Les résultats obtenus montrent que la méthodologie est efficace et fiable pour l'optimisation de systèmes thermiques de protection contre le givrage, en particulier pour les systèmes électrothermiques.

Chapter 1 INTRODUCTION

1.1 Background

1.1.1 In-Flight Icing

Today, all commercial transport and business aircraft must obtain several safety certifications before being considered airworthy. One of the most essential certifications is airworthiness for in-flight icing. Since 1997, the NTSB (National Transportation Safety Board), for instance, has classified icing among its “most wanted transportation safety improvements” [1], and the FAA (Federal Aviation Administration) has recently proposed, in a Notice of Proposed Rule Modification, tighter certification rules for new airplanes to deal with problems of supercooled large droplets (SLD) and of ice crystals (IC) ingestion in engines at high altitudes [2].

Despite continuous efforts to improve aircraft safety in known icing conditions, accidents and incidents still take place around the world. In-flight icing can occur when an aircraft is flying through a cloud of supercooled water droplets that are in a metastable¹ thermodynamic equilibrium at or below water freezing temperature. When hit by the body of the aircraft, the droplets go through a phase change from liquid to solid. They may freeze instantaneously or run downstream and freeze later. The former occurs at very

¹ Metastable is an unstable physical state in which droplets remain in the liquid phase even at temperatures far below freezing point.

cold temperatures, resulting in *rime ice*, while the latter occurs at temperatures closer to the freezing point, resulting in *glaze ice* (Figure 1.1). Other types of ice formation are also possible, e.g. mixed ice and frost.

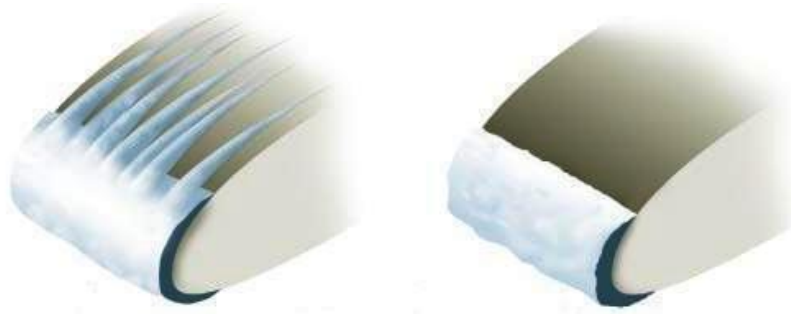


Figure 1.1: Glaze ice (left) and rime ice (right) on wing (picture adapted from *New Scientist*).

Three major factors affect the size and the shape of ice accretion: flight conditions, icing conditions and the surface conditions on which the ice accretes. Flight conditions are determined by airspeed, AoA and icing exposure time. Figure 1.2 demonstrates how different flight phases with different flight conditions affect the probability of accident. As shown, the highest percentage of accidents occurs in the shortest phases of flight. For example, landing takes only 1% of the flight time, but it accounts for about half of accidents and incidents. The second group of the influential factors, icing conditions, are characterized by cloud horizontal extent, altitude, temperature, liquid water content (LWC) and MVD. The most probable icing situations have been determined by flight safety organizations and are accessible through different icing envelopes, such as those of the FAA's FAR (Federal Airworthiness Regulations) Part 25 Appendix C. Finally, the third group of factors affecting the ice accretion is the roughness, the shape and the location of the surface on which the ice accretes. While most surfaces of the aircraft body are potentially subject to ice contamination, it is only practical to protect the most critical areas to minimize power requirements. These areas include the leading edge of wings, stabilizers, engine air intakes, propellers, Pitot tube, windshield, etc.



Figure 1.2: Time and accident percentage for different flight phases (data adapted from *Robert E. Breiling Associates*).

1.1.2 Adverse Aerodynamic Effects of Icing

Wings and lifting components are the most sensitive parts to the threat of ice accretion because their fundamental aerodynamic characteristics, i.e. drag, lift and moments, are highly affected by ice contamination. Ice accretion increases the drag by adding surface roughness, and decreases the maximum lift and stall angle of attack by inducing earlier boundary layer transition to turbulent flow (Figure 1.3). Figure 1.4 shows an instantaneous schematic of a separation bubble flow field downstream of a horn ice shape. As shown, the separation bubble occurs at the tip of the horn ice shape, after which the shear layer forms, separating the freestream flow from the recirculation region. As the shear layer moves downstream, the vortices merge and form larger vortices, which are finally shed. These ice-induced flowfield effects cause premature stall that has an important role in many accidents and incidents. Figure 1.5 shows that more than half of all events that occurred between 1978 and 2002 were due to stall. Other threatening consequences of in-flight ice accretion include tailplane stall¹ and weight increase. To avoid such detrimental effects, ice detectors, such as piezoelectric transducers, pulse echo

¹ Tailplane stall is the stall of horizontal stabilizer which is due to reduction of the maximum downward balancing force.

and microwave controllers, are used to detect any ice formation on critical surfaces. Once detected, ice may be prevented or removed by ice protection systems.

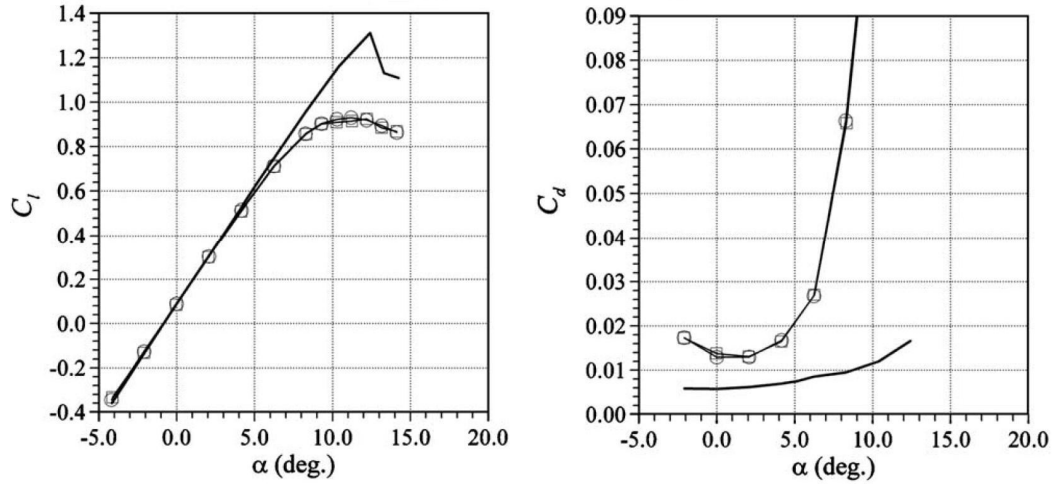


Figure 1.3: Comparison of lift (left) and drag (right) coefficients of a clean (solid line) and iced (line with circles) airfoil for $Re = 7.5 \times 10^6$ and $Ma = 0.21$ (plots adapted from [3]).

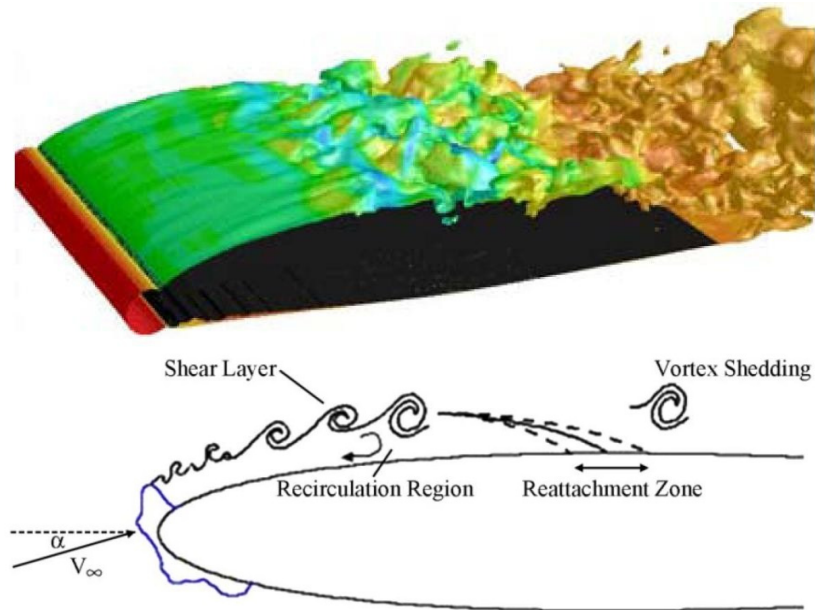


Figure 1.4: Instantaneous schematic of a separation bubble flow field downstream of a horn ice shape (picture adapted from [4] and [5]).

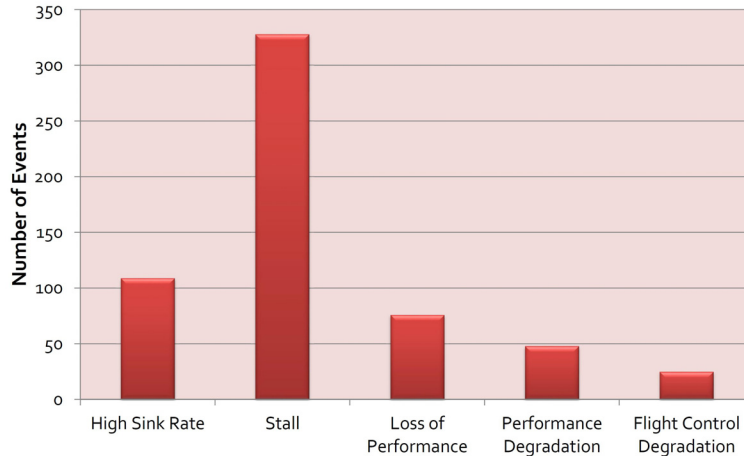


Figure 1.5: Distribution of primary occurrences due to aerodynamic, stability, control problems in the period 1978-2002 (data adapted from [6]).

1.1.3 Ice Protection Systems

Most, if not all, commercial aircraft are equipped with ice protection systems (IPS). The important role of IPS in aircraft accidents or incidents is illustrated in Figure 1.6, which is based on 693 icing events of the United States between 1978 and 2002 [6]. As shown, a large portion of the events occurred in the absence of IPS. IPS may operate in either anti-icing or de-icing modes. Anti-icing refers to prevention of ice accretion on the surface, and de-icing denotes removal of accreted ice on the surface. A wide range of ice protection systems have been developed but they, generally, can be classified into three categories in order of common use: thermal-based, mechanical-based and chemical-based methods. They are described in the following.

Thermal-based methods: In these methods, thermal energy is used for anti-icing or de-icing. There are many types of thermal-based systems, but the most common types are hot-air and electro-thermal systems. Hot-air systems consist of a number of tubes, called piccolo tubes, which transfer high-temperature bleed-air from the engine compressor, making a jet flow impingement on the inner skin of protected surfaces, such as the wing's leading edge. The bleed air then exits through holes on the lower side of the wing (Figure 1.7). Electro-thermal system is detailed in section 1.1.4.

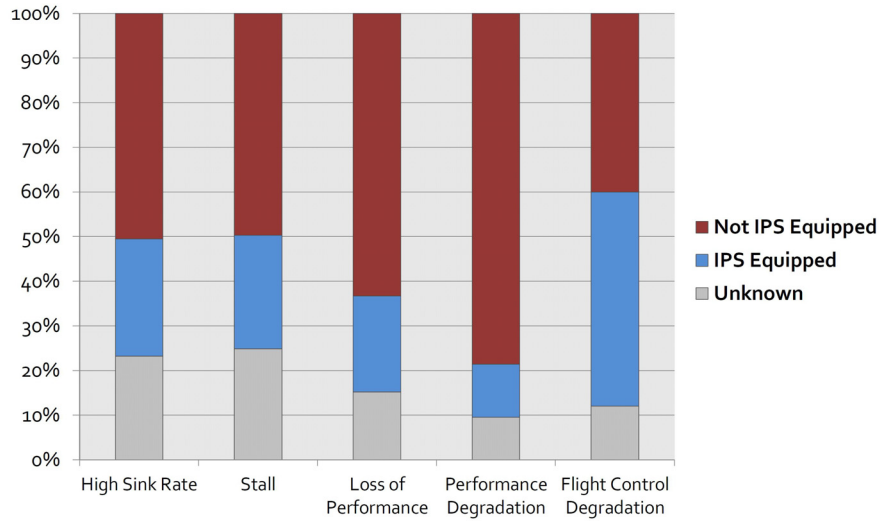


Figure 1.6: distribution of primary occurrences related to aerodynamic, stability, control, based on the use of ice protection in the period 1978-2002 (data adapted from [6]).

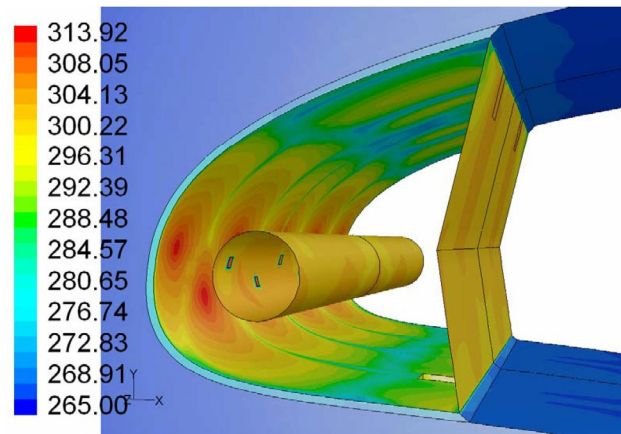


Figure 1.7: Surface temperature contour plots of a part of a wing hot-air anti-icing system (picture adapted from [7]).

Mechanical-based methods: In such methods, the iced surface suddenly deforms, imposing a stress that leads to cracking and de-bonding of the ice accumulated on the surface (Figure 1.8). Pneumatic boots are the most commonly used technique among these methods. They include rubber balloons mounted on the leading edge of the wing

and are cyclically inflated and deflated with air supplied by the pneumatic system of the airplane. Pneumatic boot systems require low power and are relatively simple and light. However, they require intensive maintenance and periodic replacement. Furthermore, they do not preserve the exact airfoil shape, especially when inflated. There is also a minimum ice thickness that can be ejected from the surface.

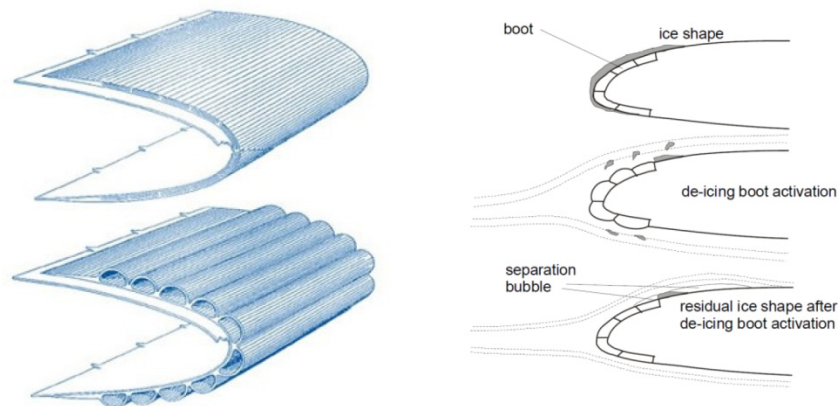


Figure 1.8: Left: *Goodrich*® pneumatic boots, before (top) and after (bottom) activation; Right: Effect of de-icing boot activation in presence of ice formation (picture adapted from [8]).

Chemical-based methods: Freezing-point depressant is a common type of chemical-based approach, in which an anti-freeze liquid solution (such as ethylene glycol) is pumped from the porous panels placed on the wings' leading edges, and vertical and horizontal stabilizers (Figure 1.9). In the case of anti-icing, the solution depresses the water freezing point when mixing with supercooled droplets, allowing the mixture to flow off the wing without freezing. In the case of de-icing, the ice-wing chemical bond is broken down by the solution, and then the ice particles are carried away by the aerodynamic forces. Beside the benefits, such as leading edge wing shape preservation, efficient ice removal, and durability [9], these systems have some drawbacks, such as fluid reservoir limitation and environmental concerns. Icephobic materials are another type of chemical-based technique. The mechanism is based on either reducing the magnitude of the adhesion

strength of the ice to less than that of the shear stress of the ice on the surface (icephobic coating), or repelling the water droplets from the surface before ice nucleation occurs (hydrophobic coating, Figure 1.10) [10]. A hydrophobic surface is able to delay icing for about 2 hours. However, it cannot completely prevent the ice formation, especially under wet and cold weather conditions [11, 12].

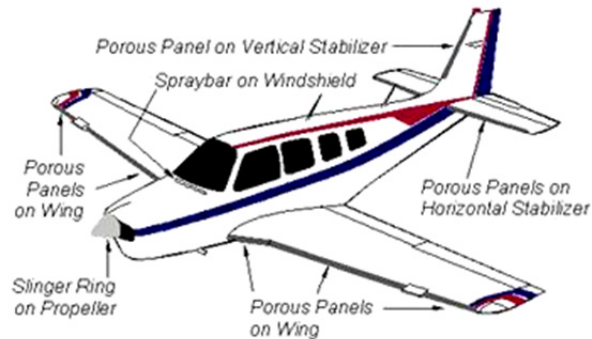


Figure 1.9: Weeping wings (picture adapted from *TKS™*).

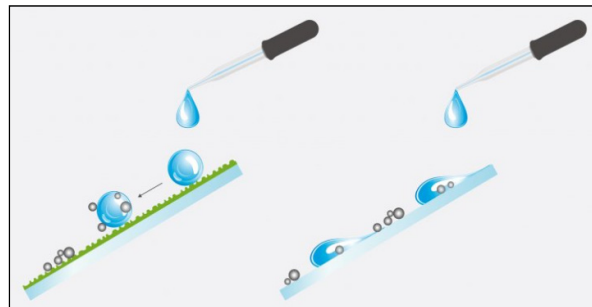


Figure 1.10: Droplet motion on a surface with (left) and without (right) hydrophobic coating (picture adapted from *Optics Balzers*).

1.1.4 Electro-Thermal IPS

In the last decades, hot-air systems have been the most widely used technology for commercial turbofan aircraft. The high amount of hot engine-core air required, from the ever-larger bypass ratio turbofans of modern aircraft, has caused the aerospace industry

to move toward *no-bleed systems*. In no-bleed systems or *more electric aircraft*, the need for bleed air and on-engine hydraulic power generation is significantly reduced and the use of electric power in the starter system of the main engine is increased [13]. The benefits of the no-bleed systems include [14]:

- Fuel consumption is improved because the extraction, transfer and usage of the secondary power are more efficient.
- Fuel consumption is reduced and range is expanded because the overall weight is lower.
- Reliability is improved because modern electronic devices are used and the engine has fewer components.
- Maintenance cost is reduced because of elimination of bleed systems, which are maintenance-intensive.
- Controlling and monitoring of the system is easier.
- An electric IPS can be fully integrated into composite structures.

The new Boeing 787 is a paradigm in this context. Figure 1.11 shows the drastic increase in the electrical power generation capacity of the 787 compared to the other types of aircraft.

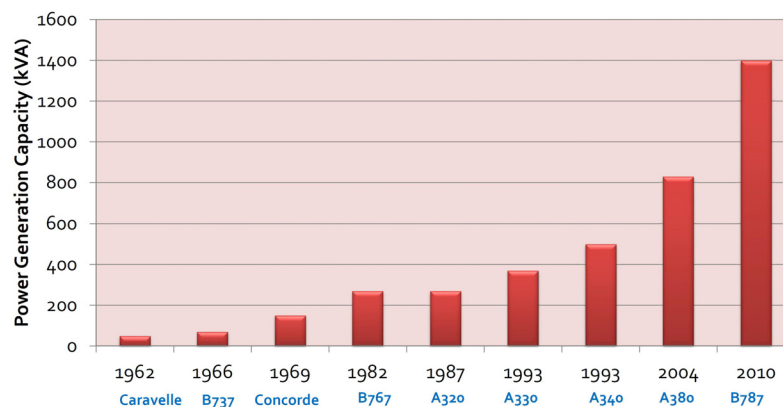


Figure 1.11: Evolution of electrical power needs (data adapted from [15]).

In contrast to conventional aircraft, in which hydraulic and pneumatic power are used in many systems (Figure 1.12), bleed air on the 787 is used only for the nacelle's ice protection system and for pressurizing hydraulic reservoirs. The wing ice protection system, the hydraulic pumps, control systems, and engine starter are the systems using electricity. The 787 uses an electro-thermal IPS, in which several electric heaters are embedded inside the skin of the leading edges (Figure 1.13). The electric heating pads may then be activated, simultaneously for anti-icing or sequentially for de-icing, to protect the wing's leading edge. Since no excess energy is exhausted, the electro-thermal IPS is more efficient and uses less power compared to the traditional hot-air system. Moreover, there are no bleed air exhaust holes in this system because it can be fully integrated into composite structures. As a result, airplane noise and drag are improved.

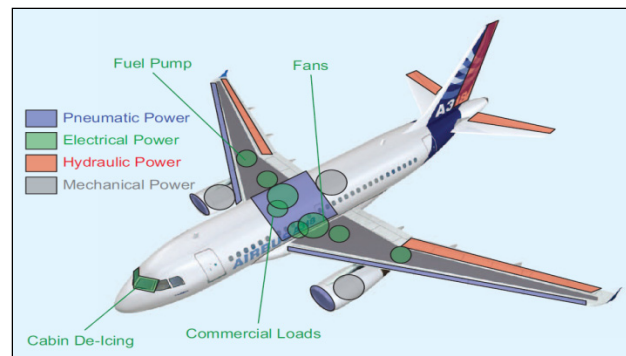


Figure 1.12: A conventional architecture with four different energy vectors (picture adapted from [15]).

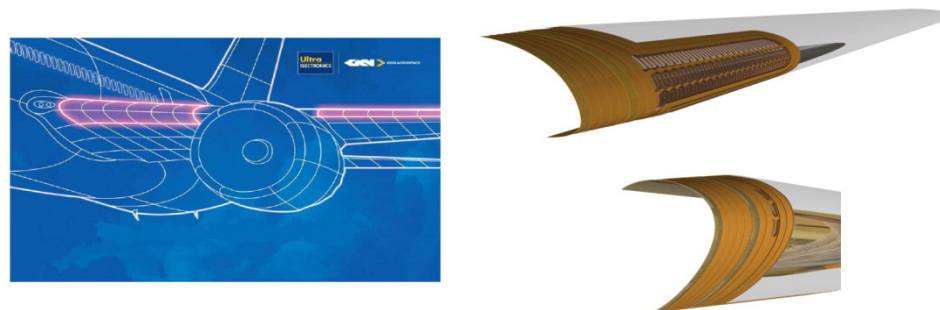


Figure 1.13: Leading edge electro-thermal IPS (pictures adapted from *GKN* and *FMLC*).

1.2 Review of Literature

1.2.1 In-Flight Icing

The earliest efforts on aircraft icing date back to the late 1920's [16] and the early 1930's [17]. The work in this area grew extensively after World War II and the postwar period in the form of wind tunnel testing and flight testing. Practical difficulties and the high cost of these two techniques, as well as advances in computer technologies, encourage engineers to use numerical simulation as a complementary tool in this context. For icing simulations, the analyses of three disciplines must be coupled: airflow, water droplet impingement and ice accretion.

A wide range of numerical methods have been used for the airflow analysis of in-flight icing simulation. Conformal mapping [18], one of the oldest methods developed for the potential flow, was used for obtaining the airflow solution around airfoils [19] and propellers [20] in icing conditions. The panel method, developed in the 1950s in the Douglas Aircraft Company [21], also presents the solution of the potential flow problems. There are a considerable number of studies using this traditional method for aircraft icing [22, 23]. The emergence of more powerful computers and progress in computational fluid dynamics (CFD) led to the simulation of inviscid compressible flows and, ultimately, turbulent viscous compressible flows for all aspects of in-flight icing [24-26].

After solving the airflow, water impingement can be determined by considering the force balance (inertial, drag, gravitational and buoyancy) on the droplets. In the Lagrangian approach [27], the trajectory of each droplet is obtained by solving the balance equation from a distant starting point to the impact point on the surface of the leading edge. This approach can be problematic and computationally expensive in the context of complex geometries. In the Eulerian approach, proposed in the late 1990's [28], the transport partial differential equations for the momentum and phase volume fraction are solved. In this approach, many difficulties of the Lagrangian method are eliminated. More extensions to this approach can be found in [29].

After obtaining the solutions of dry airflow and water impingement, thermodynamic calculations are applied to determine the surface temperature distribution, the runback and freezing flow rate, the ice accumulation rate and the resulting ice shape. The first mathematical formulation for ice accretion was developed by Tribus [30] and later improved by Messinger [31]. The Messinger model has been widely used for ice accretion prediction. The model works well for rime ice simulation, but it has some drawbacks and limitations in modeling glaze ice accretion [32].

1.2.2 Ice Protection Systems

Thermal-based methods (Hot-air systems): As previously mentioned, hot-air systems include the impingement of jets on the inner skin of the surfaces that need to be protected against icing. In this case, heat transfer consists of heat conduction through the solid skin and heat convection caused by the internal and external airflow fields. Typically, there are two main methods to handle such types of heat transfer problems: the empirical method and the conjugate method. The empirical method employs generic correlations, while in the conjugate method, the boundary conditions at all fluid-solid interfaces are iteratively exchanged until the entire domain reaches thermal equilibrium. A vast body of research activities has focused on elaboration of heat transfer correlations for jet impingement configurations, among those being the experimental [33] and numerical [34] investigation of jet arrays on flat surfaces. Empirical methods are simpler and faster, but less precise than conjugate methods. Croce *et al.* [35] studied a thermal anti-icing device by means of a 2D/3D Navier-Stokes (N-S) code. The 3D numerical results and conjugate heat transfer computations showed the capability of the N-S approach to give a more meaningful picture of the complex flow inside the slat of an aircraft wing. A mathematical model of a hot-air anti-icing system was presented by Morency *et al.* [36]. Conduction in the skin was taken into account with a one-dimensional model. A 3D unsteady thermodynamic simulation model, developed by Hua *et al.* [37], described the dynamic response of a wing anti-icing system. In this model, the unsteady internal and

external thermal flow simulation was presented and the heat conductivity inside the solid skin was simulated by a structured mesh.

Thermal-based methods (Electro-thermal systems): The first reported study on detailed modeling of electro-thermal de-icing systems was done by Keith and Witt [38]. They solved the transient heat conduction problem using a finite difference method for three different models of a composite structure: a 1D model, a 2D model taking into account lateral conduction effects and a coordinate transformed 2D model that accounts for the airfoil surface curvature. Among those, the third model gave the best results. Roelke and Keith [39] used the method of assumed states (MOAS) [40] to reduce the number of iterations for solving the energy conservation equation and calculated the transient thermal behavior of a 1D iced electro-thermal deicer pad. 2D models were later developed by Henry [41] as well as by Wright and Keith [42]. Yaslik and Witt [43] presented a 3D transient heat conduction model, in which instead of calculating ice accretion, an assumed accretion rate could be input by the user. Typically, despite having high numerical efficiency, the finite difference methods are less capable when applied to irregular 2D/3D problems. Finite element methods (FEM) can properly handle complex geometries. Huang and Keith [44, 45] employed FEM for the simulation of electro-thermal de-icing problems. Huang *et al.* [46] also used FEM to investigate the effect of surface curvature on the numerical results. They revealed that when the surface curvature is less than a specific value, curvature effects could be neglected and a rectangular shape may be used instead of the actual airfoil geometry. In 1997, experimental validation of two of NASA's codes was conducted [47]: The LEWICE/Thermal code (an electro-thermal anti-icing and de-icing simulation code) [48] and the ANTICE code (a steady state hot-air and electro-thermal anti-icing simulation code) [49]. For the LEWICE/Thermal code, the results showed that the code performed well for the warmer cases but showed significant underestimation for the colder cases. For the ANTICE code, numerical predictions were very close to the experimental measurements for the running-wet regime. For the evaporative regime, numerical results were acceptable near stagnation, but marginal elsewhere. Silva *et al.* [50, 51] developed a satisfactory estimation of heat and mass transfer around an ice-protected airfoil by considering a boundary layer mathematical model with coupled heat and mass transfer effects. Kato

[52] used a perturbation method to obtain the runback water mass flow rate and the surface temperature distributions on the body surface for an electro-thermal or a hot-air anti-icing system of an aircraft.

Mechanical-based methods: A pneumatic de-icing boot was developed by Goodrich in 1923. Although the systems have since improved, yet the operating principle remains the same. In the pneumatic impulse ice protection (PIIP) system [53], which is a variation of the pneumatic boot system, a matrix of flat, stretchable, fiber-reinforced elastomeric tubes are inflated within a very short time (about 50 μ s) which breaks up surface ice. This system was also analyzed for use in the composite rotor blade [54]. Electro-impulse de-icing (EIDI) systems, another variation, were suggested as early as 1937 by Goldschmidt. EIDI systems consists of Flat-wound coils (which are connected to a high voltage capacitor bank) made of copper ribbon wires that are placed just inside the leading edge of a wing's skin with a small gap separating the skin and coil [55]. When the capacitor is discharged through the coils, an electro-magnetic field is created that rapidly forms and collapses, inducing eddy currents in the metal skin and creating a strong but short repulsive force that results in the de-bonding and expulsion of the ice. In spite of the early interest in the EIDI system, it was not widely developed. Instead, its variation, i.e., the electro-magnetic expulsion de-icing system (EMEDS) has evolved into a system certified by the FAA [56]. Some applications of EMEDS can be found in [57, 58]. There are also a number of works investigating other mechanical-based approaches, such as the thermo-mechanical expulsion de-icing system (TMEDS) [56], the piezoelectric transducer [59] and the shape memory alloy [60].

Chemical-based methods: Application of freezing-point depressants in ice protection systems started in the 1930's and continued until World War II when porous-leading-edge wings (weeping wings) were developed by British aeronautical engineers [61]. In the context of icephobic and hydrophobic coatings, many materials have been investigated. In 1998, several coatings were tested and ranked by Mulherin *et al.* [62]. Another set of materials was tested and reported in 2004 in "Laboratory Ice Adhesion Test Results for Commercial Icephobic Coatings for Pratt & Whitney at CRREL", including a silicone coating from NuSil Technology [63]. More recently, nanotechnology

has instigated further research on the use of carbon nanotubes in hydrophobic materials [64].

1.2.3 Improvement of Thermal-Based IPS

Hot-air systems: Al-Khalil *et al.* [65] developed a 3D water droplet accretion and water runback model for the inlet cowl and nacelle of a turbofan engine to determine the temperature distribution of the surface and water and thus, to predict operating parameters required for keeping the impinged water from freezing. It was found that if most of the hot air is directed to the stagnation line on the cowl leading edge, liquid runback is maintained better. Saeed [66] simulated various arrangements of hot-jets, including a single array, two-staggered arrays at different angles and a case with an etched surface or inner liner. The results revealed that the last case yields better surface heat transfer than the others. Papadakis *et al.* [67] conducted some experimental tests with a 60-in chord business jet wing equipped with a hot-air IPS to demonstrate the effects of piccolo hot air mass flow and temperature, angle of attack, air speed, piccolo hole pattern and leading edge skin insulation on the system performance. Wong *et al.* [68] developed a full-span model of a hot-air anti-icing system to investigate the flow development inside the piccolo tube using a conjugate heat transfer analysis with a 3D N-S computer code and compared the results with the experimental data obtained by Papadakis *et al.* [67]. Planquart *et al.* [69] conducted an experimental test in which he applied the quantitative infrared thermo-graph technique for mapping of the convective heat transfer in a multi-jet hot-air anti-icing system and investigated the effects of the jet Reynolds number, the distance between the supply duct and the skin, and the span-wise and chord-wise jet arrangement on the performance of the system.

Electro-thermal systems: In [70], a wind tunnel study of electro-thermal de-icing of wind turbine blades was done to demonstrate the relationship between the wing surface temperature, the heating power, the ridge formed by liquid water runback and the meteorological conditions. Another study [71] introduced a recent development in electro-thermal heating technology that enables increased power densities on the leading

edge of aircraft wings for the purpose of de-icing. Another work [72] tested the application of conductive polymer nanocomposites in making highly efficient electro-thermal IPS. In [73, 74], numerical approaches to performance degradation analysis were performed to provide guidelines for the design of wind turbine electro-thermal anti-icing systems. *Clean Sky*, an aeronautical research program in Europe, has recently launched a project on the combination of smart coatings with electro-thermal systems to minimize the runback ice over natural laminar flow wing surfaces [75].

Despite numerous efforts on parametric studies of IPS, works on IPS optimization are relatively little and have mainly been focused on hot-air systems. Saeed and Paraschivoiu [76] employed genetic algorithms and used CANICE to find the optimum characteristics of a hot-air jet, such as the temperature, Reynolds number, nozzle size, height and spacing in case of multiple jets. Santos *et al.* [77] used a Sobol design of experiments (DOE) procedure and performed a sensitivity analysis to determine the more significant parameters in optimizing a bleed-air anti-icing system. More recently, using FENSAP-ICE, Pellissier *et al.* [78] constructed a methodology based on 3D computational fluid dynamics, reduced order models (to limit the number of necessary computations), and genetic algorithms to determine the optimal configuration of a piccolo tube of a swept wing slat. Jet angles, hole spacing and distance from the leading edge were considered as design variables and the goal was to achieve fully evaporative conditions on the upper surface and minimal runback on the lower surface.

1.3 Objectives and Outline

To provide a safe protection, the no-bleed systems require generation and storage of significant electrical power on the aircraft. There are restrictions, however, on the weight of the generators that can be installed on an aircraft because the Fuel consumption of an aircraft heavily depends on its weight. Moreover, due to aircraft design criteria and constraints, the size and number of the generators are also restricted. Therefore the power loads should be kept as low as possible. Figure 1.14 provides the typical power level for electrical loads on an aircraft. As shown, the wing IPS only trails air conditioning as the

aircraft's highest load. This highlights the necessity of minimizing the energy usage of the anti-icing system, while ensuring a safe protection. The present dissertation aims to fill the gap in knowledge in the area of optimization of electro-thermal IPS, which, to the best of our knowledge, has not been fully numerically studied. To do so, this work is focused on analyzing the energy requirements of electro-thermal ice protection systems under various icing conditions and to develop an efficient, reliable and practical methodology for optimization of such systems. In the next chapter, the numerical simulation of electro-thermal IPS is presented. Chapter 3 presents the analysis of the energy requirements of an electro-thermal IPS. This provides us with a better insight into IPS performance, which consequently makes the IPS optimization more realistic and efficient. In Chapter 4, the optimization of electro-thermal anti-icing systems is presented. A surrogate-based optimization is described in Chapter 5 as an efficient tool for reducing the computational cost. Finally, the optimization of an electro-thermal IPS in transient de-icing mode is presented in Chapter 6.

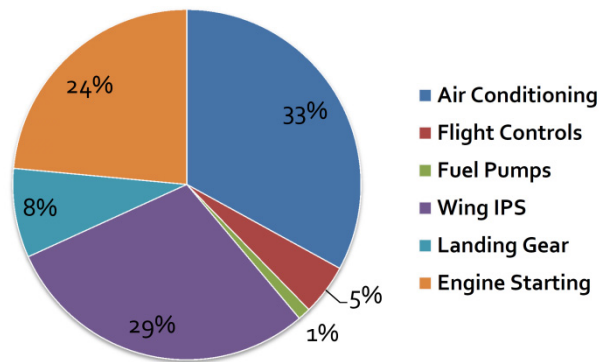


Figure 1.14: Typical power level for electrical loads on an aircraft (data adapted from [79]).

1.4 Discussion and Conclusions

In this chapter, in-flight icing as one of the most important threats to the aircraft safety was introduced and the hazardous effects of ice accretion on the aerodynamic performance of different parts of the aircraft, especially on the lifting components, such

as wings and tails were discussed. The discussion is supported by both physical and statistical evidences. As stated, in-flight ice protections systems (IPS) can be used as effective tools for avoiding such detrimental effects. They can be used in anti-icing mode (to prevent ice accretion) or de-icing mode (to remove accreted ice). Ice protection systems can be categorized into three general types: chemical-based, mechanical-based and thermal-based. There are advantages and drawbacks for each type. In the last decades, hot-air anti-icing systems, which are thermal-based IPS, have been the most prevalent. However, since the aerospace industry has recently moved toward more electric aircraft, electro-thermal systems are emerging as a viable alternative. Also, past research works in these areas, especially on electro-thermal systems that is the main focus of the present dissertation, were reviewed.

Chapter 2 SIMULATION OF ELECTRO-THERMAL ANTI-ICING

2.1 In-Flight Icing Simulation

2.1.1 Framework

Before performing the IPS simulation, the numerical simulation of in-flight icing shall be first briefly discussed. The general framework of icing simulation is illustrated in Figure 2.1: it consists of the successive solution of three parts: airflow, droplet impingement and ice accretion. The velocity field obtained by the airflow solution is used to compute the droplet impingement. Then, friction forces and heat fluxes from the airflow solution, along with droplet velocity and collection efficiency from the droplet impingement solution, are used to compute the surface node displacement due to ice accretion. In this thesis, the high-fidelity FENSAP-ICE system [80] consisting of a collection of modules (FENSAP, DROP3D, ICE3D), is used.

In order to fully account for the effects of compressibility and viscosity, the compressible Navier-Stokes equations are solved. There are a wide range of numerical approaches to simulate turbulent flows, such as Direct Numerical Simulation (DNS), Large Eddy Simulation (LES), Detached Eddy Simulation (DES) [81], etc. However, currently the Reynolds-Averaged Navier-Stokes (RANS) equations, together with a turbulence model, offer sufficiently accurate solutions at an acceptable computational cost. The

conservation and the Spalart-Allmaras turbulence equations are solved using an implicit weak-Galerkin FEM and a Newton linearization of the primitive variables. A local time-stepping approach for steady-state problems and a second-order Gear scheme for unsteady problems are used. The linear systems are solved using the Generalized Minimum Residual (GMRES) method with a diagonal pre-conditioner to iteratively solve the resulting matrix system. Being important for icing calculations, convective heat fluxes at the walls are obtained via the accurate second-order Gresho method [82]. In this method, the heat fluxes at the walls can be evaluated by the same discretized energy equation, in which temperature gradient is replaced by heat flux.

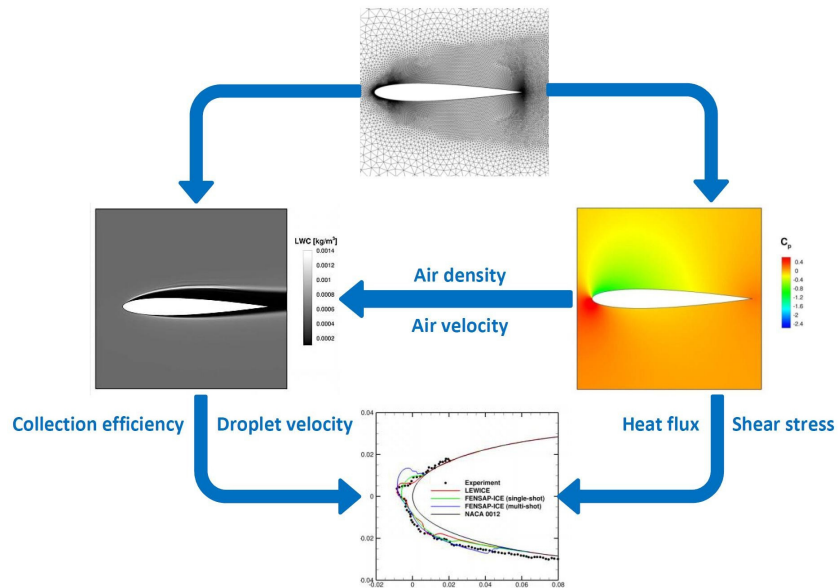


Figure 2.1: General framework of in-flight icing simulation.

The traditional Lagrangian approach for computation of droplet impingement is not suitable for complex geometries or multi-element airfoils. As an alternative, the Eulerian approach [28] is used here, in which the transport PDEs for suitable variables are solved and computed only at the nodes of the computational mesh where the airflow variables are already known. Hence, no particle tracking is required as in the Lagrangian approach.

In icing calculations, the loading¹ is of the order of 10^{-3} . Usually, two-phase flows with a loading smaller than 10^{-1} may be reasonably well modeled by a one-way coupling [83]. Thus, the Navier-Stokes equations need no modifications. The droplet equations are solved for droplets velocity \mathbf{u}_d and the ratio of the volume occupied by water over the total volume of the fluid element, α . These equations are given as follows:

$$\frac{\partial \alpha}{\partial t} + \nabla \cdot (\alpha \mathbf{u}_d) = 0, \quad 2-1$$

$$\frac{\partial \mathbf{u}_d}{\partial t} + \mathbf{u}_d \cdot \nabla \mathbf{u}_d = \frac{C_D \text{Re}_d}{24K} (\mathbf{u}_a - \mathbf{u}_d) + \left(1 - \frac{\rho_a}{\rho_w}\right) \frac{1}{\text{Fr}^2} \mathbf{g}, \quad 2-2$$

where \mathbf{u}_a and \mathbf{u}_d are the non-dimensional velocity of air and droplets, respectively, ρ_a and ρ_w are the density of air and water, respectively. The first term on the right-hand side of Eq. 2-2 represents drag force and the second term represents gravity and buoyancy forces. Re_d is the droplets Reynolds number, Fr is the Froude number and K is an inertial parameter. According to a characteristics analysis [84], boundary conditions are needed for the two variables only on the inflow, and not on the outflow or on the walls. The following initial solution is used: $\mathbf{u}_d = (\cos(AoA), \sin(AoA))$ and $\alpha = 1$ everywhere and $\mathbf{u}_d = 0$ and $\alpha = 0$ near the walls. After calculating \mathbf{u}_d and α , the local collection efficiency β , i.e. the normalized flux of water on the walls, can be computed as follow:

$$\beta = -\alpha \mathbf{u}_d \cdot \mathbf{n}, \quad 2-3$$

where \mathbf{n} is the unit vector normal to the surface. The impinging water flux, \dot{m}_{imp}'' , at the aerodynamic surface is then given by

$$\dot{m}_{imp}'' = \text{LWC}(U_\infty \beta), \quad 2-4$$

where LWC is liquid water content.

The ice accretion model should contain all the mass and heat transfer mechanisms at the body surface involved in ice accretion process. For mass and energy balances, the

¹ Loading is the ratio of the bulk density of the droplets over the bulk density of the air.

Messinger [31] thermodynamic model is used that applies the first law of thermodynamics. In icing or IPS simulations, the water film thickness is rarely above 20 μm ; therefore, the thin water film can be assumed to have a linear velocity profile. Several mechanisms contribute to the mass transfer during ice accretion, including sublimation, evaporation, water impingement and ice accretion. With these assumptions, the conservation of mass of the water film results in the following PDE:

$$\rho_w \left[\frac{\partial h_f}{\partial t} + \nabla \cdot (\bar{\mathbf{u}}_f h_f) \right] = \dot{m}''_{imp} - \dot{m}''_{evap/sub} - \dot{m}''_{ice}, \quad 2-5$$

where $\bar{\mathbf{u}}_f$ and h_f are the velocity and height of the water film, respectively, \dot{m}''_{ice} is the mass flux of ice accretion and $\dot{m}''_{evap/sub}$ is the mass flux of evaporation/sublimation, which can be evaluated by the following parametric model [22]:

$$\dot{m}''_{evap/sub} = \frac{0.7c_h}{c_{p,a}} \left[\frac{P_{v,p} - H_{r,\infty} P_{v,\infty}}{P_s} \right], \quad 2-6$$

$P_{v,p}$ being the saturation vapour pressure at the surface, $P_{v,\infty}$ the saturation vapour pressure of water in ambient air, P_s the absolute pressure above the control volume outside the boundary layer, $H_{r,\infty}$ the relative humidity, $c_{p,a}$ the specific heat capacity of air and c_h the convective heat transfer coefficient. The saturation vapor pressure is computed via an approximation [85] of the saturated steam table [86] values:

$$p_{v,p} = 3386 \left[0.0039 + 6.8096 \times 10^6 \hat{T}_s^2 + 3.5579 \times 10^7 \hat{T}_s^3 \right], \quad 2-7$$

where $\hat{T}_s = 72 + 1.8T_s$ is the surface temperature. For energy balance, various heat transfer mechanisms involved in the ice accretion process, including sublimation, evaporation, kinetic energy, sensible energy, convection, irradiation, fusion and conduction. Considering these mechanisms, the PDE for the conservation of energy can be given as follows:

$$\begin{aligned}
\rho_w \left[\frac{\partial (h_f c_{p,w} T_s)}{\partial t} + \nabla \cdot (\bar{\mathbf{u}}_f h_f c_{p,w} T_s) \right] = \dot{m}''_{imp} \left[\frac{\|\mathbf{u}_d\|^2}{2} + c_{p,w} (T_{d,\infty} - T_s) \right] \\
- \frac{1}{2} \dot{m}''_{evap/sub} (L_{evap} + L_{sub}) + \dot{m}''_{ice} (L_{fus} - c_{p,ice} (T_m - T_s)) \\
+ c_h (T_{rec} - T_s) + \sigma \varepsilon (T_\infty^4 - T_s^4),
\end{aligned} \tag{2-8}$$

where $c_{p,w}$ and $c_{p,ice}$ are the specific heat capacities of water and ice, respectively, T_s is the equilibrium temperature at the air/film/ice/wall interface, T_{rec} is the recovery temperature, T_∞ is the ambient temperature, $T_{d,\infty}$ is the farfield temperature of droplets, T_m is the melting (freezing) temperature of water, L_{evap} , L_{sub} and L_{fus} are the latent heats of evaporation, sublimation and fusion, respectively, σ is the Stefan-Boltzmann constant and ε is the solid emissivity. There are two approaches for calculating ice accretion with time: the single-shot and the multi-shot. With the single-shot approach, the ice accretion is calculated based on the initial airflow and droplet solutions. With the multi-shot approach, the airflow and droplet solutions are updated during the ice accretion at certain time steps. For mesh deformation in this approach, the arbitrary Lagrangian-Eulerian (ALE) method is used, in which the best characteristics of both the Lagrangian and the Eulerian methods are combined. That is, the nodes of the computational mesh may be moved with the body (as in the Lagrangian method), or be held fixed (as in the Eulerian method) or be moved in some way that yields a continuous rezoning [87].

2.1.2 Numerical Test Case

The numerical simulation of an icing test case is presented in this section and the results are compared with the experiments (run #316) performed in the NASA Lewis Icing Research Tunnel (IRT) [88]. The results are also compared with NASA's icing computer code, i.e. LEWICE. The model is a NACA 0012 with a chord length of 0.5334 m. The ice accretion time is 193.2 seconds. The flight and icing conditions for this test case are provided in Table 2.1.

Table 2.1: Flight and icing conditions.

Temperature [K]	Velocity [m.s ⁻¹]	LWC [g.m ⁻³]	MVD [μ m]	AoA [deg.]
262.04	102.8	0.55	20	4

Figure 2.2 shows the hybrid grid [89] around the clean airfoil and the displaced grid around the iced airfoil. The surface distributions of the clean and the iced airfoils are shown in Figure 2.3. At the tip of the horn ice shape on the upper surface, a separation bubble occurs, in which low pressure vortices move downstream. A weaker separation bubble also occurs at the tip of the ice on the lower surface. The oscillatory pressure reductions on both upper and lower surfaces are due to the separation bubbles, which formed to reduce the necessary pressure recovery. A constant pressure region was followed by recovery, which indicates shear-layer transition and reattachment of the flow. The contour plots of the turbulent viscosity are depicted in Figure 2.4, in which an earlier boundary layer transition to turbulent flow is observed in the iced case. Figure 2.5 shows the surface distributions of the collection efficiency before and after ice accretion. As shown for the iced case, the extent of the collection efficiency distribution has decreased but the peak value has increased. Figure 2.6 compares the final ice shape obtained by the experiment, LEWICE, FENSAP-ICE (single-shot) and FENSAP-ICE (multi-shot). Although the multi-shot approach does not give the best result on the upper surface, it yields the closest ice shape to the experiment on the lower surface.

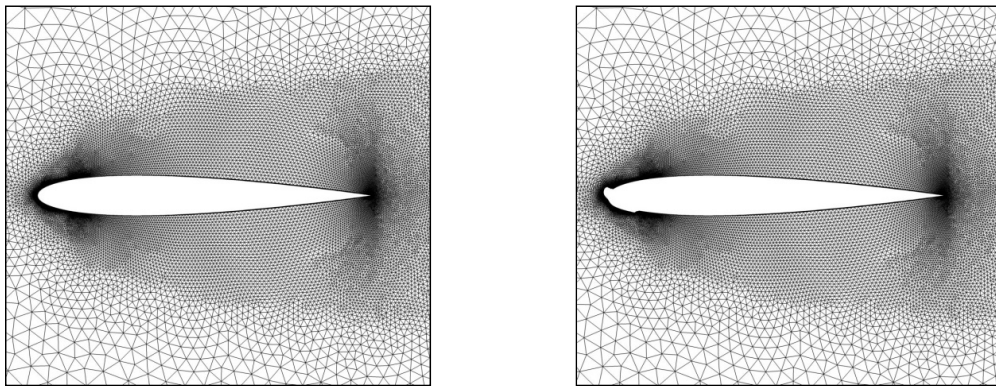


Figure 2.2: Hybrid grid around the clean airfoil (left) and displaced grid around the iced airfoil (right).

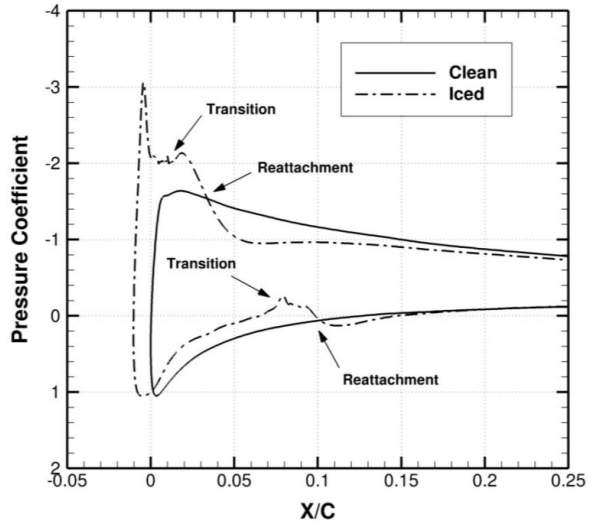


Figure 2.3: Surface distributions of pressure coefficient for clean and iced airfoils.

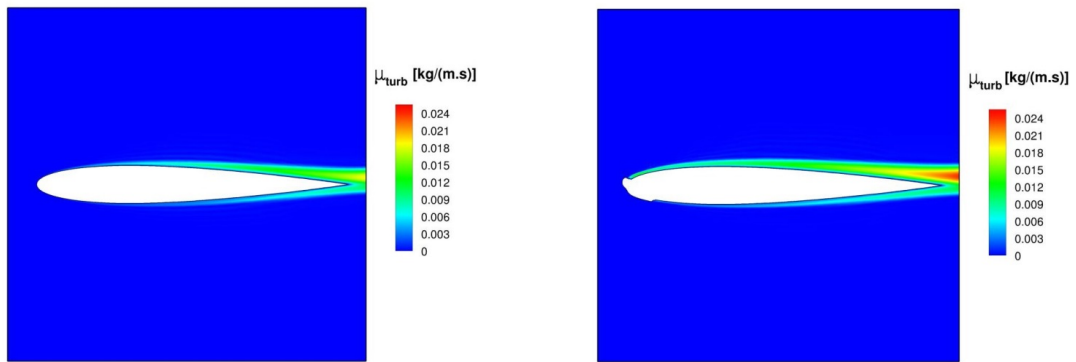


Figure 2.4: Contour plots of turbulent viscosity for clean (left) and iced (right) airfoils.

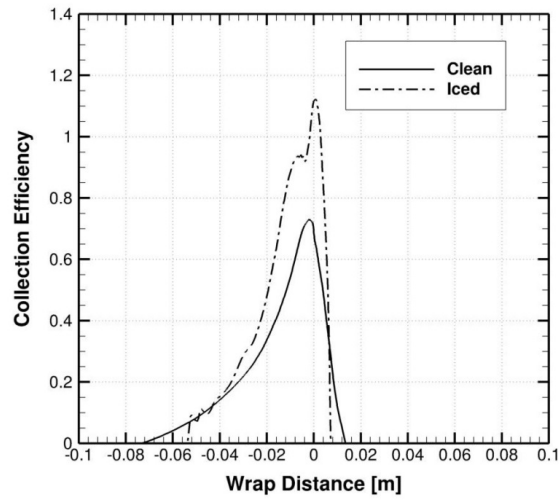


Figure 2.5: Surface distributions of collection efficiency for clean and iced airfoils.

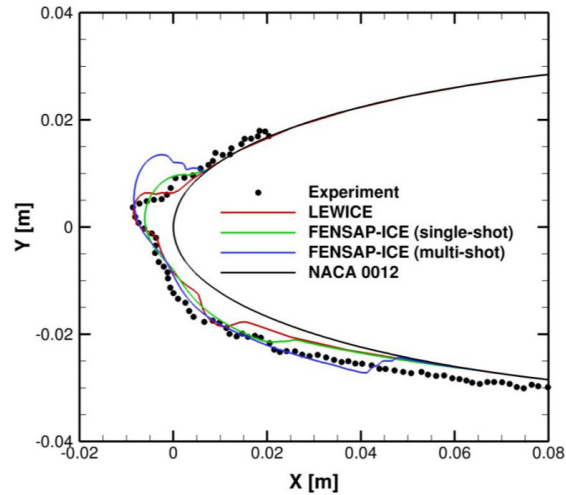


Figure 2.6: Comparison of ice shapes obtained by different methods.

2.2 IPS Simulation

For the in-flight icing simulation, it is assumed that no heat flux is transferred through the solid skin. To perform the numerical simulation of electro-thermal IPS, one needs to consider the heat conduction generated by the IPS. This heat conduction solution is coupled with the ice accretion solution to solve the conjugate heat transfer (CHT) problem between the fluid and the solid using the CHT3D [90] module of FENSAP-ICE. This is performed by making the various domains converge using a fixed-point iteration process that exchanges the thermal boundary conditions among the external airflow, water film and solid skin interfaces (Figure 2.7).

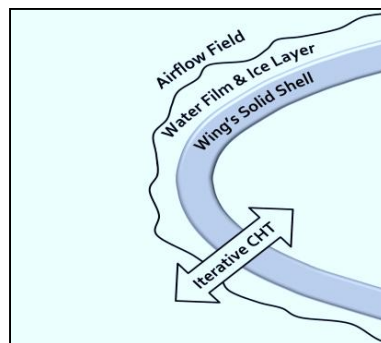


Figure 2.7: Domains involved in the CHT procedure.

To perform the IPS simulation, an electro-thermal IPS model is selected from the very few experiments available in the open literature. This model was used in the experimental tests performed in the NASA Lewis Icing Research Tunnel (RIT) [49]. It consists of seven independently controlled electric elements that are embedded inside a four-layer composite panel, including the erosion shield, elastomer, fiberglass and silicone foam. The IPS model is illustrated in Figure 2.8 and the physical properties of the materials are provided in Table 2.2. According to [49], due to fabrication errors that occurred in the experiments, the heating zones had been slightly shifted toward the upper side.

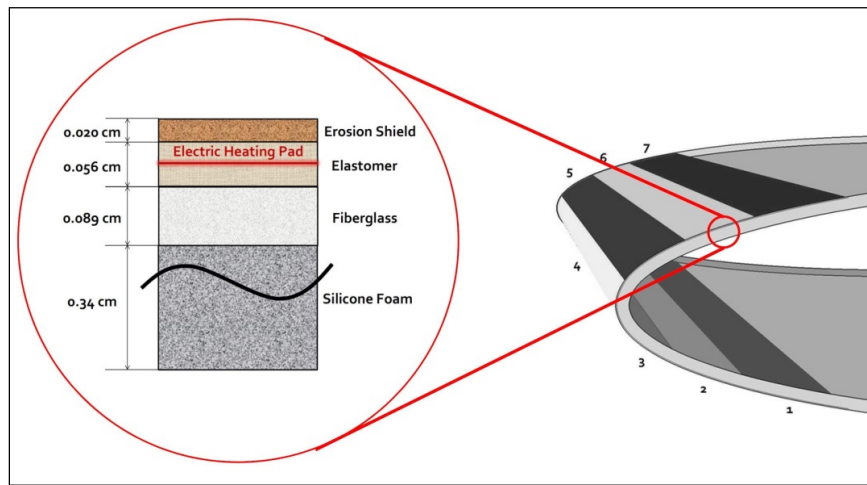


Figure 2.8: Schematic picture of the electro-thermal IPS.

Table 2.2: Material properties of the composite shell at the leading edge.

Material	ρ [kg.m ⁻³]	k [W.m ⁻¹ .K ⁻¹]	c_p [J.kg ⁻¹ .K ⁻¹]
Erosion shield, SS 301 HH	8025.25	16.269	502.42
Elastomer, COX 4300	1383.99	0.256	1256.04
Fiberglass / Epoxy composite	1794.07	0.294	1570.05
Silicone foam insulation	648.75	0.121	1130.44

The flight and icing conditions are provided in Table 2.3. The domain discretization for the fluid and the composite panel is shown in Figure 2.9. A hybrid grid [89] is used

around the airfoil and a structured one inside the leading edge's composite shell. The surface temperature distribution is shown in Figure 2.10. The measurement errors in the experiments due to positional, data acquisition and sensor uncertainties are also illustrated by the red bars. The results obtained by CHT3D and NASA's experimental and numerical results, as shown, are in close agreement with each other.

Table 2.3: Flight and icing conditions.

Temperature [K]	Velocity [m.s ⁻¹]	LWC [g.m ⁻³]	MVD [μ m]	AoA [deg.]
266.483	44.704	0.78	20	0

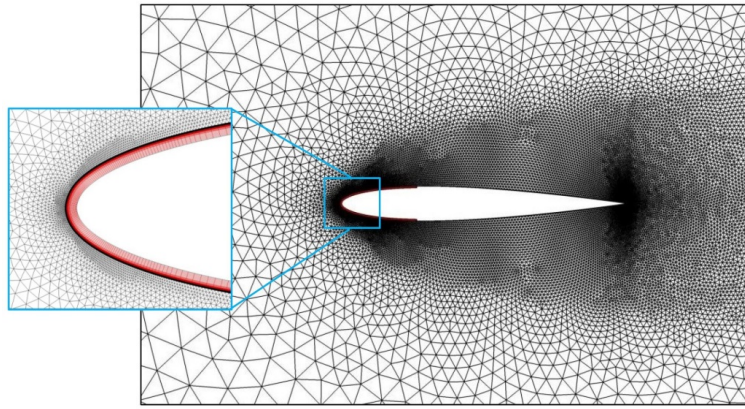


Figure 2.9: Hybrid grid around the NACA0012 airfoil and structured grid inside the leading edge composite shell.

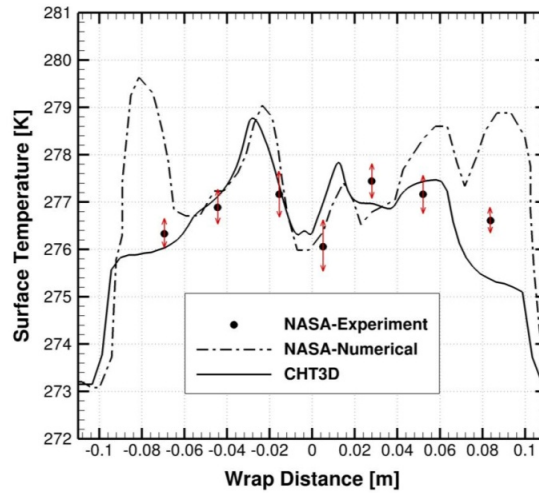


Figure 2.10: Comparison of the surface temperature distribution.

The iterative procedure of CHT is expensive, as each domain (especially the fluid domain) could take a considerable amount of time to converge. This makes it impractical to use this procedure within an optimization framework, which needs hundreds or thousands of CHT calculations. To reduce the CHT cost, several strategies may be used. One strategy would be that during the CHT iterations, one could repeatedly solve the energy equation for the external flow field, rather than the entire N-S equations. This would be a good approximation because compressibility effects are not significant if the Mach number is not high, as is typical in icing cases. Another strategy would be to use the heat transfer coefficient of the initial N-S solution, avoiding the repetition of the N-S calculation during the CHT iterations. The logic behind this is that the heat transfer coefficient, which is needed for the CHT calculation does not change much with the surface temperature. As shown in Figure 2.11, the heat flux distribution changes significantly with the surface temperature, but the variations in the heat transfer coefficient distribution are small, especially at the leading edge. Using this strategy, the accuracy of the CHT solution would not be significantly affected, yet the computational cost would be dramatically reduced. Figure 2.12 compares the surface temperature distributions and the convergence history of the minimum and maximum surface temperatures over 50 iterations of the CHT calculation. As shown, the differences between approaches are quite small.

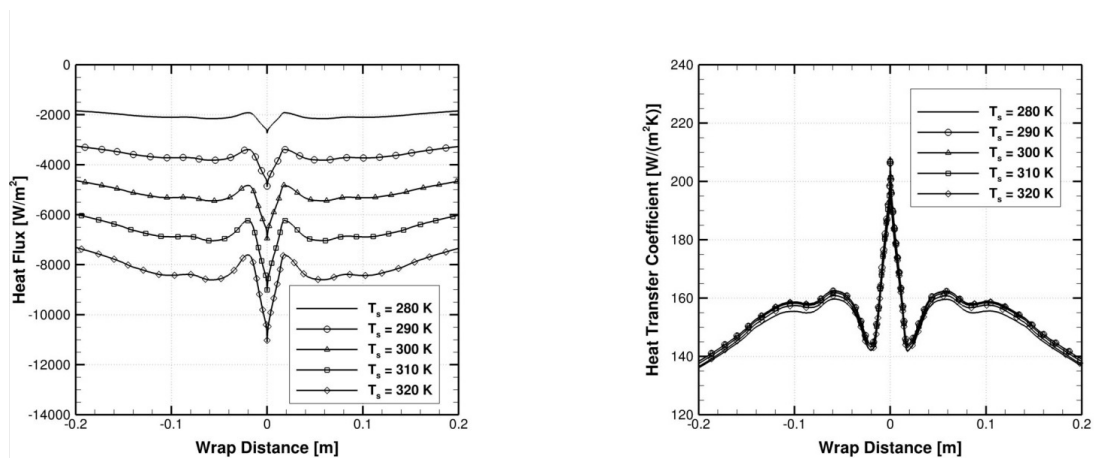


Figure 2.11: Heat flux (left) and heat transfer coefficient (right) distributions for different surface temperatures.

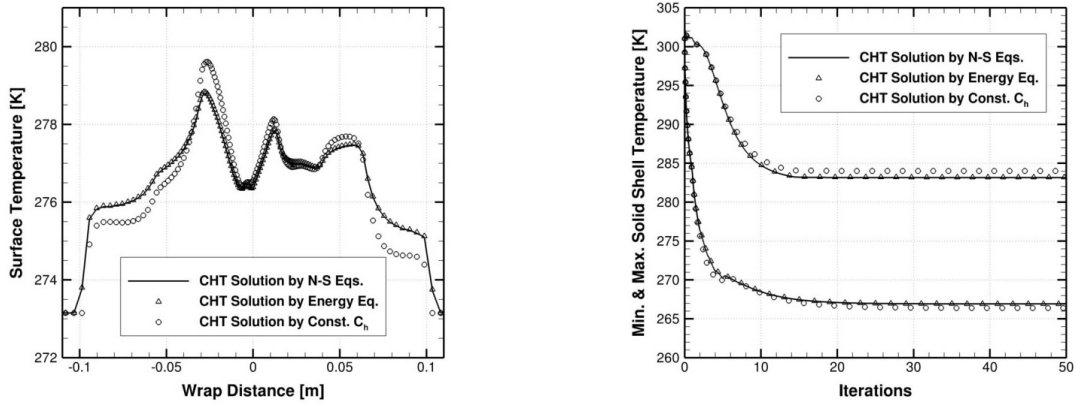


Figure 2.12: Comparison of the surface temperature distributions (left) and minimum and maximum solid shell temperature (right) obtained by different strategies.

2.3 Discussion and Conclusions

In this chapter, the framework of the numerical simulation of in-flight icing was briefly introduced, which includes three steps: the airflow solution, the droplet impingement solution and the ice accretion solution. For the airflow solution, the compressible Navier-Stokes equations are solved to account for compressibility and viscosity. To simulate turbulent flows, the RANS equations were solved in conjunction with the one-equation Spalart-Allmaras model. For the droplet impingement solution, the Eulerian approach was used, which generally performs better than the conventional Lagrangian approach. For the ice accretion solution, the Messinger model was used to apply the first law of thermodynamics. A numerical test case for the simulation of in-flight icing was presented. The physical effects of the ice accretion on the airflow and the droplet solutions were discussed. After the icing simulation, the numerical simulation of an electro-thermal IPS model was performed. To do so, the conjugate heat transfer (CHT) problem between the fluid (airflow) and solid (the IPS) domains was solved. Our results compared well with other numerical and experimental data. Since the CHT procedure is too computationally expensive to be used in an optimization process (which will be presented later), high-fidelity strategies were introduced to dramatically reduce the CHT cost.

Chapter 3 ENERGY ANALYSIS OF ANTI-ICING

3.1 Calculation of the Minimum Energy Requirements of Anti-Icing

Various mass and heat transfer mechanisms are involved in the ice accretion process. The mass transfer includes sublimation, evaporation, water impingement and ice accretion. The heat transfer includes sublimation, evaporation, kinetic energy, sensible energy, convection, irradiation, fusion and conduction. These mechanisms are schematically shown in Figure 3.1. Since understanding of the heat transfer mechanisms is of great importance in calculation of the energy requirements of IPS, they are detailed in the following before going through the calculations.

- *Kinetic energy:* When brought to rest at the body surface, the water droplets carry the kinetic energy to the control volume, thus heating up the surface. The heat flux transferred by the water droplets is given by:

$$\dot{Q}_{kin}'' = \dot{m}_{imp}'' \frac{\|u_d\|^2}{2}. \quad 3-1$$

- *Convection:* Apart from the water droplets, mentioned above, the airflow also carries kinetic energy, which causes aerodynamic heating. This energy can be implicitly taken into account by calculating the convection heat flux as follows:

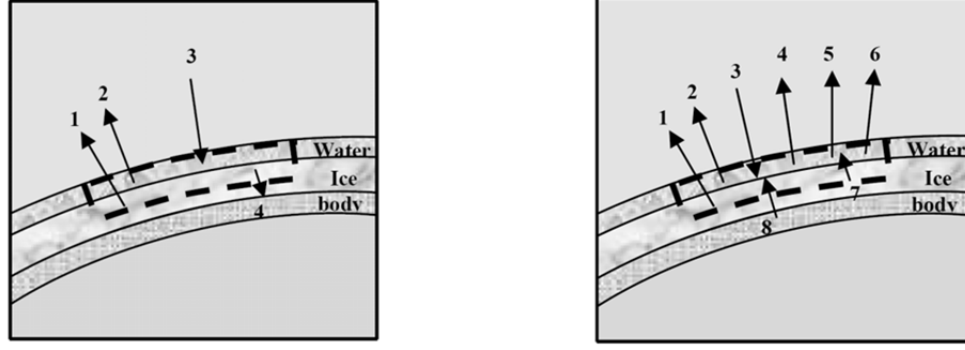


Figure 3.1: Mass transfer mechanisms (left): 1:sublimation, 2:evaporation, 3:water impingement, 4:ice accretion; heat transfer mechanisms (right): 1:sublimation, 2:evaporation, 3:kinetic energy, 4:sensible energy, 5:convection, 6:irradiation, 7:fusion, 8:conduction.

$$\dot{Q}_{conv}'' = c_h (T_{rec} - T_s), \quad 3-2$$

where T_{rec} is the recovery temperature that comes from the incomplete recovery of the kinetic energy transferred by the airflow, which is due to temperature dissipation by small scale mass transport effects. T_{rec} is less than the theoretical stagnation temperature. The convective heat transfer coefficient, c_h , can be calculated using the convective heat flux from a given airflow solution, $\dot{Q}_{conv,air}''$. Given an initial surface temperature, $T_{s,init}$, which is a function of the boundary layer thickness and above the adiabatic recovery temperature, c_h can be calculated as follows:

$$c_h = \frac{\dot{Q}_{conv,air}''}{(T_{rec} - T_{s,init})}. \quad 3-3$$

Assuming a constant c_h (as discussed before), one can calculate the convective heat flux by using Eq. 3-2, in which T_s evolves at every step.

- *Evaporation/sublimation*: Using the evaporative mass flux obtained from Eq. 2-6, the evaporation heat flux can be given by:

$$\dot{Q}_{evap/sub}'' = -\frac{1}{2} \dot{m}_{evap}'' (L_{evap} + L_{sub}). \quad 3-4$$

In this equation, it is assumed [91] that in the evaporation/sublimation process, half of the film is liquid (water) and the other half is solid (ice). This way, a non-continuous film including bumps of ice separated by water can be modeled. In case of anti-icing where the surface temperature is above the freezing temperature of water, there will be no ice on the surface, and therefore the evaporative heat flux can be simply given by $(-\dot{m}_{evap}'' L_{evap})$.

- *Sensible energy*: It is due to the temperature change of water (when impacting on the surface) and ice. The heat flux transferred by this mechanism can be given as follows:

$$\dot{Q}_{sens}'' = \dot{m}_{imp}'' c_{p,w} (T_{d,\infty} - T_s) - \dot{m}_{ice}'' c_{p,ice} (T_m - T_s), \quad 3-5$$

In case of anti-icing, where there is no ice on the surface, the second term in Eq. 3-5 is eliminated.

Fusion: This mechanism also does not occur in anti-icing. It is given by the following equation:

$$\dot{Q}_{fusion}'' = \dot{m}_{ice}'' L_{fusion}, \quad 3-6$$

- *Irradiation*: Given that the body surface temperature in a typical operation of an IPS is not usually very high, the irradiative does not play an important role compared to other mechanisms. The heat flux transferred by this mechanism is given by:

$$\dot{Q}_{rad}'' = \sigma \varepsilon (T_{\infty}^4 - T_s^4), \quad 3-7$$

where σ is the Stefan-Boltzmann constant, ε the solid emissivity, and T_{∞} the ambient temperature.

- *Conduction*: This heat flux is generated by the IPS and is transferred through the solid wall.

In order to compute the minimum heat flux required for ice-free anti-icing, the temperature distribution at the body surface must be known. Hence, after obtaining the

solutions of the airflow and droplet impingement, there is no need to solve the ice accretion equations (Eqs. 2-5 and 2-8). One just needs to calculate the following summation, written for a control volume, to compute the heat flux required:

$$\begin{aligned}
\dot{Q}''_{anti-ice} &= \dot{Q}''_{rb,out} - \dot{Q}''_{rb,in} + \dot{Q}''_{conv} + \dot{Q}''_{evap/sub} + \dot{Q}''_{sens} + \dot{Q}''_{kin} + \dot{Q}''_{rad} + \dot{Q}''_{fusion} \\
&= (\dot{m}''_{rb,out} - \dot{m}''_{rb,in}) c_{p,w} T_s + c_h (T_{rec} - T_s) \\
&\quad - \frac{1}{2} \dot{m}''_{evap} (L_{evap} + L_{sub}) + \dot{m}''_{imp} c_{p,w} (T_{d,\infty} - T_s) \\
&\quad - \dot{m}''_{ice} c_{p,ice} (T_m - T_s) + \dot{m}''_{imp} \frac{\|u_d\|^2}{2} + \sigma \mathcal{E} (T_\infty^4 - T_s^4) + \dot{m}''_{ice} L_{fusion}
\end{aligned} \tag{3-8}$$

where \dot{Q}''_{rb} and \dot{m}''_{rb} are, respectively, the heat and mass fluxes transferred by the runback water. In this equation, all variables, except \dot{m}''_{ice} and T_s , are known from the airflow and droplet impingement solutions. \dot{m}''_{ice} and T_s need to be specified based on the operating conditions of the anti-icing system.

An anti-icing system may operate in either *running-wet (RW)* or *fully-evaporative (FE)* regimes. In RW, water droplets keep running back downstream the end of the protected zone. Hence, to determine the minimum energy required for anti-icing in this regime, the following conditions must be satisfied over the protected zone:

$$\begin{aligned}
\dot{m}''_{ice} &= 0, \\
T_s &= T_m.
\end{aligned} \tag{3-9}$$

That is, over the protected zone, no ice accretes and the surface temperature is equal to the melting temperature of water. In FE, water droplets are evaporated almost upon impact on the surface. This implies the following conditions:

$$\begin{aligned}
\dot{m}''_{ice} &= 0, \\
\dot{m}''_{evap} &= \dot{m}''_{imp}.
\end{aligned} \tag{3-10}$$

Given that \dot{m}''_{evap} is a function of surface temperature, the temperature distribution at the body surface, which is needed to calculate the energy requirement, can be determined by means of Eqs. 2-6 and 2-7. Therefore, the energy requirement for RW and FE can be calculated by substituting the corresponding \dot{m}''_{ice} and T_s into Eq. 3-8.

To demonstrate a quantitative analysis, a NACA 0012 model is considered with flight and icing conditions provided in Table 3.1. In the numerical results presented in the following, the kinetic and sensible heat fluxes are merged and considered as a single heat flux, which is called the impingement heat flux, \dot{Q}_{imp}'' :

$$\dot{Q}_{imp}'' = \dot{m}_{imp}'' \left[\frac{\|u_d\|^2}{2} + c_{p,w} (T_{d,\infty} - T_s) \right]. \quad 3-11$$

It should be noted that the sensible heat flux does not include the second term in Eq. 3-5 since there is no ice accretion. Also, the irradiation heat flux is not shown in the results as its value is negligible compared to the other heat fluxes.

Table 3.1: Flight and icing conditions.

Temperature [K]	Velocity [m.s ⁻¹]	LWC [g.m ⁻³]	MVD [μm]	AoA [deg.]
254.375	44.704	0.78	20	-4

Figure 3.2 shows the distribution of the impingement, the evaporation and the convection heat fluxes required for RW and FE. As shown, while in RW convection is the dominant mechanism, in FE, evaporation is the dominant one. This is because, according to Eqs. 2-6 and 2-7, the evaporation mass flux is a function of wall temperature that is much higher in FE compared to that in RW. In both regimes, the impingement heat flux is the smallest. The total heat fluxes, including impingement, evaporation and convection, required for RW and FE are compared in Figure 3.3. For FE, an intense heat flux is required in a very small region of the leading edge in order to evaporate all water droplets upon impact. Hence, this zone is the same as the water impingement zone on the surface. In RW, since all water is not completely evaporated at the leading edge but moves in the form of a thin layer of film toward the trailing edge, the extent of the heat flux distribution is much longer than that of FE. The existence of water film after the protected zone leads to the formation of runback ice, which could be a serious threat to safety, especially in glaze icing conditions. To avoid that, the wing must be protected

along the whole chord length. This would, obviously, add to the weight of the IPS, which is not desirable. On the other hand, although there is no problem due to runback ice in FE, the intense heat flux required on a very small region could cause other problems, such as thermal fatigue as well as exceeding the maximum allowable wall temperature. A remedy to these problems would be to use an approach that can be categorized between RW and FE. This will be thoroughly elaborated in the next chapter where the optimization of anti-icing systems is discussed.

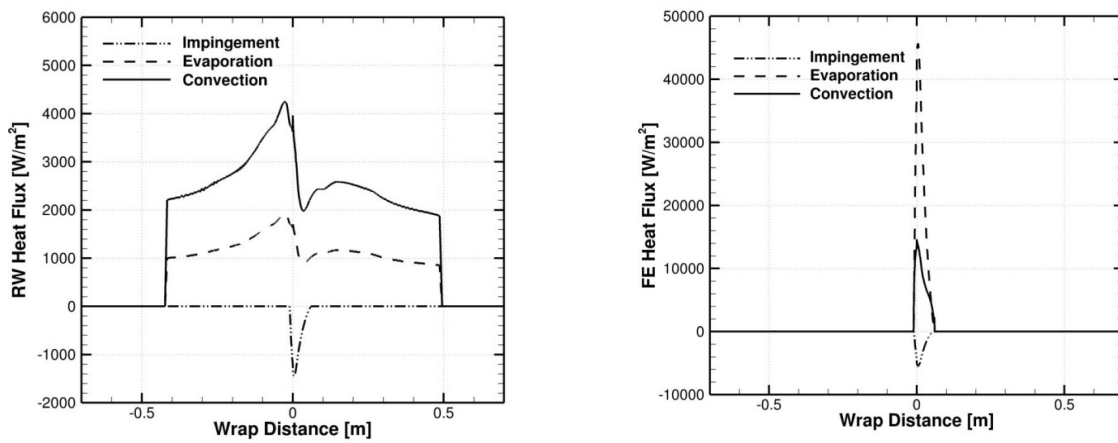


Figure 3.2: Heat flux required by various heat transfer mechanisms for the running-wet (left) and fully-evaporative (right) regimes.

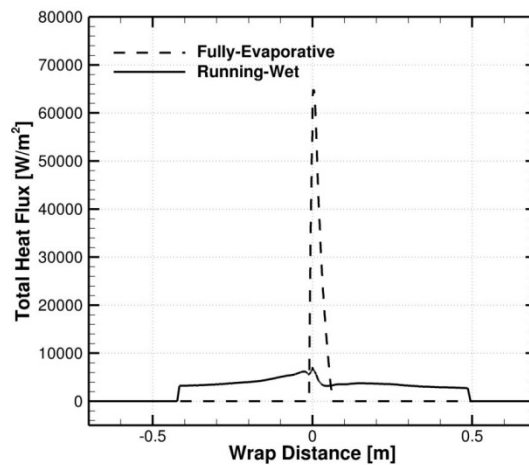


Figure 3.3: Total heat flux required for the running-wet and fully-evaporative regimes.

3.2 Influential Parameters on the Energy Requirements of Anti-Icing

There are two major factors affecting the energy requirements of anti-icing: flight conditions and icing conditions. Flight conditions are characterized by the airspeed, the AoA and the icing exposure time (or distance). These characteristics, to a large extent, are pilot-controlled. Icing conditions are characterized by the ambient temperature, the liquid water content, the droplets diameter, the altitude and the cloud horizontal extent. These characteristics, obviously, cannot be directly controlled by a pilot. Hence to avoid unforeseen circumstances, the most probable icing conditions, provided by FAA (Federal Aviation Administration), are accessible through different envelopes. Ice certifications are only given to those commercial aircraft that are able to demonstrate compliance of their IPS throughout the icing envelopes of the FAA's FAR (Federal Airworthiness Regulations) Part 25 Appendix C [92], which has been in use since 1964. These envelopes indicate the *probable maximum* (99%) average value of LWC that is to be expected over a reference distance for a given temperature and droplet diameter in the cloud [92]. The envelopes are shown in Figure 3.4. For the *continuous maximum* condition, which represents layer-type clouds or a portion of stratiform icing conditions, the reference distance is 32.225 km, and for the *intermittent maximum* conditions, which represent a portion of convective or cumuliform clouds and icing conditions, the reference distance is 4.8152 km [92]. The reference distances have been arbitrarily selected based on the measurement devices available in the late 1940s.

There are various ways for using Appendix C for IPS design purposes. For instance, a recommended MVD and a temperature appropriate to a flight level can be selected and then used to determine the probable maximum LWC [93]. Since longer (or shorter) averaging distances (horizontal extent) will result in lower (or higher) averaged value of LWC, the selected LWC must be adjusted by a factor given in the Appendix C. Figure 3.4 also shows an illustration of such distance-based conversion for MVD = 20 μm .

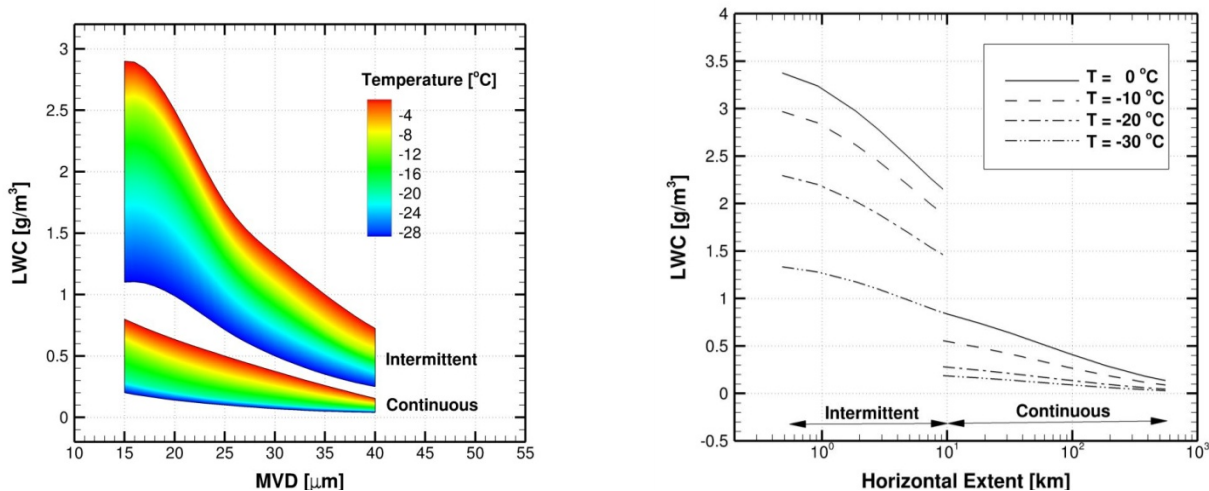


Figure 3.4: Appendix C envelopes, including intermittent and continuous maximum atmospheric icing conditions (left) and Appendix C envelopes converted to a distance-based format for $\text{MVD} = 20 \mu\text{m}$ (right) (data adapted from [92]).

3.3 Sensitivity Analysis of the Energy Requirements of Anti-Icing

In this section, sensitivity analyses of the energy requirements of anti-icing is performed with respect to both flight characteristics (including the airspeed and the angle of attack) and icing characteristics (including the ambient temperature, the liquid water content and the median volumetric diameter). To do so, the flight and icing conditions represented in Table 3.1 are considered as the reference conditions. To perform an analysis with respect to each parameter or set of parameters, the rest of the parameters are kept unchanged. It should be noted that in the first part, in which the airspeed is investigated, more details are provided. In the next parts, for the sake of brevity, similar details and explanations are not repeated.

3.3.1 Airspeed

For the sensitivity analysis with respect to the airspeed, the range between 30 m/s and 150 m/s is considered, which is quite common in typical icing conditions. Figure 3.5 shows the total heat flux distributions required for the running-wet (RW) and the fully-

evaporative (FE) regimes at different airspeeds. As can be seen, the FE heat fluxes are much larger than the RW ones, and the difference between the two grows as airspeed increases. However, as previously mentioned, the extent of the FE heat flux distribution is much shorter than that of the RW. With RW, more heat flux is required on the lower surface for all airspeeds. This is due to the negative angle of attack making the pressure lower and the velocity higher on the lower surface, which results in higher convective heat transfer coefficient on this surface. Note that not only is convection influenced by the heat transfer coefficient, but, according to Eq. 2-6, evaporation is also affected by this coefficient. Since these two mechanisms, i.e. convection and evaporation, are the most dominant ones, the total heat flux on the lower surface becomes higher for RW. In contrast, for FE, more heat flux is required on the upper surface for all the airspeeds. Based on Eq. 3-10, for this regime, the heat flux is directly related to the impingement mass flux, which in this case is obviously larger on the upper surface due to the negative angle of attack. As airspeed increases, the RW and FE heat fluxes grow both in magnitude and extent. This increases the heat rates, which depend on both magnitude and extent of the heat fluxes. The increase in the extent of heat flux required is because of the increase in the extent of the runback water film as airspeed increases (Figure 3.6).

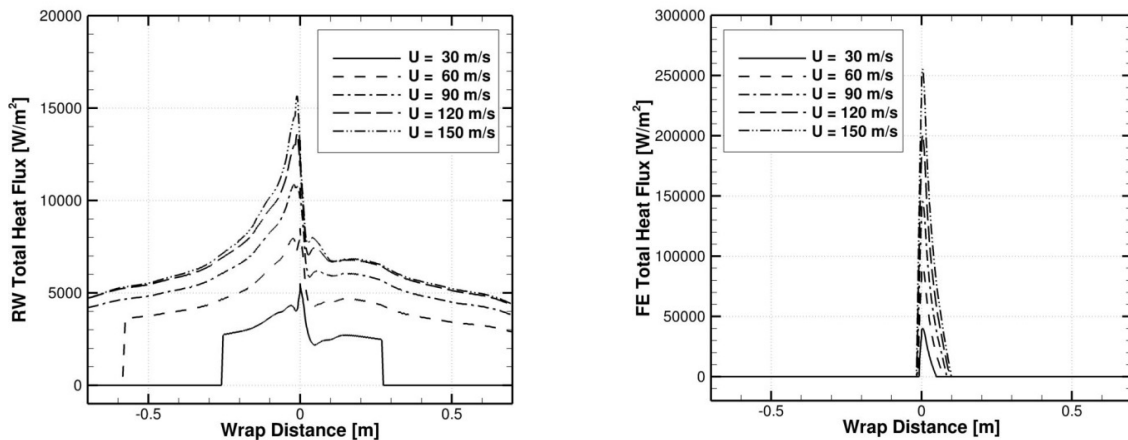


Figure 3.5: Total heat flux distributions required for the running-wet (left) and fully-evaporative (right) regimes at different airspeeds.

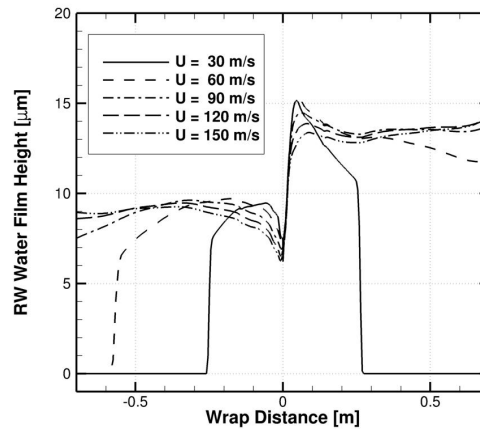


Figure 3.6: Water film height distribution for the running-wet regime at different airspeeds.

The heat rate (power) can be obtained by the integration of the heat flux distribution over the wing surface. It is worth mentioning that here 1 m of span is considered to perform this integration. The overall variations of the RW and the FE heat rates with respect to the airspeed are shown in Figure 3.7 for different heat transfer mechanisms and the total one. For both regimes the impingement heat rate has the smallest variation. For FE, the largest variation is that of the evaporation heat rate, which arises from the fact that the amount of evaporation is a strong function of the surface temperature. For RW, however, evaporation and convection have almost the same amount of variation. The total variations are also very close to each other. The sensitivities of the RW and the FE heat rates with respect to the airspeed are plotted in Figure 3.8 for each heat transfer mechanism and overall. The mechanisms are discussed in the following:

- *Impingement heat rate*: Its magnitude increases with airspeed for both RW and FE because of the increase in impingement mass rate (Figure 3.9). It is also noticed that the magnitude of the FE impingement heat rate is larger than the RW one, which is, according to Eq. 3-11, due to the higher surface temperature.
- *Evaporation heat rate*: It increases as airspeed increases for both RW and FE. This is due to the fact that the impingement mass rate (Figure 3.9) and the heat transfer coefficient strongly depend on the airspeed. The impingement mass rate's

effect on the evaporation heat rate is based on Eq. 3-10, and the heat transfer coefficient's effect is based on 2-6. This equation along with Eq. 2-7 also indicates that the higher surface temperature in FE increases the FE evaporation mass rate, making the FE evaporation heat rate larger than the RW one.

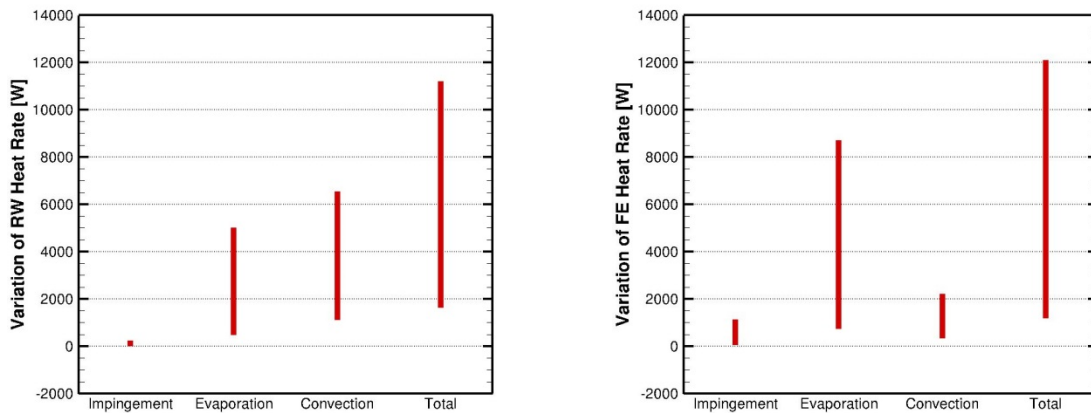


Figure 3.7: Overall variation of different heat transfer mechanisms for the running-wet (left) and fully-evaporative (right) regimes with respect to airspeed.

- Convection heat rate:* It increases with airspeed for both RW and FE. However, for RW, it starts to decline at a specific airspeed. This is due to the fact that at this airspeed, the counter effect of the aerodynamic heating starts to surpass the effect of the heat transfer coefficient increase. As stated before, the heat transfer coefficient does not change much with surface temperature. Hence, the higher surface temperature in FE does not necessarily mean a higher convection rate. In contrast, Figure 3.8 shows that the RW convection heat rate is larger than the FE one, which is due to the larger extent of the heat flux over the surface.
- Total heat rate:* It increases with airspeed for both RW and FE. However, for RW, it starts to decline at a specific airspeed because of the decrease in the convection heat rate, as mentioned above. Note that the rate of increase in total heat rate with respect to the airspeed gradually decreases. The total heat rate is larger for RW at lower airspeeds, but becomes smaller at higher ones.

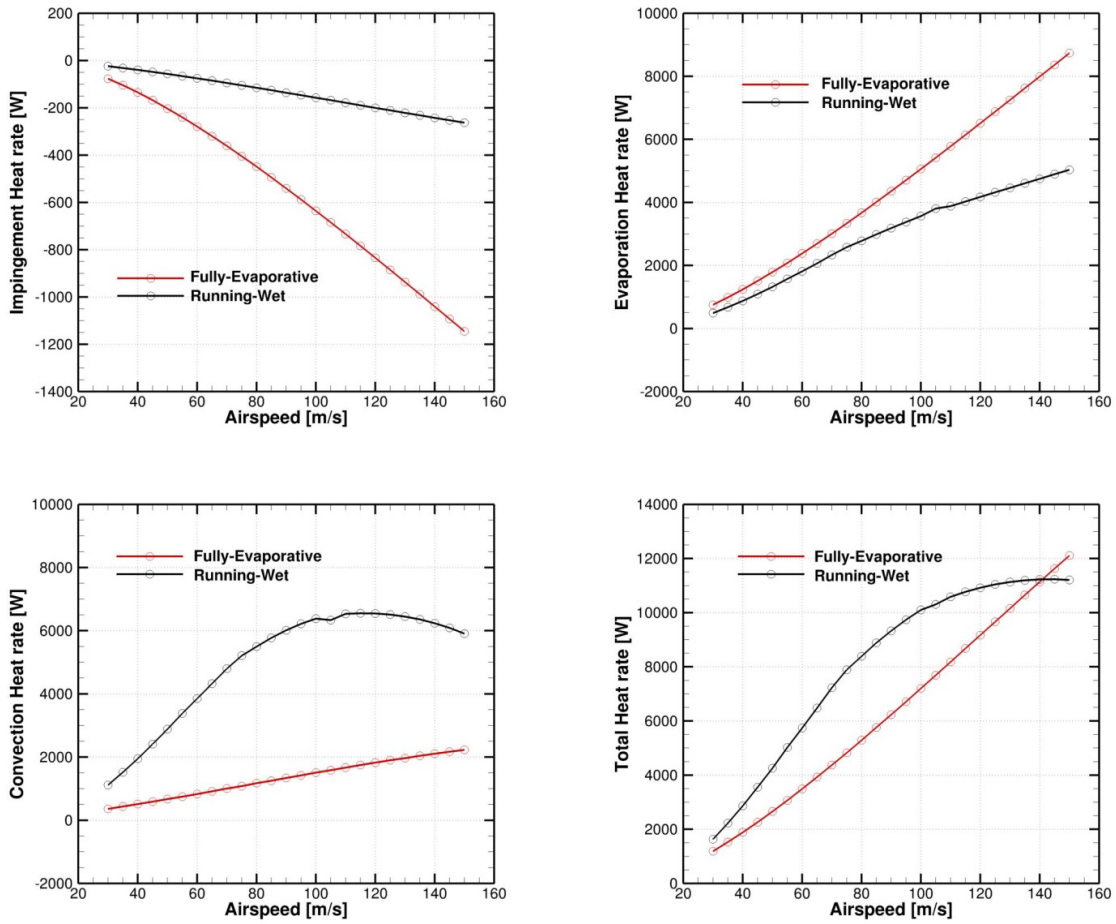


Figure 3.8: Sensitivity of impingement, evaporation, convection and total heat rate with respect to airspeed.

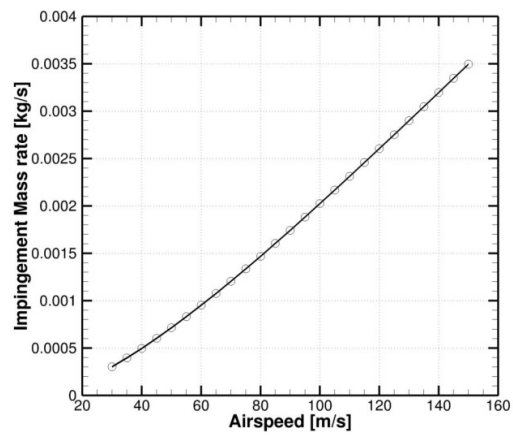


Figure 3.9: Sensitivity of the impingement mass rate with respect to airspeed.

3.3.2 Angle of Attack

For the sensitivity analysis with respect to the AoA, the range between -4° and 0° is considered. Since a symmetric wing is being investigated, positive angles of attack would have the same results, and thus are not considered. Figure 3.10 shows the total heat flux distributions required for RW and FE at different angles of attack. As the magnitude of the angle of attack increases, the RW heat flux on the upper surface decreases in the magnitude and increases in the extent, and on the lower surface vice versa. The variation in the magnitude is because of the change of the heat transfer coefficient as the angle of attack changes. The variation in the extent is due to the variation in the extent of the runback water film with the angle of attack (Figure 3.11). It should be noted that due to the negative angle of attack, the variation of the extent on the lower surface is less than that on the upper surface. The variation behaviour of the extent of the FE heat flux is similar to the RW one since the extent is only affected by the angle of attack. However, the variation of the magnitude of the FE heat flux is in opposition to the RW one, i.e. it increases on the upper surface and decreases on the lower surface as the angle of attack increases. The reason is that the FE heat flux, depends on the impingement mass flux, which is larger on the upper surface and smaller on the lower surface at higher magnitude of the angle of attack.

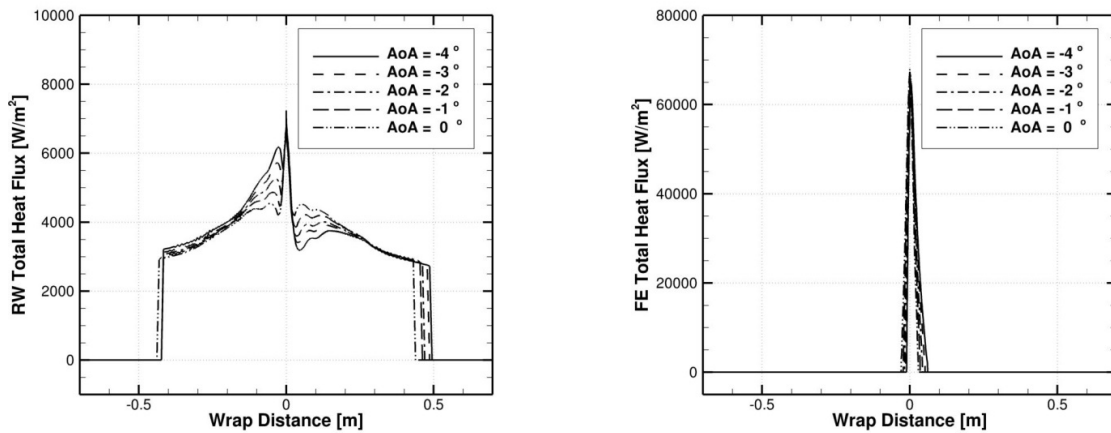


Figure 3.10: Total heat flux distributions required for the running-wet (left) and fully-evaporative (right) regimes at different angles of attack.

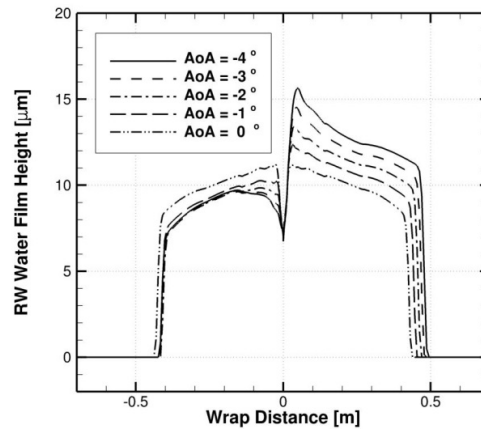


Figure 3.11: Water film height distribution for the running-wet regime at different angles of attack.

The overall variations of the RW and the FE heat rates with respect to the angle of attack are shown in Figure 3.12 for different heat transfer mechanisms and the total one. For both regimes the impingement heat rate has the smallest variation. Similar to the previous case, for FE, the largest variation is that of the evaporation heat rate. The variations of the heat rate for different mechanisms in RW are smaller than that in FE, except for convection, which is larger in RW. The total variations, however, are close to each other. The sensitivities of the RW and the FE heat rates with respect to the angle of attack are plotted in Figure 3.13 for different heat transfer mechanisms and for the total one. They are discussed in the following:

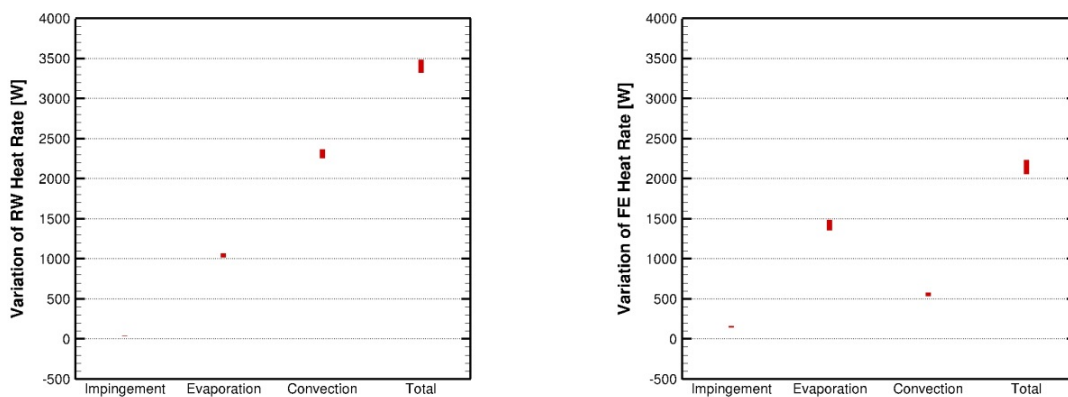


Figure 3.12: Overall variation of different heat transfer mechanisms for the running-wet (left) and fully-evaporative (right) regimes with respect to angle of attack.

- *Impingement heat rate*: Its magnitude increases as the angle of attack increases, for both RW and FE. This is because of the increase in the impingement mass rate (Figure 3.14). The rate of increase becomes larger as the magnitude of the angle of attack increases. The magnitude of the FE heat rate is larger than the RW one, which is, according to Eq. 3-11, due to higher surface temperature.
- *Evaporation heat rate*: It increases with increasing angle of attack for both RW and FE. This is due to the change of the impingement mass rate (Figure 3.14) and the heat transfer coefficient with the angle of attack.
- *Convection heat rate*: It increases as the angle of attack increases for both RW and FE. This, as stated, is because of increase of the heat transfer coefficient.
- *Total heat rate*: It increases with increasing magnitude of angle of attack for both RW and FE. In general, all mass and heat rates are less sensitive to the angle of attack compared to the airspeed.

3.3.3 Ambient Temperature

For the sensitivity analysis with respect to ambient temperature, the range of values between 243 K and 267 K is considered, which covers the greater part of Appendix C (Figure 3.4). Figure 3.15 shows the total heat flux distributions required for RW and FE at different ambient temperatures. As temperature increases, the RW heat flux on both the upper and the lower surfaces decrease in magnitude, but increase in extent. This is due to the increase in the variation of the extension of the runback water film (Figure 3.16). To explain this, recall Eqs. 2-6 and 2-7:

$$\dot{m}''_{evap/sub} = \frac{0.7c_h}{c_{p,a}} \left[\frac{P_{v,p} - H_{r,\infty} P_{v,\infty}}{P_s} \right], \quad 2-21$$

$$p_{v,p} = 3386 \left[0.0039 + 6.8096 \times 10^6 \hat{T}_s^2 + 3.5579 \times 10^7 \hat{T}_s^3 \right]. \quad 2-22$$

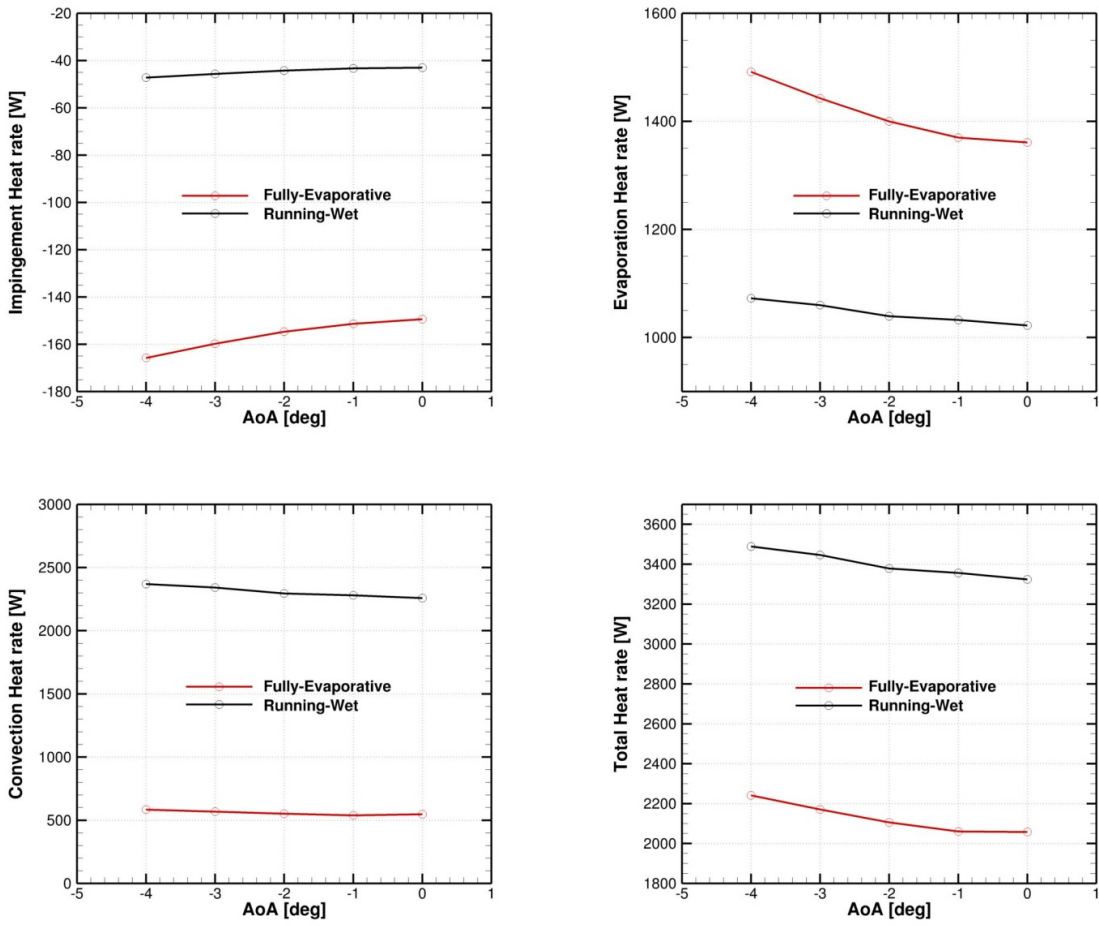


Figure 3.13: Sensitivity of impingement, evaporation, convection and total heat rate with respect to angle of attack.

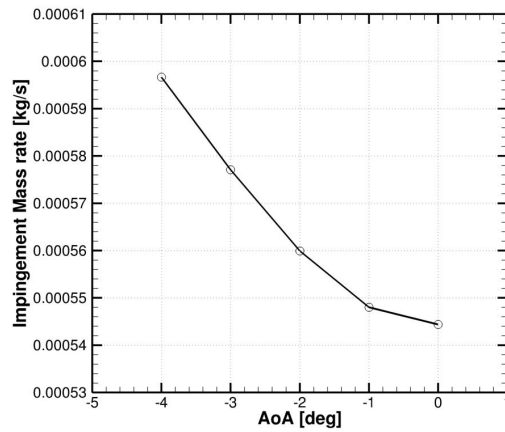


Figure 3.14: Sensitivity of the impingement mass rate with respect to angle of attack.

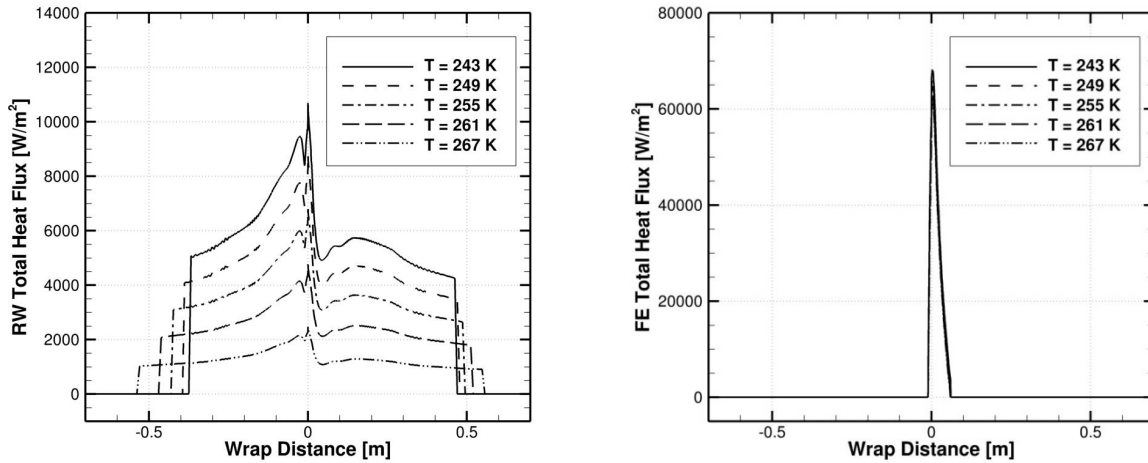


Figure 3.15: Total heat flux distributions required for the running-wet (left) and fully-evaporative (right) regimes at different ambient temperatures.

Based on these equations, the lower the difference between ambient and surface temperatures (which in the case of RW is fixed at 273.15 K), the lower the evaporation mass rate, and thus the lower the evaporation rate. Hence, the runback water film can keep moving downstream over a larger distance before it is completely evaporated. As shown in Figure 3.15, the variation of the FE heat flux distribution is very small because it depends on the impingement mass rate (Eq. 3-10). Based on Figure 3.17, the mass rate does not change much with the ambient temperature.

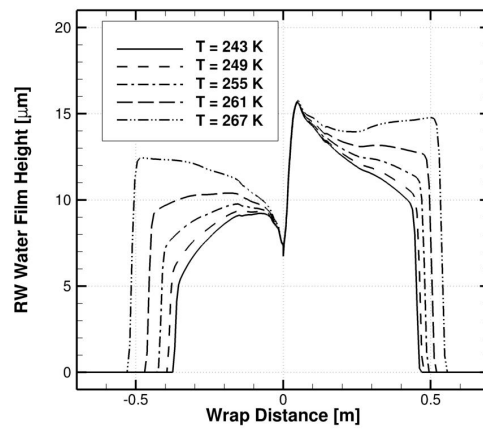


Figure 3.16: Water film height distribution for the running-wet regime at different ambient temperatures.

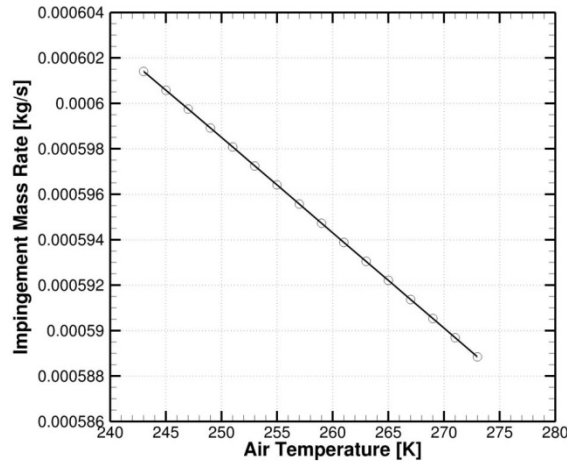


Figure 3.17: Sensitivity of the impingement mass rate with respect to ambient temperature.

The overall variations of the RW and the FE heat rates with respect to the ambient temperature are shown in Figure 3.18 for different heat transfer mechanisms and their combination. For RW, the impingement heat rate has the smallest variation and the convection heat rate has the largest one since the ambient temperature has the largest effect on convection (Eq. 3-2). Also, based on the reason explained above, all the variations for FE are smaller than those for RW. The sensitivities of the RW and the FE heat rates with respect to the ambient temperature are plotted in Figure 3.19 for different heat transfer mechanisms and their combination. They are discussed in the following:

- *Impingement heat rate*: Its magnitude for both RW and FE decreases as ambient temperature increases, which affects the second term in Eq. 3-11. The decrease of the impingement mass rate (Figure 3.17) also affects the impingement heat rate.
- *Evaporation heat rate*: It decreases with increasing ambient temperature for both RW and FE. The reasons of the decrease in the RW heat rate and the small change of the FE heat rate were discussed before.
- *Convection heat rate*: It decreases with increasing ambient temperature for both RW and FE (Eq. 3-2).

- *Total heat rate*: It decreases as the ambient temperature increases for both RW and FE. It is larger for RW at lower temperatures and becomes smaller at temperatures near the freezing point.

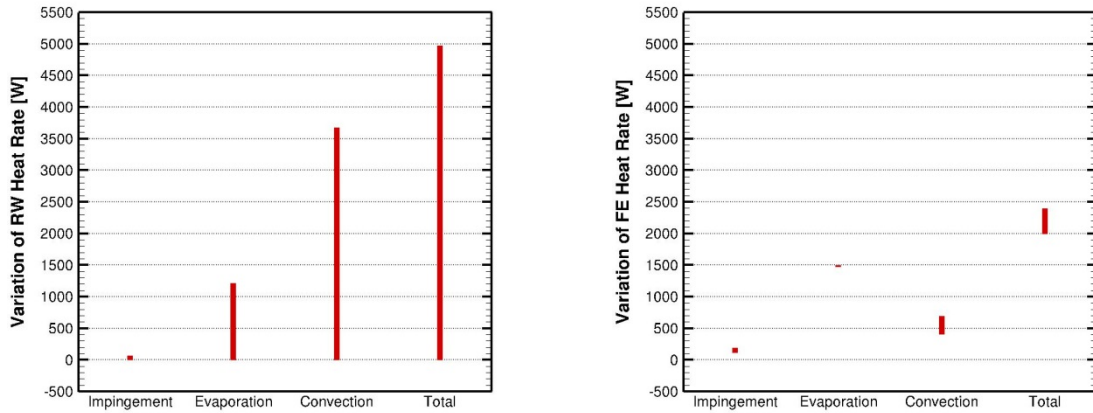


Figure 3.18: Overall variation of different heat transfer mechanisms for the running-wet (left) and fully-evaporative (right) regimes with respect to ambient temperature.

3.3.4 LWC and MVD

In order to make the sensitivity analyses with respect to LWC and MVD more practical, they are considered together on the basis of the Appendix C (Figure 3.4) for the continuous maximum condition, in which LWC and MVD are independent variables and the ambient temperature is a dependent variable. Figure 3.20 shows the sensitivity of the impingement mass rate over the entire Appendix C. In the previous section, Figure 3.17 showed that the impingement mass rate must decrease as the ambient temperature increases. However, Figure 3.20 shows that the impingement mass rate increases as the ambient temperature increases. This seemingly paradoxical behaviour arises from the fact that, here, LWC and MVD also affect the impingement mass rate, and the ambient temperature is not the only variable.

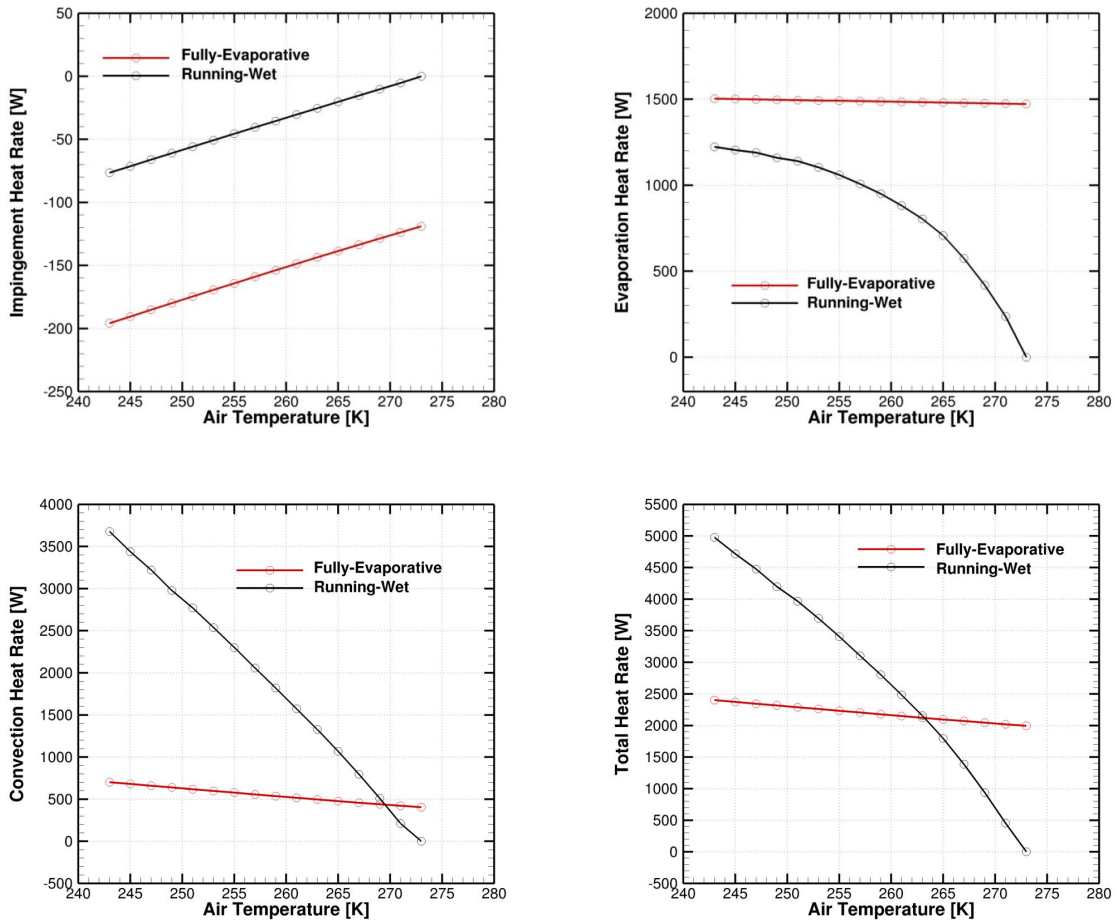


Figure 3.19: Sensitivity of impingement, evaporation, convection and total heat rate with respect to the ambient temperature.

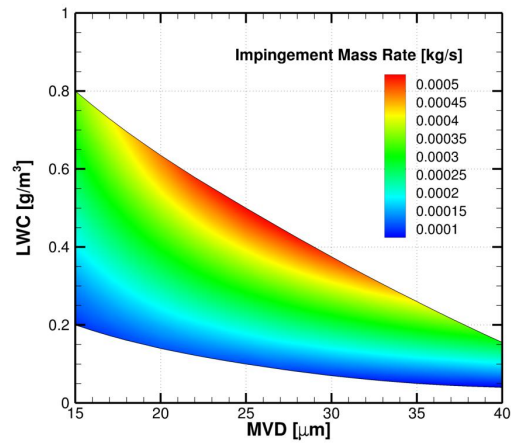


Figure 3.20: Sensitivity of the impingement mass rate with respect to the variables of Appendix C.

The sensitivities of the RW and FE heat rates over the entire Appendix C are plotted in Figure 3.21 to Figure 3.24 for each heat transfer mechanism and overall. They are discussed in the following:

- Impingement heat rate:* According to Eq. 3-11, the impingement heat rate depends on five parameters: \dot{m}''_{imp} , u_d , $c_{p,w}$, $T_{d,\infty}$ and T_s , among which u_d and $c_{p,w}$ can be assumed constant, here. For RW, T_s is fixed at 273.15 K. Hence, the lower the ambient temperature, $T_{d,\infty}$, is, the larger the magnitude of the impingement heat rate is. This can be partially seen in Figure 3.21 since the other influential parameter, i.e. \dot{m}''_{imp} has a counter effect on the heat rate (Figure 3.20). On the other side, according to the definition of the FE regime, the FE heat rate is mainly affected by the impingement mass rate. This makes them have similar distributions.
- Evaporation heat rate:* According to Eq. 3-4, the evaporation heat rate depends on \dot{m}''_{evap} and L_{evap} , the latter being assumed constant. \dot{m}''_{evap} itself depends on several parameters: P_∞ , T_∞ , P_s , T_s , c_h and $c_{p,air}$ (Eqs. 2-6 and 2-7), among which P_∞ , P_s , $c_{p,air}$ and c_h can be assumed almost constant. For RW, T_s is fixed at 273.15 K and hence, as T_∞ decreases, the evaporation heat rate must increase. However, the decrease of the impingement mass rate should not be ignored (Figure 3.20). At lower temperatures it reduces the evaporation mass rate, \dot{m}''_{evap} , thus resulting in lower RW evaporation heat rate (Figure 3.22). On the other side, the distribution of the FE evaporation heat rate is similar to that of the mass impingement heat rate for the same reason stated above for the FE impingement heat rate.
- Convection heat rate:* According to Eq. 3-2, the convection heat rate depends on c_h , T_∞ and T_s , among which c_h can be assumed almost constant, here. Therefore, similar to the impingement heat rate, T_∞ and T_s are the only influential parameters. Figure 3.23 shows that the RW convection heat rate distribution is similar to the RW evaporation one. However, there are some differences, which

arise from the fact that the convection heat rate is not strongly influenced by the impingement mass rate. The effect of the impingement mass rate on the convection heat rate is only through the water film extent, and thus changing the surface area on which heat transfer takes place. For FE, in which no runback water film exists, the impingement mass rate has very little effect on the convection heat rate. As shown, there is a strong dependence on MVD, which directly affects the heat transfer surface area. A weak dependence on T_∞ is also observable and can be explained by Eq. 2-6.

- *Total heat rate*: Figure 3.24 shows that the RW and FE total heat rate distributions are similar to the heat rate distribution of their own dominant heat transfer mechanism. RW requires the highest energy when MVD lies between 20 μm to 25 μm and LWC lies between 0.2 g/m^3 to 0.4 g/m^3 . For FE, the highest energy is required when MVD lies between 25 μm to 30 μm and LWC lies between 0.4 g/m^3 to 0.6 g/m^3 .

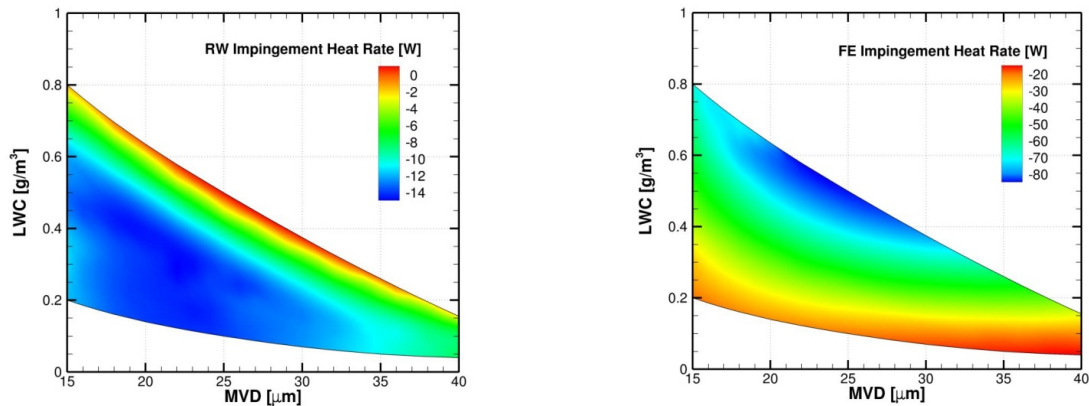


Figure 3.21: Sensitivity of the impingement heat rate for the running-wet (left) and fully- evaporative (right) regimes within the entire Appendix C.

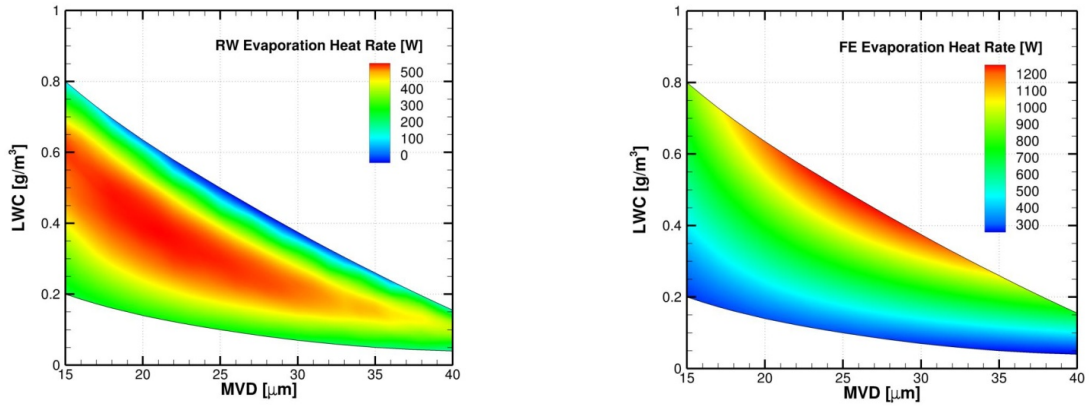


Figure 3.22: Sensitivity of the evaporation heat rate for the running-wet (left) and fully-evaporative (right) regimes within the entire Appendix C.

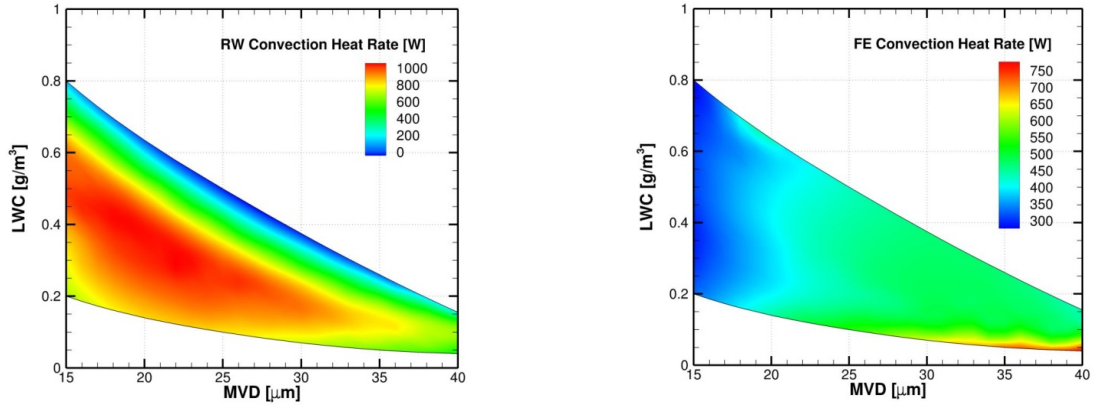


Figure 3.23: Sensitivity of the convection heat rate for the running-wet (left) and fully-evaporative (right) regimes within the entire Appendix C.

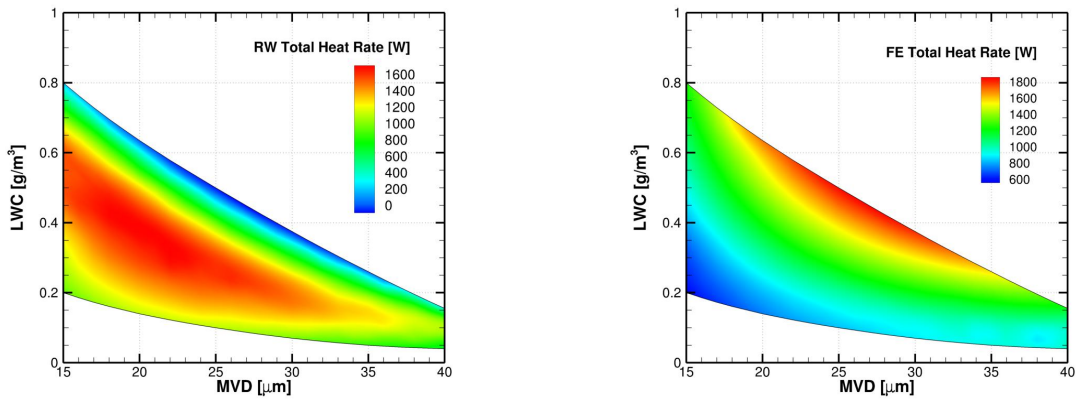


Figure 3.24: Sensitivity of the total heat rate for the running-wet (left) and fully-evaporative (right) regimes within the entire Appendix C.

3.4 Discussion and Conclusions

In this chapter, the energy requirements of anti-icing systems in both running-wet and fully-evaporative regimes were calculated. Different mass and heat transfer mechanisms involved in the anti-icing process were discussed. Then, sensitivity analyses of the energy requirements in both regimes with respect to different parameters were performed:

- **Airspeed:** For both regimes, the energy requirement increases as the airspeed increases. For the running-wet regime, however, at higher speeds, the energy requirement starts to decrease due to aerodynamic heating. This makes the energy requirement of the running-wet regime less than that of the fully-evaporative regime at higher speeds. But at lower speeds, the running-wet regime requires slightly greater energy than the fully-evaporative regime.
- **Angle of attack:** For both regimes, the energy requirement slightly increases as the angle of attack increases. At all angles of attack, the energy requirement of the running-wet regime is greater than that of the fully-evaporative regime.
- **Ambient temperature:** For both regimes, the energy requirement decreases as the ambient temperature increases. The rate of decrease is greater in the running-wet regime. Therefore, at higher temperatures, the running-wet regime requires less energy while at lower temperatures, the fully-evaporative requires less energy.
- **Liquid water content (LWC) and median volumetric diameter (MVD):** These two parameters were considered together by using the Appendix C, in which LWC and MVD are two independent parameters and temperature is a dependent parameter. The sensitivity of the energy requirement for both regimes was presented. Although it is difficult to make a general conclusion from the complex distributions of the energy requirements, one can roughly conclude that at lower temperatures within the Appendix C, the running-wet regime requires more energy while at higher temperatures, the energy requirement of the fully-evaporative regime is greater.

All these analyses can help us achieve a better insight into the energy requirements of an IPS under different conditions. However, the best design for a specific IPS in a specific condition would require solving a suitable optimization problem. This will be discussed in the next chapter.

Chapter 4 OPTIMIZATION OF IPS IN ANTI-ICING MODE

4.1 Overall Framework

In the previous chapter, the quantitative assessments of the energy requirements of an IPS in various flight-icing conditions were investigated. Those calculations can provide us with general estimations and guidelines for design of any type of thermal-based IPS, including electro-thermal and hot-air systems. However, the design of a specific IPS operating in specific flight-icing conditions requires defining and solving a proper optimization problem. In this case, the characteristics of the IPS that should be considered consist of the IPS type (electro-thermal or hot-air), the IPS mode (anti- or de-icing) and the IPS operating regime (running-wet or evaporative). The focus of the present thesis is on the electro-thermal IPS. Both the anti-icing (in this chapter and the next one) and the de-icing (in Chapter 6) modes are investigated. The operating regime is also to be considered by defining suitable objective and constraint functions. A general formulation of the optimization problem being investigated can be given as

$$\begin{aligned} \min_{\mathbf{x} \in \mathcal{Z}} \quad & f_i(\mathbf{x}), \quad i \in I, \\ \text{subject to} \quad & c_j(\mathbf{x}) \leq 0, \quad j \in J, \end{aligned} \tag{4-1}$$

where f_i 's are the objective functions, $I = \{1, \dots, n_f\}$, \mathbf{x} is the vector of n design variables, c_j 's are the constraint functions, $J = \{1, \dots, n_c\}$ and \mathcal{X} is a subset of \mathbb{R}^n . There are three types of design variables that will be used in this thesis: the electric power density of the heaters, the extent of the heaters, the extent of the heating zone and the cycling sequence time of the heaters. Since the anti-icing mode is a steady-state process, the last type is only applicable to the transient de-icing mode (Chapter 6). The objective and constraint functions are obtained by the CHT simulation, which is considered as a blackbox. An overall schematic of the optimization process is shown in Figure 4.1. The CHT simulation of the IPS is performed for the given flight-icing conditions. The solution is then used to evaluate the objective functions and constraints while the optimization algorithm is used to determine the value of the design variables iteratively until convergence is achieved relative to some defined criteria.

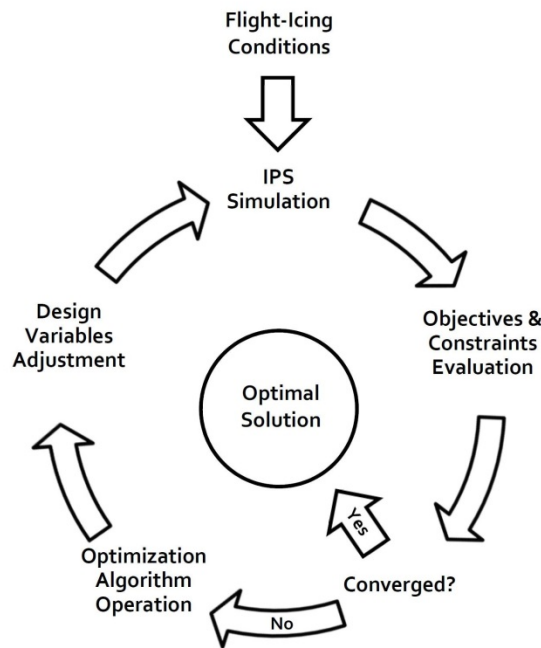


Figure 4.1: Schematic of the optimization process.

4.2 Optimization Method

The optimization problem defined in Eq. 4-1 is solved by the MADS algorithm [94]. MADS is a derivative-free method based on a search-and-poll paradigm. The search is a flexible and optional method that allows taking into accounts the specificities of the problem and the insights of the user. It can consist of any exploration method, like genetic algorithms [95], particle swarms [96], Latin hypercube [97] or variable neighborhood search [98]. In this work, the search is a surrogate-based search¹ that uses the dynaTree library [99] to build predictive models of the objective and the constraint functions. The poll is the rigorous step of MADS on which the convergence relies.

4.2.1 Poll Step

At each iteration k of the MADS algorithm, the *mesh* is defined as

$$M_k = \{x + \Delta_k^m Dz : z \in \mathbb{N}^{n_D}, x \in \mathbf{x}_k\} \subset \mathbb{R}^n, \quad 4-2$$

where $\mathbf{X}_k = \{x_1, x_2, \dots\} \in \mathbb{R}^n$ is the set of all the points previously evaluated, Δ_k^m is the *mesh size parameter* at iteration k , and the directions of D are positively spanning \mathbb{R}^n . To ensure convergence, all candidates evaluated at iteration k must lie on M_k . The set of trial points is $P_k = \{x_k + \Delta_k^p d : d \in D_k\}$, where the poll directions D_k are combinations of the directions of D whose norm is at most Δ_k^p , the *poll size parameter* that bounds the distance between the trial points and x_k . Figure 4.2 illustrates the progressive diminution of the mesh size and the poll size parameters. MADS controls the mesh size to get smaller faster than the poll size, implying the possible set of polling directions to grow dense in the unit sphere, once normalized. The MADS algorithm ensures global convergence (i.e. independent of the starting point x_0) toward a local optimum satisfying local optimality conditions based on the Clarke calculus for nonsmooth functions [100].

¹ The surrogate-based search inside the optimization algorithm should not be confused with the surrogate-based optimization by reduced order modeling, which will be described in Chapter 5.

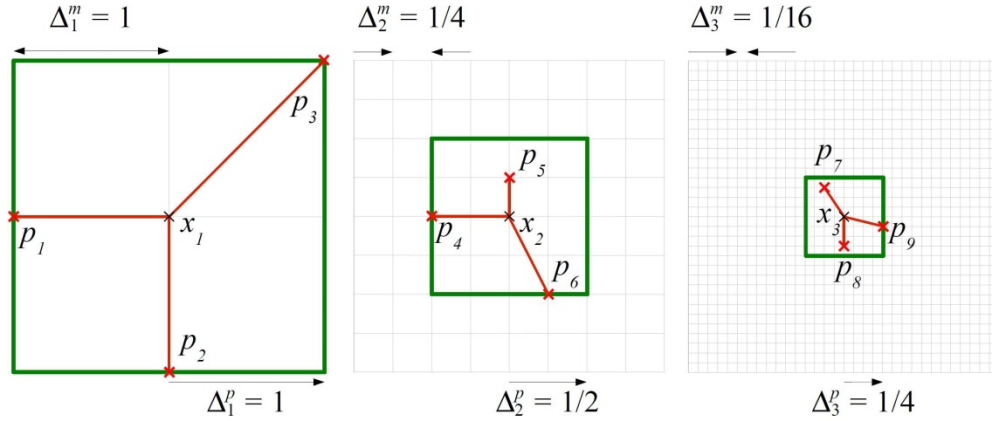


Figure 4.2: Mesh and poll size parameters.

4.2.2 dynaTree Library

The dynaTree package [99] is a statistical regression method. From \mathbf{x} and $y(\mathbf{x})$, dynaTree builds a model of the function y by building several partitioning schemes of \mathbb{R}^n and performing a linear regression in each part. Thus, the prediction on y is piecewise linear. The Bayesian framework allows parameter-free regression and quantification of the deviation of the data from the model. Thus, predictions of the variance of y are available and it is also possible to compute the cumulative density function $\mathbb{P}[y(x) \leq y_0], \forall x \in \mathbb{R}^n, y_0 \in \mathbb{R}$. These predictions are used in the search step of MADS to build statistical relevance criteria of candidates. The interested reader can refer to [99] for more details about dynaTree. In this work, the predictive mean and standard deviation of the objective in x are denoted by $\hat{f}(x)$ and $\hat{\sigma}_f(x)$. Similarly, for the constraint c_j , they are denoted by $\hat{c}_j(x)$ and $\hat{\sigma}_j(x)$, $j \in J$.

4.2.3 Statistical Relevance

The *expected improvement* [101, 102] is a statistical relevance criteria introduced for global optimization. Let f_{\min} be the objective value of the best feasible point found so

far. The *improvement* is defined as $I(x) = \max\{f_{\min} - f(x); 0\}$. Though the improvement can only be known by evaluating x , the *expected improvement* can be analytically approximated by dynaTree [99]:

$$EI(x) = \mathbb{E}[I(x)] = \int_0^{+\infty} I \Phi_f(f_{\min} - I) dI, \quad 4-3$$

where Φ_f is the probability density function of f . Figure 4.3 shows an example of dynaTree model for 24 data points $\mathbf{x} = \{x_1, \dots, x_{24}\} \subset [0; 25]$. The first part of the diagram shows the decision tree that allows finding out in which leaf $\eta \in \{\eta_1, \dots, \eta_6\}$ lies a point x . The second part of the diagram illustrates the partitioning of the interval $[0; 25]$. A linear regression is built in each of these parts. As we can see, the standard deviation of the model is larger in the ill explored areas. The third part of the diagram shows the probability of improvement $\mathbb{P}[y(x) < y_{\min}]$, where $y_{\min} = \min_{x \in X} y(x)$, and the expected improvement $EI(x), \forall x \in [0; 25]$. The probability of improvement is maximal for $x = 5$, while the expected improvement peaks at $x = 17$. This illustrates that while the function y is very likely to have a local optimum around $x = 5$, there is a promising probability of a better optimum around $x = 17$. As dynaTree provides an approximation of the cumulative density functions of the constraints, the probability of feasibility of a point can be estimated as

$$P(x) = \prod_{j \in J} \mathbb{P}[c_j(x) \leq 0]. \quad 4-4$$

This can be computed as dynaTree returns $\mathbb{P}[c_j(x) \leq 0], \forall j \in J$. This allows us to statistically describe the feasibility by one scalar value. By merging the expected improvement and the probability of feasibility, the *expected feasible improvement* is naturally defined as [103, 104]:

$$EFI(x) = EI(x)P(x). \quad 4-5$$

$EFI(x)$ describes the expected income of x regarding to the optimization problem.

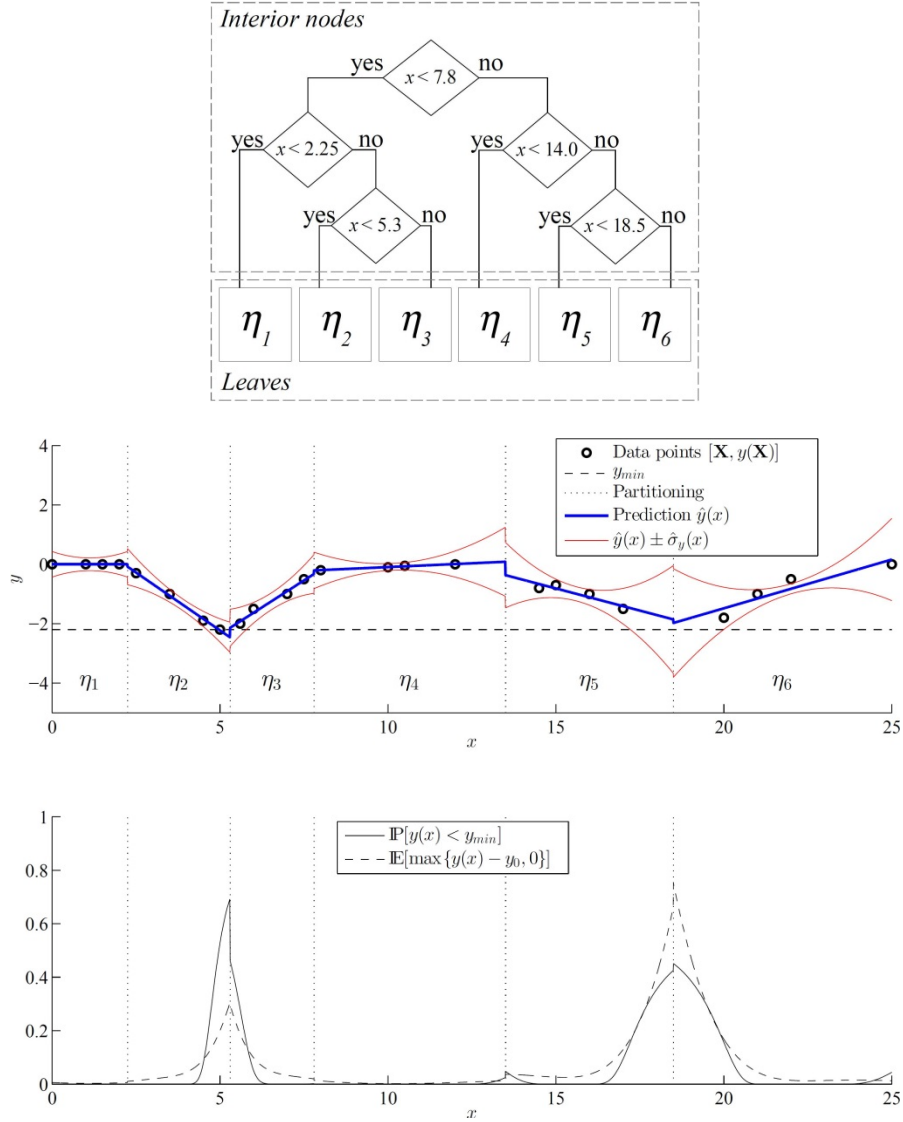


Figure 4.3: dynaTree model on 24 data points in \mathbb{R} (picture adapted from [104]).

4.2.4 Lack of Information

To improve the surrogate-based search, the candidates must not only be promising solutions to the optimization problem, but to some extent, they must also participate to improve the models of f and c_j , $j \in J$. In this regard, uncertainty of model predictability due to lack of information (areas of the design space where no simulations have been conducted) must be quantified, in order to favour the candidates in the ill-explored area of χ . Uncertainties about the objective can be quantified by the

approximated standard deviation $\hat{\sigma}_f$ returned by dynaTree [99]. For the constraints however, uncertainty about $c_j(x), \forall j \in J$ is less important than the uncertainty on the feasibility of the point x . For example, the value of $c_1(x)$ is of little interest if c_2 is known to be not satisfied in x . Finally, the uncertainties on the feasibility can be quantified by considering that the event “ x is feasible” as a Bernoulli law of parameter $P(x)$. Thus, the variance of this law is $P(x)(1-P(x))$. The *uncertainty in the feasibility* (μ) is defined [104]:

$$\mu(x) = 4P(x)(1-P(x)). \quad 4-6$$

The coefficient 4 normalizes μ in $[0;1]$. Figure 4.4 shows an example of $P(x)$ and $\mu(x)$ on a single constraint c . The model of c is built from 30 evaluations in $[0; 10]$. The feasibility threshold is represented by the horizontal dashed line $c = 0$ and the feasible domain is approximately $[4; 7]$. The uncertainty μ is maximal for $x = 4$, where $c = 0$. However, the sharp variation of c at $x = 7$ does not induce a high value of μ as the feasibility prediction is adamant.

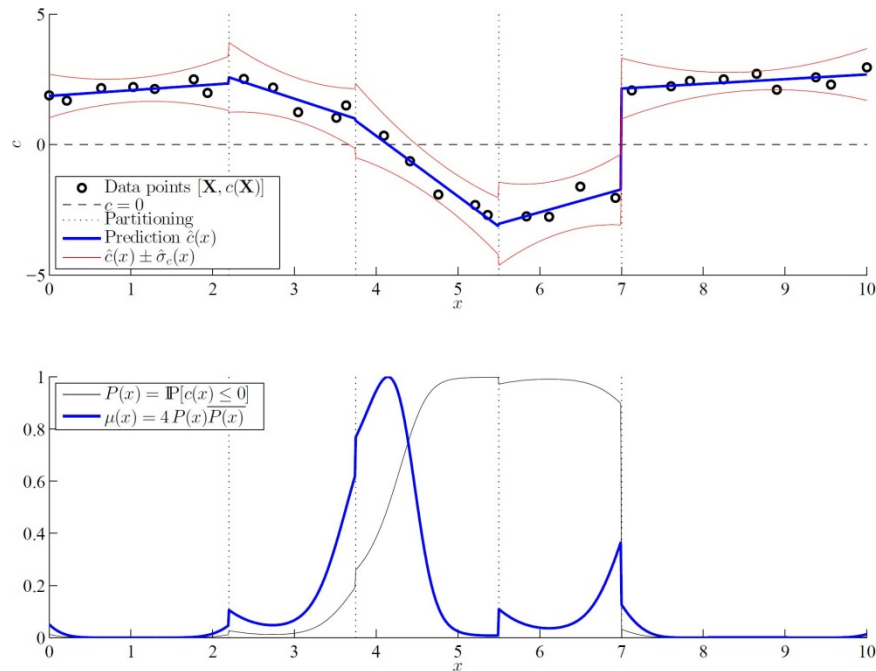


Figure 4.4: Probability of feasibility and uncertainty about feasibility (picture adapted from [104]).

4.2.5 Surrogate-Based Search

The two surrogate-based searches considered in this work are the methods *FSP* and *EFIC* described in [104]. The *FSP* formulation consists of minimizing the model of the objective under the *chance constraint* $P(x) \geq 1/2$. To improve this search, exploration terms based on the standard deviation of the models are added [99]. The standard deviation of the objective is considered favourably as it can lead to an improvement of the solution. The exploration term is weighted by a coefficient $\lambda \in [0, 1]$, leading to the formulation:

$$\begin{aligned} \min_{x \in \mathcal{X}} \quad & \hat{f}(x) + \lambda \hat{\sigma}_f(x), \\ \text{subject to} \quad & P(x) \geq \frac{1}{2}. \end{aligned} \tag{4-7}$$

The constraint $P(x) \geq 1/2$ ensures that, through the whole optimization process, half of the candidates returned by the search should be feasible. Moreover, this search will favor the exploration of the frontier of the feasible domain, where $P(x) = 1/2$. The λ parameter permits adjusting the magnitude of the exploration. While $\lambda = 0.01$ is considered as light, $\lambda = 1$ implies an intense exploration [99].

The *EFIC* formulation consists of an unconstrained optimization problem based on the expected feasible improvement. *EFI* does not take into account the information brought by x to the models of f and c_j , $j \in J$. Thus, an exploration term $EI(x)\mu(x) + P(x)\hat{\sigma}_f(x)$ is added. The term $EI(x)\mu(x)$ aims to favor the points with a promising objective but with an uncertain feasibility. This term will improve the representation of the frontier of the feasible domain, where $\mu(x)$ is maximal. Conversely, the term $P(x)\hat{\sigma}_f(x)$ favours feasible points with an uncertain objective, leading to an improvement of the model of f in the feasible domain. This lead to the following formulation:

$$\max_{x \in \mathcal{X}} \quad EFI(x) + \lambda \left(EI(x)\mu(x) + P(x)\hat{\sigma}_f(x) \right). \tag{4-8}$$

4.3 Formulations of the Objective and Constraint Functions

In all engineering design problems, reducing the cost is one of the most important goals. However, reducing the cost is desirable as long as the safety is not affected. In fact, a design process is a proper trade-off between the cost and the safety. In the context of optimization, this can be achieved by defining suitable objective and constraint functions. The success of an optimization approach heavily depends on the formulation of these functions. In a good formulation, not only are the physical viewpoints taken into account, the mathematical viewpoints are considered as well. In this section, the objective and constraint functions are carefully formulated and proposed from both viewpoints. These functions are provided in Table 4.1. They are described in the following. The numerical results should also be studied to fully understand these functions.

- **TEP:** The amount of power used for anti-icing determines the cost. *TEP*, which stands for “total electric power”, gives the consumption of the electric power, i.e. power density multiplied by the surface area. It is given by

$$\int_{s_{el}}^{s_{eu}} P''(s) ds, \quad 4-9$$

where s is the wrap (surface) distance measured from the leading edge, which is negative on the lower and positive on the upper surface, and $P''(s)$ is the power density at position s . The domain of integration is the interval between the wrap distance of the end of the heating zone on the lower surface, s_{el} , and that on the upper surface of the wing, s_{eu} .

- **MIG:** The ice growth is the key parameter in controlling the in-flight icing events. Larger ice growth normally leads to more serious problems. *MIG*, which stands for “maximum ice growth”, gives the maximum ice growth over the heating zone:

$$MIG = \max \left\{ \dot{m}_{ice}''(s) \right\}_{s_{el}}^{s_{eu}} - \dot{m}_{ice*}''(s), \quad 4-10$$

where $\dot{m}_{ice}''(s)$ is the ice growth at position s on the surface and $\dot{m}_{ice*}''(s)$ is the largest ice growth allowed over the heating zone.

Table 4.1: Formulations of the objective and constraint functions.

Type	Formulation	Description
TEP	$\int_{s_{el}}^{s_{eu}} P''(s) ds$	Total electric power
MIG	$\max \{ \dot{m}_{ice}''(s) \}_{s_{el}}^{s_{eu}} - \dot{m}_{ice*}''(s)$	Maximum ice growth
MWT	$T_0(s) - \min \{ T(s) \}_{s_{el}}^{s_{eu}}$	Minimum wall temperature
TWT	$\int_{s_{el}}^{s_{eu}} T_t(s) - T(s) ds$	Target wall temperature
$(TMWT)_d$	$\int_{s_{el}}^{s_{eu}} \tau_d(T) ds$	Target-minimum wall temperature (discontinuous)
$(TMWT)_c$	$\int_{s_{el}}^{s_{eu}} \tau_c(T) ds$	Target-minimum wall temperature (continuous)
EFH	$h_f(s_{el}) + h_f(s_{eu})$	End film height
$(DEFH)_{lo}$	$\eta(h_f(s_{el}))$	Distance-end film height (lower surface)
$(DEFH)_{up}$	$\eta(h_f(s_{eu}))$	Distance-end film height (upper surface)
MST	$\max \{ T_{shell} \} - T_{shell*}$	Maximum shell temperature

- **MWT** : As an alternative to the ice growth, the wall (surface) temperature, which actually determines the amount of the ice growth on the surface, can be used. The wall temperature could be more advantageous as it also enables one to respect a specific margin of safety when intending to reach an ice-free surface. In this case, MIG can only return a zero value, which may indicate a condition that is either

near to or far from the marginal freezing condition. By using the wall temperature, one can respect a specific margin with respect to the conditions required for an ice-free surface. This characteristic is also useful in surrogate modeling, which will be discussed in the next chapter. *MWT*, which stands for “minimum wall temperature”, gives the minimum wall temperature over the heating zone:

$$MWT = T_0(s) - \min \{T(s)\}_{s_{el}}^{s_{eu}}, \quad 4-11$$

where $T(s)$ is the wall temperature at position s on the surface and $T_0(s)$ is the smallest temperature allowed over heating zone. Obviously, to have an ice-free surface, $T_0(s)$ has to be greater than the freezing temperature.

- ***TWT***: The previous function, i.e. *MWT*, only ensures that the minimum wall temperature is greater than a specific temperature. The value of the wall temperature at the other parts of the heating zone is not considered by *MWT*. If our goal is to reach a definite temperature distribution, it would be more efficient to set a target temperature distribution. *TWT*, which stands for “target wall temperature”, gives the difference between the wall temperature distribution and the target one:

$$TWT = \int_{s_{el}}^{s_{eu}} |T_t(s) - T(s)| ds \quad 4-12$$

where $T_t(s)$ is the target wall temperature at position s on the surface, which, obviously, has to be above the freezing temperature. Note that *TWT* is a non-negative valued function.

- ***(TMWT)_d***: In some cases, it may not be possible or practical to completely reach a target temperature distribution. Therefore, it would be beneficial to combine the properties of *MWT* and *TWT*. *(TMWT)_d*, which stands for “target-minimum wall temperature (discontinuous)”, provides us with such capability by using the following conditional function:

$$\tau_d(T) = \begin{cases} (T_0(s) - T(s)) & \text{if } \min\{T(s)\}_{s_{el}}^{s_{eu}} \geq T_0, \\ \max\{0, (T_0(s) - T(s))\} & \text{if } \min\{T(s)\}_{s_{el}}^{s_{eu}} < T_0. \end{cases} \quad 4-13$$

The above equation separates the definition of the feasible regions, i.e. $\min\{T(s)\}_{s_{el}}^{s_{eu}} \geq T_0$, from that of the infeasible regions, i.e. $\min\{T(s)\}_{s_{el}}^{s_{eu}} < T_0$. Figure 4.5 illustrates a schematic picture of $\tau_d(T)$. The reason for using such definition, and not simply using $(T_0(s) - T(s))$ for all ranges of $\min\{T(s)\}_{s_{el}}^{s_{eu}}$, is that the integral of the feasible regions may outbalance that of the infeasible regions, resulting in a net feasible output even if there are some regions with infeasible temperature (Figure 4.6). Having defined $\tau_d(T)$, one can now calculate $(TMWT)_d$ as follows:

$$(TMWT)_d = \int_{s_{el}}^{s_{eu}} \tau_d(T) ds \quad 4-14$$

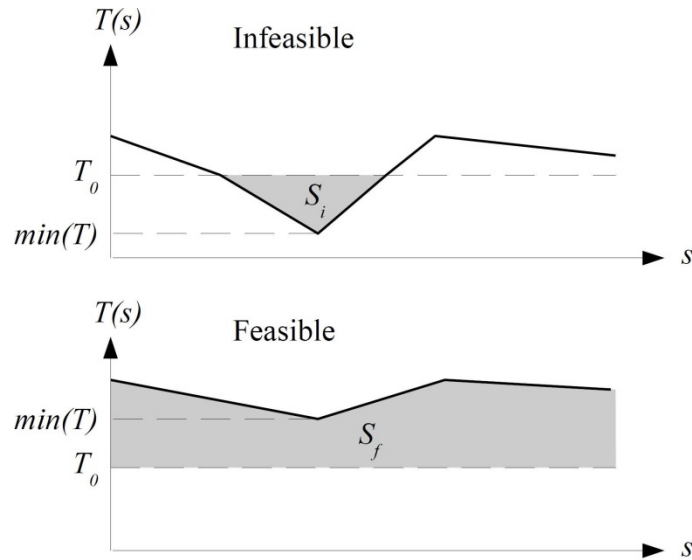


Figure 4.5: Illustration of the function $TMWT$ for infeasible and feasible cases (S_i is the surface integration of temperature profile over infeasible parts and S_f is that over feasible parts).

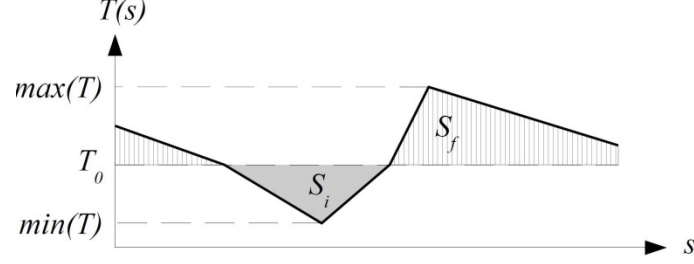


Figure 4.6: An infeasible case with net feasible output (S_i is the surface integration of temperature profile over infeasible parts and S_f is that over feasible parts).

- **(TMWT)_c**: It is noticed that for marginal cases where $\min\{T(s)\}_{s_{el}}^{s_{eu}}$ is very close to $T_0(s)$, if $\min\{T(s)\}_{s_{el}}^{s_{eu}}$ slightly varies, a discontinuous jump in the function value occurs. The discontinuity may affect the performance of the optimization process. Furthermore, it can decrease the accuracy of the surrogate models, which will be discussed in the next chapter. **(TMWT)_c**, which stands for “target-minimum wall temperature (continuous)”, circumvents this problem by defining the following conditional function:

$$\tau_c(T) = \begin{cases} \min\{T(s)\}_{s_{el}}^{s_{eu}} & \text{if } \min\{T(s)\}_{s_{el}}^{s_{eu}} \geq T_0, \\ \max\{0, (T_0(s) - T(s))\} & \text{if } \min\{T(s)\}_{s_{el}}^{s_{eu}} < T_0. \end{cases} \quad 4-15$$

We can see that the function for the second condition is similar to that of $\tau_d(T)$, but the function for the first condition is changed to a point value.

- **EFH**: As previously mentioned, the runback ice can be a serious threat to the safety even if there is a completely clean surface around the leading edge. The formation of the runback ice is due to the water film moving downstream beyond the heating zone, where the water film can immediately freeze. Therefore, to avoid the runback ice, water film shall not pass beyond the heating zone. **EFH**, which stands for “end film height”, controls the amount of the water film passing beyond the heating zone. It can be given as follows:

$$EFH = h_f(s_{el}) + h_f(s_{eu}), \quad 4-16$$

where $h_f(s_{el})$ and $h_f(s_{eu})$ are the water film height at the end of the heating zone on the lower and the upper surfaces, respectively.

- **(DEFH)_{lo} & (DEFH)_{up}**: *EFH* is a non-negative valued function and this affects the searchability of the design space for feasible solutions. This would not be desirable when *EFH* is used as a constraint. According to Figure 4.7, a good constraint formulation would be a quantifiable constraint, i.e. one that provides a distance to infeasibility as well as a distance to feasibility. *(DEFH)_{lo}* and *(DEFH)_{up}*, which stand for “distance-end film height on the lower and upper surface, respectively, provide such capability by defining the following conditional function:

$$\eta(h_f(s_e)) = \begin{cases} h_f(s_e) & \text{if } h_f(s_e) > 0, \\ -d_f(s_e) & \text{if } h_f(s_e) = 0. \end{cases} \quad 4-17$$

where $d_f(s_e)$ is the distance between the point at which the water film is completely evaporated and the end of the heating zone on the upper or lower surfaces (Figure 4.8). *(DEFH)_{lo}* and *(DEFH)_{up}* can then be given as follows:

$$(DEFH)_{lo} = \eta(h_f(s_{el})) \quad 4-18$$

$$(DEFH)_{up} = \eta(h_f(s_{eu})) \quad 4-19$$

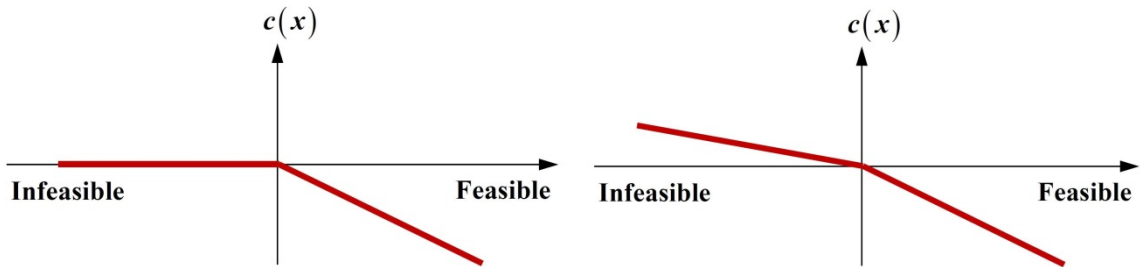


Figure 4.7: Bad (left) and good (right) constraint formulations.

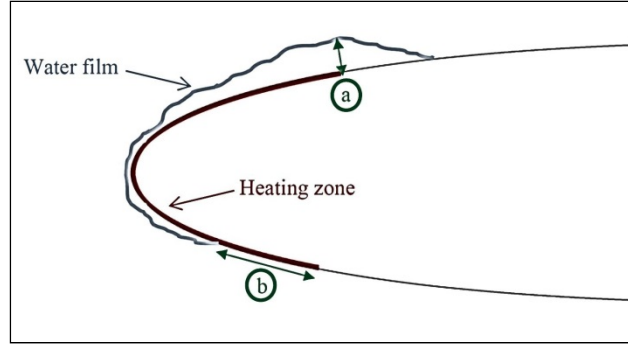


Figure 4.8: Illustration of the function $DEFH$ for positive (a) and negative (b) values.

- MST**: The mechanical properties of aircraft structures are highly dependent on temperature. The ultimate strength, the yield strength and the fatigue life of many composite materials decrease as temperature increases [105]. Moisture is also more corrosive at higher temperatures because of the normal increase in reaction rate and the larger hydrogen ion activity due to lower pH [106]. This becomes more critical when considering thermal spiking, which describes the effect of a rapid increase in temperature of a composite with high moisture content [107]. It can damage the matrix, giving rise to moisture absorption into the composite and limiting the maximum temperature at which a composite can operate. Finally, large temperature differences cause non-uniform expansions in different parts of the structure, resulting in higher thermal stresses, added to the other imposed stresses [108]. In light of the abovementioned motives, it seems essential to restrict the maximum temperature of the composite shell, inside which the electro-thermal IPS is embedded. For this purpose, MST , standing for “maximum shell temperature”, can be defined as follows:

$$MST = \max \{ T_{shell} \} - T_{shell*}, \quad 4-20$$

where T_{shell*} is the highest temperature allowed for the shell. It should be noted that the maximum temperature takes place inside the shell and not on the external wall, as the heating blankets are placed inside the shell.

4.4 Numerical Test Cases

The optimization results are obtained using the C-based MADS implementation from the NOMAD package [109] and the R dynaTree library [110]. Also, in the dynaTree-based optimization cases, $\lambda = 0.1$ is used as the exploration parameter. The flight-icing conditions for the optimization test cases are provided in Table 4.2.

Table 4.2: Flight-icing conditions.

Temperature [K]	Velocity [m.s ⁻¹]	LWC [g.m ⁻³]	MVD [μ m]	AoA [deg.]
254.375	44.704	0.78	20	-4

In Chapter 3, the pros and cons of the running-wet and the fully-evaporative regimes were discussed. An operating regime having the advantages of both regimes while avoiding their drawbacks would be the best option in many cases. In this kind of regime, which is called the evaporative regime, the impinging water droplets are not evaporated upon impact on the surface. Nonetheless, no water film is allowed to pass beyond the heating zone. The runback water film is gradually evaporated before the end of the heating zone. The optimization results will be presented for both the running-wet and the evaporative regimes. The proposed formulations are used to define suitable optimization problem statements. The results for each regime are divided into four parts:

- *Primary optimization*: It is a preliminary step toward the power optimization. In all power optimization cases, the power densities (in W/m²) can vary within the interval [1,000; 15,000] for the running-wet regime and within [1,000; 30,000] for the evaporative regime. In the primary optimization part, a bi-objective optimization problem is solved to better understand the relationship between various functions and to achieve a better estimation of the proper values that should be used as the constraints.

- *Power optimization*: In this part, the power densities of the heaters are optimized based on different constraint formulations, in all of which *TEP* (total electric power) is the only objective function. The matrix of the test cases of this part is provided in Table 4.3, which includes three cases for the running-wet regime and seven cases for the evaporative regime. In this table, the constraint(s) used for each test case are identified.
- *Optimization under lack of energy*: In some crucial situations, the amount of energy available on the aircraft is not enough. Therefore, one is only able to achieve the best possible solution, and not the best solution. In other words, we should answer this question: what is the best we can do with what we have? The test cases of this part are concerned with this kind of situations.
- *Power-extent optimization*: In this part, not only are the power densities of the heaters considered as design variables, the heating zone extents are included in the design variables as well.

Table 4.3: Matrix of test cases for power optimization.

	MIG	MWT	TWT	(TMWT) _d	(TMWT) _e	EFH	(DEFH) _{lo}	(DEFH) _{up}	MST
W-I	✓								
W-II		✓							
W-III			✓						
E-I	✓					✓			✓
E-II		✓				✓			✓
E-III				✓		✓			✓
E-IV					✓	✓			✓
E-V		✓					✓	✓	✓
E-VI				✓			✓	✓	✓
E-VII					✓		✓	✓	✓

4.4.1 Running-Wet Regime

4.4.1.1 Primary Optimization

The goal in the running-wet regime is to achieve an ice free surface over the heating zone with no concern about the runback ice after the zone. For this purpose, a bi-objective problem with TEP (total electric power) and MIG (maximum ice growth) as the objective functions can be defined (Case W-P):

$$\begin{aligned} f_1(\mathbf{x}) &\equiv TEP, \\ f_2(\mathbf{x}) &\equiv MIG, \end{aligned} \tag{4-21}$$

where $\dot{m}_{ice^*}'' = 0$. Figure 4.9 shows the Pareto front of this bi-objective problem. As we can see, achieving an ice-free surface, where the maximum ice growth is zero, is possible. Based on this graph, the least amount of total electric power needed for this purpose is about 1200 W.

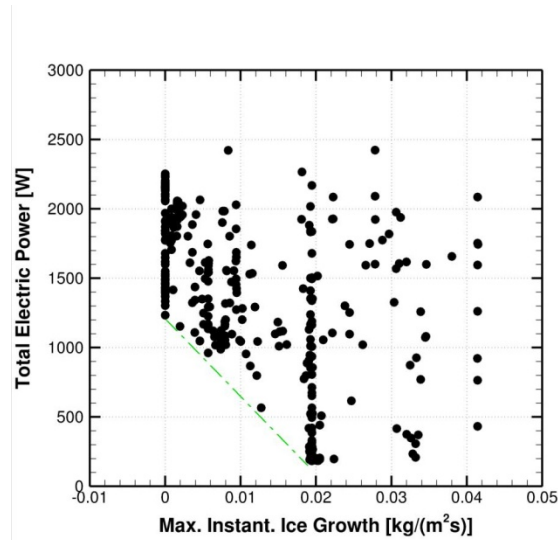


Figure 4.9: Pareto front (Case W-P).

4.4.1.2 Power Optimization

As mentioned before, in all power optimization problems, TEP (total electric power) is the only objective function to be considered:

$$f_1(\mathbf{x}) \equiv TEP. \quad 4-22$$

According to Table 4.3, *MIG* (maximum ice growth) is the constraint of Case W-I:

$$c_1(\mathbf{x}) \equiv MIG, \quad 4-23$$

where $\dot{m}_{ice}'' = 0$. Figure 4.10 shows the convergence history of the best feasible objective values, i.e. the objective values when $c_1 \leq 0$ (actually the ice growth is a non-negative value, so feasible solutions satisfy $c_1 = 0$). The optimized total electric power is 1,051 W, which is about 12% less than the value used in the experimental test (Run #91, TTMS #123), i.e. 1,199 W [49]. Figure 4.10, also, depicts the convergence history of the best feasible design variables values throughout the optimization process. Figure 4.11 compares the optimized and experimental power densities. The heaters on the lower surface, i.e. heaters 1, 2 and 3, require more power density compared to the ones on the upper surface, i.e. heaters 5, 6 and 7. This is due to the negative angle of attack resulting in greater heat transfer on the lower surface because of lower pressure and higher velocity (Figure 4.12).

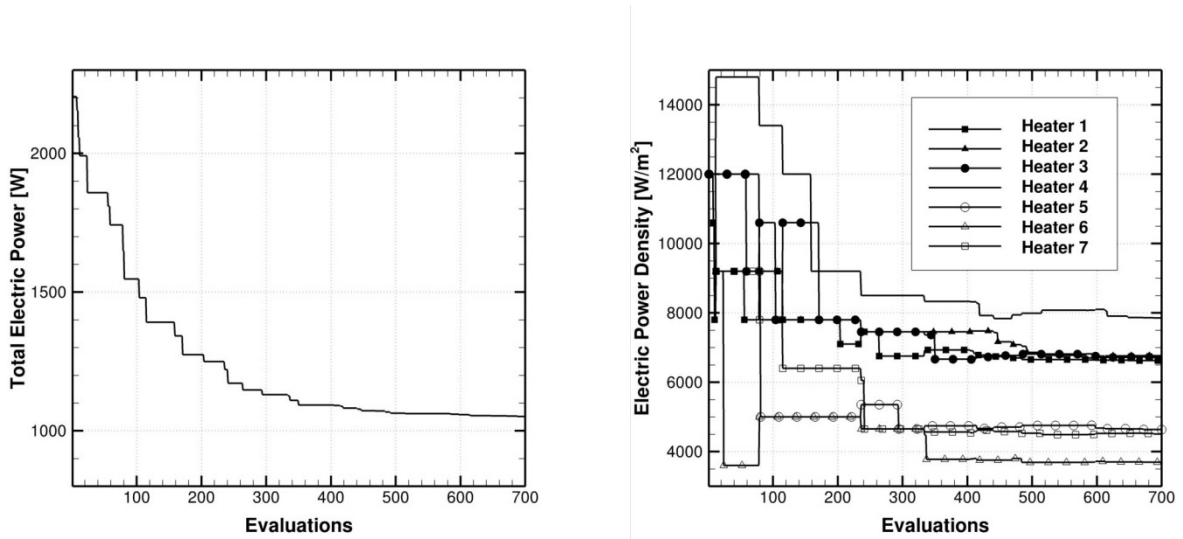


Figure 4.10: Convergence history of the best feasible objective function and design variables values (Case W-I).

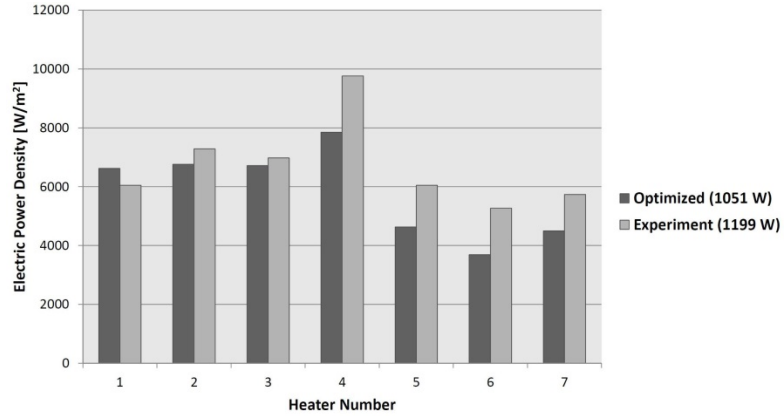


Figure 4.11: Optimized and experimental values of power densities (Case W-I).

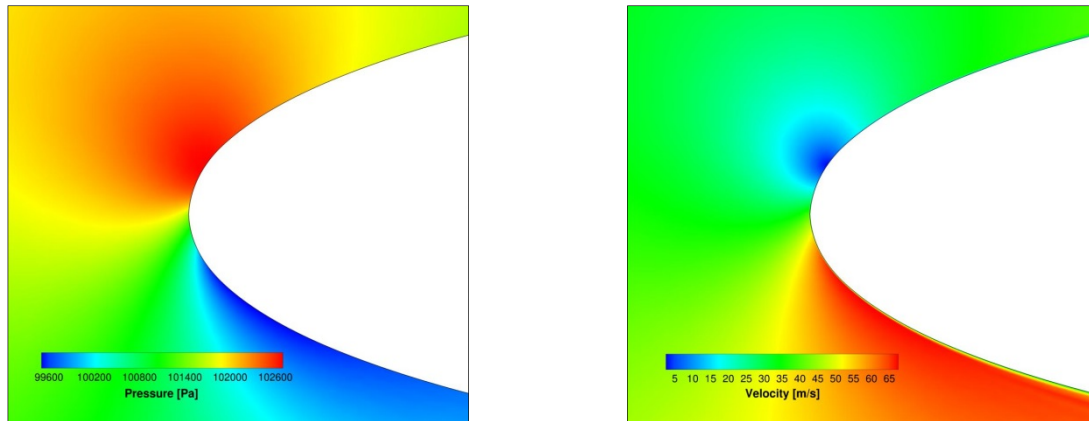


Figure 4.12: Pressure (left) and velocity (right) contour plots (Case W-I).

The previous case, i.e. Case W-I, does not seem to be conservative enough since no margin of safety can be considered in such formulation (as discussed before). To account for that, the following constraint on the minimum wall temperature may be used for Case W-II:

$$c_1(\mathbf{x}) \equiv MWT, \quad 4-24$$

where $T_0 = 276$. Hence, a margin is considered with respect to the freezing temperature, i.e. 273.15 K. In order for MWT to be efficient, the margin should not be too large otherwise it would require excessive power usage. The minimum total electric power

reached in this case is 1,386 W (Figure 4.13) which, because of the margin, is 32% larger than that of Case W-I, i.e. 1,051 W.

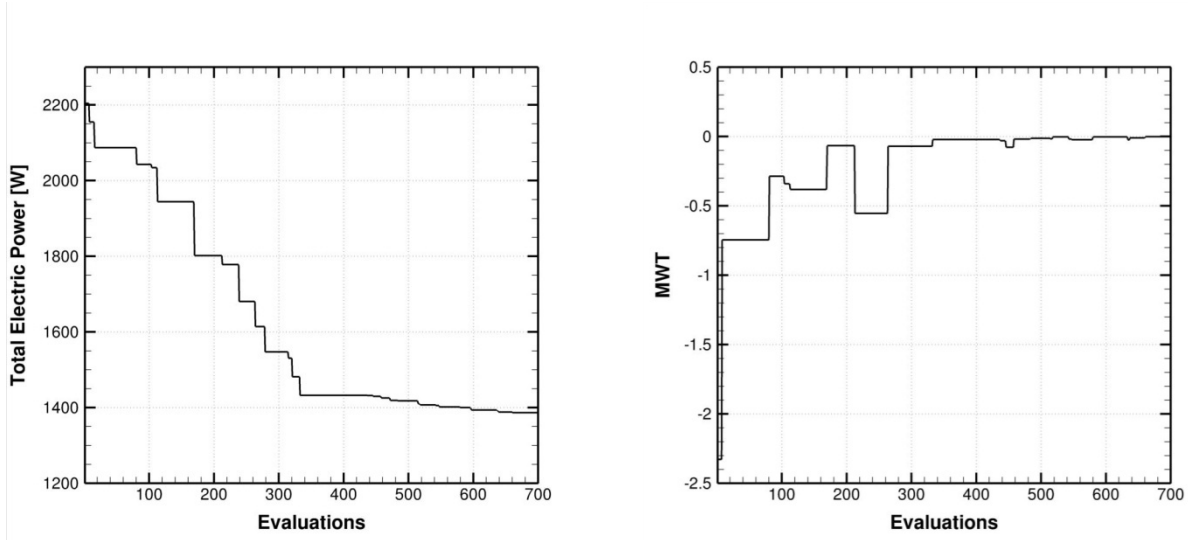


Figure 4.13: Convergence history of the best feasible objective function (left) and constraint violation (right) values (Case W-II).

Another alternative being more suitable for the running-wet regime is a target wall temperature, as follows (Case W-III):

$$c_1(\mathbf{x}) \equiv TWT, \quad 4-25$$

where $T_t = 276$ is used as the target temperature. This constraint can be more efficient than MWT in terms of power usage as it ensures that the surface temperature all over the heating zone is not higher than what is actually needed. Based on the definition of TWT , this constraint never yields a feasible solution, i.e. a solution with a negative constraint value. Hence, the objective function history is plotted based on the best constraint values (Figure 4.14). The total electric power is reached to 1,172 W, which is 15% less than that obtained in Case W-II. Figure 4.15 compares the optimized power densities between the two cases. As shown, the power density of all heating pads for Case W-III is less than that for Case W-II.

In order to better compare the performance of the running-wet test cases, i.e. W-I, W-II and W-III, the profiles of three surface quantities at their optimal states are compared in Figure 4.16. As expected for the running-wet regime, runback ice is observed in all test cases because the water film passes beyond the protected zone. However, the largest amount of ice on the upper and the lower surfaces accretes in Case W-I. The temperature profile of Case W-III shows that the optimal state closely captures the target temperature, i.e. $T_i = 276$. It is also interesting to note that the temperature profile of Case W-I is very similar to that of Case W-III with a vertical shift toward the freezing temperature. According to these results and what was previously mentioned about respecting a safety margin, one can conclude that Case W-III, which is based on the TWT function, is the most promising case for the running-wet regime. However, one should not ignore the fact that, as stated before, TWT does not allow having a negative constraint value. Therefore, even a small value of TWT does not necessarily guarantee an ice-free heating zone. To ensure that the heating zone is ice-free, one need to check the ice growth profile of the optimized solution.

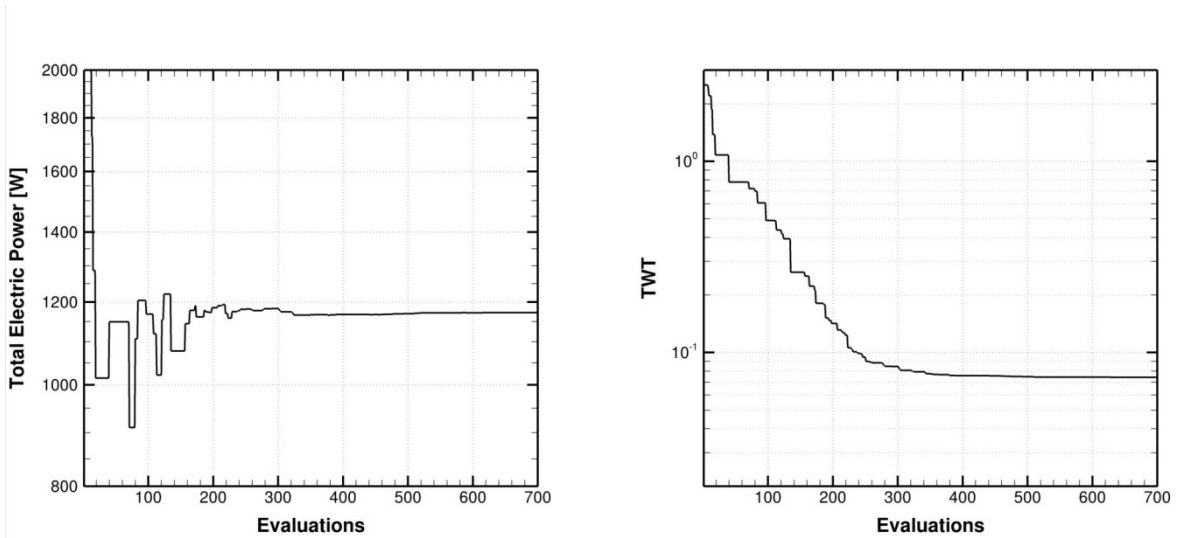


Figure 4.14: Convergence history of the objective function values (left) based on the best constraint violation values (right) (Case W-III).

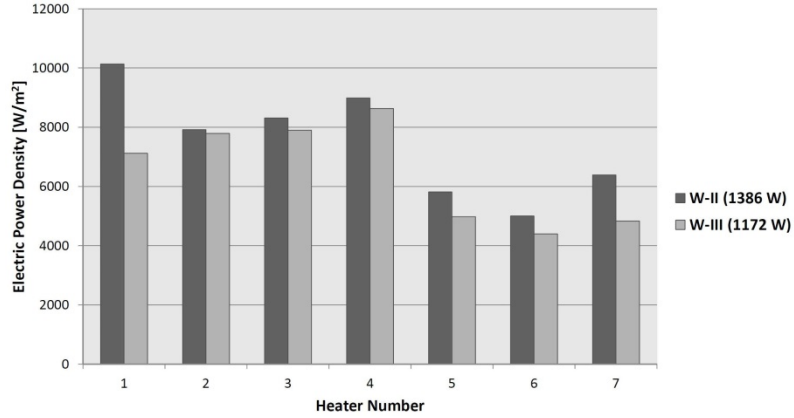


Figure 4.15: Optimized values of power densities.

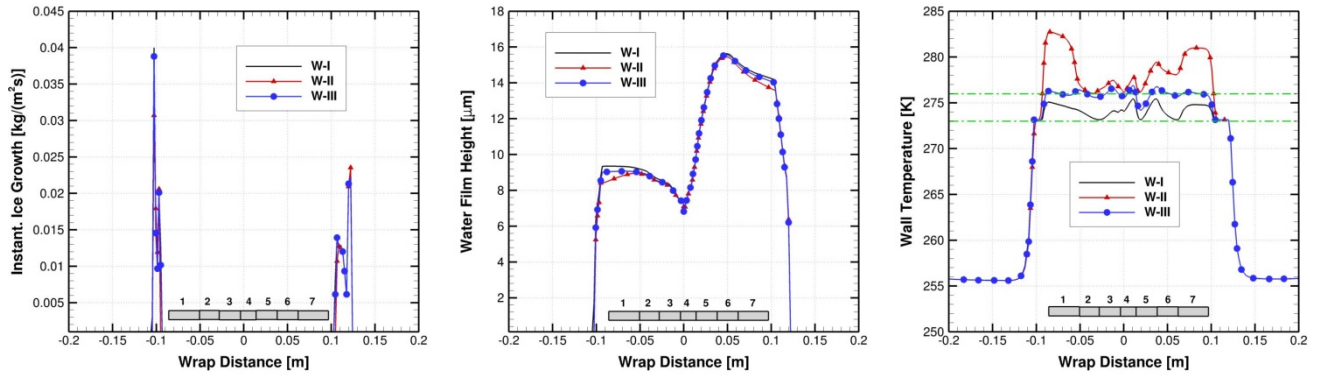


Figure 4.16: Profiles of three surface quantities at optimal states.

The previous test cases have been optimized using MADS without statistical surrogates in the search step. To demonstrate the influence of these surrogates on the optimization results, case W-III is MADS's optimized in conjunction with the *FSP* and *EFIC* formulations. As shown in Figure 4.17, *EFIC* has no significant effect on MADS, but *FSP* has reduced the objective value to 1,059 W, which is about 9% less than that obtained by *EFIC*. This reduction is, however, at the cost of converging to a larger constraint violation, resulting in a temperature profile that corresponds less to the target value, which is 276 K (Figure 4.18). This causes the runback ice to occur within the protected zone on the upper surface.

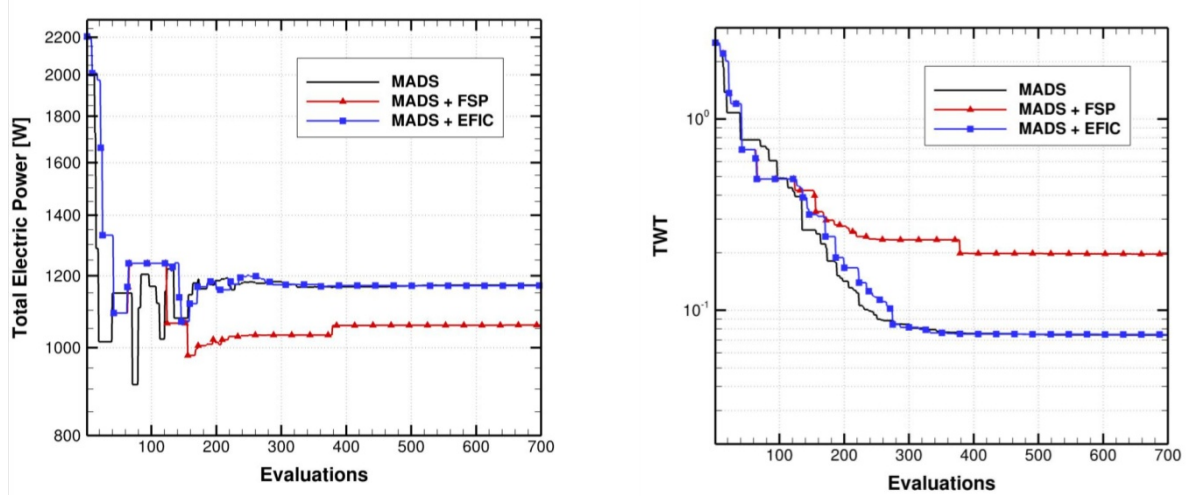


Figure 4.17: Convergence history of the objective function values (left) based on the best constraint violation values (right) (Case W-III).

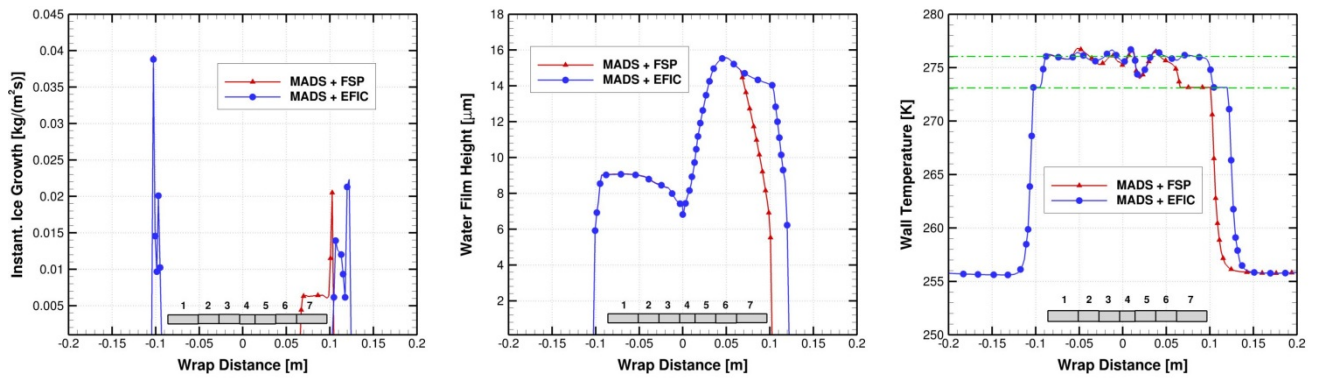


Figure 4.18: Profiles of three surface quantities at optimal states (Case W-III).

4.4.1.3 Optimization under Lack of Energy

In all the cases presented so far, no constraint is imposed on the electric power. In fact, optimization is performed regardless of the amount of the energy available on the aircraft. However, it is possible that the optimal solution needs a total electric power that exceeds the capacity of the aircraft. For example, suppose that only 950 W of electric power is available in a crucial case. According to the optimal solution of Case W-I in the previous part, one would need at least 1,051 W to have zero ice growth over the heating zone. It is evident that it is not possible to reach a completely ice-free zone with only 950 W. In this case, one should look for the smallest amount of maximum ice growth that can be

reached with this amount of power available. To do so, the following objective and constraint functions should be considered (Case W-LE):

$$\begin{aligned} f_1(\mathbf{x}) &\equiv \text{MIG}, \\ c_1(\mathbf{x}) &\equiv \text{TEP} - 950, \end{aligned} \tag{4-26}$$

where $\dot{m}_{ice^*}'' = 0$. Figure 4.19 shows the convergence history of the best feasible objective function values and Figure 4.20 shows the profile of the three surface quantities at the optimal state. Note that *MIG* is a measurement only over the protected zone and not beyond the zone. The least amount of ice growth over the heating zone, as shown, is about $0.005 \text{ kg}/(\text{m}^2 \cdot \text{s})$. This is the best scenario with this amount of power available.

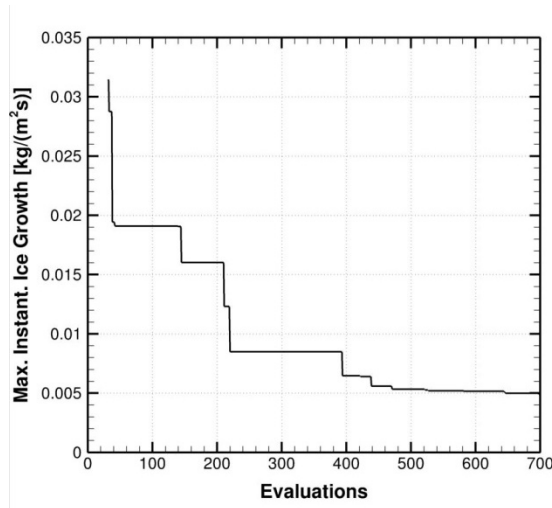


Figure 4.19: Convergence history of the best feasible objective function values (Case W-LE).

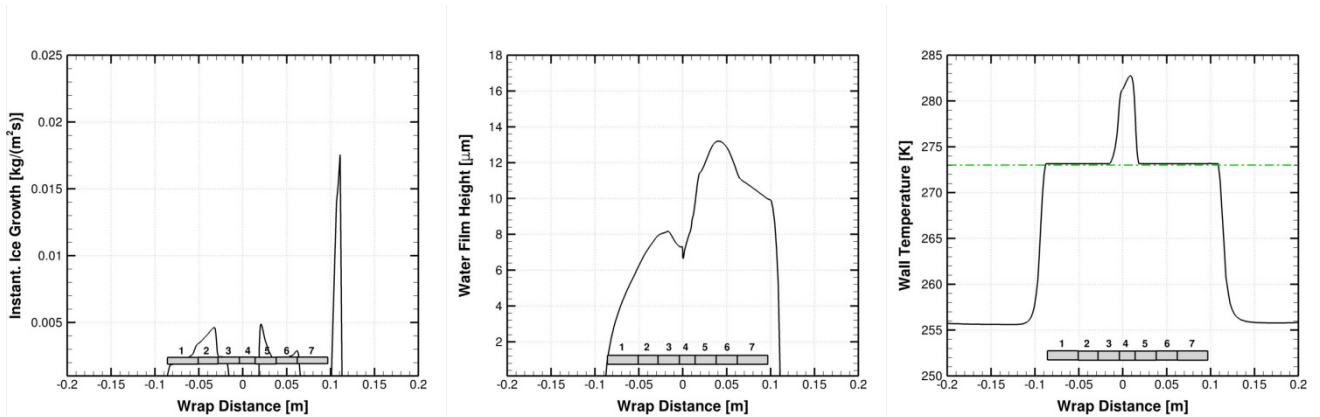


Figure 4.20: Profiles of three surface quantities at optimal state (Case W-LE).

4.4.1.4 Power-Extent Optimization

So far, the power densities of the electric heaters are considered as the design variables. In this section, two other types of design variables are introduced: the heaters extent and the heating zone extent. All types of design variables are schematically shown in Figure 4.21, in which HP denotes the heater's power density, HE denotes the heater's extent and ZE denotes the heating zone extent. It should be noted that the ZE variables will be considered only in the evaporative regime. In the running-wet regime where runback ice is not of concern, using the ZE variables would be meaningless. Here, the effects of including the heaters' extents into the design variables are investigated on the optimization results for the running-wet test cases, i.e. W-I, W-II and W-III.

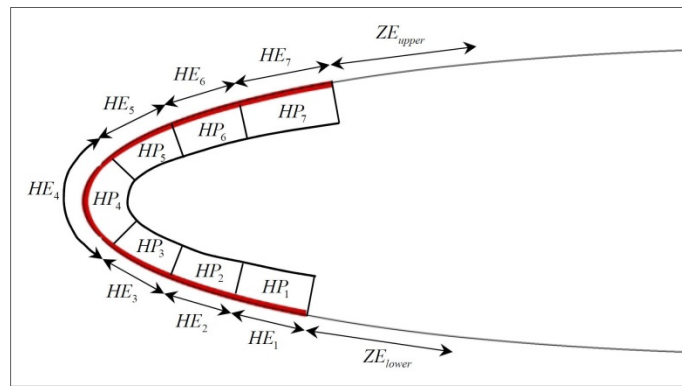


Figure 4.21: Schematic picture of the design variables.

Figure 4.22 shows the convergence history of the best feasible objective function values for cases W-I and W-II and Figure 4.23 shows the convergence history of the objective function values based on the best constraint violation values for Case W-III (as mentioned before, Case W-III does not yield any feasible solution, and so the convergence history is plotted based on the best constraint violation values). It is worth mentioning that because of having a larger number of design variables in power-extent optimization, more evaluations were used. The optimized total electric power values for these test cases are provided in Table 4.4. As can be seen, considering both the heaters' power densities (HP) and the heaters' extents (HE) as the design variables results in no

reduction in Case W-I, 2% reduction in Case W-II and 14% reduction in Case W-III. Hence, Case W-III has the largest decrease. Figure 4.24 compares the original heaters' extents with the optimized ones for this case. As shown, the extents of heaters 1 and 2 on the lower surface have had the largest change. The optimized power densities of this case are shown in Figure 4.25. The figure shows that the power densities have not changed much, except the power density of heater 6, which has significantly decreased. In fact, this heater has the highest contribution in the large reduction of the objective function value in Case W-III, which uses *TWT*. However, one should not ignore that this large reduction has been achieved at the expense of reaching a larger constraint violation value (Figure 4.23). Hence, the surface quantity profiles should be investigated to ensure that the heating zone is ice-free. As shown in Figure 4.26, the heating zone is not ice-free as a part of the surface temperature profile on the upper side reaches the freezing temperature. Therefore, Case W-III is not the most suitable case for the power-extent optimization in the running wet regime. Among the three cases, Case W-II is the most promising one as it both guarantees an ice-free heating zone and causes a reduction in the total power electric, even though the reduction is not as much as that of the unsafe Case W-III.

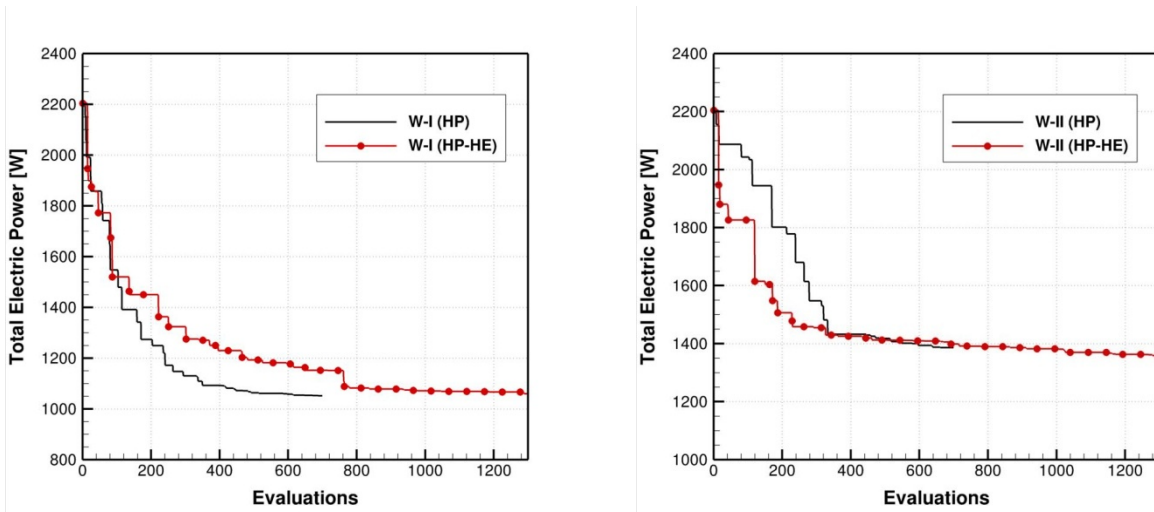


Figure 4.22: Convergence history of the best feasible objective function values for Case W-I (left) and Case W-II (right).

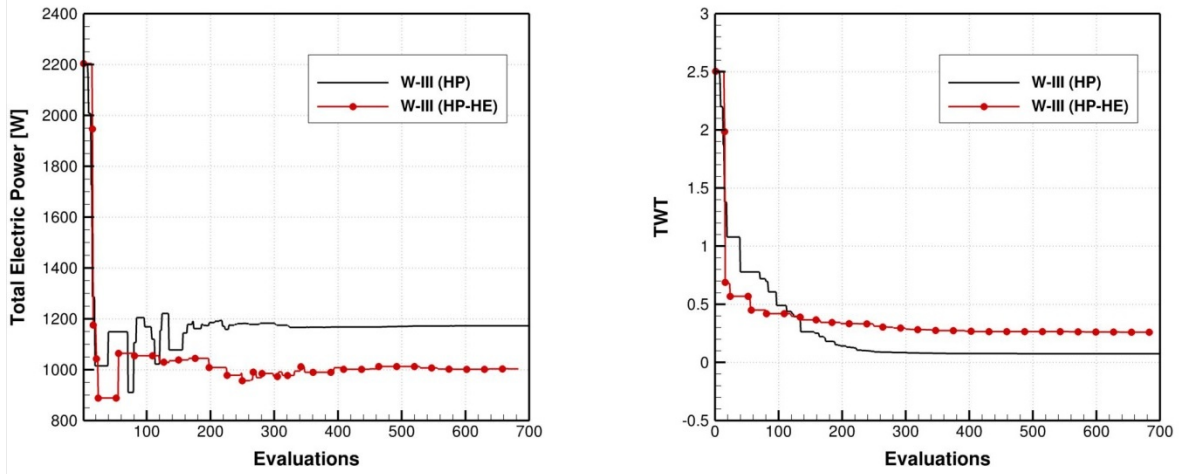


Figure 4.23: Convergence history of the objective function values (left) based on the best constraint violation values (right) (Case W-III).

Table 4.4: Optimized total electric power values for different cases.

	HP	HP-HE
W-I	1052 W	1060 W
W-II	1386 W	1359 W
W-III	1172 W	1003 W

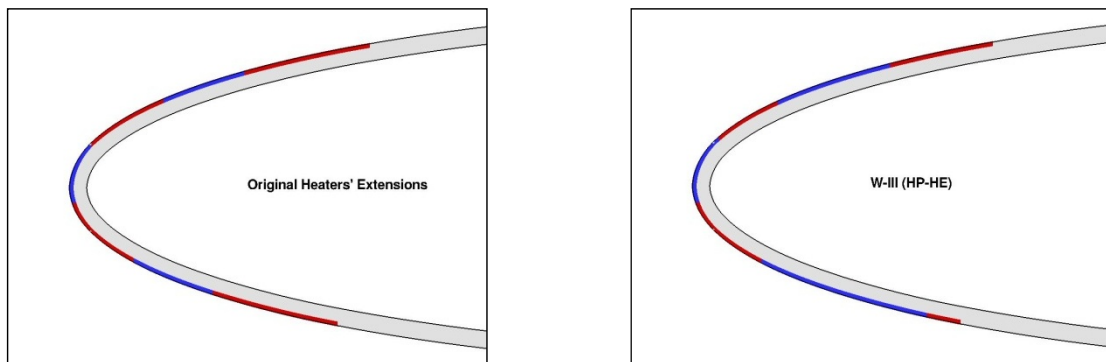


Figure 4.24: Original and optimized heaters' extents of Case W-III (HP-HE).

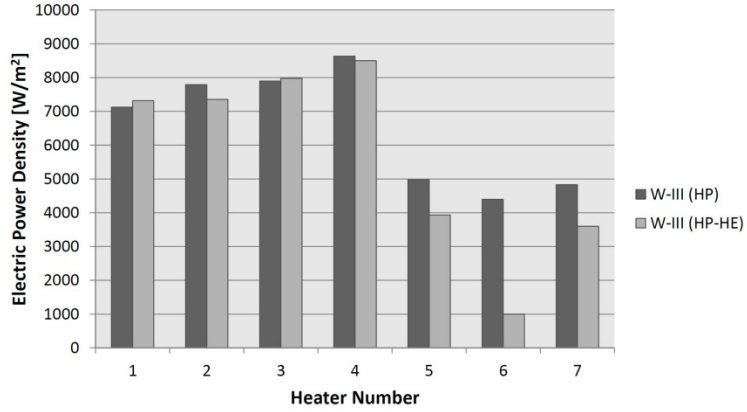


Figure 4.25: Optimized values of power densities.

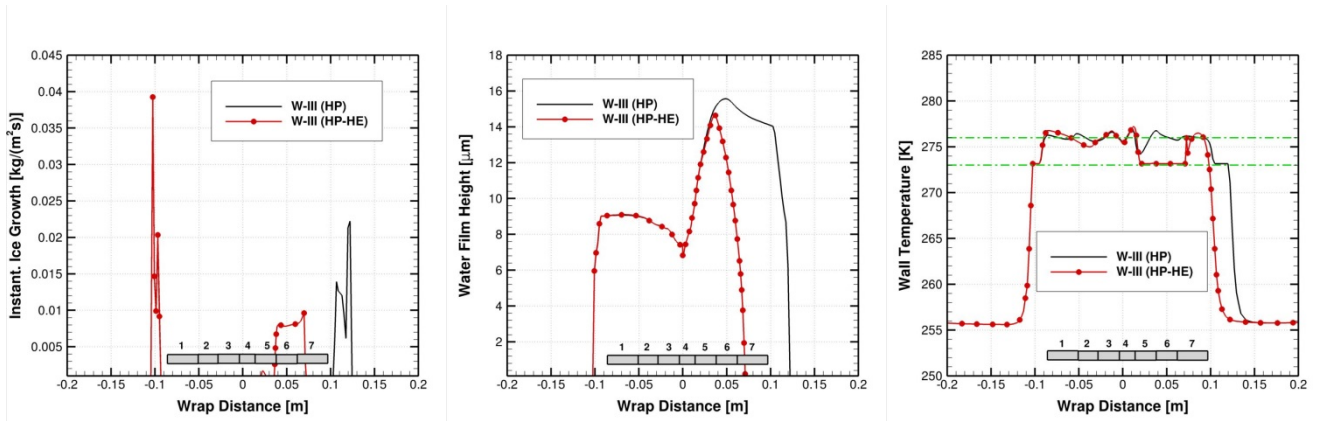


Figure 4.26: Profiles of three surface quantities at optimal state (Case W-III).

4.4.2 Evaporative Regime

4.4.2.1 Primary Optimization

In the evaporative regime, not only is the protected zone kept free of ice, no runback ice formation is allowed beyond the zone as well. Hence, a constraint should also be imposed to ensure that no water film passes beyond the heating zone. Furthermore, since the evaporative regime operates at higher temperatures, another constraint should be imposed to ensure that the temperature of the composite shell does not exceed the maximum temperature allowed for the shell, which here is assumed to be 345 K [111]. Therefore, a constrained bi-objective problem with *TEP* (total electric power) and *MIG* (maximum ice

growth) as the objective functions and EFH (end film height) and MST (maximum solid temperature) as the constraints can be defined (Case E-P):

$$\begin{aligned}
 f_1(\mathbf{x}) &\equiv TEP, \\
 f_2(\mathbf{x}) &\equiv MIG, \\
 c_1(\mathbf{x}) &\equiv EFH, \\
 c_2(\mathbf{x}) &\equiv MST,
 \end{aligned}
 \tag{4-27}$$

where $\dot{m}_{ice^*}'' = 0$ and $T_{shell^*} = 345$. The Pareto front is shown in Figure 4.27, in which both feasible and infeasible points are plotted. According to this graph, with the abovementioned constraints, a zero ice growth is possible by means of about 3000 W electric power.

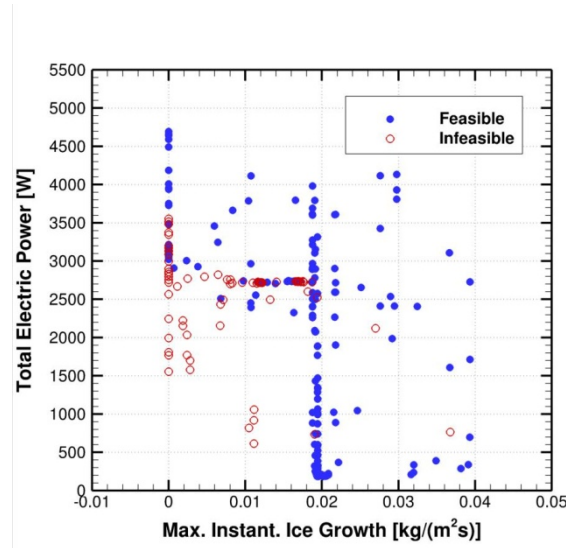


Figure 4.27: Pareto front (Case E-P).

4.4.2.2 Power Optimization

Similar to the running-wet regime, TEP is the only objective function used in the power optimization cases:

$$f_1(\mathbf{x}) \equiv TEP.
 \tag{4-28}$$

In the first evaporative case, i.e. Case E-I, the following constraints are considered:

$$\begin{aligned}
c_1(\mathbf{x}) &\equiv \text{MIG}, \\
c_2(\mathbf{x}) &\equiv \text{EFH}, \\
c_3(\mathbf{x}) &\equiv \text{MST},
\end{aligned}
\tag{4-29}$$

where $\dot{m}_{ice^*}'' = 0$ and $T_{shell^*} = 345$. The convergence history of the best feasible objective values is shown in Figure 4.28 and the optimized and experimental power densities are compared in Figure 4.29. The optimized total electric power is 2,782 W, which is, remarkably, 35% less than the value used in the experimental test (Run #91, TTMS #122), i.e. 4,269 W [49]. This significant reduction in the power usage not only saves energy but also avoids high temperature values inside the composite shell. Figure 4.30 shows that the maximum temperature value inside the composite shell for the optimized state is 337 K, which is 95 K less than the maximum experimental value, i.e. 432 K. The temperature contour plots also suggest that it is more efficient to push back the intense power density on the upper surface to the end of the protected zone.

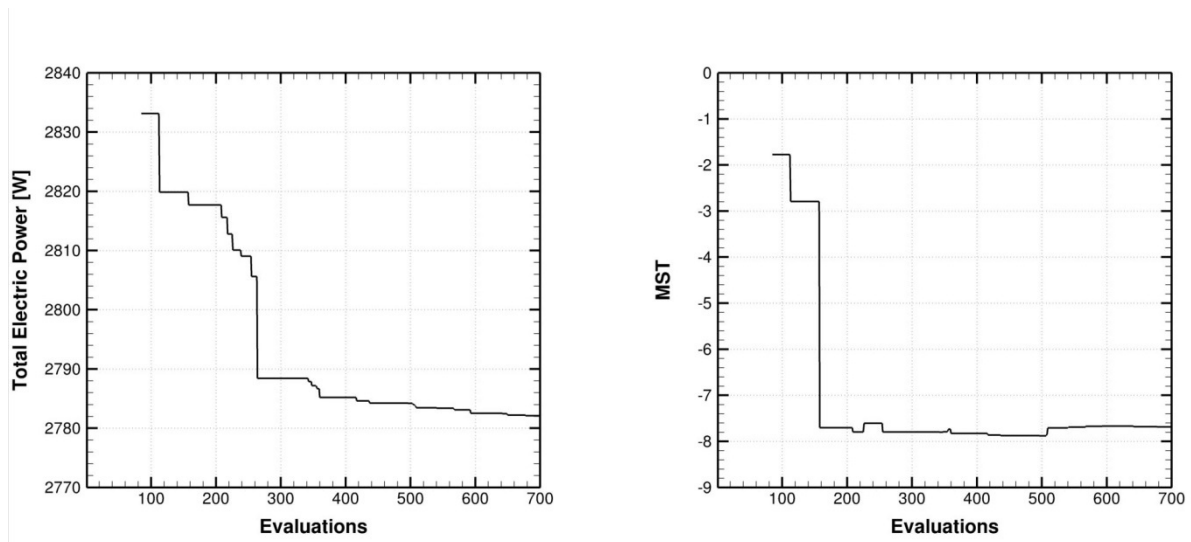


Figure 4.28: Convergence history of the best feasible objective function (left) and constraint violation (right) values (Case E-I).

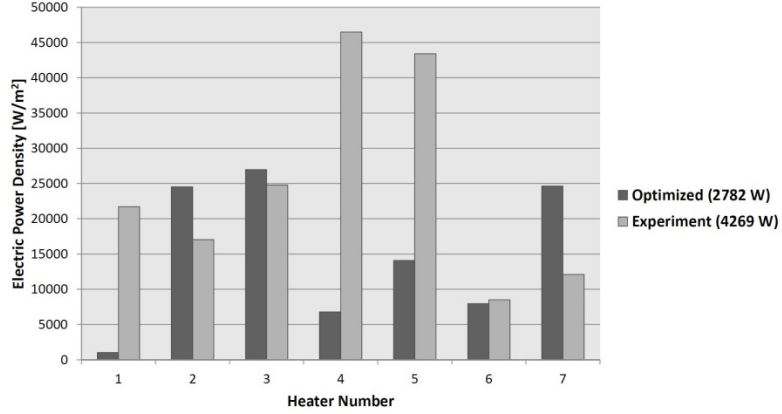


Figure 4.29: Optimized and experimental values of power densities (Case E-I).

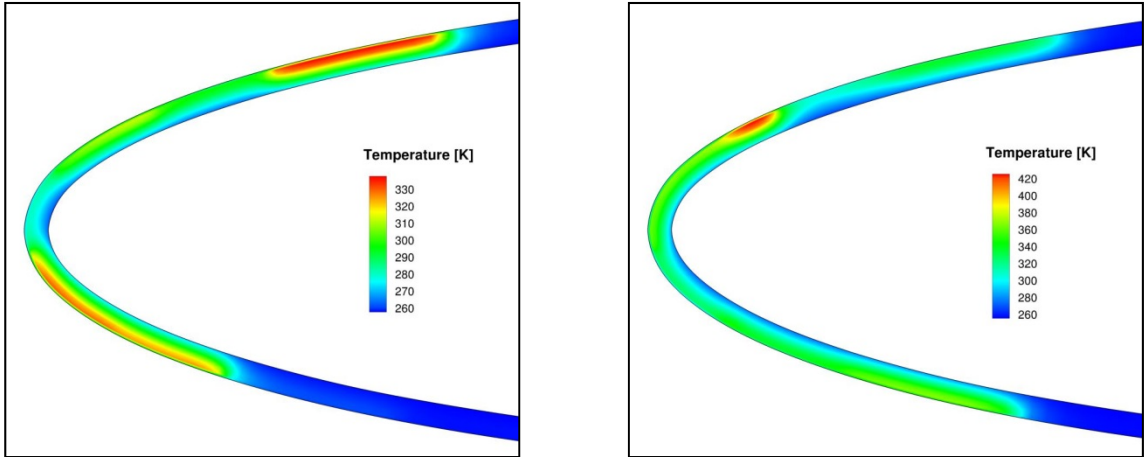


Figure 4.30: Optimized (left) and experimental (right) temperature contour plots inside the solid shell (Case E-I).

Similar to the running-wet regime, MIG can be replaced by MWT , with $T_0 = 276$ K:

$$\begin{aligned}
 c_1(\mathbf{x}) &\equiv MWT, \\
 c_2(\mathbf{x}) &\equiv EFH, \\
 c_3(\mathbf{x}) &\equiv MST,
 \end{aligned}
 \tag{4-30}$$

where $T_0 = 276$ and $T_{shell*} = 345$. Figure 4.31 shows that the optimized total electric power is 2,987 W, which is 7% larger than that obtained in Case E-I, i.e. 2,782 W, because of the margin taken above the freezing temperature. Comparing the power

increase of Case E-II with respect to Case E-I (7%) with that of Case W-II with respect to Case W-I (32%), one can conclude that respecting a specific margin in the running-wet regime is more expensive than that in the evaporative regime.

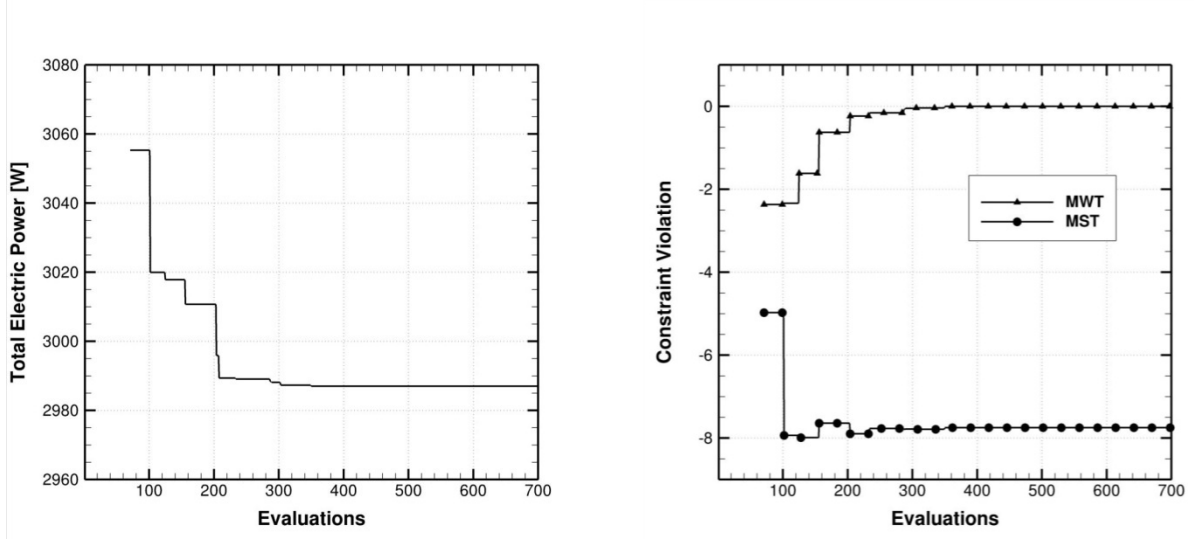


Figure 4.31: Convergence history of the best feasible objective function (left) and constraints violation (right) values (Case E-II).

In the evaporative regime, it would be meaningless to use TWT because it is in contradiction to EFH . Instead, the following sets of the constraints are used in cases E-III and E-IV, respectively:

$$\begin{aligned}
 c_1(\mathbf{x}) &\equiv (TMWT)_d, \\
 c_2(\mathbf{x}) &\equiv EFH, \\
 c_3(\mathbf{x}) &\equiv MST,
 \end{aligned}
 \tag{4-31}$$

$$\begin{aligned}
 c_1(\mathbf{x}) &\equiv (TMWT)_c, \\
 c_2(\mathbf{x}) &\equiv EFH, \\
 c_3(\mathbf{x}) &\equiv MST,
 \end{aligned}
 \tag{4-32}$$

where $T_0 = 276$ and $T_{shell*} = 345$. Figure 4.32 compares the history of the best feasible objective function values for cases E-II, E-III and E-IV. It shows that Case E-II has the best performance in terms of convergence rate and final optimized value. Figure 4.33

shows that the optimized power densities for the three cases are closely similar except for heaters 5 and 7 in Case E-IV. The profiles of two surface quantities at their optimal states are compared among the different cases in Figure 4.34 (In the evaporative regime, there is no ice accretion on the surface, and thus the ice growth profiles are not plotted). In all cases, the complete evaporation of water film takes place prior to the end of the heating zone. Also as expected, the surface temperature profiles show that Case E-I are not reliable enough as the minimum temperature is very close to the freezing point.

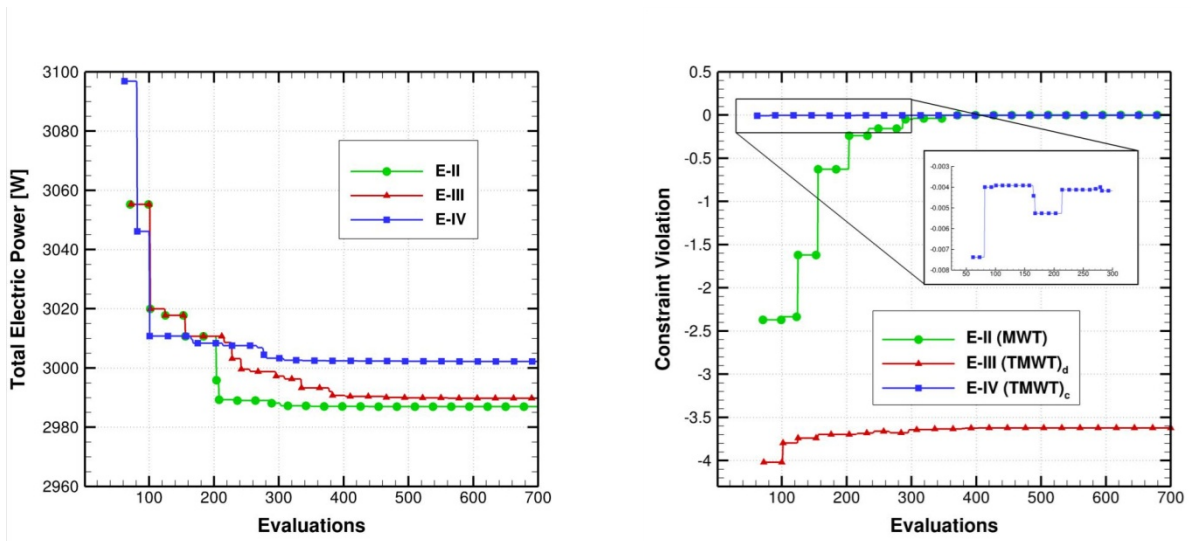


Figure 4.32: Convergence history of the best feasible objective function (left) and constraints violation (right) values.

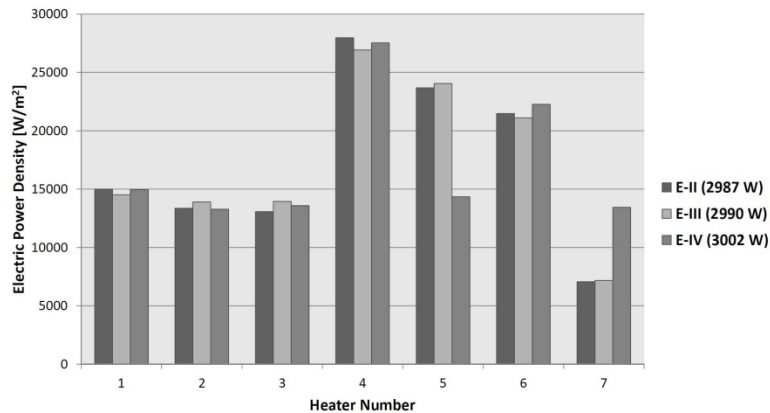


Figure 4.33: Optimized power densities.

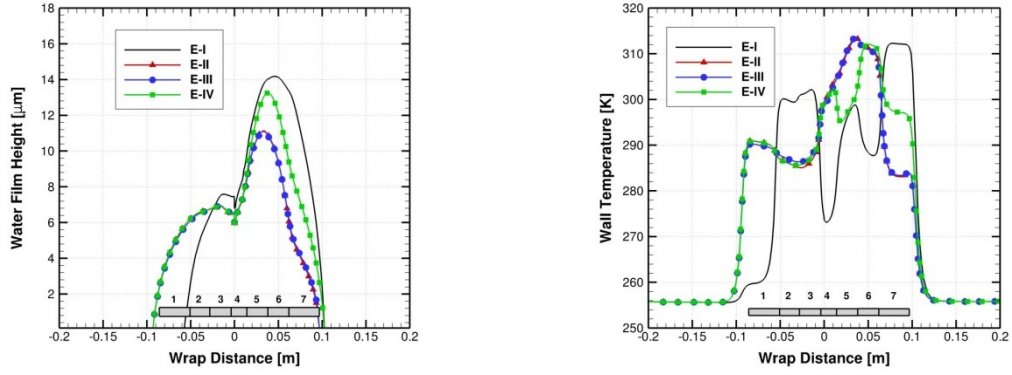


Figure 4.34: Profiles of two surface quantities at optimal state.

Each of the cases E-II to E-IV, may be restated using *DEFH* as the following four-constraint sets for cases E-V to E-VII, respectively:

$$\begin{aligned}
 c_1(\mathbf{x}) &\equiv MWT, \\
 c_2(\mathbf{x}) &\equiv (DEFH)_{up}, \\
 c_3(\mathbf{x}) &\equiv (DEFH)_{lo}, \\
 c_4(\mathbf{x}) &\equiv MST,
 \end{aligned}
 \tag{4-33}$$

$$\begin{aligned}
 c_1(\mathbf{x}) &\equiv (TMWT)_d, \\
 c_2(\mathbf{x}) &\equiv (DEFH)_{up}, \\
 c_3(\mathbf{x}) &\equiv (DEFH)_{lo}, \\
 c_4(\mathbf{x}) &\equiv MST,
 \end{aligned}
 \tag{4-34}$$

$$\begin{aligned}
 c_1(\mathbf{x}) &\equiv (TMWT)_c, \\
 c_2(\mathbf{x}) &\equiv (DEFH)_{up}, \\
 c_3(\mathbf{x}) &\equiv (DEFH)_{lo}, \\
 c_4(\mathbf{x}) &\equiv MST,
 \end{aligned}
 \tag{4-35}$$

where $T_0 = 276$ and $T_{shell*} = 345$. The histories of the best feasible objective function values for cases E-V, E-VI and E-VII are shown in Figure 4.35. The superior performance of Case E-VI, which uses $(TMWT)_d$, is clearly seen in terms of both

convergence rate and final optimized value. Figure 4.36 shows the optimized power densities for the three cases. To compare the influence of EFH and $DEFH$, the convergence history for cases E-II to E-VII is illustrated in Figure 4.37. It shows that each $DEFH$ case has a better performance, i.e. lower total power electric, compared to its own equivalent EFH case. It also reveals that Case VI has the best performance among all test cases. A feature of Case VI that was found to be distinct from the other cases is that the maximum composite shell temperature in this case is almost equal to the boundary value, i.e. 345 K, while in all other cases, the maximum temperature varied between 335 K and 338 K (Figure 4.37).

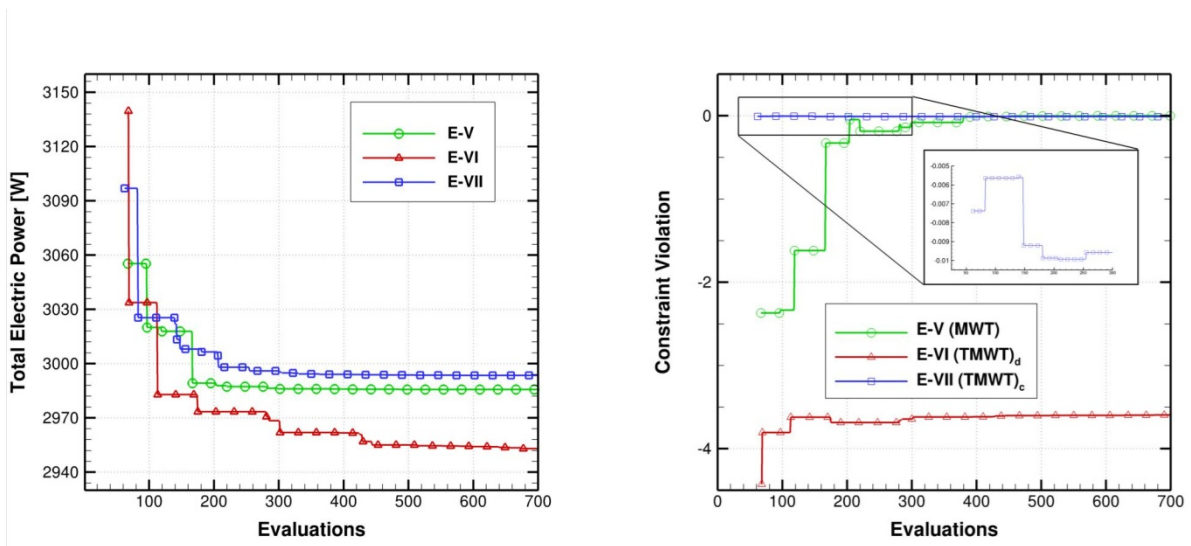


Figure 4.35: Convergence history of the best feasible objective function (left) and constraints violation (right) values.

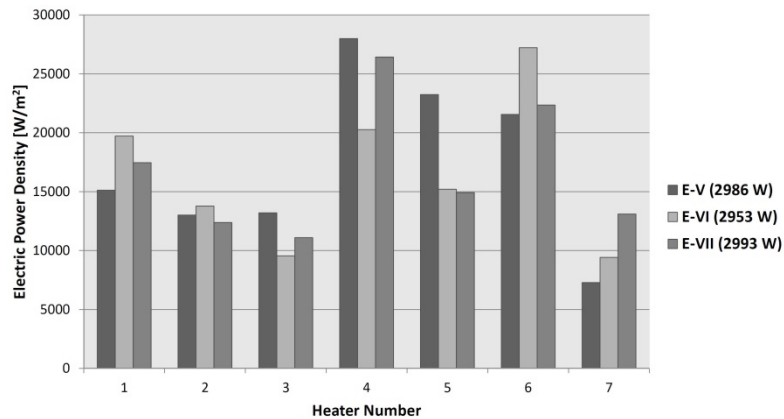


Figure 4.36: Optimized power densities.

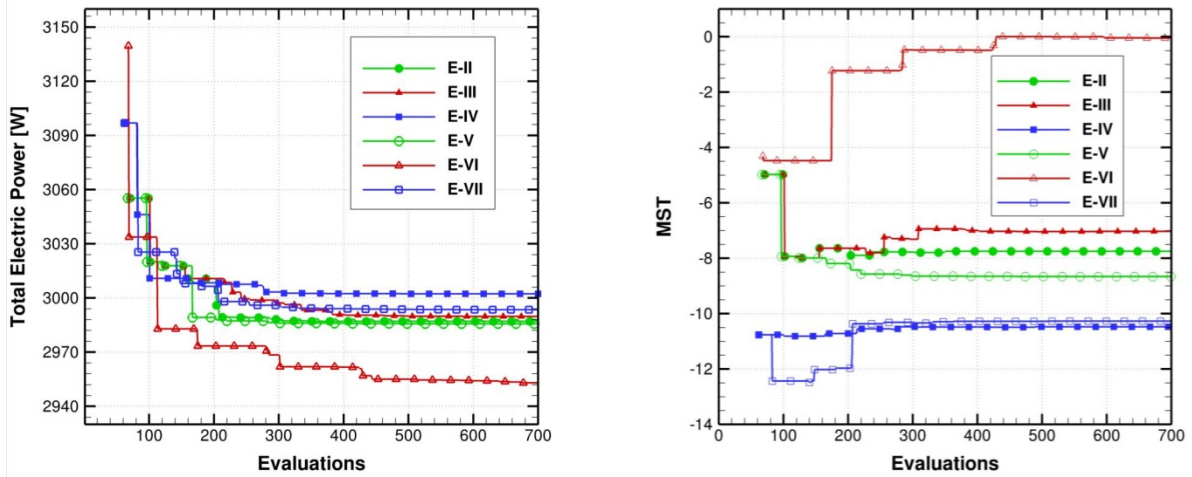


Figure 4.37: Convergence history of the best feasible objective function (left) and constraints violation (right) values.

The evaporative test cases presented so far has been optimized using MADS without statistical surrogates. To demonstrate the influence of these surrogates on the optimal results, the best test case, i.e. Case E-VI, is optimized by MADS in conjunction with *FSP* and *EFIC* models. Figure 4.38 shows that these two models have almost the same convergence rate up to the 500th evaluation, after which *FSP* makes a progressive reduction. The figure also shows that both models have improved the convergence rate as well as the final optimized value compared to MADS without any statistical surrogates.

4.4.2.3 Optimization under Lack of Energy

Suppose that only 2300 W of electric power is available on the aircraft in a crucial case. According to the optimal solution of Case E-I in the previous part, one would need at least 2,782 W to have zero ice growth over the protected zone and zero runback ice after the zone. Moreover, the maximum solid shell temperature shall not exceed 345 K. With only a certain amount of power available, Case E-I can be reformulated using the following objective and constraint functions (Case E-LE):

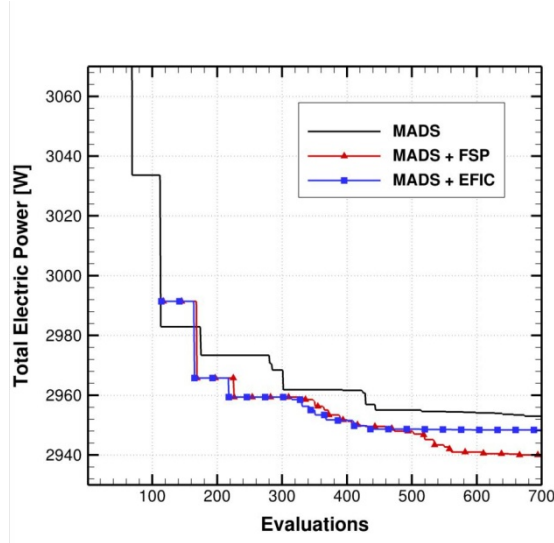


Figure 4.38: Convergence history of the best feasible objective function values (Case E-VI).

$$\begin{aligned}
 f_1(\mathbf{x}) &\equiv \text{MIG}, \\
 f_2(\mathbf{x}) &\equiv \text{EFH}, \\
 c_1(\mathbf{x}) &\equiv \text{TEP} - 2300, \\
 c_2(\mathbf{x}) &\equiv \text{MST},
 \end{aligned}
 \tag{4-36}$$

where $\dot{m}_{ice}'' = 0$ and $T_{shell*} = 345$. Note that the maximum solid shell temperature is a characteristic of the leading edge material and cannot be exceeded in any case. Therefore, it should remain as a constraint and not as an objective function. Figure 4.39 shows the Pareto front of this bi-objective problem for 1,000 evaluations, among which about 750 points are feasible. One of the feasible points having both small maximum ice growth and small end-water-film-height is selected. The profiles of the three surface quantities for this point are shown in Figure 4.40. The maximum ice growth is less than $0.007 \text{ kg}/(\text{m}^2 \cdot \text{s})$ and the end-water-film-height is 3 m, because of which the runback ice is observed on the upper surface after the heating zone. But, it should be remarked again that this is the best scenario one can achieve with the limited amount of power available.

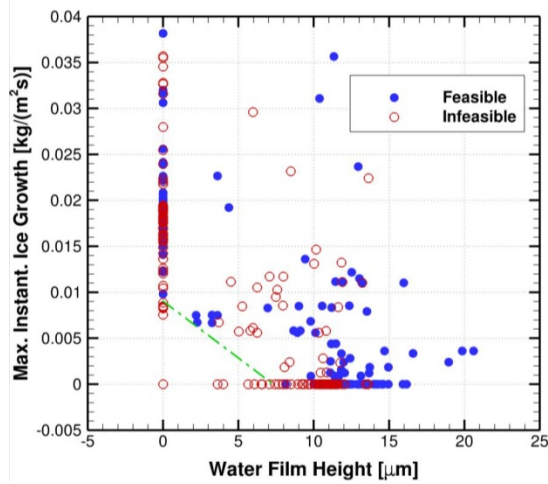


Figure 4.39: Pareto front (Case E-LE).

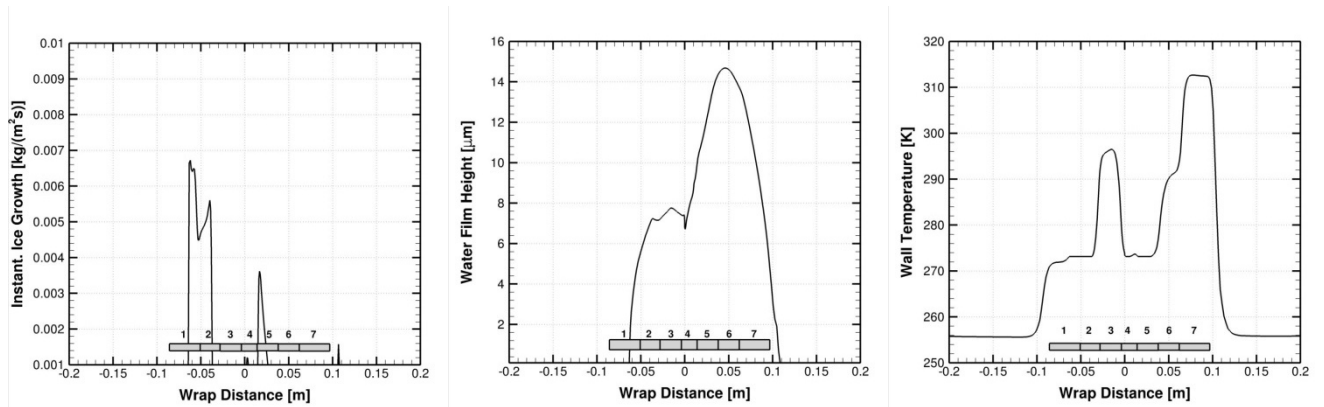


Figure 4.40: Profiles of three surface quantities at optimal state (Case E-LE).

4.4.2.4 Power-Extent Optimization

For the running-wet regime, three test cases were presented for the power-extent optimization and showed the effect of including the heaters' extents into the design variables on the optimization results. In the present section, three test cases for the evaporative regime will be presented: E-I, E-II and E-IV. In contrast to the running-wet regime, here, all types of the design variables depicted in Figure 4.21 can be used.

The convergence history of the best feasible objective function values for cases E-I, E-II and E-IV are illustrated in Figure 4.41 to Figure 4.43, respectively. The optimized total

electric power values for these test cases are provided in Table 4.5. As we can see, including the heaters' extents (*HE*) into the design variables results in no reduction in Case E-I, 3% reduction in Case E-II and 2% reduction in Case E-IV. Also, by including the heating zone extents (*ZE*) into the design variables, no reduction in cases E-I and E-II and 2% reduction in Case E-IV can be achieved. Figure 4.44 and Figure 4.45 show the original and optimized heaters' extents for the cases, in which the total power decreased, i.e. E-II (HP-HE), E-IV (HP-HE) and E-IV (HP-ZE). As shown, the extent of heater 6 on the upper surface decreased in cases E-II (HP-HE) and E-IV (HP-HE). In Case E-IV (HP-ZE), in which the heating zone extents on the upper and lower surfaces are considered as design variables, the heating zone extent on the upper surface increased and on the lower surface decreased. This is due to the negative angle of attack, which causes the runback water film to cover a larger area on the upper surface. Optimized power densities for these test cases are given in Figure 4.46 and Figure 4.47. As shown, heater 6, which has a small extent, also has a small power density in cases E-II (HP-HE) and E-IV (HP-HE). Figure 4.48 shows the surface quantity profiles for the test cases. The profile of the ice growth is not plotted as there is no ice growth in the evaporative regime. It should be noted that the heaters on the plots show the original extents, not the optimized ones. For example in Case E-IV (HP-ZE), it seems that the runback water film moves beyond the heating zone on the upper surface. However, it is actually not true since the heating zone extent has increased on the upper surface in this test case (Figure 4.45).

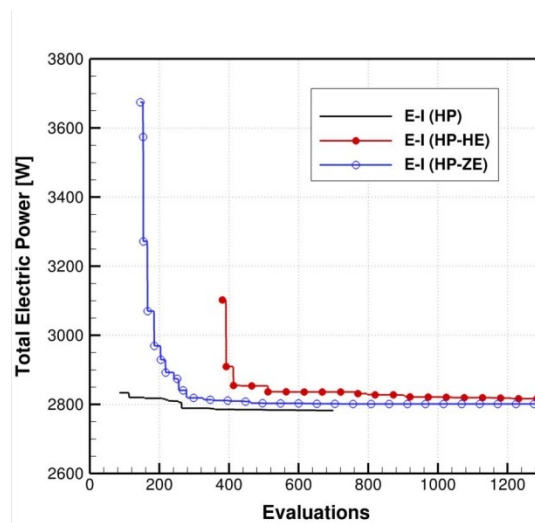


Figure 4.41: Convergence history of the best feasible objective function values (Case E-I).

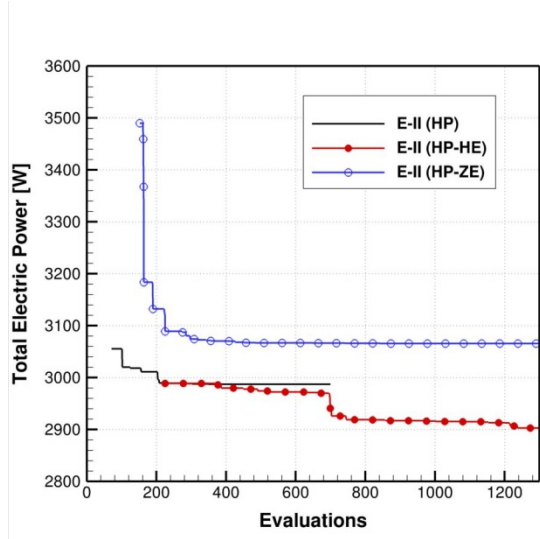


Figure 4.42: Convergence history of the best feasible objective function values (Case E-II).

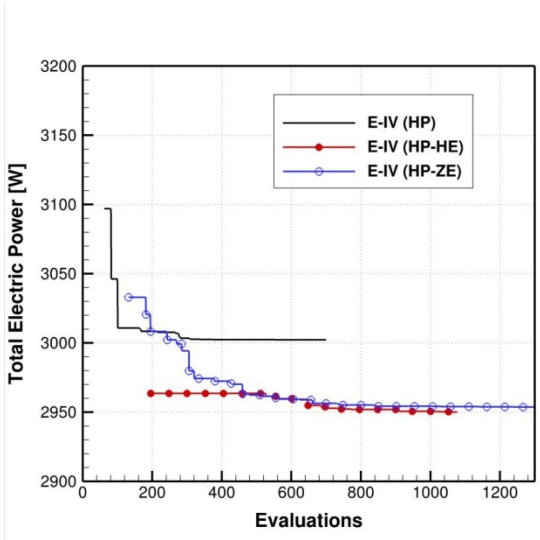


Figure 4.43: Convergence history of the best feasible objective function values (Case E-IV).

Table 4.5: Optimized total electric power values for different cases.

	HP	HP-HE	HP-ZE
E-I	2782 W	2816 W	2801 W
E-II	2987 W	2903 W	3065 W
E-IV	3002 W	2950 W	2954 W

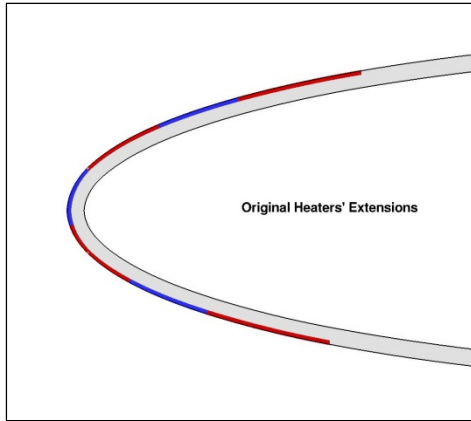


Figure 4.44: Original heaters' extents.

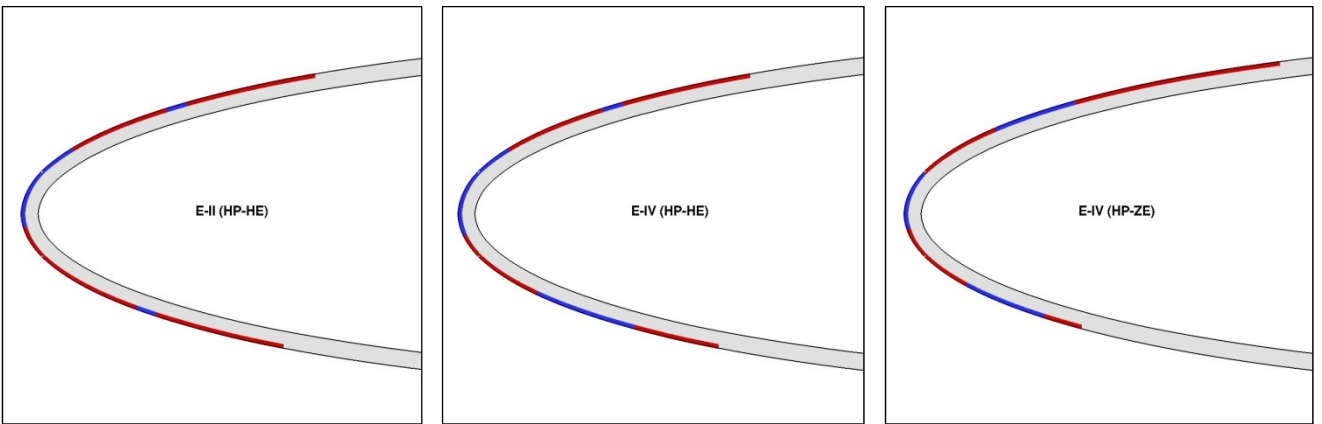


Figure 4.45: Optimized heaters' extents for Case E-II and Case E-IV.

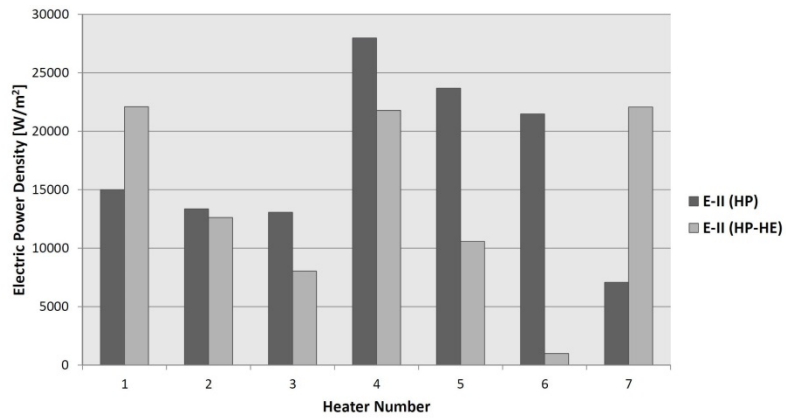


Figure 4.46: Optimized power densities (Case E-II).

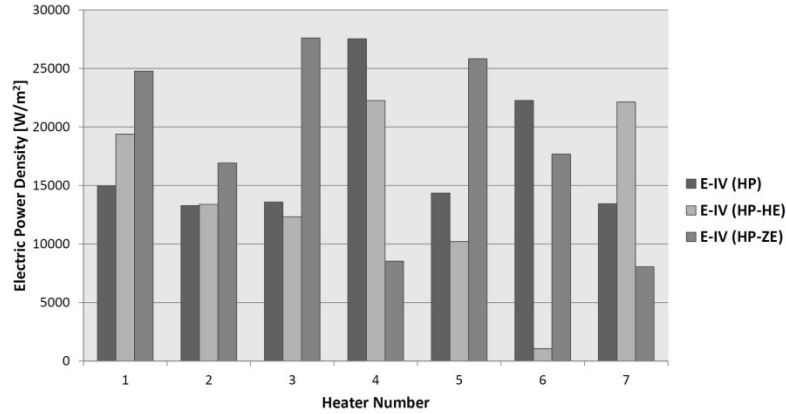


Figure 4.47: Optimized power densities (Case E-IV).

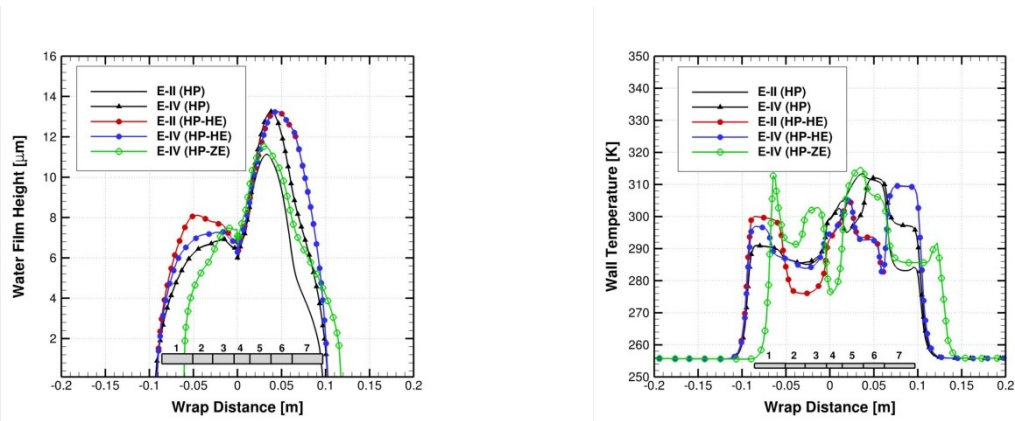


Figure 4.48: Profiles of two surface quantities at optimal state.

4.5 Discussion and Conclusions

In this chapter, the optimization of an electro-thermal anti-icing system was presented. Different formulations for the objective and constraint functions were carefully proposed based on mathematical and physical viewpoints. An engineering viewpoint was also considered by accounting for both cost and safety. These functions were used to define suitable problem formulations for the running-wet and the evaporative regimes. As mentioned, the evaporative regime as an alternative to the fully-evaporative regime was introduced. It may be considered as the best operating regime for an IPS. The optimization results for each regime were presented in four parts: primary optimization,

power optimization, optimization under lack of energy and power-extent optimization. Each of these parts intended to consider different aspects of the problem in realistic conditions. In the primary optimization part, an overall insight into the feasibility of the problem was achieved by solving a bi-objective problem. In the power optimization part, various test cases with different constrained problem formulations were investigated, in which the power densities of the electric heaters were considered as the design variables. Considering cost and safety together, among these test cases, Case W-III, i.e. the case with the TWT function, yielded the best results for the running-wet regime, and Case E-VI, i.e. the case with the $(TMWT)_d$ function, yielded the best results for the evaporative regime. In the part concerning the optimization under lack of energy, it was assumed crucial circumstances, under which there is not enough energy available on the aircraft. Suitable problem formulations were proposed for these situations. Finally, a number of test cases were presented in which not only the power density of the heaters, but also their extents, were considered as design variables (power-extent optimization). This slightly improved the optimized results of some of the test cases in both the running-wet and the evaporative regimes. Generally, in both regimes, the cases with the MWT function were the most suitable ones for the power-extent optimization.

Chapter 5 SURROGATE-BASED OPTIMIZATION

5.1 Background

Many engineering problems involve large-scale analyses and simulations that may be required in real-time and/or in response to a large number of different inputs. The latter case includes, but is not restricted to, control, optimization, and uncertainty or sensitivity analysis. These simulations are often based on discretized systems of differential equations, in which more accuracy is achieved by more discretization points, i.e. more dimensions (degrees of freedom). This implies, of course, more computational complexity and time. In CFD, for instance, discretization schemes, such as finite difference, finite volume and finite element, include basis functions (vectors) that span a few grid points, and therefore only capture local dynamics and not global ones. In other words, the number of dimensions is almost equivalent to the number of grid points. This so-called *curse of dimensionality* would pose a serious impediment to the efficient application of optimization methods to such problems. Beside technical remedies, such as parallelization and GPU-assisted simulation [112], approximation models have also been widely used since 1970's [113]. As these models were more heuristic rather than mathematical, they failed to offer valid solutions for a wide range of problems.

In recent years, with development of some supporting mathematical theories, a broad group of approximation-based optimization methods, namely *surrogate-based optimization (SBO)* or *model management framework*, have been presented. The

convergence of these methods is guaranteed under specific mathematical circumstances. Surrogate-based optimization methods generally fall into three categories: data fit, model hierarchy and reduced-order model [114]. Data fit, a non-physical approach, is based on the interpolation or regression of a data set from the original model. For example, spline, response surface, radial basis function, neural network and Kriging may be placed in this category. In the model hierarchy, in contrast to data fit, the model is still physics-based, but with a lower fidelity compared to the original high-fidelity model. Coarser discretization, lower order element and omitted physics (e.g. using the Euler equations instead of the Navier-Stokes ones) may be put into this category. The third type of SBO, i.e. a reduced order model (ROM), such as proper orthogonal decomposition (POD), is not only physics-based, but also is of high-fidelity through the use of a reduced basis. In the present thesis, all the three approximation methods are used. The model hierarchy is used through performing the conjugate heat transfer calculation using constant convective heat transfer coefficient (Chapter 3). A combination of reduced order model and data fit is also described and applied in this chapter.

5.2 Reduced Order Modeling

5.2.1 Proper Orthogonal Decomposition

In reduced order modeling (ROM), a simplified low-dimensional representation of a complicated full model, with nearly the same input/output responses, is obtained. Features of the full model should be retained in the reduced order model as much as possible. The more information is retained, the more accuracy is obtained. There are many methods to reduce the order of a system, such as modal analysis, Krylov and Singular Value Decomposition (SVD). In the present work, an extension of the SVD approach to nonlinear systems is used which is called proper orthogonal decomposition (POD), also known as Karhunen-Loeve decomposition or principal component analysis or empirical eigenfunctions. It was first introduced in the context of turbulent flow in the late 1960s [115, 116], based on some preceding works that had contributed to its development [117-121]. Since then, POD has been extensively applied in various fields.

POD is essentially an empirical spectral method with two steps: providing a set of snapshots (also called POD training) and projecting the system of PDEs on the most energetic POD modes generated from the set of snapshots. The two procedures result in a system of ODEs that is called reduced order model. Since the snapshots might be linearly dependent, they are not directly used to construct the reduced basis. Instead, an orthonormal reduced basis is formed that is optimal in the sense that it has a smaller mean square error than any other basis. This way, it finds the most significant part, or in other words, the most energetic contributions to the solution. In its original formulation, POD may be of a prohibitive cost for computation-intensive problems. To reduce the cost needed for large-scale systems, Sirovich proposed the “method of snapshots” [122], which will be used in this thesis. It is described in the following. It should be noted that in the present thesis, an in-house Fortran-based ROM code [123] has been used and adapted to suit the current work.

5.2.2 Method of Snapshots

In a family of methods, generally referred to as Galerkin methods, a field, u , can be decomposed to a series of fundamental modes using the expansion theorem. This is performed by a linear combination of the modal basis functions φ_i and the associated coefficients ω_i :

$$u(x) = \sum_{i=1}^{\infty} \omega_i \varphi_i(x), \quad 5-1$$

where $\phi = \{\varphi_1, \varphi_2, \dots\}$ are the modal basis that span the domain. Galerkin methods especially suit vibration analysis where the modes are naturally chosen as a Fourier series. In fluid dynamics, however, specifying an admissible group of modal basis functions would be very difficult, if not impossible. POD offers a stochastic tool for computing the optimal linear basis functions. To do so, a set of n discrete observations (snapshots), either experimental or numerical, are collected over a q -dimensional design space:

$$U = \{u_i(x)\}_{i=1}^n, \quad u_i \in \mathbb{R}^p, \quad x \in \mathbb{R}^q, \quad 5-2$$

where p is the degree of freedom and $n \ll p$. The optimal orthonormal basis functions can then be computed by maximizing the projection of the snapshots onto to the basis functions [124]:

$$\begin{aligned} \max \quad & \frac{\langle |(U, \phi)^2| \rangle}{(\phi, \phi)} \\ \text{subject to} \quad & (\phi, \phi) = 1 \end{aligned} \quad 5-3$$

where $\langle \rangle$ and $()$ denote an averaging operation and the inner product, respectively. It can be shown that the POD basis vectors are eigenfunctions of the Kernel K given by

$$K(x, x') = \langle U(x), U^*(x') \rangle, \quad 5-4$$

where U^* denotes the hermitian of U . The empirical basis functions are then the eigenvectors of the covariance (correlation) matrix given by:

$$R = \frac{1}{n} U U^T. \quad 5-5$$

Note that $R \in \mathbb{R}^{p \times p}$ since $U \in \mathbb{R}^{p \times n}$. In a CFD problem, p corresponds to the grid size and can easily surpass 10^5 , making it prohibitive to extract the eigenvectors. The method of snapshots circumvents this problem by determining the eigenfunctions without explicitly calculating the Kernel. The POD basis can then be expressed as a linear combination of the snapshots:

$$\phi(x) = \sum_{i=1}^n \xi_i u_i(x). \quad 5-6$$

The weight coefficients, ξ_i , in Eq. 5-6 are eigenvectors of the solution to

$$R' \xi = \Lambda \xi, \quad 5-7$$

where

$$R' = \frac{1}{n} U^T U. \quad 5-8$$

Here $R' \in \mathbb{R}^{n \times n}$. This reduces the problem size from $p \times p$ to $n \times n$ (note that the number of snapshots n is much smaller than the grid size p). The i^{th} eigenvector of Eq. 5-1 contains the weight coefficients to assemble the i^{th} POD mode. The eigenvectors of R' determine how to construct the POD basis vectors (using Eq. 5-6) while the eigenvalues determine the importance of the eigenvectors. The relative “energy” (measured by the Euclidean norm) captured by the i^{th} basis vector is given by

$$e_i = \frac{\Lambda_i}{\sum_{j=1}^n \Lambda_j}. \quad 5-9$$

The approximate prediction of the field U can then be given by a linear combination of the eigenfunctions:

$$U \approx \sum_{i=1}^m \omega_i \varphi_i(x), \quad 5-10$$

where $m \ll n$ is the number of dominant modes that is chosen to capture the desired level of energy. At the uncalculated design variables of interest that are not included in the snapshots, the interpolated values of the coefficients ω_i can be used. To do so, the Kriging interpolation method is used, which is described in the next section.

5.2.3 Kriging

Kriging was originally developed in geostatistics by the South African mining engineer called Krige [125], and then was mathematically developed by Matheron [126]. It was then used in engineering design problems following the work of Sacks et al. [127], who applied the method to the approximation of computer experiments. Kriging is actually a form of weighted averaging, in which the weights are chosen such that the predictor error is less than any other linear sum [128]. In Kriging, the unknown scalar function of interest $y(x)$ is expressed as

$$y(x) = \gamma(x) + \delta(x), \quad 5-11$$

where $\gamma(x)$, which provides a “global” approximation, is a known polynomial and $\delta(x)$, which creates a “local” deviation, is a realization of a Gaussian random process with a mean of zero, variance of σ^2 and a non-zero covariance of [129]

$$\text{cov}[\delta(x^i), \delta(x^j)] = \sigma^2 \mathbf{R}, \quad \mathbf{R} = [R(x^i, x^j)], \quad 5-12$$

where \mathbf{R} is an $n \times n$ (n is the number of observed points or snapshots) symmetric correlation matrix with ones along diagonal and $R(x^i, x^j)$ for off-diagonal entries. $R(x^i, x^j)$, which is the correlation function between any two observed points x^i and x^j , is assumed to be the following Gaussian exponential function:

$$R(x^i, x^j) = \exp\left[-\sum_{k=1}^q \theta_k |x_k^i - x_k^j|^2\right] \quad 5-13$$

where θ_k is an unknown correlation parameter, and x_k^i and x_k^j are the k^{th} components of the observed points x^i and x^j , respectively. The estimate \hat{y} at an unobserved point x^* is given by

$$\hat{y} = \hat{\mu} + \mathbf{r}^T(x^*) \mathbf{R}^{-1} (\mathbf{y} - \mathbf{p}\hat{\mu}), \quad 5-14$$

where \mathbf{y} is the column vector of length n , containing the values of y at each observed point, \mathbf{p} is a column vector with n components, being filled with ones when $p(x)$ is constant, and

$$\hat{\mu} = (\mathbf{p}^T \mathbf{R}^{-1} \mathbf{p})^{-1} \mathbf{p}^T \mathbf{R}^{-1} \mathbf{y}, \quad 5-15$$

$$\mathbf{r}^T(x^*) = [R(x^*, x^1), R(x^*, x^2), \dots, R(x^*, x^n)]. \quad 5-16$$

Also, the estimate of variance $\hat{\sigma}^2$ for Eq. 5-11 is given by

$$\hat{\sigma}^2 = \frac{(\mathbf{y} - \mathbf{p}\hat{\mu})^T \mathbf{R}^{-1} (\mathbf{y} - \mathbf{p}\hat{\mu})}{n}. \quad 5-17$$

The only unknowns to be estimated are θ_k . The maximum likelihood estimate of θ_k (> 0) in Eq. 5-13 can be obtained by maximizing the natural logarithm of the likelihood with constant terms removed, which is called the *concentrated ln-likelihood function*:

$$Ln(\hat{\mu}, \hat{\sigma}^2, \boldsymbol{\theta}) = -\frac{n \ln(\hat{\sigma}^2) + \ln|\mathbf{R}|}{2}. \quad 5-18$$

The mean squared error s^2 for an unobserved point x^* using Kriging is given by

$$s^2(x^*) = \hat{\sigma}^2 \left(1 - \mathbf{r}^T \mathbf{R}^{-1} \mathbf{r} + \frac{(1 - \mathbf{p}^T \mathbf{R}^{-1} \mathbf{r})^2}{\mathbf{p}^T \mathbf{R}^{-1} \mathbf{p}} \right). \quad 5-19$$

Statistically, the root mean squared error or the standard deviation $s(x^*)$ represents the predicted deviation of the Kriging estimation from the actual response.

5.3 Overall Optimization Framework

The overall framework of the surrogate-based optimization is illustrated in Figure 5.1. Note that the CHT simulations needed for the snapshots are performed off-line prior to the optimization process. Then through the optimization, the CHT simulations needed at each iterate of the optimization is replaced by ROM. The ROM-based CHT is discussed in the next section.

5.4 ROM-Based CHT

5.4.1 Design of Experiments

In the present thesis, ROM is to be used as a substitution for CHT. In this section, the ROM-based CHT and the ways to improve its accuracy are investigated. As stated before, a set of data snapshots over the design space is needed to construct the reduced order model. This procedure, i.e., generating a set of data points, is commonly called design of experiments (DOE). The distribution of these data points obviously affects the quality of the surrogate model. The assessment of a distribution should be performed based on the nature of the problem being investigated. For example, if there is no *a priori* information regarding the characteristics of the design space, the best choice may be a uniform distribution of snapshots. There are numerous methods for DOE, such as Monte

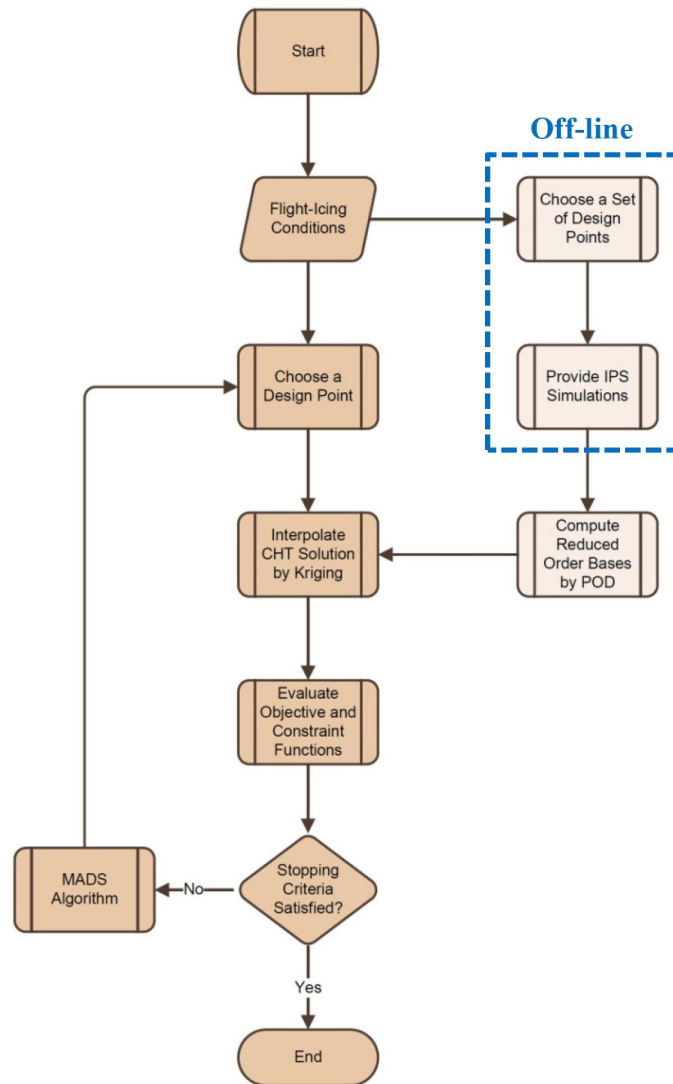


Figure 5.1: Overall framework of surrogate-based optimization.

Carlo, Latin hypercubes, orthogonal-array-based Latin hypercubes, LP_τ and CVT (centroidal Voronoi tessellation). The last two methods are able to generate the most uniform distributions. Although CVT normally generates a more uniform snapshot set, LP_τ has the advantage that in case of requiring more data points, they can be added to the current set without disturbing the uniformity. In this thesis, the LP_τ sampling method is used [130]. It generates deterministic sequence of uniformly distributed points in n -dimensional space. To compute the sequence, lookup tables provided by Sobol' and

Statnikov [131] are used, which correspond to the uniform sequence of numbers. To do the ROM-based CHT, a seven-design-variable problem is considered. The design variables include the power densities of the seven heaters. Assuming that the snapshots are to be generated for a running-wet optimization case, (1,000; 15,000) is considered as the range of the power densities. The flight-icing conditions are provided in Table 5.1. Figure 5.2 shows the profiles of the ice growth, the water film height and the wall temperature obtained by CHT simulation for 60 snapshots.

Table 5.1: Flight-icing conditions.

Temperature [K]	Velocity [m.s ⁻¹]	LWC [g.m ⁻³]	MVD [μ m]	AoA [deg.]
254.375	44.704	0.78	20	-4

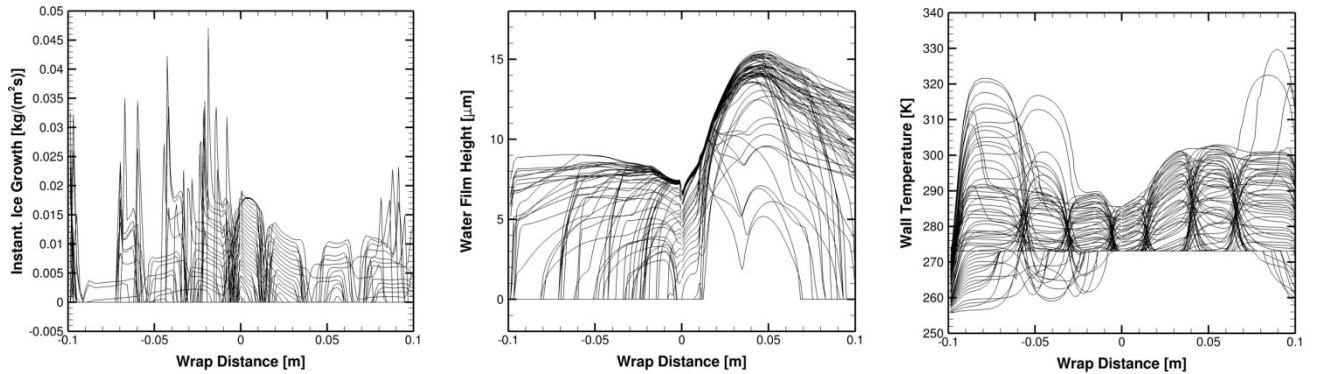


Figure 5.2: Profiles of three surface quantities for 60 snapshots.

5.4.2 Surrogate Modeling

In order to examine the performance of the ROM-based CHT, three sample target data sets in different positions of the design space are to be used. These target data sets are given in Table 5.2. Figure 5.3 shows the true and the ROM profiles of the three surface quantities for different targets. In these plots, “60 sh” stands for 60 snapshots. On the lower surface, the water film height profiles seem to be more accurate while on the upper surface, the wall temperature profiles are more accurate. The reason may be due to the fact that according to Figure 5.2, the snapshot profiles vary within a smaller range on the

lower surface for the water film height and on the upper surface for the wall temperature. The high nonlinearity of the ice growth profiles makes it difficult to reach such conclusions.

Table 5.2: Three sample target data sets.

Target	P_1	P_2	P_3	P_4	P_5	P_6	P_7
I	8375	7875	1375	10375	4375	1125	10875
II	12375	11875	5375	14375	8375	5125	6875
III	9375	4875	8375	9375	1375	4125	1875

5.4.3 Improvement Strategies

In order to improve the ROM-based CHT in terms of accuracy and computational cost, three strategies are proposed: splitting, scalarization and localization. They are discussed in the following.

5.4.3.1 Splitting

In this strategy, the surrogate modeling is split into two sub-problems: one for the upper and one for the lower surface of the wing, each of which has four design variables. Hence, the power density of the heating pad at the leading edge is a common design variable between these two surrogate models. This decomposition is possible as the design variables in one sub-problem do not significantly affect the solution of the other sub-problem. This is schematically illustrated in Figure 5.4. As shown, the effect of each design variable on the field to be represented by the surrogate model is higher (which is shown by darker color) near the geometrical position of that design variable. Hence, for each sub-problem, the effect of the design variables that are located in the other sub-problem can be neglected. This decreases the dimension of ROM, resulting in more accurate surrogate models. Although with this method, two surrogate models must be obtained instead of one, the computational cost is reduced as a result of reducing the dimension of ROM. Furthermore, the dimension reduction also means one need a less

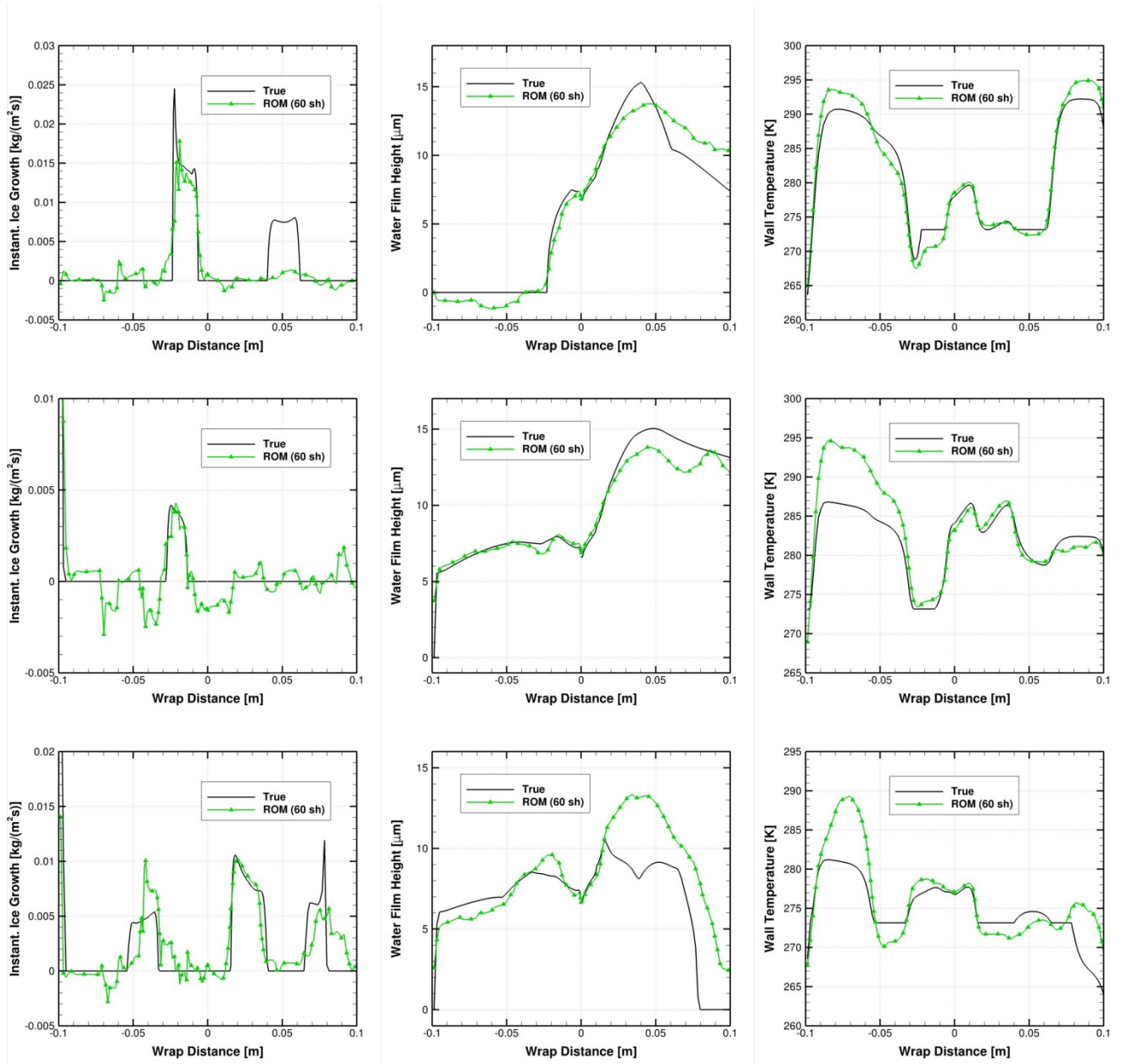


Figure 5.3: Profiles of three surface quantities for Target I, II and III, from top to bottom, respectively.

number of snapshots, which makes the surrogate modeling faster. Overall, the computational cost would decrease by more than half. Figure 5.5 compares the results of the normal ROM with those of the split ROM for the three targets. As shown, in several cases, the split ROM with 60 snapshots outperforms the normal ROM with 60 snapshots and even the normal ROM with 90 snapshots.

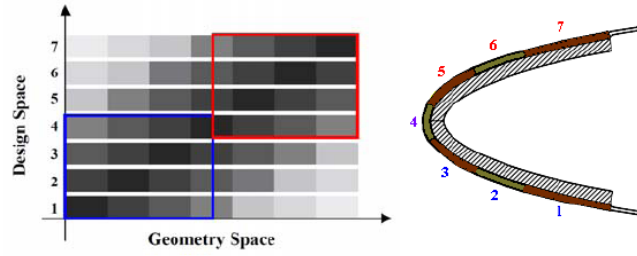


Figure 5.4: Schematic of the split ROM.

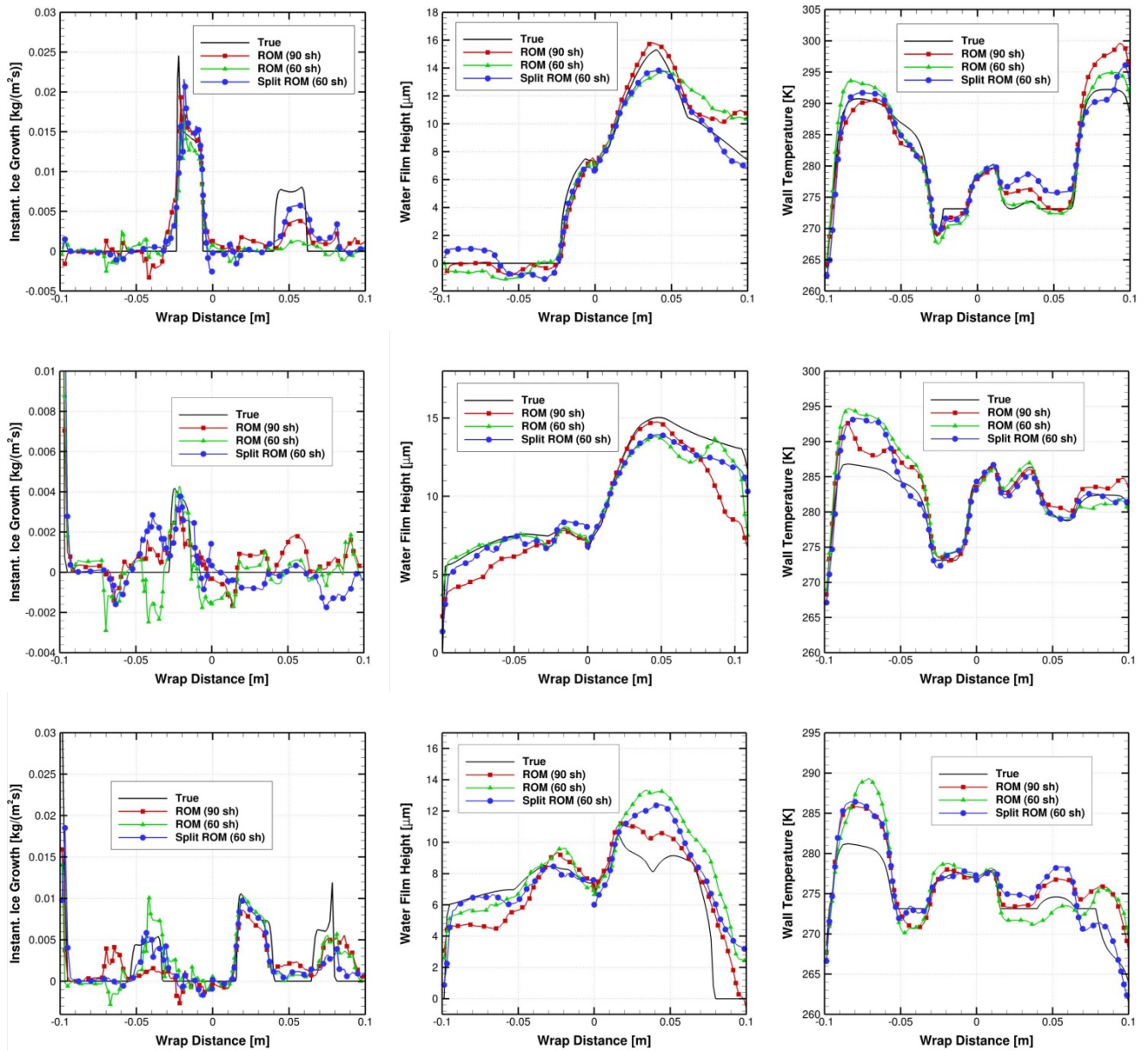


Figure 5.5: Profiles of three surface quantities for Target I, II and III, from top to bottom, respectively.

5.4.3.2 Scalarization

The final goal for surrogate modeling of the profiles of the ice growth, the water film height and the wall temperature is to compute the various objective and constraint functions (introduced in the previous chapter) during the optimization process. This suggests an idea, based on which instead of surrogate modeling of the profiles, which are actually vectors, one can construct the surrogate models by means of the snapshots that are the scalar function values. In other words, instead of having vector snapshots and vector ROM output, one can use scalar snapshots to have scalar ROM output. To do so, one should convert the snapshot profiles to their corresponding function values before constructing the surrogate, and then use these scalar values as the snapshots. This leads to a drastic decrease in the ROM cost. This operation may seem to reduce the accuracy of ROM. Figure 5.6 illustrates the errors (surrogate value relative to true value) of various functions for the different targets. They show that the accuracy of the vector ROM is not necessarily higher than that of the scalar ROM. Even in several cases, the accuracy of the scalar one is higher.

5.4.3.3 Localization

In surrogate-based optimization, one specifically wants to ensure that the surrogate models give accurate approximation of the objective and constraint function values during the optimization process. Hence, the accuracy of the models at other points in the design space is of no concern. *Transductive inference* means reasoning from observed cases to specific cases. In contrast to *inductive inference*, which means reasoning from observed cases to general rules, which are then applied to specific cases. Transduction was introduced in the 1990's by Vapnik [132]: “*When solving a problem of interest, do not solve a more general problem as an intermediate step. Try to get the answer that you really need but not a more general one.*” This concept suggests that one can construct local surrogate models using snapshots that lie in the vicinity of the target design point of an optimization iterate. In other words, instead of using a global ROM, a local ROM can be constructed on the fly whenever the objective and constraint function values must be computed at a design point. This way, not only the accuracy can be increased, but also

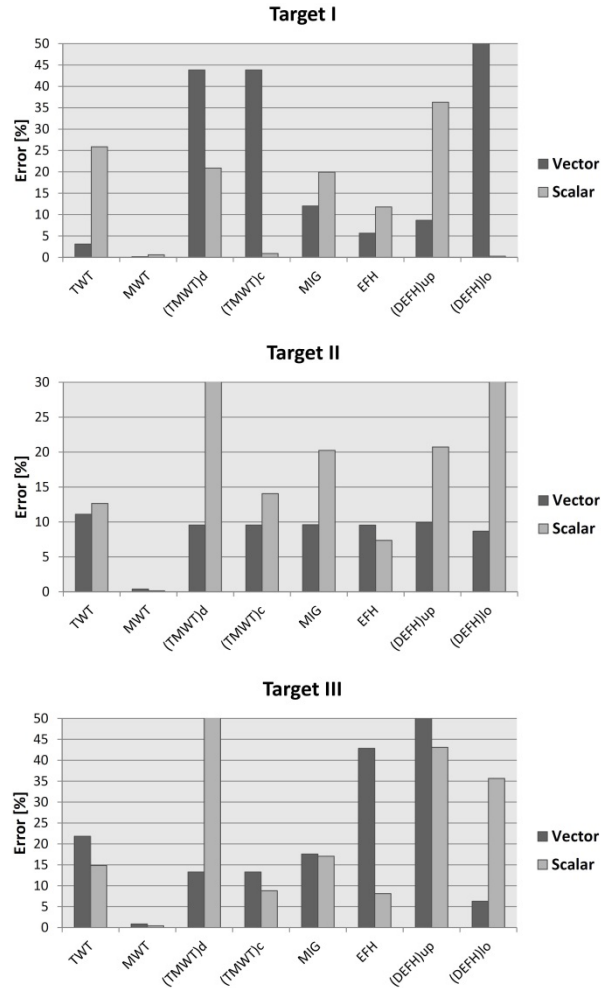


Figure 5.6: Relative error of different functions for vector and scalar ROMs for targets I, II and III.

the computational cost is decreased (due to the decrease of the number of snapshots). This can be done in two ways: either using the n nearest neighbors of the design point or using the neighbors of the design point that lie inside a hyperspherical region whose center is located at the design point. The former is called *local-number (LN)* and the latter *local-distance (LD)*. The distance is measured based on the non-dimensionalized Euclidean distance metric. The logic behind localization is actually improving ROM via including the most influential observations and excluding less influential ones. Figure 5.7 shows a schematic picture of these two localization methods for a 2D design space. In LN, the 11 nearest data points are selected and in LD, the data points inside a circle with

a radius of d are selected. The performance of these methods will be investigated through the numerical test cases.

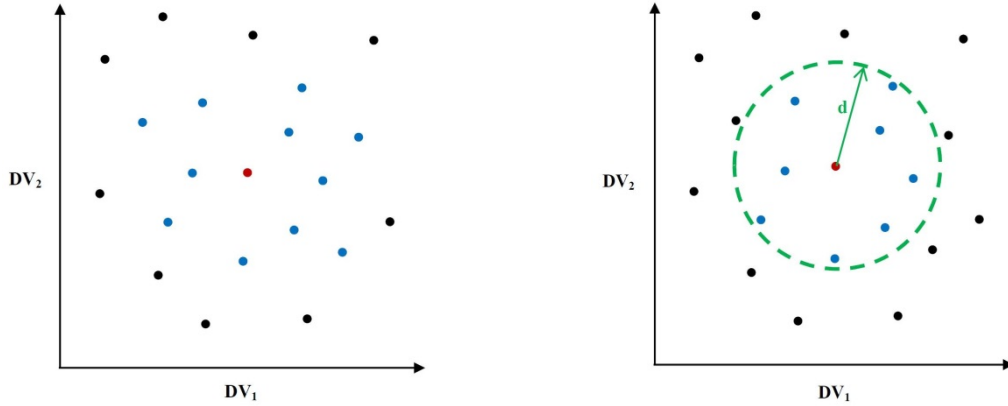


Figure 5.7: Selection of snapshots in a 2D design space based on local number (left) and local distance (right).

5.5 Numerical Test Cases

In order to demonstrate the performance of the surrogate-based optimization, the power optimization test cases presented in the previous chapter for the running-wet and the evaporative regimes are used. It should be noted that, here, all the improvement strategies, i.e. splitting, scalarization and localization are employed

5.5.1 Running-Wet Regime

In the running-wet regime, all cases, i.e. W-I, W-II and W-III, are considered for surrogate-based optimization. Figure 5.8 shows the convergence history of the best feasible objective function values for Case W-I. The optimal solution obtained by CHT simulation in the previous chapter is called the true solution, here. It is compared with two global ROMs with 80 and 60 snapshots (G-80 and G-60), an LD with a radius of 0.6 (LD-0.6) and an LN with 60 snapshots (LN-60). As shown, LD-0.6 has the largest

discrepancy and LN-60 has the smallest discrepancy with respect to the true objective function value. It is also interesting to note the close proximity between the convergence of LN-60 and that of true within the first 100 evaluations. Figure 5.9 shows the optimized power densities for different methods. The ROM values of the heaters on the lower surface, i.e. heaters 1, 2, 3 and partially 4, are, in general, closer to the true values. In other words, the surrogate models on the lower surface are more accurate than that on the upper surface. The profiles of the ice growth, the water film height and the wall temperature at optimal state are shown in Figure 5.10. Despite imposing a zero ice growth constraint, we can see a little amount of ice growth over the heating zone. Due to inaccuracy, these optimal solutions are considered feasible by ROM while they are not actually feasible. The ice growth is very small for the most successful method, i.e. LN-60. It should be noted that LD-0.6, which has the largest discrepancy with respect to the true objective function value, yields no ice over the heating zone. This means that LD-0.6 is a conservative approximation, especially on the lower surface (Figure 5.9). This has caused its objective function value to be the highest among all the methods. This can also be observed from the wall temperature profile, where temperature on the lower surface is the highest in this method.

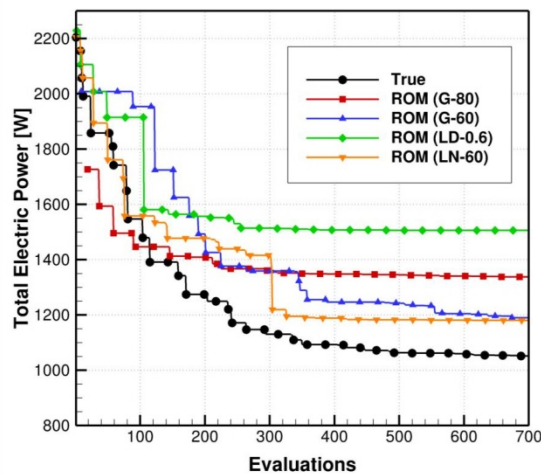


Figure 5.8: Convergence history of the best feasible objective values (Case W-I).

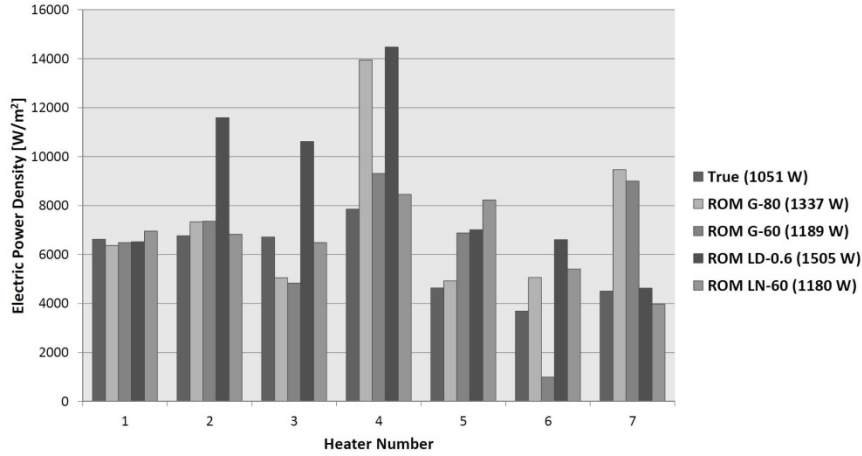


Figure 5.9: Optimized power densities (Case-W-I).

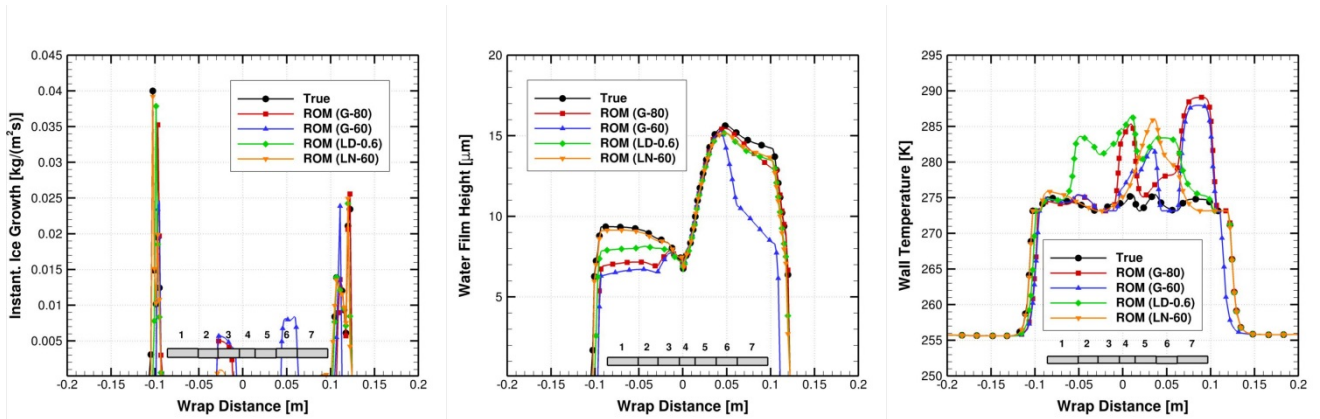


Figure 5.10: Profiles of three surface quantities at optimal states (Case W-I).

Figure 5.11 shows the convergence history for Case W-II. Similar to the previous case, LD-0.6 has the largest discrepancy and LN-60 has the smallest one with respect to the true objective function value. The optimized power densities are also shown in Figure 5.12. To check the performance of the ROM-based methods in terms of physical solution, the profiles of the three surface quantities are illustrated in Figure 5.13. According to the constraint of Case W-II, which is MWT , the wall temperature over the heating zone must actually be above 276 K. This has not completely happened for the ROM-based methods due to their inherent inaccuracy. Again, we can see how conservative LD-0.6 is, especially on the lower surface.

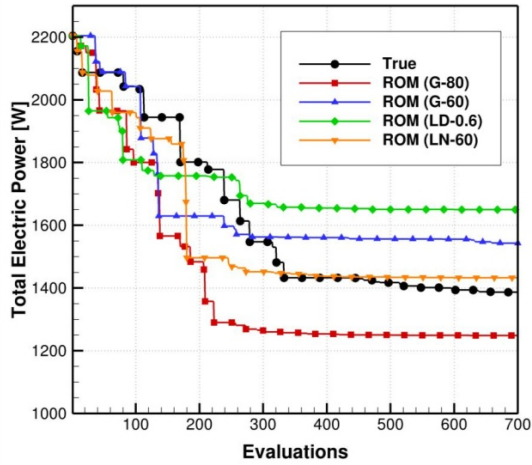


Figure 5.11: Convergence history of the best feasible objective values (Case W-II).

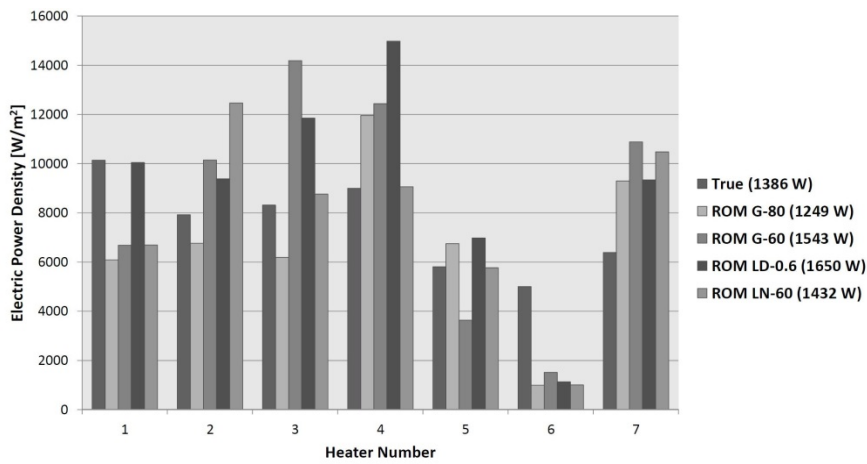


Figure 5.12: Optimized power densities (Case-W-II).

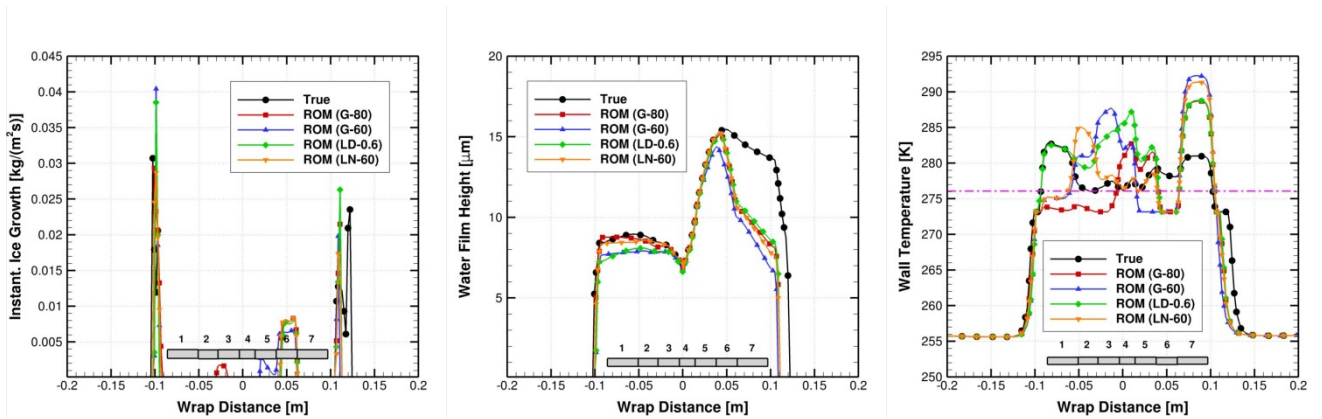


Figure 5.13: Profiles of three surface quantities at optimal states (Case W-II).

Figure 5.14 shows the convergence history of the best feasible objective and constraint values for Case W-III. Note that similar to the previous chapter, the objective function history is plotted based on the best constraint values since *TWT* does not allow a feasible solution. In terms of the objective function value, G-60 has the largest and LD-0.6 has the smallest discrepancy with respect to the true solution. The optimized power densities are shown in Figure 5.15. As can be seen, the discrepancies between the various methods are generally less than the other running-wet test cases. This shows that *TWT* is more suitable for surrogate modeling. This can also be observed in Figure 5.16, where the profiles of the three surface quantities are illustrated. As shown, the temperature profiles of the ROM methods are reasonably close to that of the true method.

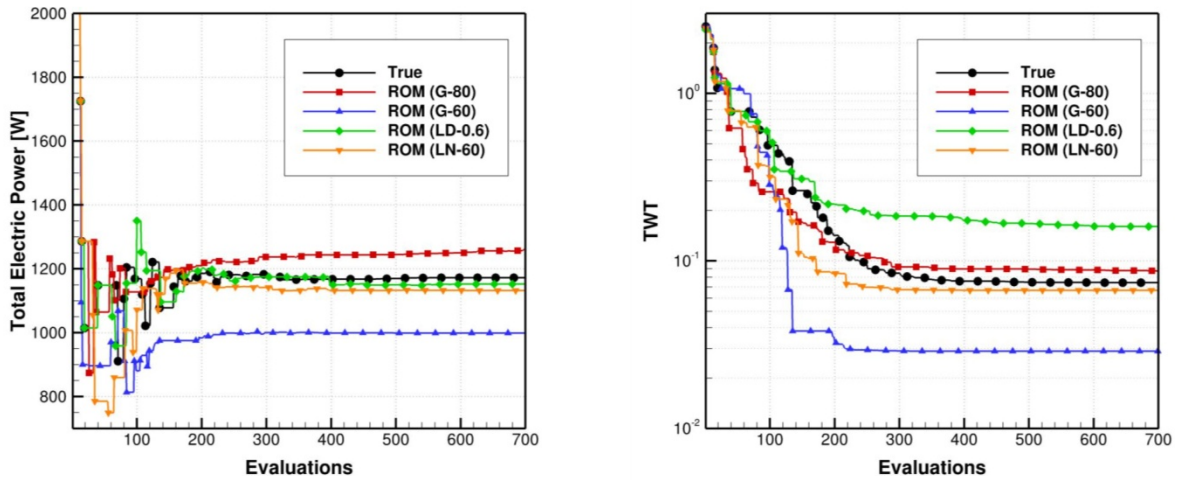


Figure 5.14: Convergence history of the objective function values (left) based on the best constraint violation values (right) (Case W-III).

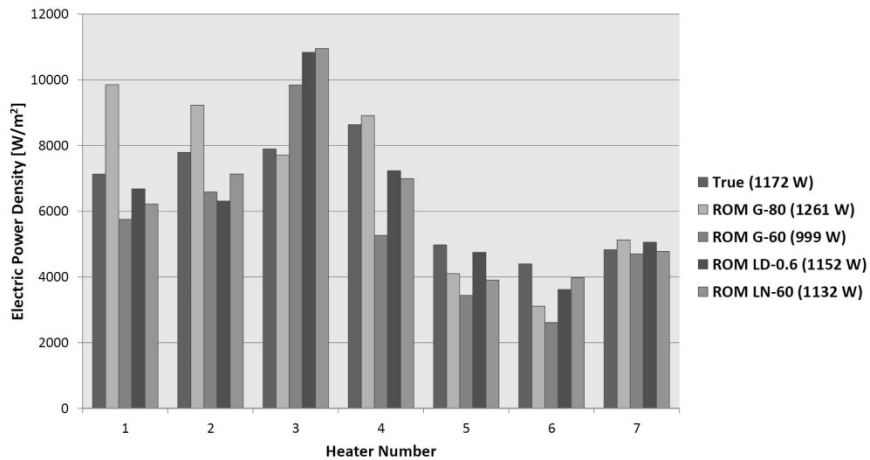


Figure 5.15: Optimized power densities (Case-W-III).

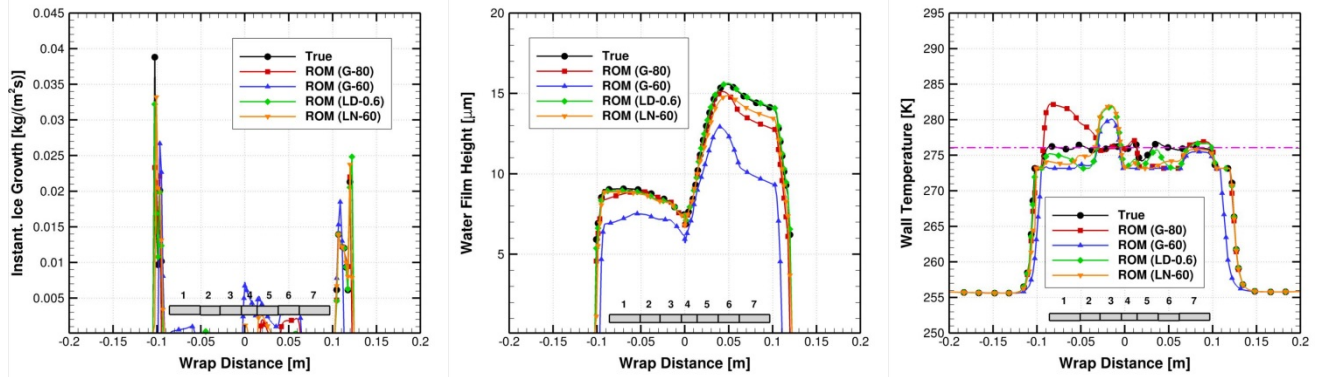


Figure 5.16: Profiles of three surface quantities at optimal states (Case W-III).

5.5.2 Evaporative Regime

For the evaporative regime, cases E-I, E-II, E-IV, E-V and E-VII are considered for surrogate-based optimization. Cases E-III and E-VI are not considered as they led to unsatisfactory results. In the previous chapter, it was mentioned that using the continuous form of $TMWT$, i.e. $(TMWT)_c$, also has some benefits to surrogate modeling. Now we can realize that the reduced order modeling of the discontinuous function $(TMWT)_d$ is problematic. A vast amount of research has, so far, tried to overcome the difficulties with the surrogate modeling of sharp gradients or discontinuities, such as shock waves [133]. Since the size of the design space to be explored is larger in the evaporative regime compared to the running-wet regime¹, the performance of surrogate modelling in the evaporative regime is not as successful as in the running-wet regime. It should be mentioned that for each evaporative case, only the most successful ROM-based solution will be compared with the true one.

Figure 5.17 shows the convergence history of the best feasible objective and constraint function values for Case E-I. The final objective function value of the ROM-based method is noticeably different from that of the true-based method. The optimized power densities for Case E-I are shown in Figure 5.18 and the profiles of the three surface

¹ Recall that the power densities can vary in the interval [1,000; 15,000] for the running-wet regime and in [1,000; 30,000] for the evaporative regime.

quantities are shown in Figure 5.19. A little amount of ice growth is observed on the lower surface over the heating zone despite the fact that a zero ice growth constraint was imposed. Reviewing cases W-I and E-I, generally, one can conclude that ROM has the least success in surrogate modeling of *MIG* (maximum ice growth) compared to the other functions. In these two cases, i.e. W-I and E-I, the constraint functions impose a zero ice growth profile over the heating zone. Obviously, a profile with negative values is not physical for the ice growth. Therefore as Figure 5.2 also shows, all the snapshots have either zero or positive values. This kind of set of snapshots with one-sided values with respect to the target value, which is zero, would reduce the accuracy of ROM. In the previous chapter, it was mentioned that apart from respecting a margin of safety, there is another benefit for using the wall temperature instead of the ice growth in the constraint function. It now becomes clear that another benefit is the fact that the snapshots of the wall temperature have two-sided values with respect to the target, which is 275 K (Figure 5.2). This makes the surrogate modeling of *MWT* (minimum wall temperature) more successful than that of *MIG*. This can be verified by Figure 5.20 to Figure 5.23, which show the results for Case E-II. The objective and constraint functions values, the optimized power densities, especially on the upper surface, and the surface quantities compares well with the true values. Interestingly, in contrast to Case E-I, there is no ice growth over the heating zone.

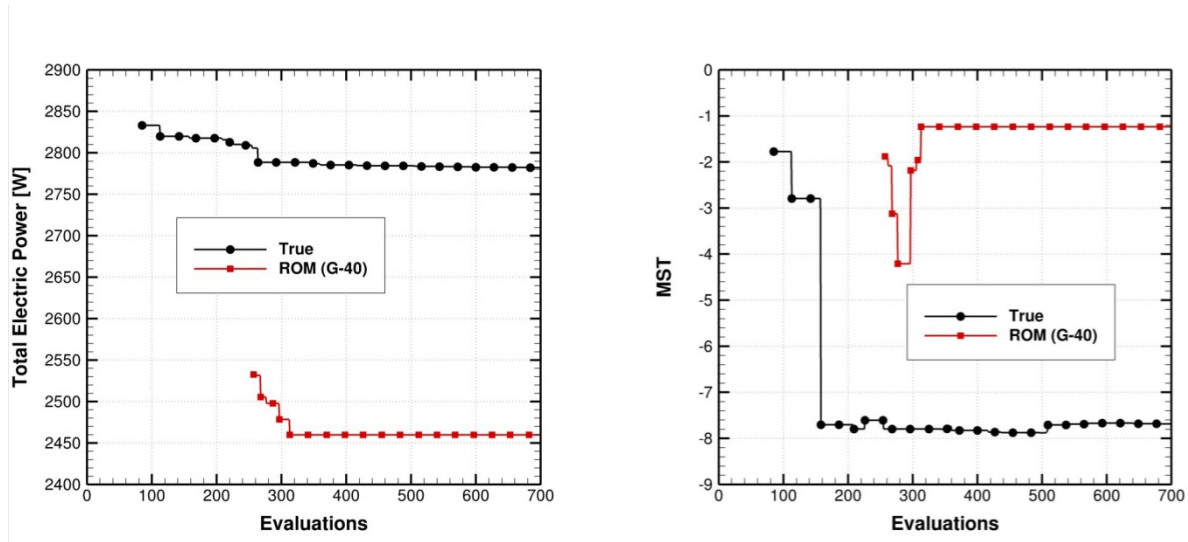


Figure 5.17: Convergence history of the best feasible objective function values (left) and constraint violation values (right) (Case E-I).

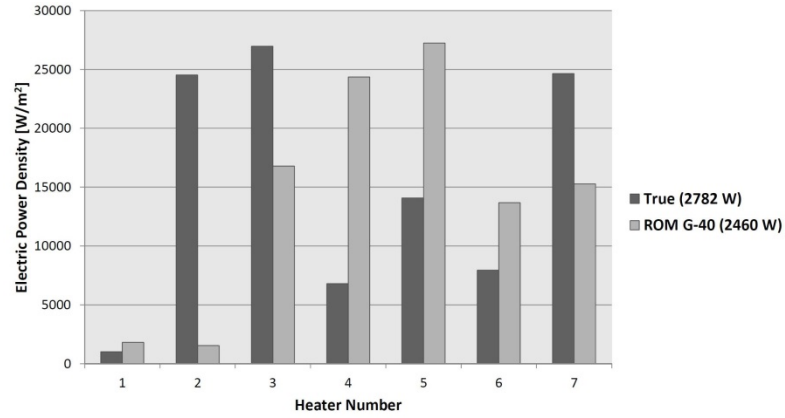


Figure 5.18: Optimized power densities (Case E-I).

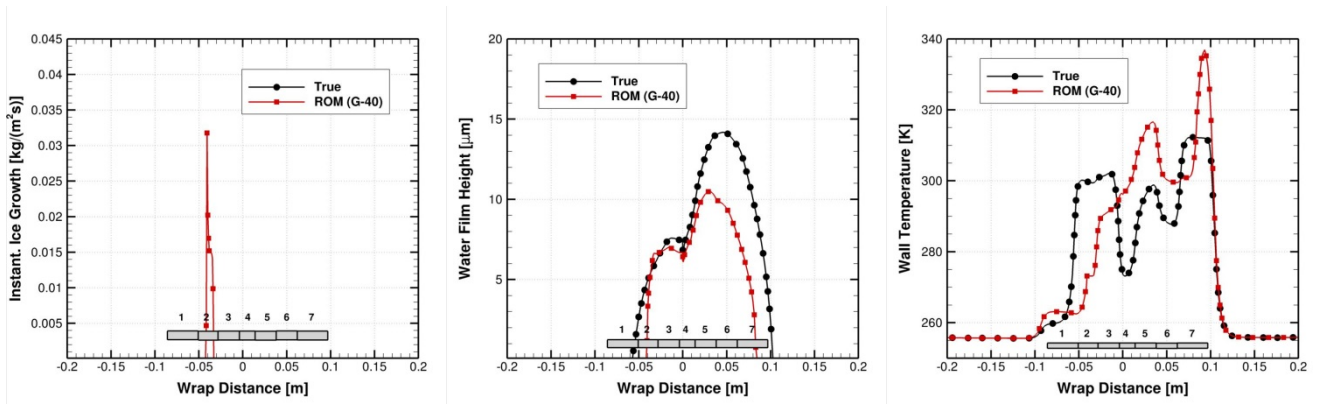


Figure 5.19: Profiles of three surface quantities at optimal states (Case E-I).

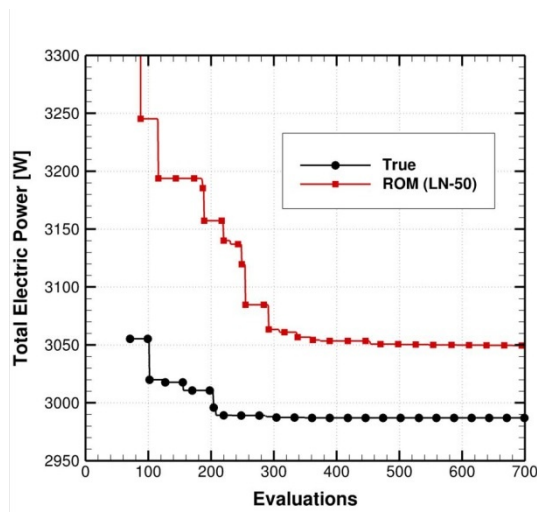


Figure 5.20: Convergence history of the best feasible objective values (Case E-II).

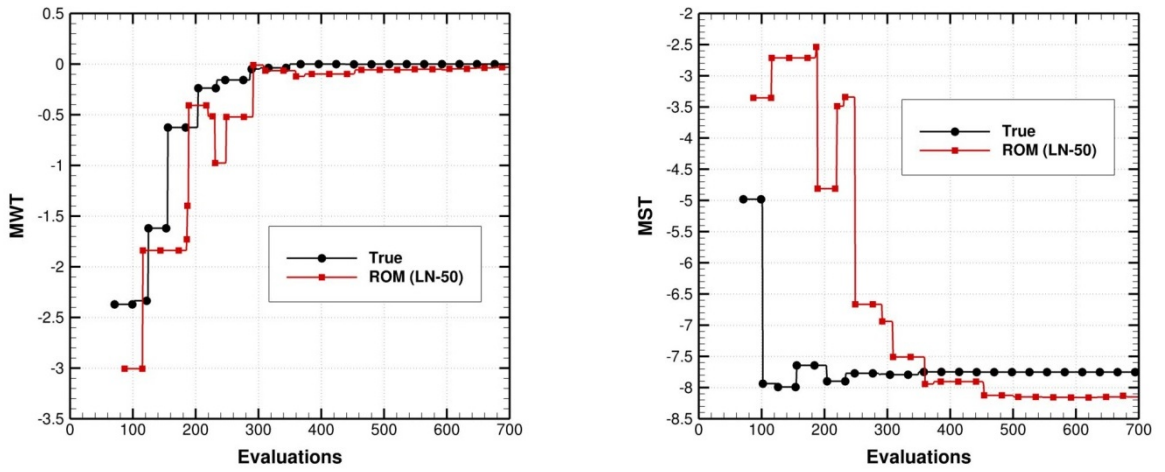


Figure 5.21: Convergence history of the best feasible constraint violation values (Case E-II).

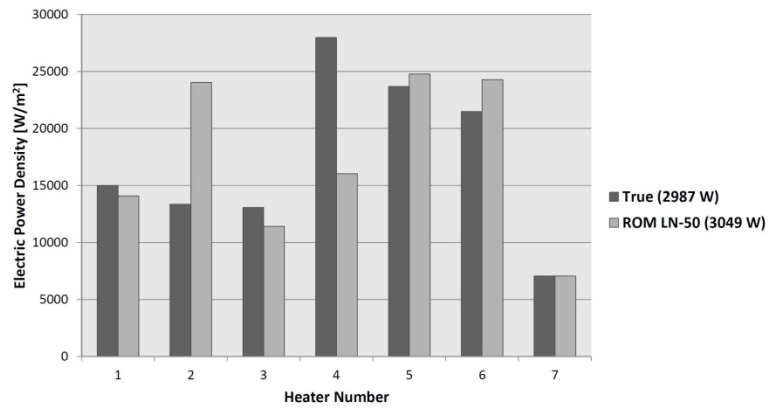


Figure 5.22: Optimized power densities (Case E-II).

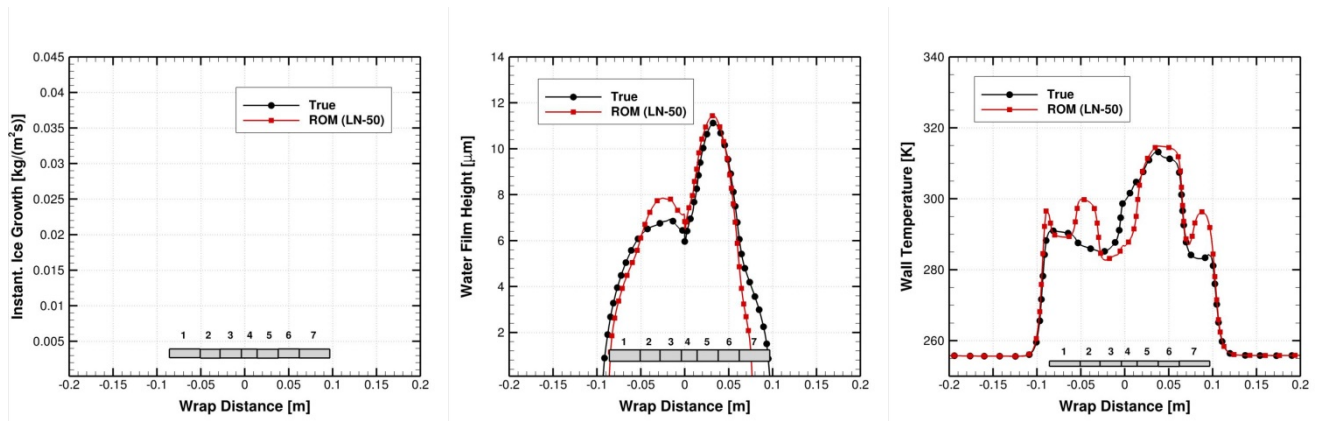


Figure 5.23: Profiles of three surface quantities at optimal states (Case E-II).

Figure 5.24 to Figure 5.27 show the results for Case E-IV. They are less satisfactory compared to Case E-II. For instance, in contrast to Case E-II, the ice growth is observed beyond the heating zone (runback ice), but it is still less than the runback ice of Case E-I. The fact that the ice growth occurred outside the heating zone, and not inside, shows that most part of the discrepancy with respect to the true solution has been due to the surrogate modeling of EFH , and not $(TMWT)_c$. In other words, the surrogate modeling of EFH has been less accurate than that of MWT . In Chapter 4, it was stated that a good constraint formulation would be a quantifiable constraint, i.e. one that provides a distance to infeasibility as well as a distance to feasibility. For this reason, $DEFH$ that has both negative and positive values is defined. Beside this benefit, we will see in the following test cases that the surrogate modeling of $DEFH$ would be more satisfactory than that of EFH . This can be explained by the same reasoning mentioned for MIG since EFH is also a one-sided value quantity while $DEFH$ is a two-sided value quantity.

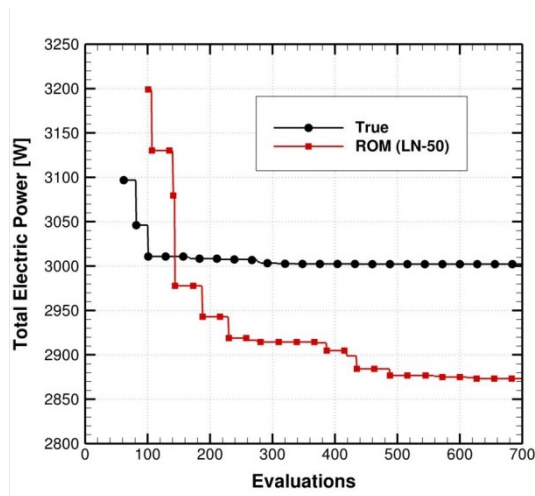


Figure 5.24: Convergence history of the best feasible objective values (Case E-IV).

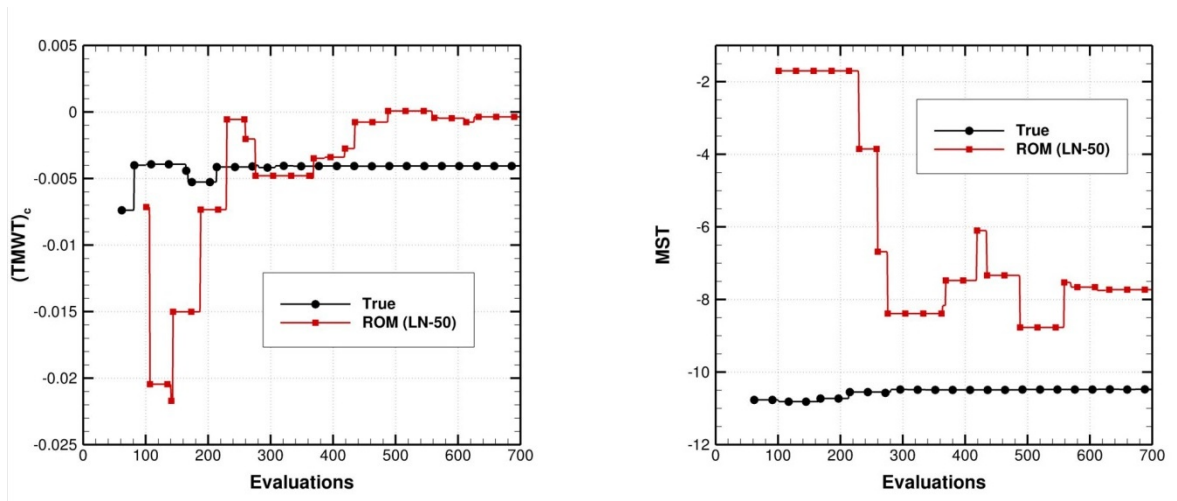


Figure 5.25: Convergence history of the best feasible constraint violation values (Case E-IV).

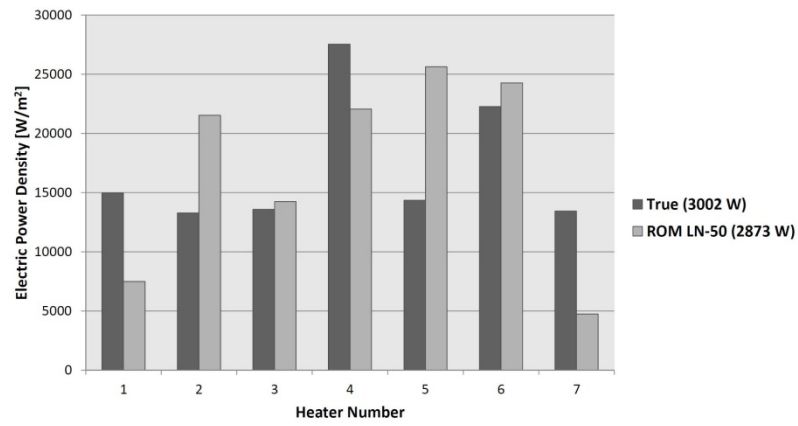


Figure 5.26: Optimized power densities (Case E-IV).

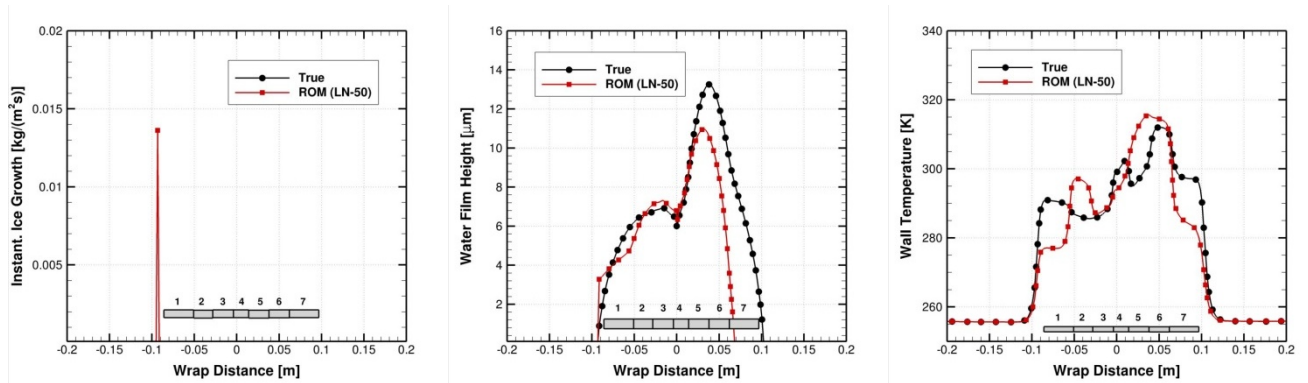


Figure 5.27: Profiles of three surface quantities at optimal states (Case E-IV).

Figure 5.28 to Figure 5.31 show the results for Case E-V. Although there is some ice growth over the heating zone, its amount is much less than that in Case E-I. This again shows that for surrogate modelling, *MWT* is more suitable than *MIG*. Comparison of this case, i.e. Case E-V, with its *EFH* equivalent, i.e. Case E-II, is not proper for comparing the performance of surrogate modeling of *EFH* and *DEFH* because the ice growth over the heating zone may have affected the ice growth beyond the zone, and hence the effect of *DEFH* could not be purely revealed. For this purpose, the comparison of Case E-VII with its equivalent *EFH*, i.e. Case E-IV, would be more suitable. They both have zero ice growth over the heating zone. The results for Case E-VII are shown in Figure 5.32 to Figure 5.35. As shown, the ice growth beyond the heating zone is not as much as we have in Case E-IV. This shows that *DEFH* is better than *EFH* for ROM, as discussed before.

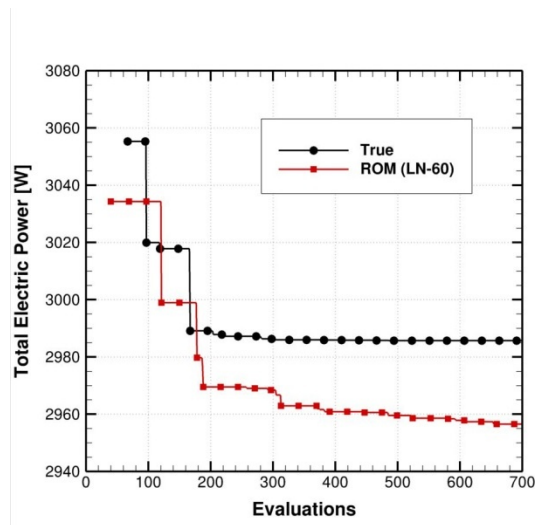


Figure 5.28: Convergence history of the best feasible objective values (Case E-V).

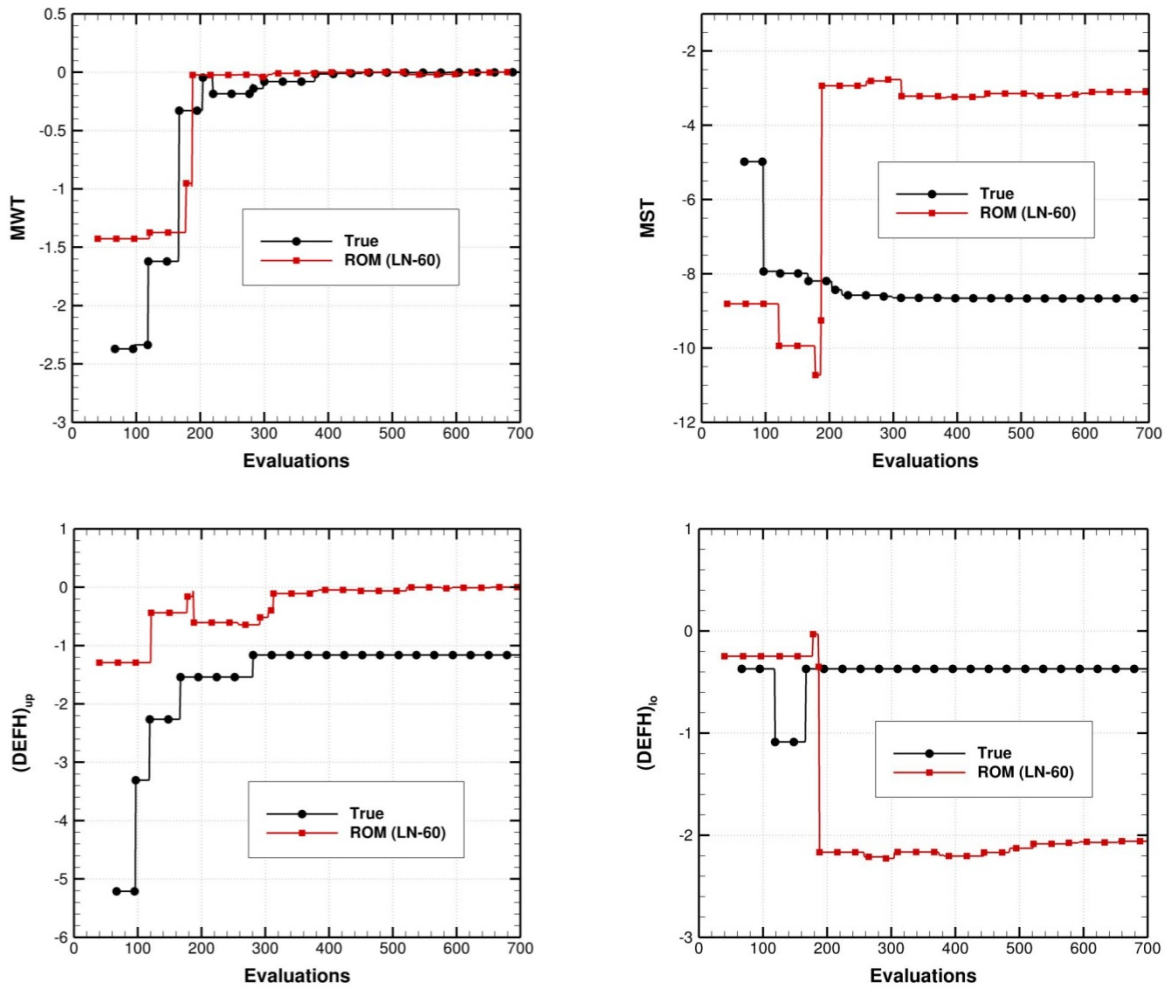


Figure 5.29: Convergence history of the best feasible constraint violation values (Case E-V).

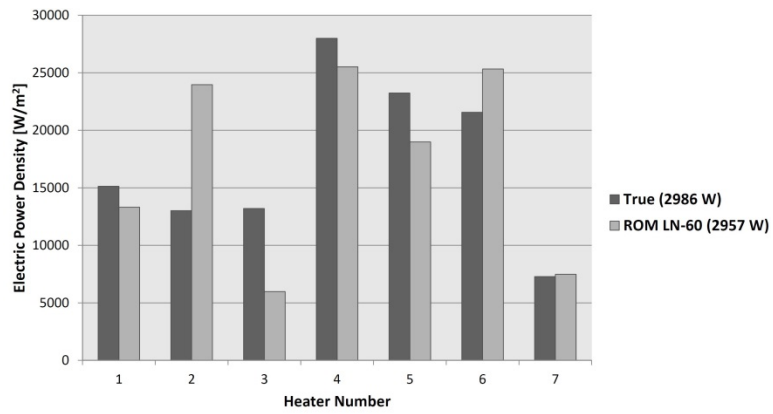


Figure 5.30: Optimized power densities (Case E-V).

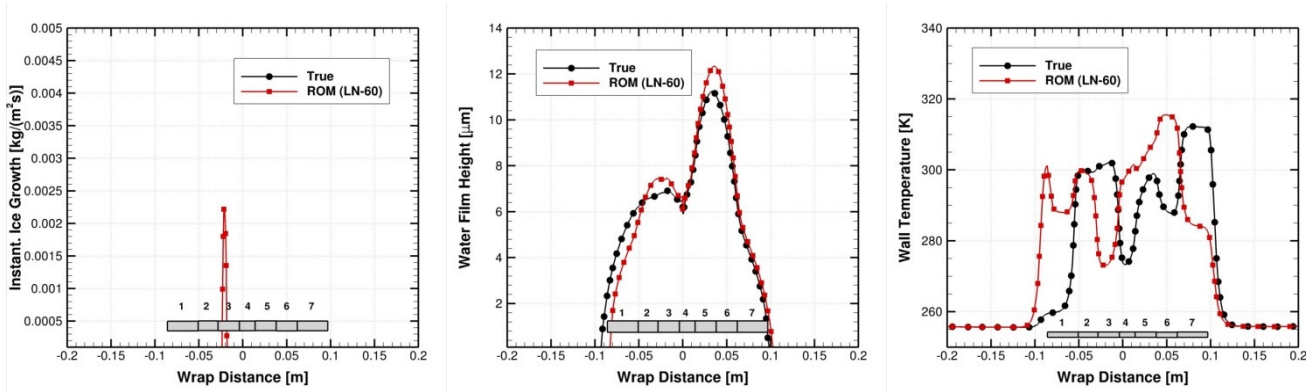


Figure 5.31: Profiles of three surface quantities at optimal states (Case E-V).

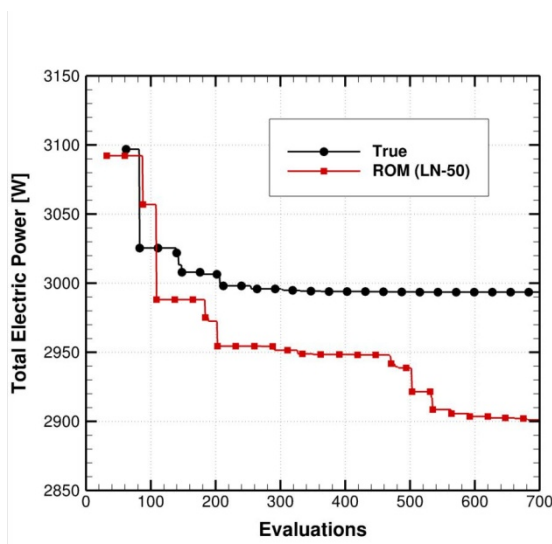


Figure 5.32: Convergence history of the best feasible objective values (Case E-VII).

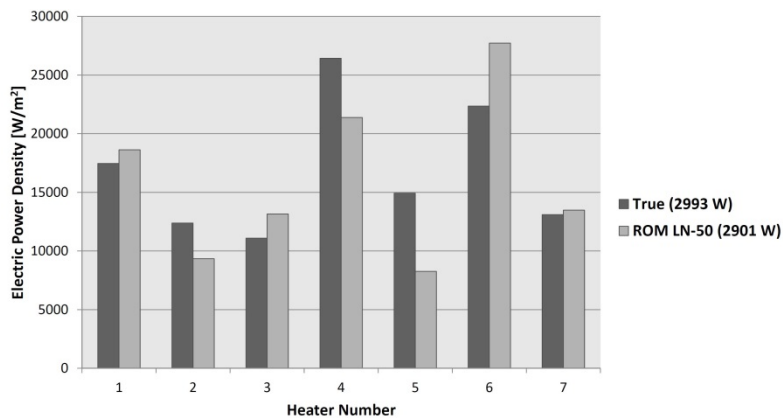


Figure 5.33: Optimized power densities (Case E-VII).

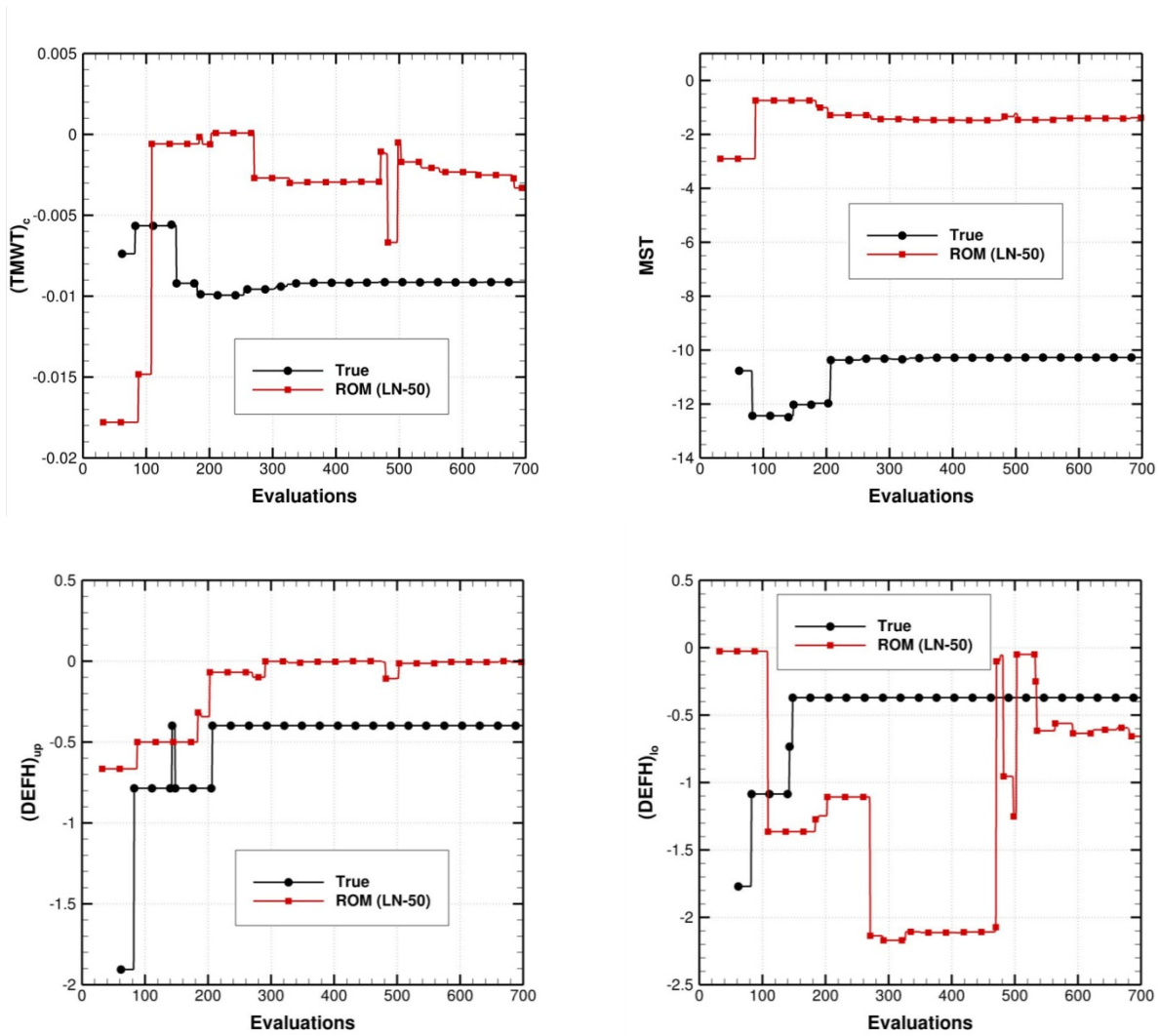


Figure 5.34: Convergence history of the best feasible constraint violation values (Case E-VII).

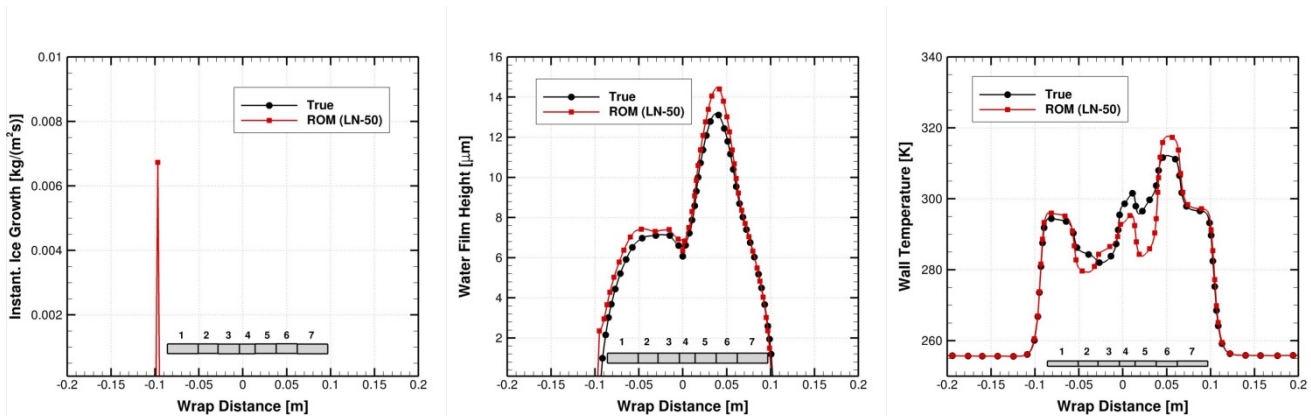


Figure 5.35: Profiles of three surface quantities at optimal states (Case E-VII).

5.6. Adaptive Surrogate-Based Optimization

So far, it has been shown that localization can improve the accuracy of ROM. As discussed, localization can be performed based on two parameters: either the number of snapshots or the distance of snapshots to the target of interest. Beside these two parameters, the density of the snapshots surrounding the target is also of great importance. For example, in Figure 5.7, if there were more snapshots around the target, the 11 snapshots selected in the LN method would be closer to the target, and thus they would capture more characteristics of the target. This would make the surrogate model more accurate. Also, in the LD method, there would be a larger number of snapshots inside the circle if there were more snapshots around the target. In order to increase the density of the snapshots, one way would be to increase the global number of snapshots. However, as discussed earlier, we are only interested in increasing the accuracy of ROM for the data points that are being searched through the optimization process. The accuracy of the models at other points in the design space is of no concern. By increasing the global number of snapshots, we may add some computational cost that would be unnecessary and could be avoided. Instead, one can add snapshots on the fly whenever they are required using the following guideline:

For a target point of interest, if the number of snapshots inside a hypersphere, with a radius of “RA” and a center located at the target point, is less than “NA” then perform a true simulation and add it to the snapshots set. Otherwise construct the surrogate model.

This way, not only do we avoid unnecessary computations, but also we can make direct use of the additional true simulations through the optimization. To assess the performance of this method, it is applied to Case E-I, for which satisfactory results could not be obtained in previous sections. Also, to show the effect of the adaptive parameters, i.e. NA and RA, two sets of parameters are used. They are given in Table 5.3.

Table 5.3: Parameters of two adaptive test cases.

	NA	RA
Adaptive I	10	0.05
Adaptive II	20	0.1

For localization, LN-60 is used. Figure 5.36 shows the history of the objective function of Case E-I for Adaptive I and Adaptive II. It should be noted that to show all the true simulations performed during the optimization, here the history of the objective function, and not the history of the best feasible objective function are plotted. As shown, in both Adaptive I and Adaptive II, after a certain evaluation, the design space becomes so enriched that, thereafter, no more true simulations are needed. Note that Adaptive I, which has stricter conditions, needs more true simulations. However, the final objective function values are very close to each other. Therefore, using a proper set of adaptive parameters, we can avoid additional computations, yet we can have a fairly accurate solution. Figure 5.37 shows how much improvement is achieved by the adaptive method and how close the adaptive profiles are to the true ones. Note that in the adaptive cases, ice growth does not exist either over the heating zone or beyond it.

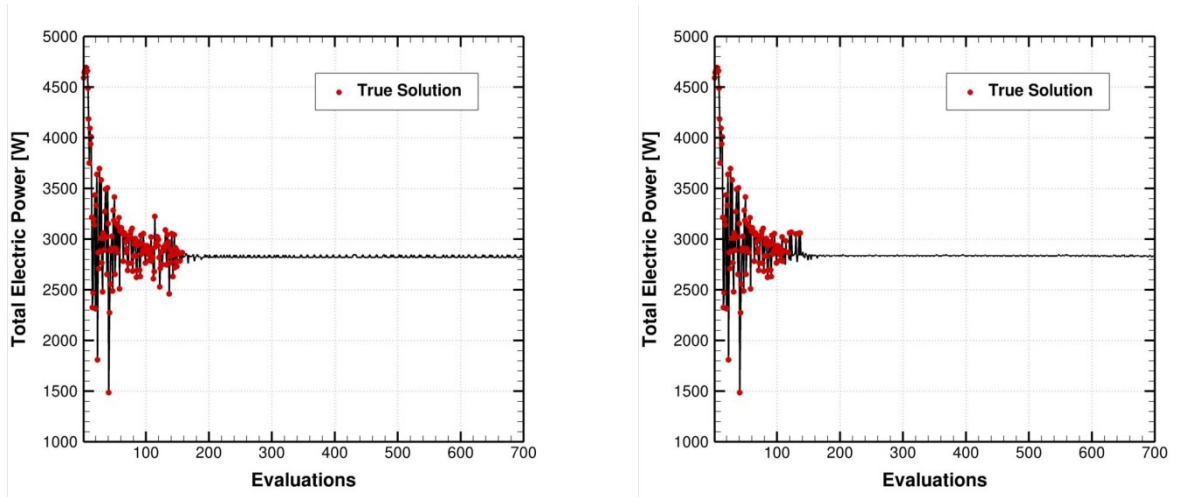


Figure 5.36: Convergence history of the objective function values for Adaptive I (left) and Adaptive II (Case E-I).

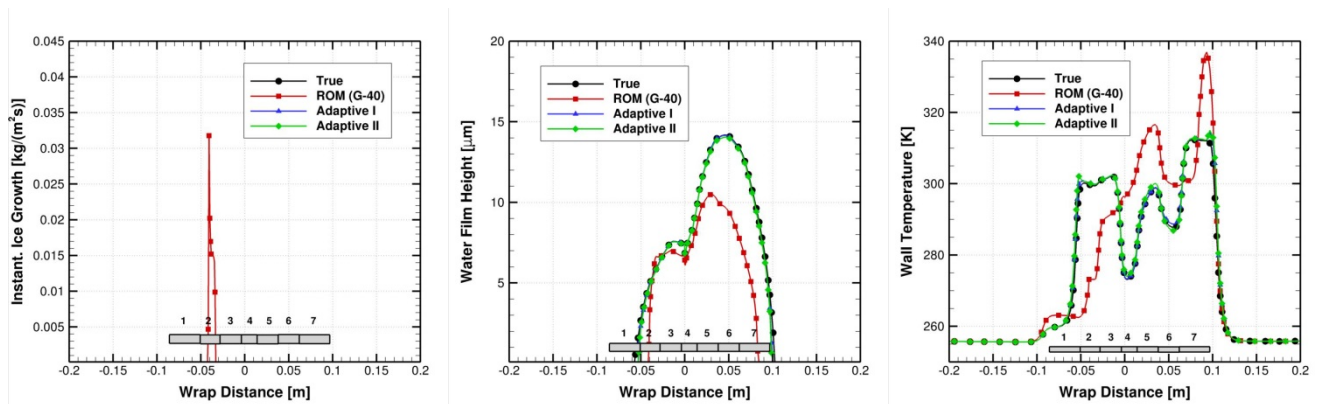


Figure 5.37: Profiles of three surface quantities at optimal states (Case E-I).

5.7 Discussion and Conclusions

In this chapter, an efficient methodology for the surrogate-based optimization of anti-icing systems was presented. In this methodology, reduced order models (ROM) are used to replace the expensive CHT simulations required during the optimization process. Various strategies were proposed to improve the accuracy of ROM. They include splitting, scalarization and localization. The performance of each strategy was demonstrated through numerical examples. Several optimization test cases were presented for both the running-wet and the evaporative regimes. For the running-wet regime, the results of Case W-III, i.e. the case with the TWT function, were closer to the true solution compared to the other cases. For the evaporative regime, the results of Case E-II, i.e. the case with the MWT function, were the closest one. Finally, the adaptive surrogate-based optimization was presented, in which the reduced order models gradually become more accurate during the optimization process. It was shown, through a numerical test case, that this approach can significantly improve the optimization results.

In this chapter and the previous one, the optimization of electro-thermal anti-icing systems were thoroughly. As mentioned before, electro-thermal systems can also operate in a transient de-icing mode. Analysis and optimization of de-icing systems is more challenging, as the unsteadiness has also to be considered. This will be discussed in the next chapter.

Chapter 6 IPS IN TRANSIENT DE-ICING MODE

6.1 Unsteady CHT Simulation of De-Icing System

Electro-thermal systems can operate in either anti-icing or de-icing modes. The electric heaters are continuously activated in the anti-icing mode and cyclically activated in the de-icing mode. Therefore, in contrast to anti-icing, de-icing is an unsteady transient process. This makes the simulation and optimization of the de-icing systems more challenging than those of the anti-icing systems because, in addition to all parameters considered in anti-icing, the activation time of the heaters also needs to be considered. The electro-thermal system to be investigated in this chapter is the same used for anti-icing (Figure 2.8). While the basic principles of the CHT simulation of de-icing are the same as those of anti-icing, the ice shape needs to be modified as time evolves. In fact, at each unsteady time step, one needs a converged steady-state anti-icing solution.

To demonstrate the performance of the de-icing simulation, a test case is selected among the experiments performed in the NASA Lewis Icing Research Tunnel (IRT) [48]. The flight-icing conditions for this test case are provided in Table 6.1, and the time sequencing pattern is illustrated in Figure 6.1, in which the values of the power densities are given in W/m^2 . As shown, the heater at the leading edge, i.e. heater 4, commonly called the “parting strip”, is continuously activated. The cycle includes three time periods: in the first one, which takes 100 seconds, only heater 4 is activated; in the second one, which takes 10 seconds, heaters 3 and 5 are activated in addition to heater 4; in the

third one, which also takes 10 seconds, heaters 1, 2, 6 and 7 are activated in addition to heater 4. Figure 6.2 shows the temperature history beneath heater 3 for five cycles, i.e. 600 seconds. The result obtained by CHT3D and NASA's experimental and numerical results, as shown, are in close agreement with each other.

Table 6.1: Flight-icing conditions.

Temperature [K]	Velocity [m.s ⁻¹]	LWC [g.m ⁻³]	MVD [μm]	AoA [deg.]
266.483	44.704	0.78	20	0

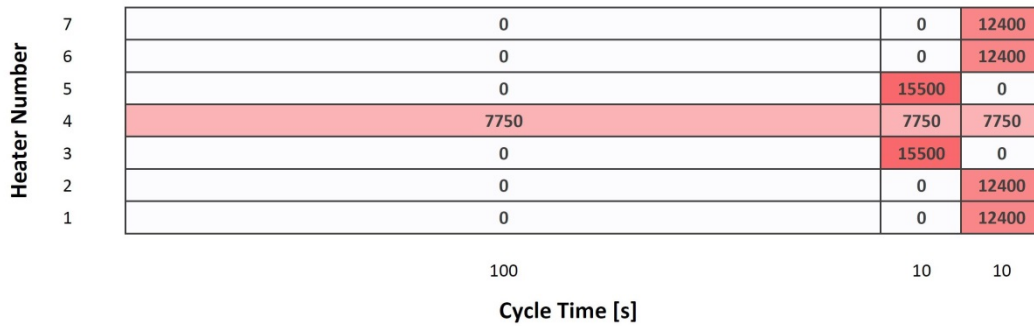


Figure 6.1: Heater cycling sequence pattern for validation test case (power densities shown in W/m²).

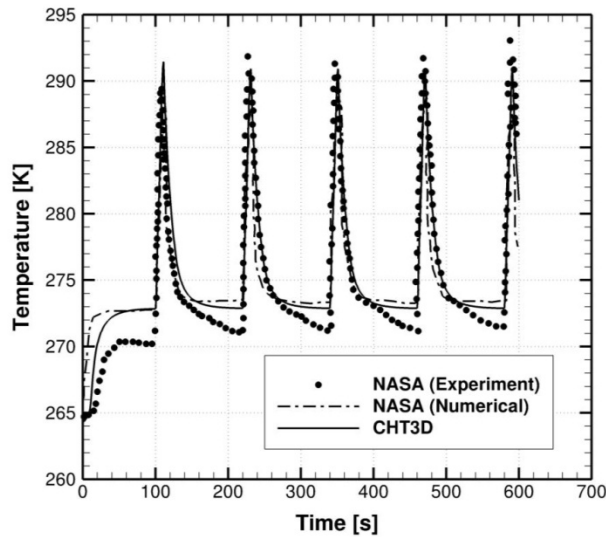


Figure 6.2: Comparison of the temperature history underneath heater 3.

6.2 Primary Modifications

Prior to the main optimization procedure, two major modifications to the de-icing system shall be performed to improve the final optimization outputs. The first one is concerned with the time sequencing pattern. In all of NASA's test cases [48], the duration of the first period is at least 100 seconds. According to our investigation and consultation with the industry, this duration seems to be too long for an optimal operation. Hence, the duration of the whole cycle, which is 120 seconds, is reduced by half. The second modification is concerned with the parting strip. All of NASA's test cases [48] were performed with a continuously activated parting strip. The reasoning behind this mode of operation is most likely to provide more safety at the critical zone of the leading edge. However, it was found that in some aspects, a continuously activated parting strip could be less efficient than a cyclically activated parting strip.

To demonstrate these modifications, another of NASA's test cases with the flight-icing conditions provided in Table 6.2 is considered. The time sequencing pattern for this test case is shown in Figure 6.3. The profiles of the ice thickness, the water film height and the wall temperature at the moment of maximum ice thickness and at the end of the cycle, i.e. 120th second, are shown in Figure 6.4. The maximum ice thickness during the whole cycle is about 4 mm, occurring at 105th second, on the lower surface immediately after the parting strip. Note that heaters 3 and 4 are activated at the 100th second. This means that it takes 5 seconds for melting to start. This is called the *preheating duration*. Understanding the influential parameters on preheating duration is helpful in setting and analysing the optimization test cases. Hence, it is briefly explained in the following paragraphs.

Table 6.2: Flight-icing conditions.

Temperature [K]	Velocity [m.s ⁻¹]	LWC [g.m ⁻³]	MVD [μ m]	AoA [deg.]
254.375	44.704	0.78	20	-4

Heater Number	7	0	0	23250
	6	0	0	24800
	5	0	24800	0
	4	18600	18600	18600
	3	0	24800	0
	2	0	0	24800
	1	0	0	23250
		100	10	10
		Cycle Time [s]		

Figure 6.3: Heater cycling sequence pattern for the modification test case (power densities shown in W/m^2).

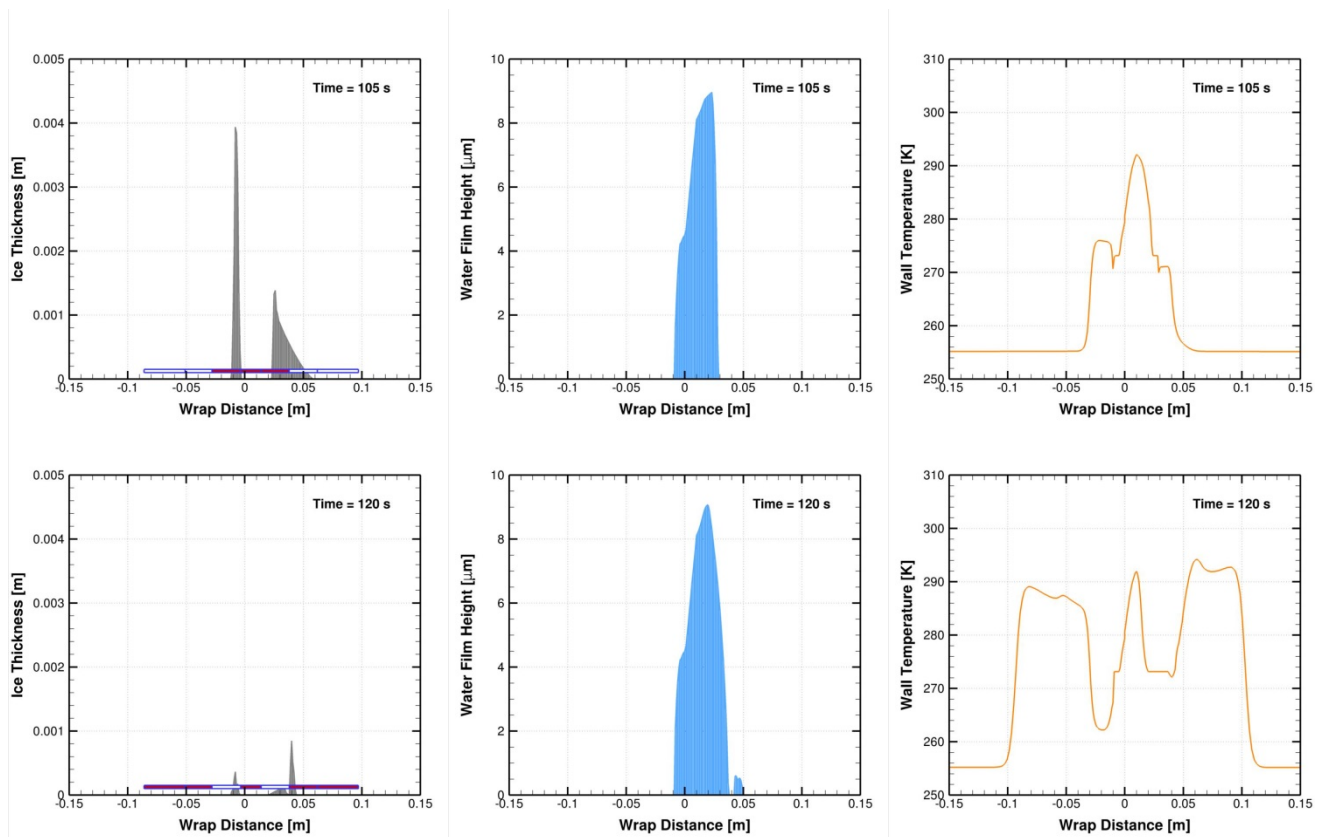


Figure 6.4: Profiles of three surface quantities at the moment of maximum ice thickness and at the end of the cycles for the modification test case.

In icing problems, the ice layer is usually so thin, compared to the other dimensions, that we can assume the ice layer as a semi-infinite body. Suppose that the ice layer has a uniform initial temperature of T_0 , which is below the melting point T_m . At time $t = 0$, a

constant heat flux, q_0'' , is applied to the wall. Since the initial temperature of the ice is below the melting point, melting does not start until the wall temperature reaches this point. Hence, the problem can be divided into two sub-problems: preheating and melting. In the preheating stage, when no melting occurs, we have a pure conduction problem with the following mathematical description for the temperature distribution inside the ice:

$$\frac{\partial^2 T}{\partial x^2} = \frac{1}{\zeta} \frac{\partial T}{\partial t} \quad 0 < x < \infty, \quad 0 < t < t_m, \quad 6-1$$

where t_m is the duration of preheating and α is the thermal diffusivity of ice, defined by

$$\zeta = \frac{k}{\rho c_p}, \quad 6-2$$

where ρ , k and c_p are the density, the thermal conductivity and the specific heat capacity of the ice. The boundary and the initial conditions for Eq. 6-1 are as follows:

$$\frac{\partial T}{\partial x} = -\frac{1}{k} q_0'' \quad x = 0, \quad 0 < t < t_m, \quad 6-3$$

$$T(x, t) \rightarrow T_0 \quad x \rightarrow \infty, \quad 0 < t < t_m, \quad 6-4$$

$$T(x, t) = T_0 \quad 0 < x < \infty, \quad t = 0. \quad 6-5$$

Assuming a second-degree polynomial for the temperature profile, the solution can be obtained by the integral approximate method [134]:

$$T(x, t) = T_0 + \frac{q_0'' \nu}{2k} \left(1 - \frac{x}{\nu}\right)^2, \quad 6-6$$

where ν is the thermal penetration depth, which can be obtained by substituting Eq. 6-6 into the integral equation and integrating Eq. 6-1 in the interval of $(0, \delta)$. This yields [134]:

$$\nu = \sqrt{6\alpha t}. \quad 6-7$$

The temperature of the ice layer is highest at its surface, i.e. at $x = 0$, which is

$$T_s(t) = T_0 + \frac{q_0'' \nu}{2k}. \quad 6-8$$

Melting starts when the surface temperature reaches the melting point, T_m . At this moment, the thermal penetration depth is equal to

$$v_m = \frac{2k(T_m - T_0)}{q_0''}. \quad 6-9$$

The duration of preheating can be obtained by combining Eqs. 6-7 and 6-9:

$$t_m = \frac{2k\rho c_p (T_m - T_0)^2}{3q_0''^2}. \quad 6-10$$

The above equation shows that for a specific solid material, the higher the initial temperature, T_0 , or the heat flux, q_0'' , the shorter the duration of preheating. Note that t_m does not depend on ice thickness. After melting starts, the governing equations in the solid and liquid phases must be specified, separately.

To compare the continuously activated and the cyclically activated parting strips, the two time sequencing patterns shown in Figure 6.5 are investigated. Note that all power densities are set to have the same values to eliminate any possible effects of the difference in the power densities on the investigation. As stated before, the cycle duration is to be reduced by half. Thus, there are now two 60-second cycles, instead of one 120-second cycle. Figure 6.6 and Figure 6.7 show the surface quantity profiles at the moment of maximum ice thickness and at the end of the two cycles for the continuously and cyclically activated parting strips, respectively. As shown, in the continuous case, the duration of preheating is longer and the maximum ice thickness is larger, even though the leading edge's temperature at the moment of maximum ice thickness is higher compared to the cyclical case. In fact, continuous activation of the parting strip causes larger amounts of runback water film to move downstream, where it starts to freeze as soon as the heaters are inactivated.

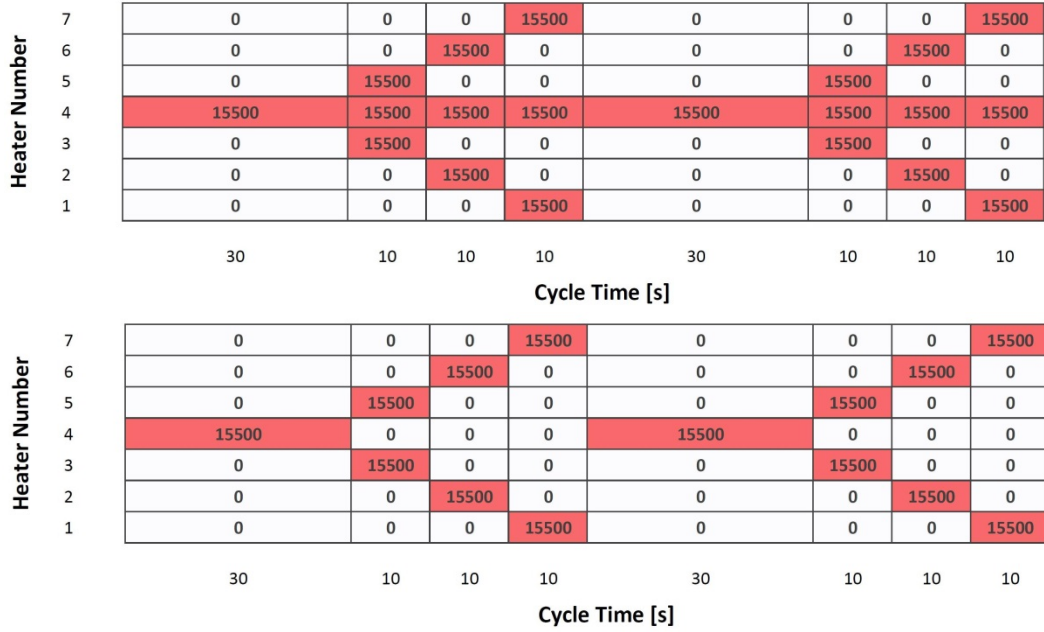


Figure 6.5: Heater cycling sequence patterns for continuously (top) and cyclically (bottom) activated parting strip cases (power densities shown in $[\text{W}/\text{m}^2]$).

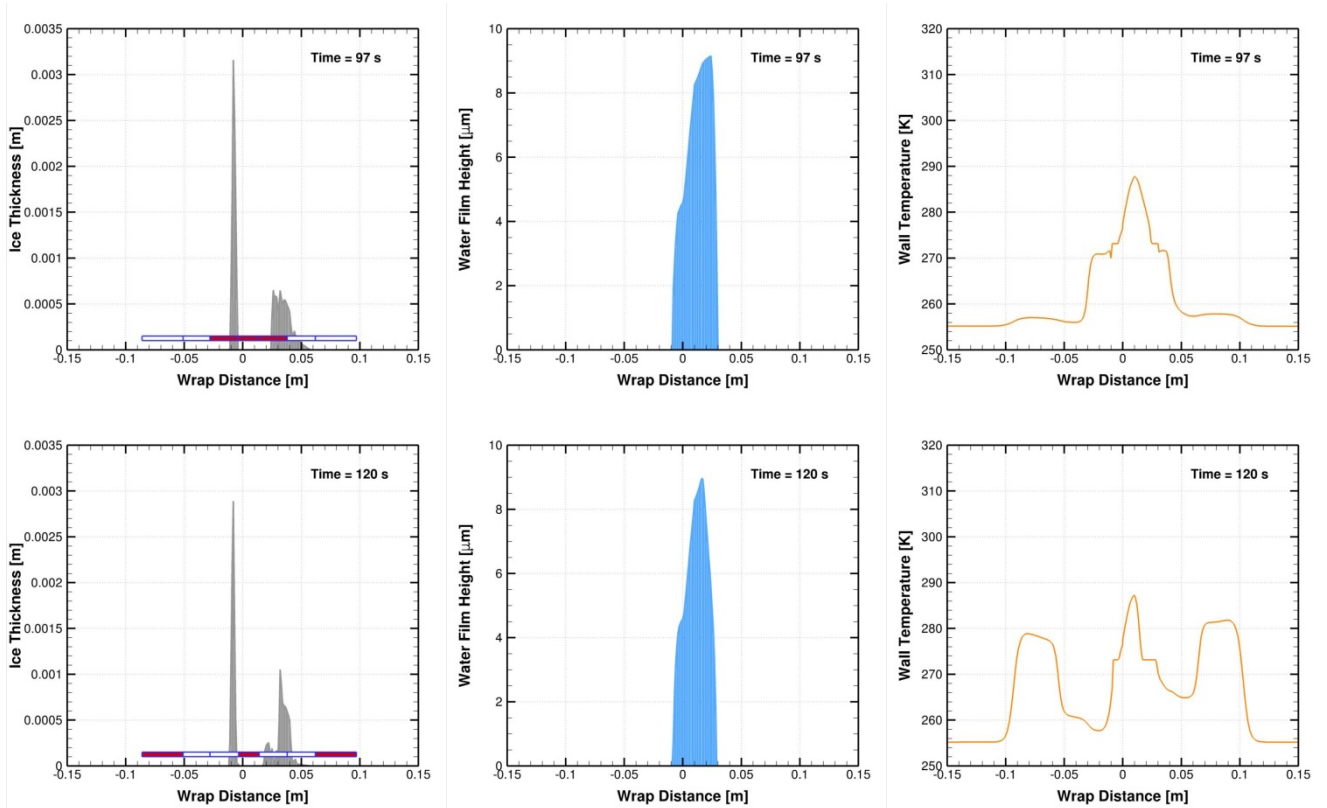


Figure 6.6: Profiles of three surface quantities at the moment of maximum ice thickness and at the end of the cycles for continuously activated parting strip.

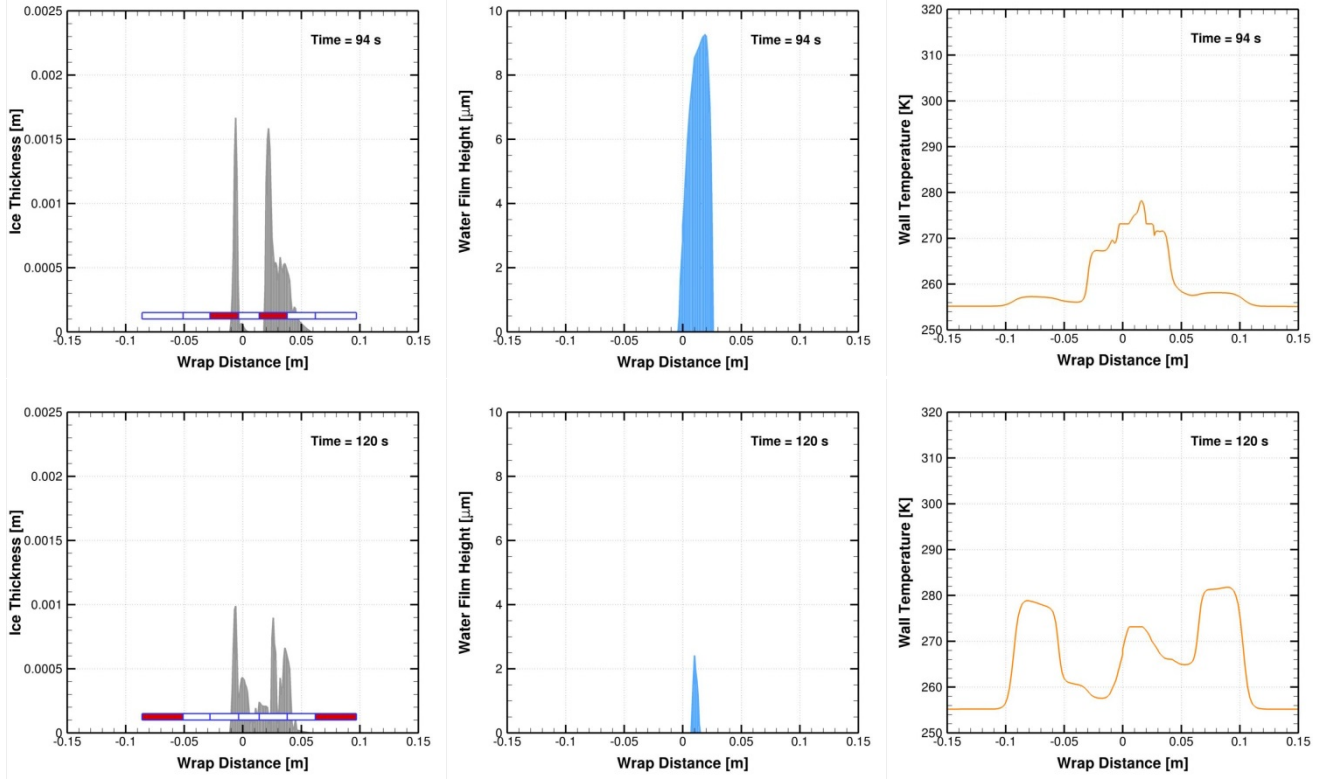


Figure 6.7: Profiles of three surface quantities at the moment of maximum ice thickness and at the end of the cycles for cyclically activated parting strip.

6.3 Formulations of the Objective and Constraint Functions

The objective and constraint functions should, of course, be different from those introduced for the anti-icing optimization. These functions, which are provided in Table 6.3, are described in the following:

- **TEE:** The amount of energy consumed for de-icing determines the cost. *TEE*, which stands for “total electrical energy”, gives the energy consumption, i.e. power multiplied by time, over the cycles being investigated:

$$TEE = \int_0^{t_e} \int_{s_{el}}^{s_{eu}} P''(s, t) ds dt, \quad 6-11$$

where $P''(s, t)$ is the power density at location s and time t , and t_e is the duration of the whole cycle.

Table 6.3: Formulation of the objective and constraint functions.

Type	Formulation	Description
<i>TEE</i>	$\int_0^{t_e} \int_{s_{el}}^{s_{eu}} P''(s, t) ds dt$	Total electric energy
<i>MIT</i>	$\max \left\{ h_{ice}(s, t) \right\}_{0, s_{el}}^{t_e, s_{eu}} - h_{ice}^*$	Maximum ice thickness
<i>FIV</i>	$\int_{s_{el}}^{s_{eu}} h_{ice}(s, t_e) ds$	Final ice volume
<i>ISI</i>	$\int_0^{t_e} \sigma_d dt$	Ice shape irregularity
<i>IPD</i>	$\left s(MIT) - s(C_{p, \min}) \right $	Ice-pressure distance

- **MIT:** Maximum ice thickness is one of the most important parameters affecting the aerodynamic characteristics of the iced wing. Larger ice thickness usually leads to more aerodynamic degradation. *MIT*, which stands for “maximum ice thickness”, gives the maximum ice thickness with respect to a reference value over the entire cycles:

$$MIT = \max \left\{ h_{ice}(s, t) \right\}_{0, s_{el}}^{t_e, s_{eu}} - h_{ice}^* \quad 6-12$$

where $h_{ice}(s, t)$ is the ice thickness at time t and wrap distance s , and h_{ice}^* is the largest ice thickness allowed over the whole cycles.

- **FIV:** An actual in-flight icing event may take up to 1 hour or more. The CHT simulation of such long event would be computationally prohibitive, especially for optimization purposes, which require hundreds or thousands of such simulations. Therefore, in the optimization test cases to be presented here, only two 60-second cycles will be considered. In order to account for the next cycles, the ice accretion state at the end of the cycles should be considered. The more ice

remaining at the end of the cycles, the more energy is needed for de-icing in the next cycles. Note that a de-icing case with a small value of maximum ice thickness does not necessarily correspond to a case with a small volume of ice at the end of the cycles. For instance, the maximum ice thickness in the test case presented for the cyclically activated parting strip (Figure 6.7) is much smaller than that in the NASA test case (Figure 6.4). However, the ice volume at the end of the cycles of the cyclical case is significantly larger than that of the NASA case. Considering all of these discussions, it was found that the ice volume at the end of the cycles should be taken into accounts. *FIV*, which stands for “final ice volume”, gives the volume of the ice at the end of the whole cycles:

$$FIV = \int_{s_{el}}^{s_{eu}} h_{ice}(s, t_e) ds \quad 6-13$$

- **ISI:** Two sample ice shapes over the heating zone are shown in Figure 6.8. They both have the same maximum thickness at the same location on the lower surface. However, it can be understood that the jagged shape would result in greater aerodynamic penalty. To assess the jaggedness or irregularity of the ice shape, one can use the “standard deviation” of the grid points making the ice profile. The standard deviation, σ , measures the amount of variation or dispersion of a data set from the average. A low standard deviation indicates that the points are close to the average value, and a high standard deviation indicates that the data points are scattered out over a large range of values. The standard deviation is defined as follows:

$$\sigma = \sqrt{\frac{1}{N} \sum_{i=1}^N (h_{ice}(s_i, t) - \bar{h}_{ice}(t))^2}, \quad 6-14$$

where N is the number of grid points over the heating zone, $h_{ice}(s_i, t)$ is the ice thickness at i^{th} point at time t and $\bar{h}_{ice}(t)$ is the average of the thickness values at time t :

$$\bar{h}_{ice}(t) = \frac{1}{N} \sum_{i=1}^N h_{ice}(s_i, t). \quad 6-15$$

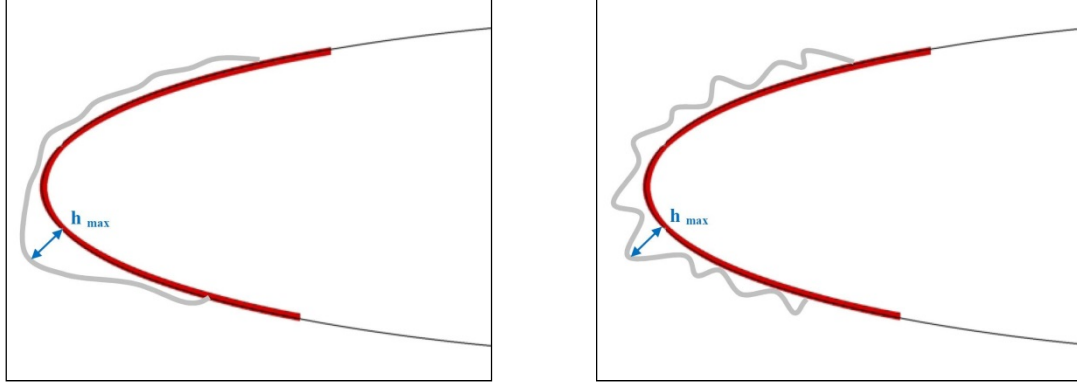


Figure 6.8: Smooth (left) and irregular (right) ice shapes with the same maximum ice thickness at the same location.

To assess the overall smoothness of the ice shape through the whole cycles, one shall integrate over time:

$$\text{overall std. dev.} = \int_0^{t_c} \sigma(t) dt. \quad 6-16$$

Although the standard deviation can provide a criterion for the amount of dispersion of a data set, it was found that it does not characterize the “spatial” dispersion of a data set. In other words, for the standard deviation, it does not matter where each data point is located. To account for this, instead of calculating the standard deviation for the data points, one may calculate it for the difference of the neighboring data points:

$$\sigma_d = \sqrt{\frac{1}{N-1} \sum_{i=1}^{N-1} (h'_{ice}(s_i, t) - \bar{h}'_{ice}(t))^2}, \quad 6-17$$

where

$$h'_{ice}(s_i, t) = |h_{ice}(s_{i+1}, t) - h_{ice}(s_i, t)| \quad 6-18$$

and

$$\bar{h}'_{ice}(t) = \frac{1}{N-1} \sum_{i=1}^{N-1} h'_{ice}(s_i, t). \quad 6-19$$

On this basis, *ISI*, which stands for “ice shape irregularity”, can be quantified by integrating this type of “differential standard deviation” over time as follows:

$$ISI = \int_0^{t_e} \sigma_d dt, \tag{6-20}$$

To demonstrate the difference between the standard deviation and the differential one, consider a simple mathematical function, $f = x^2$, that is formed by 100 points. This smooth function is shown in Figure 6.9 on the left side. To make a jagged profile using the same set of data points, the location of every two adjacent points is exchanged. This results in a jagged profile, as shown in Figure 6.9 on the right side. Both profiles have the same average and standard deviation values. However, the differential standard deviation of the jagged profile is greater than that of the smooth one.

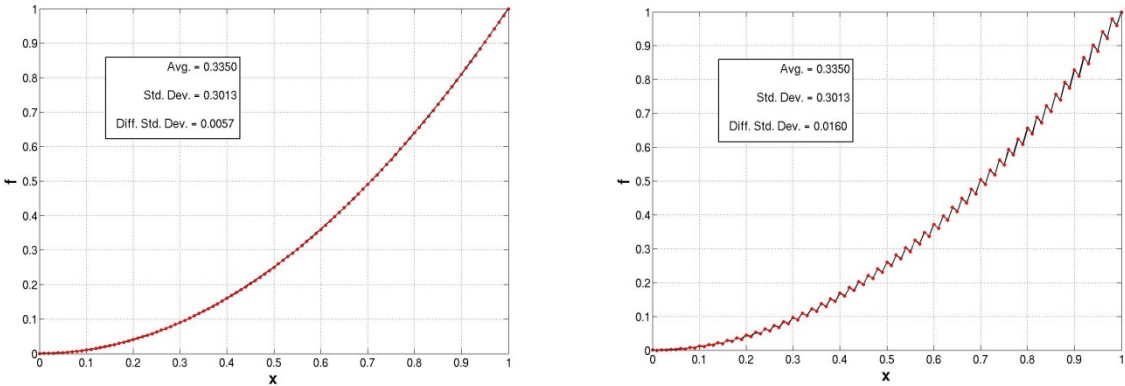


Figure 6.9: Two sets of points with same data values, average and standard deviation, but with different data locations and differential standard deviation.

- **IPD:** The aerodynamic performance degradation depends not only on the value of the maximum ice thickness, but also on its location. A small ice thickness in a critical location may lead to a large penalty while a large ice thickness in a non-critical location may lead to a small penalty. It may be thought that the leading edge is the most critical location for ice accretion. However, this is not always

true. In fact, the most critical location of a protuberance heavily depends on its height. Figure 6.10 shows the variation of the maximum lift of a NACA 0012 airfoil with respect to the location of protuberances with different heights. For protrusions smaller than the local boundary layer thickness, the most critical location is the leading edge. However for larger protrusions ($k/c > 0.001$), the leading edge is not necessarily the most critical location. Similar to the lift, the drag change due to a protuberance also depends on the location of the protuberance. According to Bowden [135], the maximum drag increase occurs when the protuberance is placed near the location of the minimum pressure coefficient (or maximum local velocity). When placed at this location, the protuberance extracts the greatest amount of boundary layer momentum and a large separation bubble forms downstream of the ice [136]. *IPD*, which stands for “ice-pressure distance”, gives the distance between the location of the maximum ice thickness and the location of the minimum pressure coefficient:

$$IPD = \left| s(MIT) - s(C_{p,\min}) \right| \quad 6-21$$

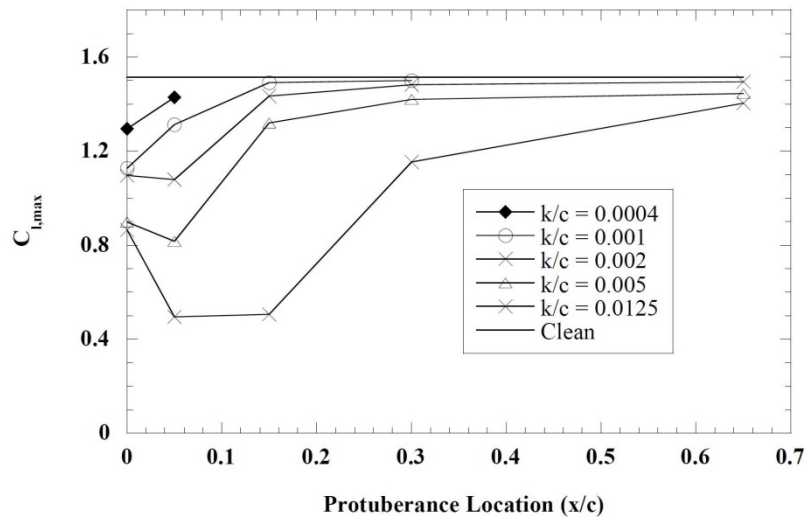


Figure 6.10: Variation of maximum lift of NACA 0012 airfoil with respect to the chord-wise location of protuberances with different heights (k/c); $Re = 3.1 \times 10^6$ (picture adapted from [137] and [17]).

6.4 Optimization Approach

Similar to the anti-icing cases, the mesh adaptive direct search (MADS) is used as the optimization method. For the anti-icing optimization, both CHT-based (Chapter 4) and surrogate-based (Chapter 5) optimizations were performed. However for de-icing, only the surrogated-based optimization (using ROM) is to be performed since the cost of the CHT de-icing simulation is prohibitive and much more than that of the anti-icing simulation. In the ROM-based CHT for de-icing, the same improvement strategies introduced in Chapter 4 for anti-icing are applied, i.e. splitting, scalarization and localization.

To demonstrate the performance of the ROM-based CHT for de-icing, consider an arbitrary sample target for which we are to compute the maximum ice thickness. The design variables include the power densities of the seven heaters, whose values are provided in Table 6.4. The cycling sequence pattern is similar to that of the cyclically activated parting strip shown in Figure 6.5. To construct ROM, 200 snapshots with true CHT simulations are provided. The profiles of the maximum ice thickness as a function of time for these snapshots are shown in Figure 6.11. Figure 6.12 shows the target profiles obtained by the true CHT and ROM. The true profiles show that the maximum ice thickness during the whole cycles is 0.002850 m, which occurs on the lower surface at the end of the cycles, i.e. the 120th second. Although the maximum ice thickness in the ROM profile occurs at around the 116th second, its value is 0.00282 m, which is very close to the true one. Also similar to the maximum ice thickness in the true profile, the maximum thickness in the ROM profile occurs on the lower surface.

Table 6.4: Sample target data set.

P_1	P_2	P_3	P_4	P_5	P_6	P_7
23613.2812	2542.96875	1089.84375	21433.5938	2542.96875	1089.84375	21433.5938

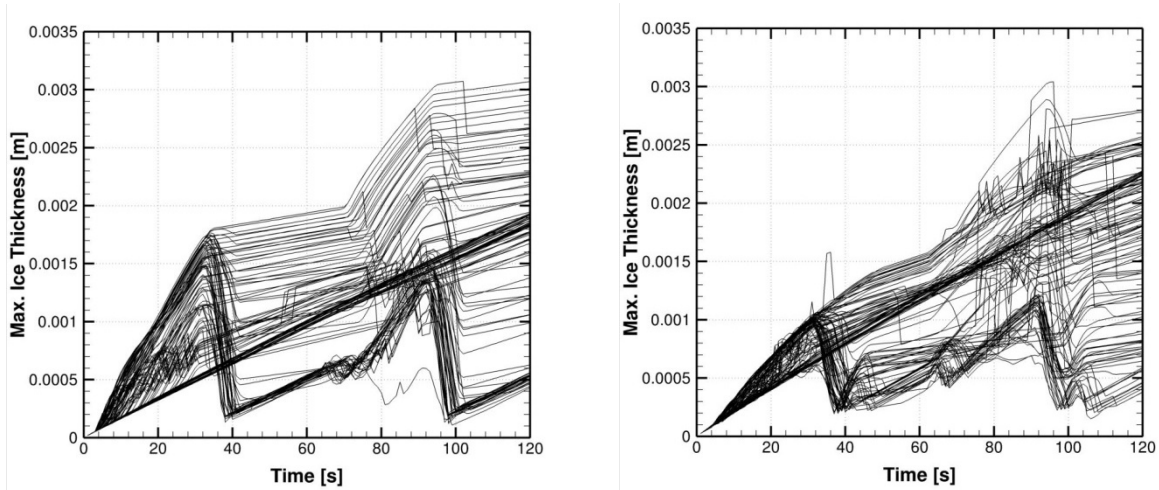


Figure 6.11: Variation of maximum ice thickness as through time for 200 snapshots on the lower (left) and upper (right) surfaces of the wing.

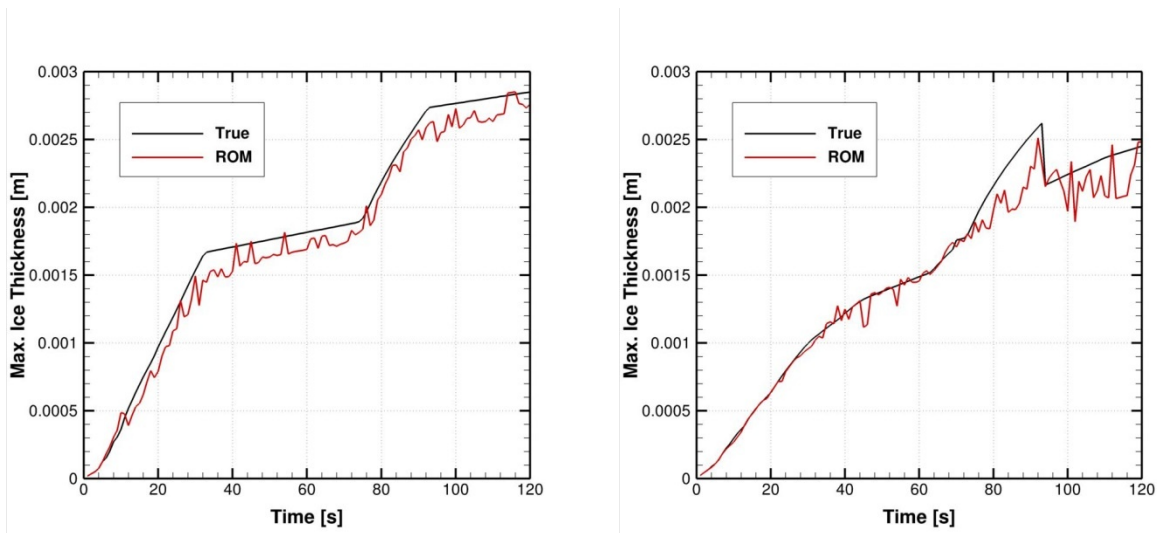


Figure 6.12: Variation of maximum ice thickness through time for the target on the lower (left) and upper (right) surfaces of the wing.

6.5 Numerical Test Cases

The flight-icing conditions provided in Table 6.2 are used for all the test cases presented in this section. The mathematical statement of the optimization problem is the same as that which was defined for anti-icing:

$$\begin{aligned} \min_{\mathbf{x} \in \chi} \quad & f_i(\mathbf{x}), \quad i \in I, \\ \text{subject to} \quad & c_j(\mathbf{x}) \leq 0, \quad j \in J, \end{aligned} \tag{6-22}$$

where f_i 's are the objective functions, $I = \{1, \dots, l\}$, \mathbf{x} is the vector of n design variables, c_j 's are the constraints, $J = \{1, \dots, m\}$ and χ is a subset of \mathbb{R}^n . The design variables include the power densities of the seven electric heaters, which vary within the interval $[1,000; 30,000]$ W/m². Two types of cycling sequence patterns are to be used in the optimization results: Pattern A and Pattern B, which are illustrated in Figure 6.13. As shown, Pattern A includes two 60-second cycles, and Pattern B includes three 40-second cycles. The total duration of both patterns is 120 seconds. Beside the power densities, in some of the test cases, the activation times of the heaters are also included into the design variables. In these test cases, for pattern A, which consists of four time periods in each cycle, the duration of the first period can vary within the interval $[15; 45]$ seconds, and the duration of the next three periods can vary within $[5; 15]$. For Pattern B, which consists of three time periods in each cycle, the duration of the first period can vary within $[10; 30]$, and the duration of the next two periods can vary within $[5; 15]$. The different sets of the objective and constraint functions used for the different test cases are provided in Table 6.5. The matrix of 14 test cases is given in Table 6.6. The objective and constraint functions set (I or II or III or IV, based on Table 6.5), the design variables (power densities, P, and durations of the periods, T) and the cycling sequence pattern (A or B) are indicated for each test case.

Table 6.5: Different sets of objective and constraint functions.

	f_1	f_2	c_1
I	<i>TEE</i>		<i>MIT</i>
II	<i>TEE</i>	<i>FIV</i>	<i>MIT</i>
III	<i>TEE</i>	<i>ISI</i>	<i>MIT</i>
IV	<i>TEE</i>	<i>IPD</i>	<i>MIT</i>

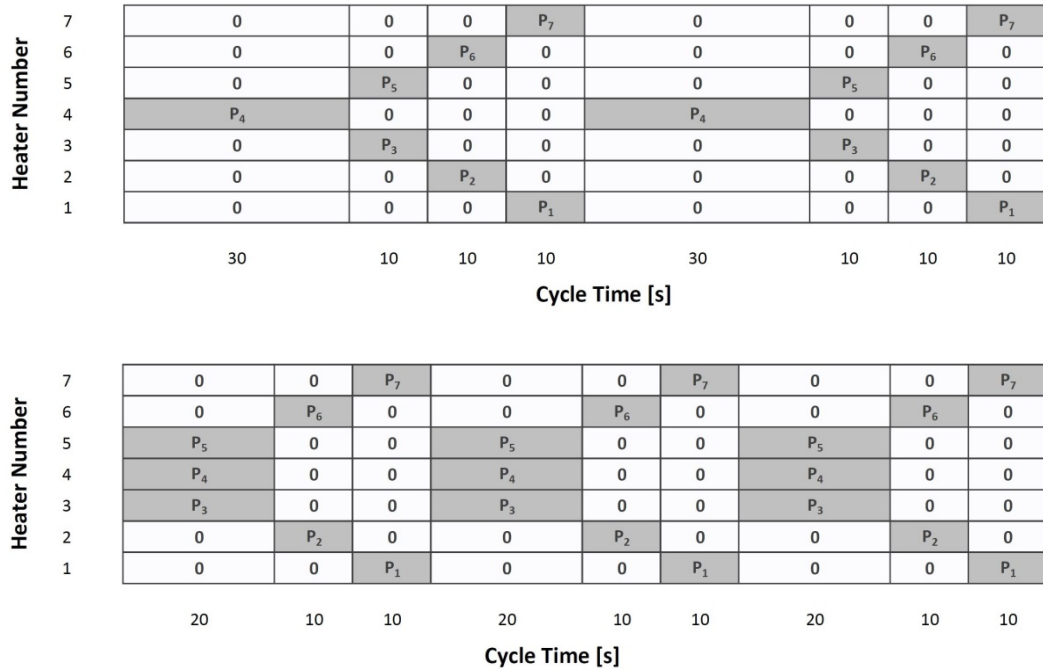


Figure 6.13: Two types of cycling sequence patterns: Pattern A (top), Pattern B (bottom).

Table 6.6: Matrix of test cases.

Case	Function Set	Design Variables	Cycling Pattern
I-P-A	I	P	A
I-P-B	I	P	A
I-PT-A	I	P & T	B
I-PT-B	I	P & T	B
II-P-A	II	P	A
II-P-B	II	P	A
II-PT-A	II	P & T	B
II-PT-B	II	P & T	B
III-P-A	III	P	A
III-P-B	III	P	A
III-PT-A	III	P & T	B
III-PT-B	III	P & T	B
IV-P-A	IV	P	A
IV-P-B	IV	P	B

In the first four test cases, i.e. I-P-A, I-P-B, I-PT-A and I-PT-B, the following objective and constraint functions are used:

$$\begin{aligned} f_1(\mathbf{x}) &\equiv TEE, \\ c_1(\mathbf{x}) &\equiv MIT, \end{aligned} \tag{6-23}$$

where the largest ice thickness, h_{ice}^* , allowed over the heating zone is 1.4 mm. It should be noted that the largest ice thickness allowed in a real icing event may be greater than 1.4. However, as mentioned before, only a part of an icing event is being considered. Therefore, by assuming a small h_{ice}^* , a margin of safety is actually being respected. The above formulation gives the smallest amount of energy required for de-icing provided that the maximum ice thickness during the whole cycles is less than 1.4 mm. In the cases I-P-A and I-P-B, the power densities, and in the cases I-PT-A and I-PT-B, both the power densities and the periods' durations are considered as the design variables.

Figure 6.14 shows the convergence history of the best feasible objective function values. The optimized total energy for Case I-P-A is 31,912 J, for Case I-P-B is 63,766 J, for Case I-PT-A is 27,990 J and for Case I-PT-B is 49,330 J. All of these values are less than the total energy used in the experiment [48], i.e. 79,611 J. The amounts of the decrease in the cases with Pattern A, i.e. cases I-P-A and I-PT-A, are remarkably 60%, which is much more than the amounts of the decrease in the cases with Pattern B, i.e. cases I-PT-A and I-PT-B. This emphasizes the important influence of the cycling sequence pattern on the optimal results. In Pattern B, as shown in Figure 6.13, the parting strip zone is extended by the simultaneous activation of heaters 3, 4 and 5. This may be thought of as a strategy to increase the protection and the safety of the leading edge. However, the results show that one can limit the maximum ice thickness with a more economical pattern, i.e. Pattern A. Another point that is understood from Figure 6.14 is that by including the periods' durations into the design variables, one can reduce the optimized total energy in both patterns A and B. This can be found by comparing Case I-P-A with Case I-PT-A (12% reduction) as well as by comparing Case I-P-B with I-PT-B (23% reduction). In fact, the increase in the number of design variables has increased the degrees of freedom in searching the design space. Here, it is shown that the optimal solutions of the two cases have better performance, i.e. cases I-P-A and I-PT-A. The

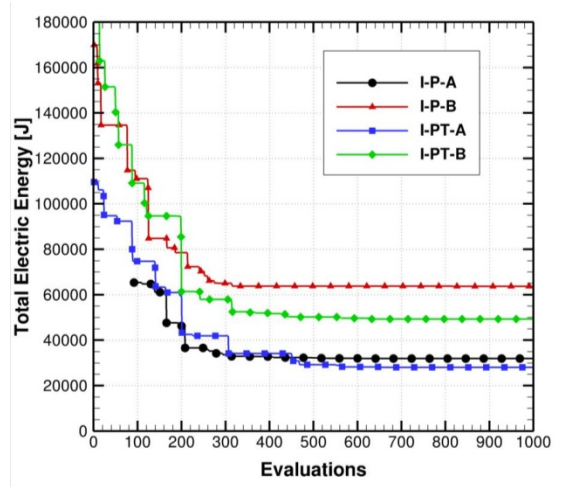


Figure 6.14: Convergence history of the best feasible objective function values for cases I-P-A and I-P-B.

optimal power densities and cycling sequence patterns for these two cases are shown in Figure 6.15. The highest amount of power density is allocated to heaters 3, 4 and 5. This could be helpful if one were to improve the result of Case I-P-A by performing another optimization. For instance, given the duration of the first period is decreased in Case I-PT-A, a better choice for the cycling sequence pattern for Case I-P-A would be [20, 10, 10, 10] instead of [30, 10, 10, 10], which is already considered. Figure 6.16 shows the surface quantity profiles at the moment of maximum ice thickness and at the end of the cycles for the optimal solution of Case I-P-A. The maximum ice thickness is about 1.7 mm, which slightly violates the 1.4 mm constraint. The discrepancy is due to the use of reduced order modeling in place of CHT simulations. The maximum ice thickness occurs at the 92nd second, i.e. 2 seconds after heaters 3 and 5 are activated. Thus, the duration of preheating is 2 seconds. The surface quantity profiles at the end of the cycles for the optimal solution of Case I-PT-A are shown in Figure 6.17. Note that in this test case, the maximum ice thickness occurs at the end of the cycles. It is interesting to note that despite consuming large amount of energy, the experimental case (Figure 6.4) yields a maximum ice thickness that is about three times larger than that in the optimized case.

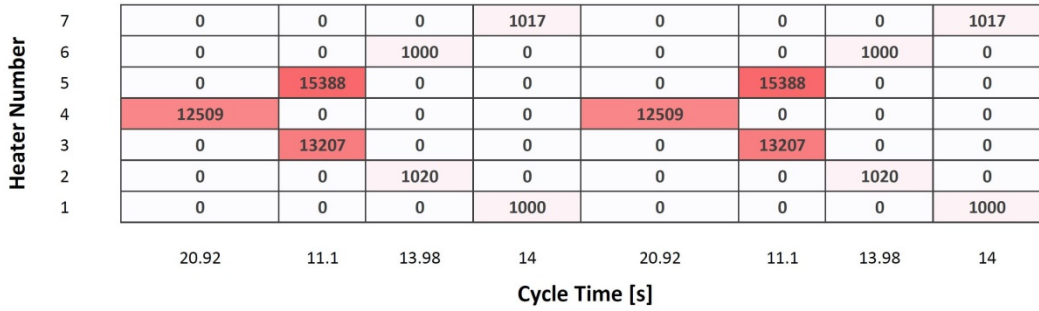
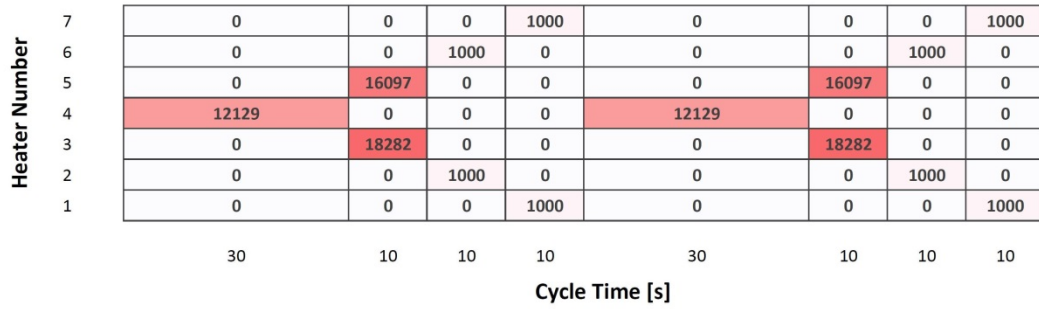


Figure 6.15: Power densities (W/m^2) and cycling sequence patterns for optimal solutions of Case I-P-A (top) and Case I-PT-A (bottom).

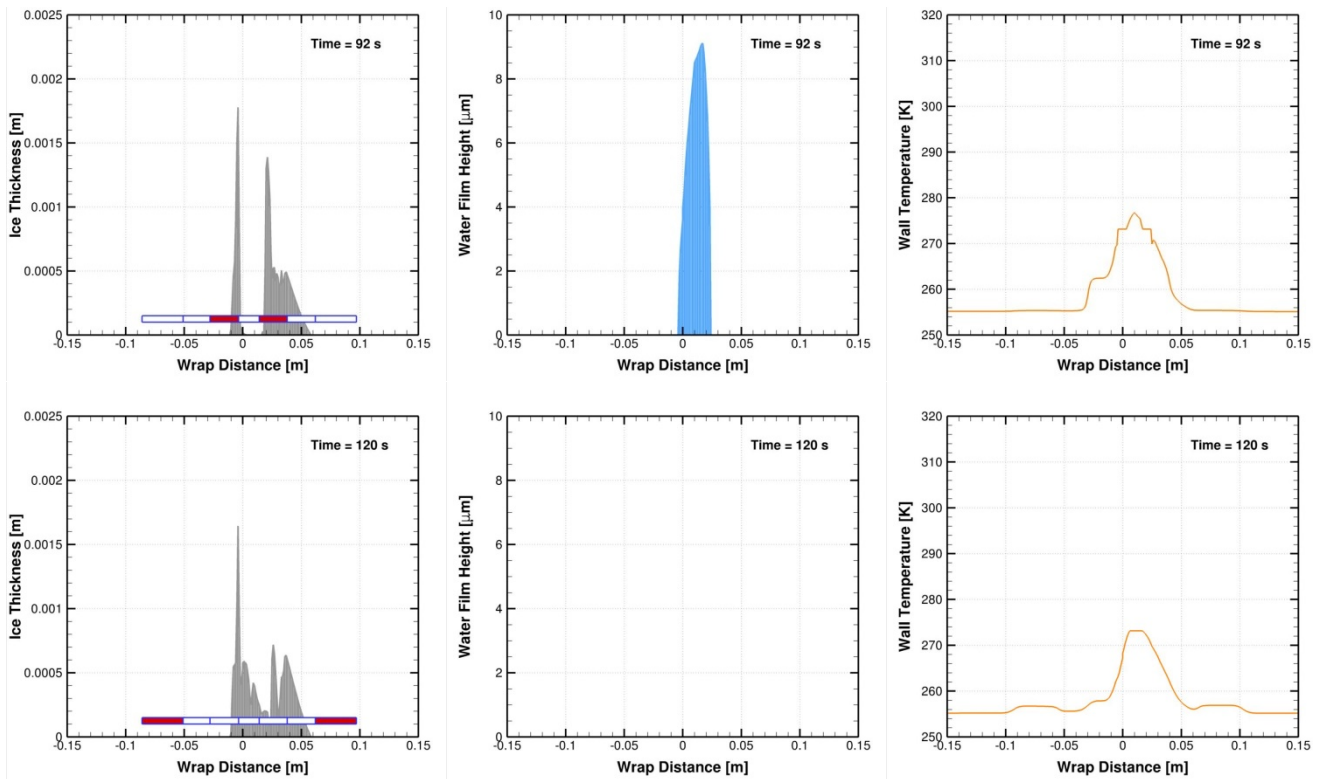


Figure 6.16: Profiles of three surface quantities at the moment of maximum ice thickness and at the end of the cycles for Case I-P-A.

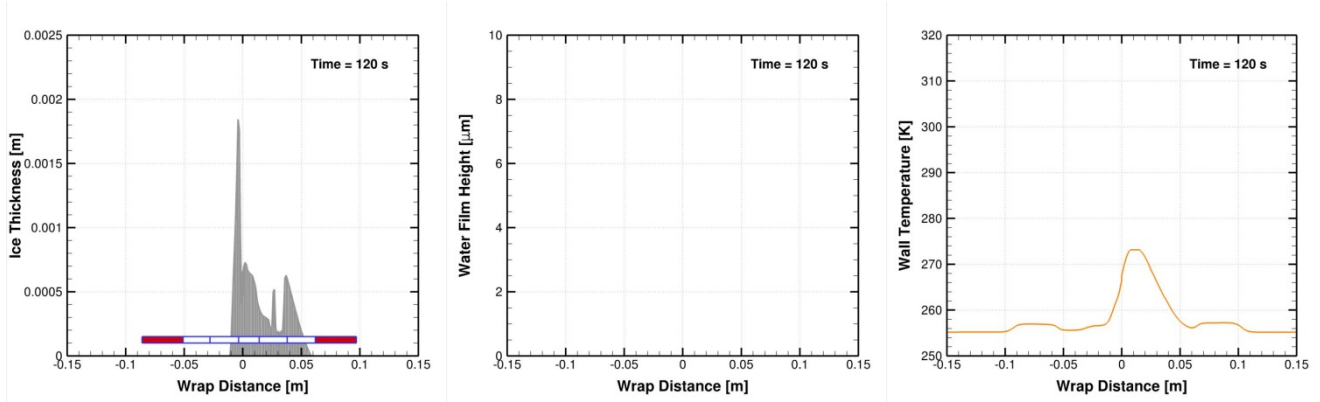


Figure 6.17: Profiles of three surface quantities at the moment of maximum ice thickness and at the end of the cycles for Case I-PT-A.

In the next four test cases, i.e. II-P-A, II-P-B, II-PT-A and II-PT-B, the following objective and constraint functions are used:

$$\begin{aligned}
 f_1(\mathbf{x}) &\equiv TEE, \\
 f_2(\mathbf{x}) &\equiv FIV, \\
 c_1(\mathbf{x}) &\equiv MIT,
 \end{aligned}
 \tag{6-24}$$

where the largest ice thickness, h_{ice}^* , allowed over the heating zone is 1.4 mm. The above formulation gives the smallest amount of the energy required for de-icing provided that as small ice volume as possible remains at the end of the cycles and the maximum ice thickness during the whole cycles is less than 1.4 mm. In cases II-P-A and II-P-B, the power densities, and in cases II-PT-A and II-PT-B, both the power densities and the activation times are considered as the design variables.

Figure 6.18 shows the Pareto fronts of the four test cases for 1000 function evaluations. There are two features distinguishing the cases with Pattern B from those with Pattern A: the infeasible points are more dispersed and both the feasible and infeasible points, overall, have higher total electric energy values. Therefore, Pattern A surpasses Pattern B, similar to the previous test cases. This figure also shows that by including the periods' durations into the design variables, more feasible points are found, especially in the areas with high total energy.

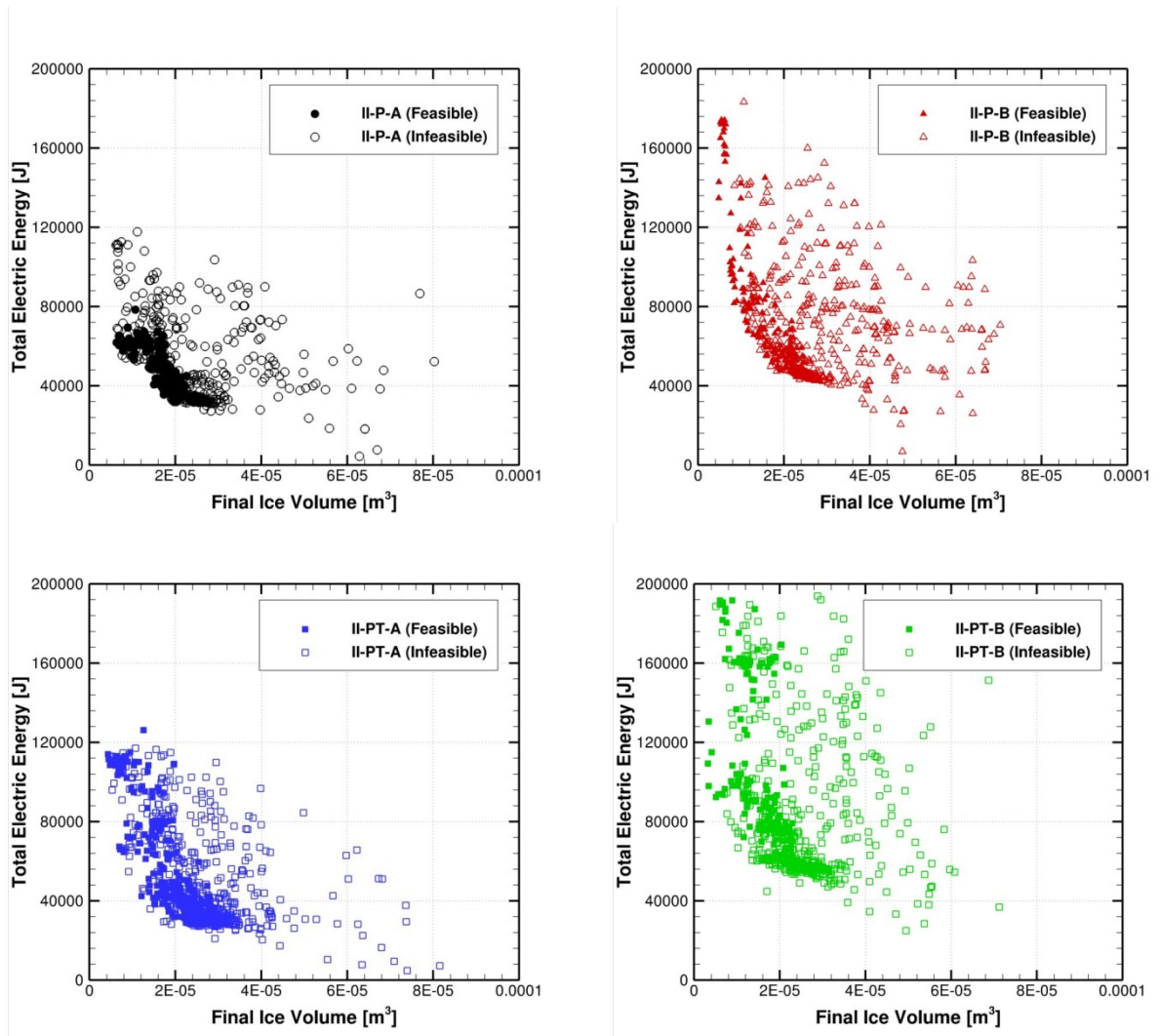


Figure 6.18: Pareto fronts of cases with function set II.

For a better comparison, the feasible points of the four cases are plotted together in Figure 6.19. This figure clearly shows the superior performance of Pattern A. It also should be noted that Case II-P-A results in the best overall solutions. Although one can find feasible points with final ice volumes less than the smallest final ice volume of Case II-P-A, none of these points requires a total energy less than that of the experimental test case, i.e. 79,611 J. Therefore, one of the best feasible points of Case II-P-A is selected. Figure 6.20 shows the optimal power densities and the cycling sequence pattern for the selected point (shown in Figure 6.19). This point has the smallest final ice volume that still consumes less energy than the experimental test case. The final ice volume for this

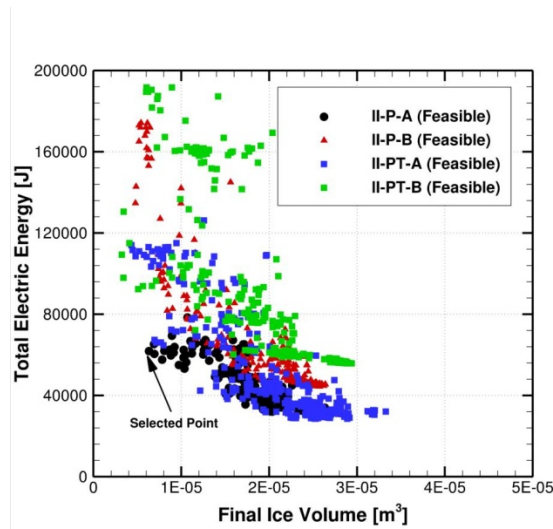


Figure 6.19: Feasible Pareto fronts for cases with function set II.

point is $9 \times 10^{-6} \text{ m}^3$ and the total energy is 61,094 J. We can see that all the power densities in Case II-P-A are larger than those in Case I-P-A (Figure 6.15). The increase is very considerable for heater 6. This shows that heater 6 has a significant effect on the final ice volume and not on the maximum ice thickness, due to the negative angle of attack. Figure 6.21 shows the surface quantity profiles at the moment of maximum ice thickness and at the end of the cycles. The maximum ice thickness is about 1.3 mm, which occurs at the 94th second, i.e. 4 seconds after heater 3 is activated. Hence, the duration of preheating is 4 seconds, which is 2 seconds longer than that in Case I-P-A. As previously discussed, the duration of preheating of a phase-change-material is a function of both initial temperature and heat flux. Although, the heat flux, i.e. power density, of heater 3 in Case II-P-A is greater than that in Case I-P-A, the initial temperature (i.e. temperature when maximum ice thickness occurs) over heater 3 in Case II-P-A is less than that in Case I-P-A, resulting in a longer preheating. At the end of the cycles, the ice volume, as shown, is significantly reduced compared to Case I-P-A.

7	0	0	0	3900	0	0	0	3900
6	0	0	27100	0	0	27100	0	0
5	0	27100	0	0	0	27100	0	0
4	13400	0	0	0	13400	0	0	0
3	0	27100	0	0	0	27100	0	0
2	0	0	4700	0	0	0	4700	0
1	0	0	0	3900	0	0	0	3900
	30	10	10	10	30	10	10	10

Cycle Time [s]

Figure 6.20: Optimal power densities (W/m^2) and cycling sequence pattern for Case II-P-A.

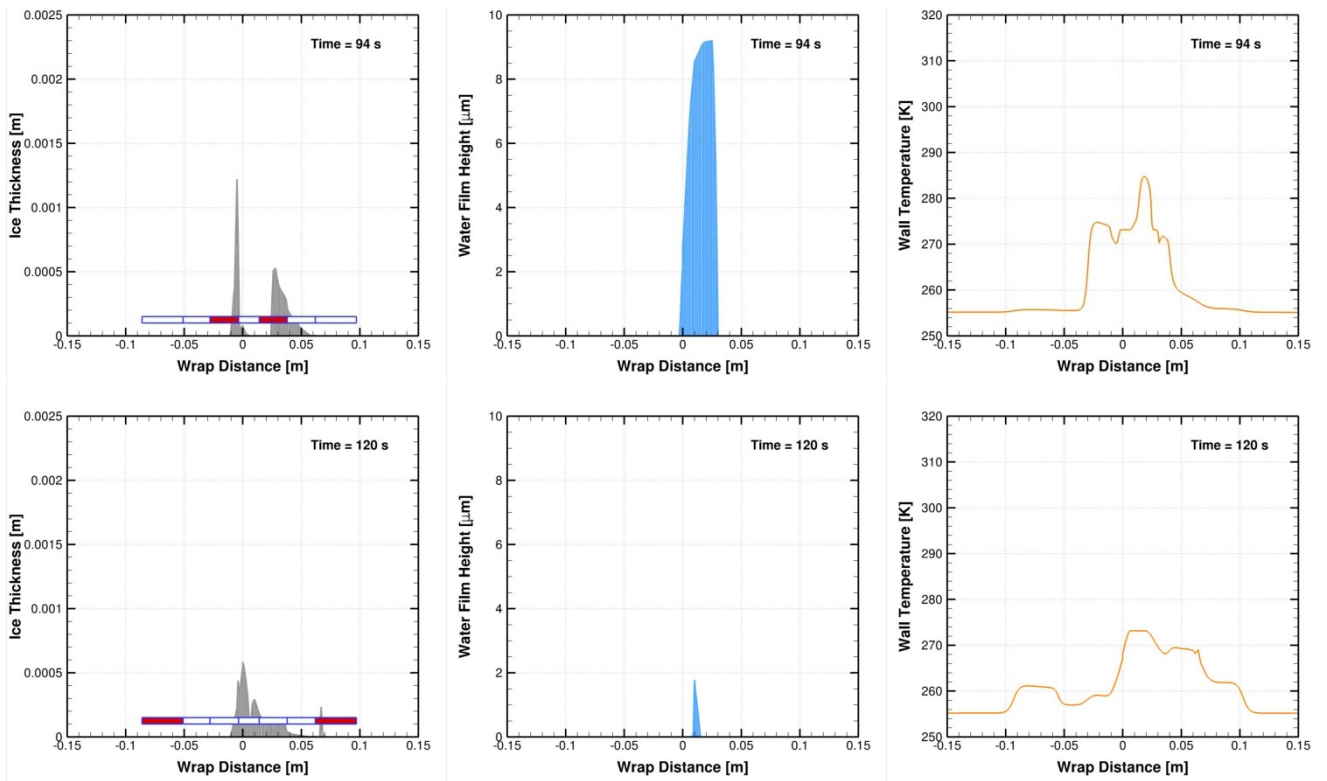


Figure 6.21: Profiles of three surface quantities at the moment of maximum ice thickness and at the end of the cycles for Case II-P-A.

In the next four test cases, i.e. III-P-A, III-P-B, III-PT-A and III-PT-B, the following objective and constraint functions are used:

$$\begin{aligned}
 f_1(\mathbf{x}) &\equiv TEE, \\
 f_2(\mathbf{x}) &\equiv ISN, \\
 c_1(\mathbf{x}) &\equiv MIT,
 \end{aligned}
 \tag{6-25}$$

where the largest ice thickness, h_{ice}^* , allowed over the heating zone is 1.4 mm. The above formulation gives the smallest amount of the energy required for de-icing provided that the ice shape remains as smooth as possible and the maximum ice thickness during the whole cycles is less than 1.4 mm. In cases III-P-A and III-P-B, the power densities, and in cases III-PT-A and III-PT-B, both the power densities and the periods' durations are considered as the design variables. Figure 6.22 shows the Pareto fronts of the four test cases. As before, Pattern A performs better since the values of the total energy in the cases with Pattern A is overall smaller than that in the cases with Pattern B. To better compare them, the feasible Pareto fronts of the four test cases are plotted together in Figure 6.23. One of the points of Case III-PT-A, which is surrounded by a circle in the

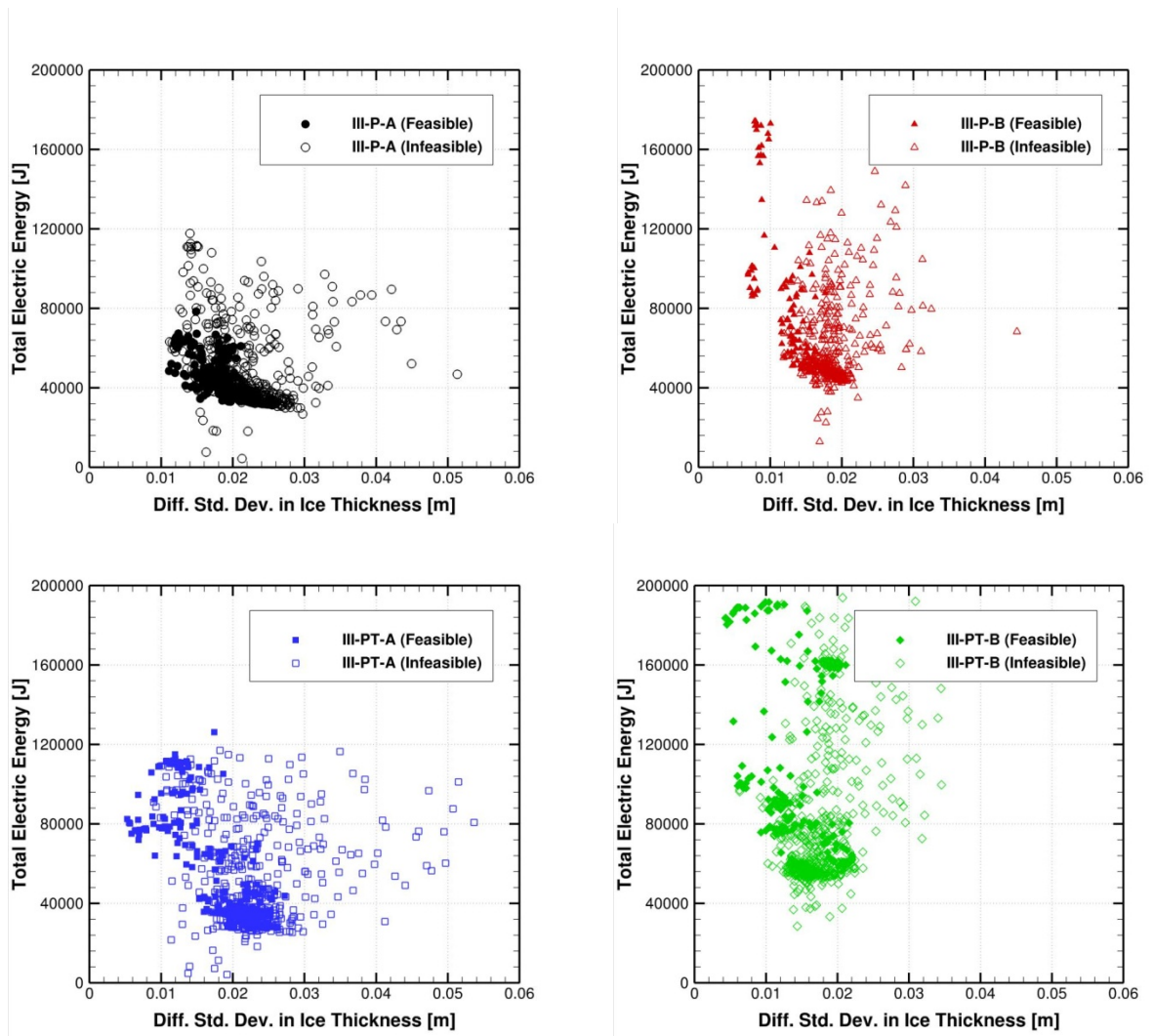


Figure 6.22: Pareto fronts of cases with function set III.

figure, could be a proper option to be selected because it has a small *ISI* and has a total energy that is reasonably less than the experiment. However, one of the points of Case III-P-A is selected, as shown in the figure, because, compared to the circled point, it has a smaller total energy, yet its *ISI* is not much greater. The total energy for this point is 48,511 J and the differential standard deviation is 0.011. Figure 6.24 shows the optimal power densities and the cycling sequence pattern for this point. As we can see, the power requirement is not as large as in the previous case, where *FIV* was considered. We can also see that the power density of heater 6, which was mentioned as an important factor on the final ice volume, is not highly influential, here. Figure 6.25 shows the surface quantity profiles at the moment of maximum ice thickness and at the end of the cycles. The maximum ice thickness is limited to 1.4 mm, as imposed by the constraint. Since *FIV* is not involved here, the final ice volume in this case is larger than that in Case II-P-A. It should be mentioned that there is no illustrative capability, here, to show that the optimal solution has overall smoother ice shapes as time evolves.

In the last two test cases, i.e. IV-P-A and IV-P-B, the following objective and constraint functions are used:

$$\begin{aligned}
 f_1(\mathbf{x}) &\equiv TEE, \\
 f_2(\mathbf{x}) &\equiv IPD, \\
 c_1(\mathbf{x}) &\equiv MIT,
 \end{aligned}
 \tag{6-26}$$

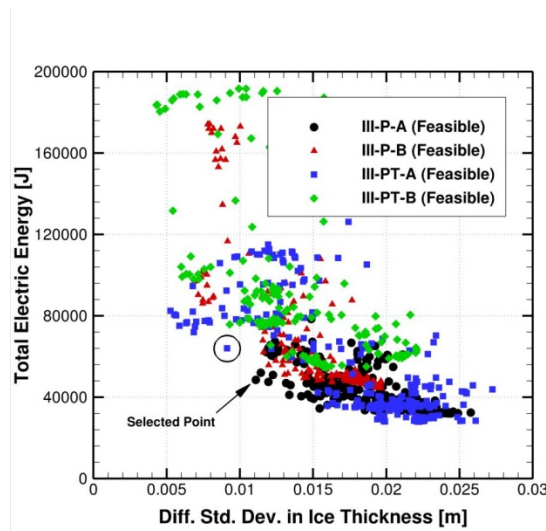


Figure 6.23: Feasible Pareto fronts for cases with function set III.

Heater Number	7	0	0	0	6800	0	0	0	6800		
	6	0	0	6800	0	0	0	6800	0		
	5	0	19200	0	0	0	19200	0	0		
	4	16300	0	0	0	16300	0	0	0		
	3	0	18400	0	0	0	18400	0	0		
	2	0	0	4700	0	0	0	4700	0		
	1	0	0	0	3900	0	0	0	3900		
			30	10	10	10	30	10	10	10	
			Cycle Time [s]								

Figure 6.24: Optimal power densities (W/m^2) and cycling sequence pattern for Case III-P-A.

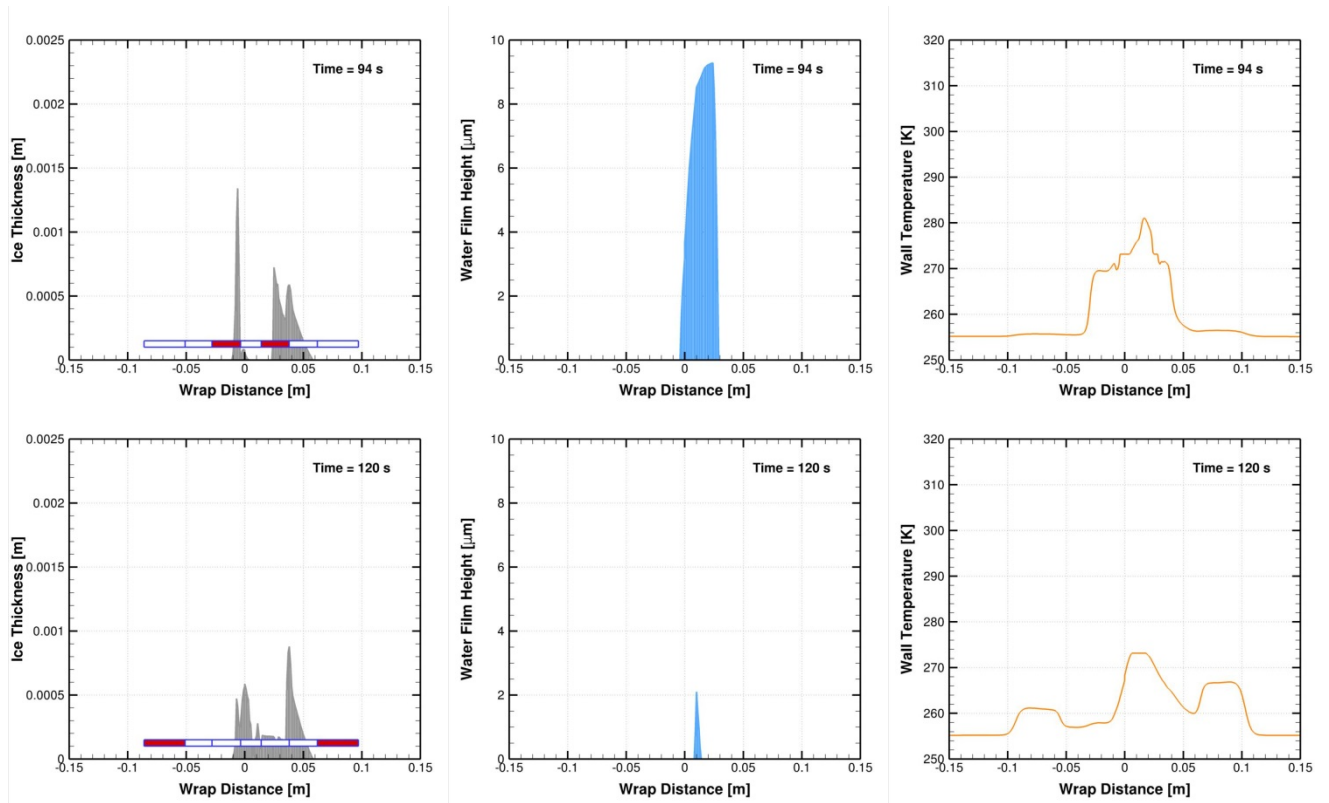


Figure 6.25: Profiles of three surface quantities at the moment of maximum ice thickness and at the end of the cycles for Case III-P-A.

where the largest ice thickness, h_{ice}^* , allowed over the heating zone is 1.4 mm. The above formulation gives the smallest amount of the energy required for de-icing, provided that the maximum ice thickness during the whole cycles is less than 1.4 mm and it is located

as far as possible from the minimum pressure. In both cases, the power densities are considered as the design variables. Figure 6.26 shows the feasible and infeasible Pareto fronts of the two cases. Similar to the previous cases, although the points of Pattern B are more dispersed, Pattern A outperforms Pattern B in terms of the objective function values. This is more visible in Figure 6.27, where the feasible Pareto fronts of both cases are plotted together. One of the feasible points of Case IV-P-A is selected, as indicated in the figure. The total energy for this point is 67,215 J and the IPD is 0.024 m. Figure 6.28 shows the surface quantity profiles at the moment of maximum ice thickness and at the end of the cycles. The maximum ice thickness, which occurs at the 93rd second, is limited to 1.4 mm, as imposed by the constraint. The dashed line in the ice thickness plot indicates the location of the minimum pressure coefficient. The situation of the maximum ice thickness and the minimum pressure with respect to each other is depicted together in Figure 6.29 and Figure 6.30. As shown, the maximum ice thickness is located before the minimum pressure near the leading edge. An optimal result could also have a solution with a maximum ice thickness located after the minimum pressure. However, the current cycling sequence patterns have not allowed such an optimal solution.

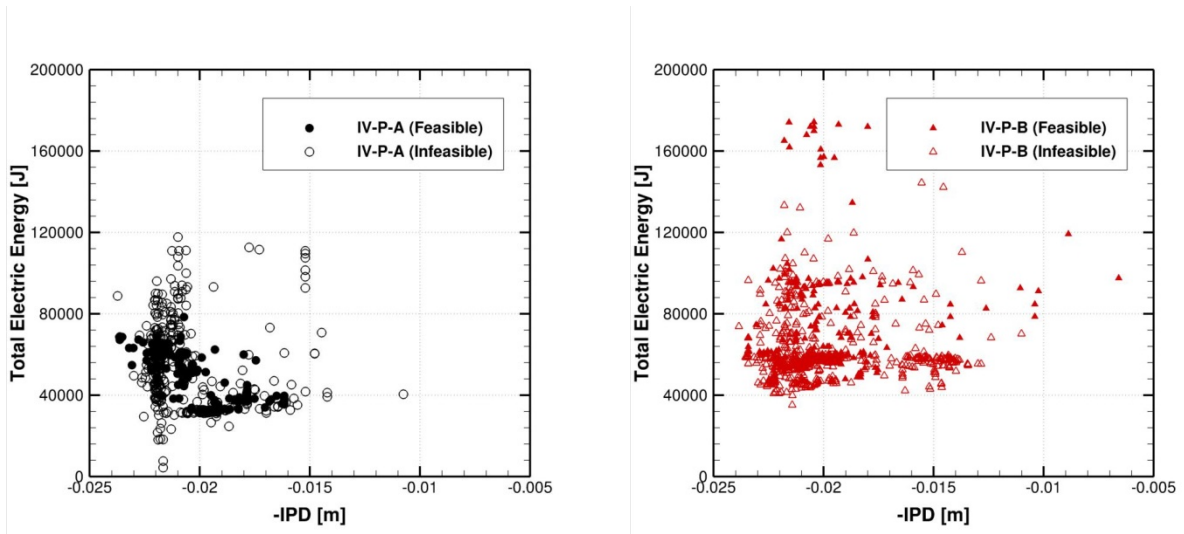


Figure 6.26: Pareto fronts of cases with function set IV.

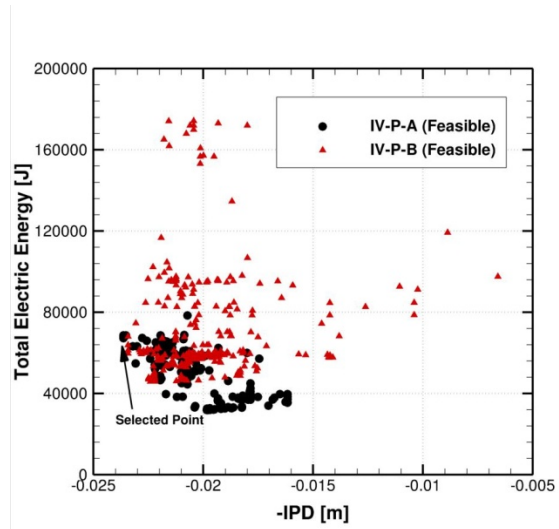


Figure 6.27: Feasible Pareto fronts for cases with function set IV.

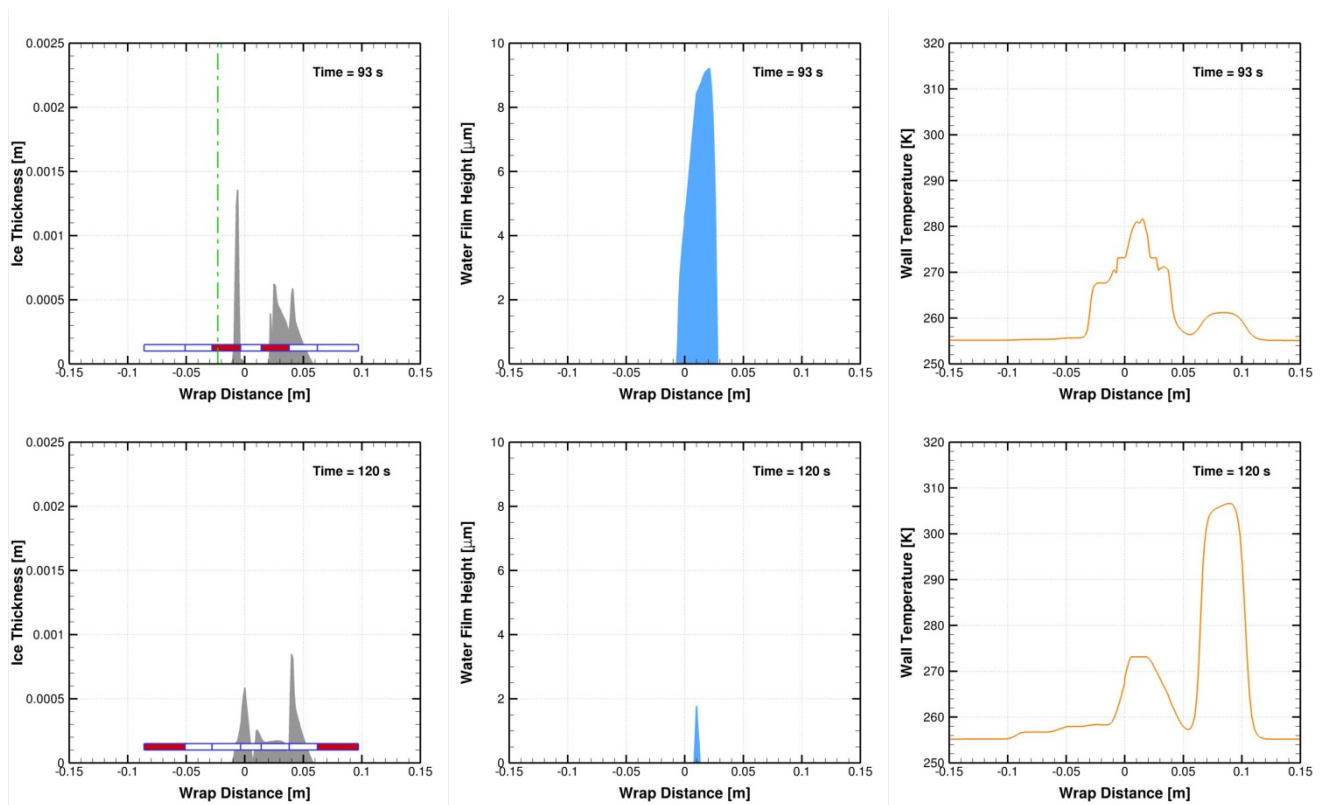


Figure 6.28: Profiles of three surface quantities at the moment of maximum ice thickness and at the end of the cycles for Case IV-P-A.

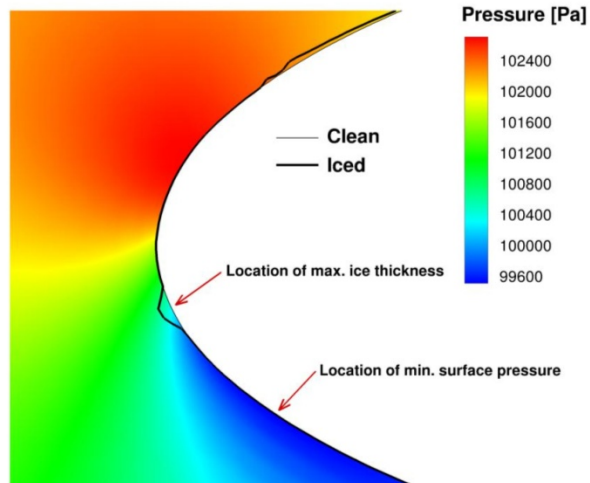


Figure 6.29: Pressure contour plot and locations of maximum ice thickness and minimum surface pressure.

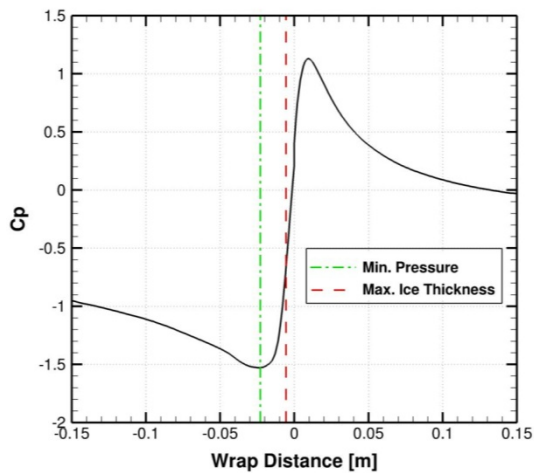


Figure 6.30: Pressure coefficient distribution and locations of maximum ice thickness and minimum pressure coefficient.

6.6 An Addendum on the Aerodynamic Effects of Surface Heating

In the previous sections, numerous effects of the inter-cycle ice accretion on the aerodynamic performance were taken into account to formulate the objective and

constraint functions. Another phenomenon during the de-icing process, which may affect the aerodynamic performance, is the surface heating. The research endeavors in this area are rooted in the emergence of unmanned aerial vehicles (UAV) and micro-aerial vehicles (MAV). The heat transfer effects are most pronounced on small size lifting components at low Reynolds numbers due to the growth of the boundary layer compared to the characteristic length. The increase in temperature can decelerate the flow, thus destabilizing the boundary layer and inducing an earlier boundary layer transition and separation [138]. A number of studies also show that a locally fixed temperature boundary condition at a tiny area near the leading edge can lead to a delay in transition [139]. According to another study [140], an increase in lift, a decrease in drag and an increase in the envelope of operation can be achieved when the upper surface of the wing is cooled and the lower surface is heated (with a positive angle of attack). Since the effect of surface heating is not very significant in large size components at high Reynolds numbers, it was not taken into account in the formulations. It, however, could be an interesting potential research area for future works.

6.7 Discussion and Conclusions

In this chapter, the numerical simulation and optimization of electro-thermal systems in de-icing mode were presented. In contrast to the anti-icing mode, the de-icing mode is an unsteady transient process. An experimental IPS model was numerically simulated, which showed that our results compare well with other numerical and experimental data. Prior to the optimization of the experimental model, two modifications on the model were performed to improve the performance of the optimization. These modifications were concerned with the duration and the pattern of the activation of the parting strip. The modified model was, then, used in several optimization test cases. The surrogate modeling approach used in the optimization cases was discussed. In each test case, a specific problem formulation was considered based on different objective and constraint functions. Both aerodynamic and thermodynamic viewpoints were taken into accounts in formulating these functions. Two different cycling sequence patterns were considered

and the better pattern was discerned through the numerical results. Different types of design variables were also used including the power densities. In some of the test cases, the activation times of the electric heaters were also included into the design variables. This improved the optimal solution in the mono-objective formulation while in the bi-objective formulations, no improvement was observed.

Chapter 7 CLOSURE

A numerical study on the analysis and optimization of in-flight electro-thermal ice protection systems (IPS) was presented. The general contributions and achievements can be briefly summarized as follows:

- Bringing mathematical rigor to an important engineering application: To the best of the author's knowledge, the optimization of electro-thermal IPS has not been fully numerically studied. The present research can fill the evident gap in this area. Furthermore, the drawbacks of other types of IPS and the latest trends of the aerospace industry toward "more electric aircraft" highlight the necessity of this research.
- Comprehensive parametric analysis of anti-icing systems: Different parameters that influence the cost and performance of anti-icing systems were identified and quantified. The parameters include airspeed, angle of attack, ambient temperature, liquid water content and median volumetric diameter. This parametric analysis can provide an IPS designer with general guidelines and estimations for preliminary design.
- Considering both cost and safety: The objective and constraint functions were carefully formulated such that low cost is achieved while maintaining the highest degree of safety by bringing together physics, applied mathematics,

thermodynamics, aerodynamics and structural analysis. Not only would the formulations be useful for the present problem, but also other engineering design problems can be benefited by the proposed ideas.

- Developing fast high-fidelity optimization methodologies: To compute the objective and constraint functions at each iterate of the optimization, we need to solve a conjugate heat transfer (CHT) problem with a prohibitive cost. A surrogate-based optimization algorithm was established, in which the CHT simulations were replaced by reduced order models. In addition, different strategies were introduced to improve the accuracy of the surrogate models of such high dimensional and highly nonlinear problem. These strategies make the methodology practical and reliable.

Future works potentially may include the following areas:

- Improving the accuracy of the CHT simulation by accounting for the ice shedding and cracking.
- Improving the heat transfer within the solid shell by optimization of the physical and geometrical properties of the leading edge materials.
- Improving the heat transfer within the solid shell by optimization of the directional-dependent thermal properties of the anisotropic composite materials of the leading edge.
- Combinatorial optimization of de-icing system, in which the pattern of the cycling sequence is also considered as a design variable.
- Taking into account the effect of ice accretion on the aerodynamic characteristics by defining objective and constraint functions based on the lift, drag and moment.

REFERENCES

- [1] "Most wanted transportation safety improvements, aviation issue areas," 2011; http://www.nts.gov/recs/mostwanted/aviation_issues.htm.
- [2] "Airplane and Engine Certification Requirements in Supercooled Large Drop, Mixed Phase, and Ice Crystal Icing Conditions, Proposed Rule," 124, Federal Register, June 29, 2010, pp. 37311-37339.
- [3] H. E. Addy, A. P. Broeren, J. G. Zoeckler, and S. Lee, "A wind tunnel study of icing effects on a business jet airfoil," AIAA Paper 2003-0727, 41st Aerospace Sciences Meeting and Exhibit, Reno, Nevada, US, 2003.
- [4] M. F. Alam, D. K. Walters, and D. S. Thompson, "Simulations of separated flow around an airfoil with ice shape using hybrid RANS/LES models," AIAA Paper 2011-3972, 29th AIAA Applied Aerodynamics Conference, Honolulu, Hawaii, US, 2011.
- [5] H. M. Gurbachi, and M. B. Bragg, "Unsteady aerodynamic measurements on an iced airfoil," AIAA Paper 2002-0241, 40th AIAA Aerospace Sciences Meeting & Exhibit, Reno, NV, USA, 2002.
- [6] S. D. Green, "A study of US inflight icing accidents and incidents, 1978 to 2002," AIAA Paper 2006-82, 44th AIAA Aerospace Sciences Meeting and Exhibit, Reno, NV, USA, 2006.
- [7] H.-T. Liu, and J. Hua, "Three-dimensional integrated thermodynamic simulation for wing anti-icing system," *Journal of aircraft*, vol. 41, no. 6, pp. 1291-1297, 2004.
- [8] G. Mingione, and M. Barocco, *Flight in icing conditions summary*, French DGAC, 1997.
- [9] S. K. Thomas, R. P. Cassoni, and C. D. MacArthur, "Aircraft anti-icing and de-icing techniques and modeling," *Journal of Aircraft*, vol. 33, no. 5, pp. 841-854, 1996.
- [10] Y. H. Yeong, R. Mudafort, A. Steele, I. Bayer, and E. Loth, "Water droplet impact dynamics at icing conditions with and without superhydrophobicity," AIAA Paper 2012-3134, 4th AIAA Atmospheric and Space Environments Conference, New Orleans, LA, USA, 2012.
- [11] P. Guo, Y. Zheng, M. Wen, C. Song, Y. Lin, and L. Jiang, "Icephobic/anti-icing properties of micro/nanostructured surfaces," *Advanced Materials*, vol. 24, no. 19, pp. 2642-2648, 2012.
- [12] L. Zhu, J. Xue, Y. Wang, Q. Chen, J. Ding, and Q. Wang, "Ice-phobic coatings based on silicon-oil-infused polydimethylsiloxane," *ACS applied materials & interfaces*, vol. 5, no. 10, pp. 4053-4062, 2013.
- [13] J. Rosero, J. Ortega, E. Aldabas, and L. Romeral, "Moving towards a more electric aircraft," *Aerospace and Electronic Systems Magazine, IEEE*, vol. 22, no. 3, pp. 3-9, 2007.
- [14] M. Sinnett, "787 No-bleed systems: saving fuel and enhancing operational efficiencies," *Boeing Commercial AERO magazine*, vol. 4, no. 1, pp. 6-11, 2007.

- [15] X. Roboam, B. Sareni, and A. D. Andrade, "More electricity in the air: toward optimized electrical networks embedded in more-electrical aircraft," *Industrial Electronics Magazine, IEEE*, vol. 6, no. 4, pp. 6-17, 2012.
- [16] T. Carroll, and W. McAvoy, "Formation of ice on airplanes," *Airway Age*, pp. 58-59, 1928.
- [17] E. Jacobs, "Airfoil section characteristics as affected by protuberances," *NACA Rep*, vol. 446, pp. 1932, 1932.
- [18] T. Theodorsen, *Theory of wing sections of arbitrary shape*: Government Print Office, 1932.
- [19] M. B. Bragg, "Rime ice accretion and its effect on airfoil performance," Ph.D. Dissertation, The Ohio State University, 1981.
- [20] T. L. Miller, K. D. Korkan, and R. J. Shaw, "Analytical determination of propeller performance degradation due to ice accretion," *Journal of Aircraft*, vol. 24, no. 11, pp. 768-775, 1987.
- [21] A. Smith, "The panel method: its original development," *Applied computational aerodynamics*, vol. 125, 1990.
- [22] C. MacArthur, J. Keller, and J. Luers, "Mathematical modeling of ice accretion on airfoils."
- [23] S. Özgen, and M. Canibek, "Ice accretion simulation on multi-element airfoils using extended Messinger model," *Heat and Mass Transfer*, vol. 45, no. 3, pp. 305-322, 2009.
- [24] J. Chung, A. Reehorst, Y. Choo, M. Potapczuk, and J. Slater, "Navier-Stokes analysis of flowfield characteristics of an ice-contaminated aircraft wing," *Journal of Aircraft*, vol. 37, no. 6, pp. 947-959, 2000.
- [25] R. P. Koomullil, D. S. Thompson, and B. K. Soni, "Iced airfoil simulation using generalized grids," *Applied Numerical Mathematics*, vol. 46, no. 3-4, pp. 319-330, 2003.
- [26] M. Mirzaei, M. Ardekani, and M. Doosttalab, "Numerical and experimental study of flow field characteristics of an iced airfoil," *Aerospace Science and Technology*, vol. 13, pp. 267-276, 2009.
- [27] I. Langmuir, and K. Blodgett, "A mathematical investigation of water droplet trajectories," *The Collected Works of Irving Langmuir*, vol. 10, pp. 348-393, 1944.
- [28] Y. Bourgault, Z. Boutanios, and W. G. Habashi, "3D Eulerian approach to droplet impingement simulation using FENSAP-ICE, part 1: model, algorithm, and validation," *Journal of Aircraft*, vol. 37, no. 1, pp. 95-103, 2000.
- [29] R. Da Silveira, C. Maliska, D. Estivam, and R. Mendes, "Evaluation of collection efficiency methods for icing analysis," 17th International Congress of Mechanical Engineering, Sao Paulo, 2003.
- [30] M. Tribus, "Intermittent heating for aircraft ice protection with application to propellers and jet engines," *Aircraft Gas Turbine Divs., Gen. Elec. Co. (Lynn, Mass.)*, 1949.
- [31] B. L. Messinger, "Equilibrium temperature of an unheated icing surface as a function of air speed," *Journal of the Aeronautical Sciences*, vol. 20, no. 1, pp. 29-41, 1953.

- [32] T. Myers, "Extension to the messinger model for aircraft icing," *AIAA Journal*, vol. 39, no. 2, pp. 211-218, 2001.
- [33] M. Goodro, J. Park, P. Ligrani, M. Fox, C. Engineer, and H. K. Moon, "Effect of temperature ratio on jet array impingement heat transfer," *Journal of Heat Transfer*, vol. 131, no. 1, pp. 012201, 2009.
- [34] J. Badra, A. R. Masri, M. Freeman, and M. Fitch, "Enhanced heat transfer from arrays of jets impinging on plates," 16th Australasian Fluid Mechanics Conference, Crown Plaza, Gold Coast, Australia, 2007.
- [35] G. Croce, W. G. Habashi, G. Guevremont, and F. Tezok, "3D thermal analysis of an anti-icing device using FENSAP-ICE," AIAA Paper 98-0193, 36th AIAA Aerospace Sciences Meeting and Exhibit Reno, NV, USA, 1998.
- [36] F. Morency, F. Tezok, and I. Paraschivoiu, "Anti-icing system simulation using CANICE," *Journal of Aircraft*, vol. 36, no. 6, pp. 999-1006, 1999.
- [37] J. Hua, F. Kong, and H. H. T. Liu, "Unsteady thermodynamic computational fluid dynamics simulations of aircraft wing anti-icing operation," *Journal of Aircraft*, vol. 44, no. 4, pp. 1113-1117, 2007.
- [38] T. G. Keith, K. J. De Witt, W. B. Wright, and K. C. Masiulaniec, "Overview of numerical codes developed for predicted electrothermal deicing of aircraft blades," AIAA Paper 88-0288, 26th AIAA Aerospace Sciences Meeting, Reno, NV, USA, 1988.
- [39] R. J. Roelke, T. G. Keith, K. J. De Witt, and W. B. Wright, "Efficient numerical simulation of a one-dimensional electrothermal deicer pad," *Journal of Aircraft*, vol. 25, no. 12, pp. 1097-1105, 1988.
- [40] G. E. Schneider, and M. J. Raw, "An implicit solution procedure for finite difference modeling of the Stefan problem," *AIAA Journal*, vol. 22, no. 11, pp. 1685-1690, 1984.
- [41] R. Henry, "Development of an electrothermal de-icing/anti-icing model," 92-0526, 30th AIAA Aerospace Sciences Meeting and Exhibit, Reno, NV, USA, 1992.
- [42] W. B. Wright, T. G. Keith, and K. J. De Witt, "Numerical analysis of a thermal deicer," AIAA Paper 92-0527, 30th AIAA Aerospace Sciences Meeting and Exhibit, Reno, NV, USA, 1992.
- [43] A. D. Yaslik, K. J. De Witt, and T. G. Keith, "Further developments in three-dimensional simulation of electrothermal deicing systems," AIAA Paper 92-0528, 30th AIAA Aerospace Sciences Meeting and Exhibit, Reno, NV, USA, 1992.
- [44] J. R. Huang, T. G. Keith, and K. J. De Witt, "Investigation of an electrothermal de-icer pad using a three-dimensional finite element simulation," AIAA Paper 93-0397, 31th AIAA Aerospace Sciences Meeting and Exhibit, Reno, NV, USA, 1993.
- [45] J. R. Huang, T. G. Keith, and K. J. De Witt, "Efficient finite element method for aircraft deicing problems," *Journal of Aircraft*, vol. 30, no. 5, pp. 695-704, 1993.
- [46] J. R. Huang, T. G. Keith, and K. J. De Witt, "Effect of curvature in the numerical simulation of an electrothermal de-icer pad," *Journal of Aircraft*, vol. 32, no. 1, pp. 84-92, 1995.

- [47] D. Miller, T. Bond, S. D. W. Wright, T. Langhals, K. Al-Khalil, and H. Broughton, "Validation of thermal ice protection computer codes: part 1-program overview," AIAA Paper 97-0049, 35th AIAA Aerospace Sciences Meeting and Exhibit, Reno, NV, USA, 1997.
- [48] W. Wright, K. Al-Khalil, and D. Miller, "Validation of NASA thermal ice protection computer codes: part 2-the validation of LEWICE/Thermal," AIAA Paper 97-0050, 35th AIAA Aerospace Sciences Meeting and Exhibit, Reno, NV, USA, 1997.
- [49] K. Al-Khalil, C. Horvath, D. Miller, and W. Wright, "Validation of thermal ice protection computer codes: part 3-the validation of ANTICE," AIAA Paper 97-0051, 35th Aerospace Sciences Meeting and Exhibit, Reno, NV, USA, 1997.
- [50] G. da Silva, O. de Mattos Silveas, and E. de J Zerbini, "Numerical simulation of airfoil thermal anti-Ice operation, part 2: implementation and results," *Journal of Aircraft*, vol. 44, no. 2, pp. 635-641, 2007.
- [51] G. A. L. da Silva, O. de M Silveas, and E. J. G. de J Zerbini, "Numerical simulation of airfoil thermal anti-ice operation, part 1: mathematical modeling," *Journal of Aircraft*, vol. 44, no. 2, pp. 627-634, 2007.
- [52] S. Kato, "Solution for aircraft anti-icing system simulation by a modified perturbation method," *Journal of Aircraft*, vol. 43, no. 2, pp. 544-554, 2006.
- [53] C. A. Martin, and J. C. Putt, "Advanced pneumatic impulse ice protection system (PIIP) for Aircraft," *Journal of Aircraft*, vol. 29, no. 4, pp. 714-716, 1992.
- [54] N. A. Weisend, "Design of an advanced pneumatic de-icer for the composite rotor blade," *Journal of Aircraft*, vol. 26, no. 10, pp. 947-950, Jan. 11-14, 1988, 1989.
- [55] G. Zumwalt, R. Schrag, W. Bernhart, and R. Friedberg, *Electro-impulse de-icing testing analysis and design*, NASA Contractor Report 4175, 1988.
- [56] K. Al-Khalil, "Thermo-mechanical expulsion deicing system-TMEDS," AIAA Paper 2007-0692, 45th AIAA Aerospace Sciences Meeting and Exhibit, Reno, NV, USA, 2007.
- [57] K. Al-Khalil, T. Ferguson, and D. Phillips, "A hybrid anti-icing ice protection system," AIAA Paper 97-0302, 35th AIAA Aerospace Sciences Meeting and Exhibit, Reno, NV, USA, 1997.
- [58] K. Al-Khalil, L. Salamon, and G. Tenison, "Development of the Cox icing research facility," AIAA Paper 98-0097, 36th AIAA Aerospace Sciences Meeting and Exhibit, 1998.
- [59] S. V. Venna, Y. J. Lin, and G. Botura, "Piezoelectric transducer actuated leading edge de-icing with simultaneous shear and impulse forces," *Journal of Aircraft*, vol. 44, no. 2, pp. 509-515, 2007.
- [60] R. B. Ingram, and J. J. Gerardi, *Shape memory alloy de-icing technology*, to Innovative Dynamics, Inc., Ithaca, U. S. Patent, 1997.
- [61] T. Horne, "Weeping Wings," *AOPA Pilot*, pp. 36-38, 1984.
- [62] N. Mulherin, R. Haehnel, and Jones, "Toward developing a standard shear test for ice adhesion," 8th International Workshop on Atmospheric Icing Structures, Reykjavik, Iceland, 1998.
- [63] S. L. Sivas, B. Riegler, R. Thomaier, and K. Hoover, "A silicone-based ice-phobic coating for aircraft," AMPE Fall Technical Conference: From Art to

- Science: Advancing Materials & Process Engineering, Cincinnati, OH, USA, 2007.
- [64] O. Gohardani, D. M. Williamson, and D. W. Hammond, "Multiple liquid impacts on polymeric matrix composites reinforced with carbon nanotubes," *Wear*, vol. 294, pp. 336-346, 2012.
 - [65] K. Al-Khalil, T. G. Keith, K. J. De Witt, J. K. Nathman, and D. A. Dietrich, "Thermal analysis of engine inlet anti-icing systems," *Journal of Propulsion and Power*, vol. 6, pp. 628-634, 1990.
 - [66] F. Saeed, "Numerical simulation of surface heat transfer from an array of hot-air jets," *Journal of Aircraft*, vol. 45, no. 2, pp. 700, 2008.
 - [67] M. Papadakis, S. H. Wong, H. W. Yeong, S. C. Wong, and G. T. Vu, "Icing tunnel experiments with a hot air anti-icing system," AIAA Paper 08-444, 46th AIAA Aerospace Sciences Meeting and Exhibit, Reno, NV, USA, 2008.
 - [68] S. H. Wong, M. Papadakis, and A. Zamora, "Computational investigation of a bleed air ice protection system," AIAA Paper 09-3966, 1st AIAA Atmospheric and Space Environments Conference, San Antonio, Texas, USA, 2009.
 - [69] P. Planquart, G. Van den Borre, and J. Buchlin, "Experimental and numerical optimization of a wing leading edge hot air anti-icing system," AIAA Paper 2005-1277, 43rd AIAA Aerospace Sciences Meeting and Exhibit, Reno, NV, USA, 2005.
 - [70] C. Mayer, A. Ilinca, G. Fortin, and J. Perron, "Wind tunnel study of electrothermal de-icing of wind turbine blades," *International Journal of Offshore and Polar Engineering*, vol. 17, no. 3, pp. 182, 2007.
 - [71] R. H. Strehlow, and R. Moser, "Capitalizing on the increased flexibility that comes from high power density electrothermal deicing," *Flight Dynamics*, vol. 2000, pp. 03-01, 2009.
 - [72] S. T. Buschhorn, N. Lachman, J. Gavin, B. L. Wardle, S. S. Kessler, and G. Thomas, "Electrothermal icing protection of aerosurfaces using conductive polymer nanocomposites," AIAA Paper 13-1729, 54th AIAA/ASME/ASCE/AHS/ASC Structures, Structural Dynamics, and Materials Conference, Boston, Massachusetts, USA, 2013.
 - [73] T. Reid, G. S. Baruzzi, I. Ozcer, D. Switchenko, and W. G. Habashi, "FENSAP-ICE simulation of icing on wind turbine blades, part 1: performance degradation," AIAA Paper 13-0750, 51st AIAA Aerospace Sciences Meeting including the New Horizons Forum and Aerospace Exposition, Grapevine, Texas, USA, 2013.
 - [74] T. Reid, G. S. Baruzzi, I. Ozcer, D. Switchenko, and W. G. Habashi, "FENSAP-ICE simulation of icing on wind turbine blades, part 2: ice protection system design," AIAA Paper 13-0751, 51st AIAA Aerospace Sciences Meeting including the New Horizons Forum and Aerospace Exposition, Grapevine, Texas, USA, 2013.
 - [75] "New aircraft de-icing concept based on functional coatings coupled with electrothermal system ", Clean Sky Research Program, 2013.
 - [76] F. Saeed, and I. Paraschivoiu, "Optimization of a hot-air anti-icing system," AIAA Paper 03-0733, 41st AIAA Aerospace Meeting and Exhibit, Reno, NV, USA, 2003.

- [77] L. C. C. Santos, R. H. Domingos, R. B. Maria, and M. F. Leal, "Sensitivity analysis of a bleed air anti-ice thermal model to geometrical and operational parameters," AIAA Paper 08-0445, 46th AIAA Aerospace Sciences Meeting and Exhibit, Reno, NV, USA, 2008.
- [78] M. P. Pellissier, W. G. Habashi, and A. Pueyo, "Optimization via FENSAP-ICE of hot-air anti-icing systems," *Journal of Aircraft*, vol. 48, no. 1, pp. 265-276, 2011.
- [79] P. Wheeler, "The more electric aircraft: Why aerospace needs power electronics?," 13th European Conference on Power Electronics and Applications, EPE, 2009.
- [80] H. Beaugendre, F. Morency, and W. G. Habashi, "Development of a second generation in-flight icing simulation code," *Journal of Fluids Engineering*, vol. 128, no. 2, pp. 378-387, 2006.
- [81] R. A. Khurram, Y. Zhang, and W. G. Habashi, "Multiscale finite element method applied to the Spalart–Allmaras turbulence model for 3D detached-eddy simulation," *Computer Methods in Applied Mechanics and Engineering*, vol. 233, no. 1, pp. 180-193, 2012.
- [82] P. M. Gresho, R. L. Lee, R. L. Sani, M. K. Maslanik, and B. E. Eaton, "The consistent Galerkin FEM for computing derived boundary quantities in thermal and or fluids problems," *International Journal for Numerical Methods in Fluids*, vol. 7, no. 4, pp. 371-394, 1987.
- [83] C. Crowe, "Review-numerical models for dilute gas-particle flows," *Journal of fluids engineering*, vol. 104, no. 3, pp. 297-303, 1982.
- [84] Y. Bourgault, W. G. Habashi, J. Dompierre, and G. S. Baruzzi, "A finite element method study of Eulerian droplets impingement models," *International journal for numerical methods in fluids*, vol. 29, no. 4, pp. 429-449, 1999.
- [85] A. Pueyo, "Simulation numérique de la formation de la glace pour des écoulements tridimensionnels," M.Sc.A. Thesis, École Polytechnique, Université de Montréal, 1993.
- [86] C. A. Meyer, R. McClintock, and G. Silvestri, *ASME steam tables: American Society of mechanical engineers*, 1993.
- [87] J. Donea, A. Huerta, J. Ponthot, and A. Rodríguez-Ferran, "Arbitrary Lagrangian–Eulerian methods," *Encyclopedia of computational mechanics*, 2004.
- [88] W. B. Wright, and A. Rutkowski, *Validation results for LEWICE 2.0*, and CD-ROM, January 1999.
- [89] D. Dussin, M. Fossati, A. Guardone, and L. Vigevano, "Hybrid grid generation for two-dimensional high-Reynolds flows," *Computers & Fluids*, vol. 38, no. 10, pp. 1863-1875, 2009.
- [90] G. Croce, H. Beaugendre, and W. G. Habashi, "CHT3D: FENSAP-ICE conjugate heat transfer computations with droplet impingement and runback effects," AIAA Paper 2002-0386, 40th Aerospace Sciences Meeting and Exhibit, Reno, NV, USA, 2002.
- [91] T. Hedde, "Modélisation tridimensionnelle des dépôts de givre sur les voitures d'aéronefs," Ph.D. Dissertation, Université Blaise-Pascal, Clermont-Ferrand II, 1993.

- [92] R. K. Jeck, *Icing design envelopes (14 CFR Parts 25 and 29, Appendix C) converted to a distance-based format*, FAA Technical Report DOT/FAA/AR-00/30, William J. Hughes Technical Center, Atlantic City International Airport, NJ, 2002.
- [93] A. Heinrich, R. Ross, G. Zumwalt, J. Provorse, and V. Padmanabhan, *Aircraft icing handbook*, FAA Technical Report DOT/FAA/CT-88/8-1, FAA Technical Center, Atlantic City, New Jersey, 1991.
- [94] C. Audet, and J. Dennis, "Mesh adaptive direct search algorithms for constrained optimization" *SIAM Journal on Optimization*, vol. 17, no. 1, pp. 188-217, 2006.
- [95] D. E. Goldberg, *Genetic algorithms in search, optimization, and machine learning*, Menlo Park, California, USA: Addison-Wesley, 1989.
- [96] A. I. F. Vaz, and L. N. Vicente, "A particle swarm pattern search method for bound constrained global optimization," *Journal of Global Optimization*, vol. 39, no. 2, pp. 197-219, 2007.
- [97] M. D. McKay, R. J. Beckman, and W. J. Conover, "A comparison of three methods for selecting values of input variables in the analysis of output from a computer code," *Technometrics*, vol. 42, no. 1, pp. 55-61, 2000.
- [98] C. Audet, V. Béchar, and S. Le Digabel, "Nonsmooth optimization through mesh adaptive direct search and variable neighborhood search," *Journal of Global Optimization*, vol. 41, no. 2, pp. 299-318, 2008.
- [99] M. A. Taddy, R. B. Gramacy, and N. G. Polson, "Dynamic trees for learning and design," *Journal of the American Statistical Association*, vol. 106, no. 493, pp. 109-123, 2011.
- [100] F. H. Clarke, *Optimization and nonsmooth analysis*, New York, USA: John Wiley & Sons, 1983.
- [101] D. R. Jones, "A taxonomy of global optimization methods based on response surfaces," *Journal of Global Optimization*, vol. 21, no. 4, pp. 345-383, 2001.
- [102] D. R. Jones, M. Schonlau, and W. J. Welch, "Efficient global optimization of expensive black-box functions," *Journal of Global Optimization*, vol. 13, no. 4, pp. 455-492, 1998.
- [103] M. Schonlau, W. J. Welch, and D. R. Jones, "Global versus local search in constrained optimization of computer models," 1997 Joint AMS-IMS-SIAM Summer Conference, Washington, Seattle, USA, 1997.
- [104] B. Talgorn, S. Le Digabel, and M. Kokkolaras, *Problem formulations for simulation-based design optimization using statistical surrogates and direct search*, Technical Report G-2014-04, Technical Report, Les cahiers du GERAD G-2014-04, 2014.
- [105] H. Mivehchi, and A. Varvani-Farahani, "The effect of temperature on fatigue strength and cumulative fatigue damage of FRP composites," *Procedia Engineering*, vol. 2, no. 1, pp. 2011-2020, 2010.
- [106] N. Hackerman, "Effect of temperature on corrosion of metals by water," *Industrial & Engineering Chemistry*, vol. 44, no. 8, pp. 1752-1755, 1952.
- [107] A. A. Baker, S. Dutton, and D. W. Kelly, *Composite materials for aircraft structures*, Second ed., Reston, Virginia, USA: AIAA, 2004.

- [108] E. A. J. Starke, *Accelerated aging of materials and structures, the effects of long-term elevated-temperature exposure*, Washington D.C., USA: National Academy Press, 1996.
- [109] S. Le Digabel, "Algorithm 909: NOMAD: Nonlinear optimization with the MADS algorithm," *ACM Transactions on Mathematical Software*, vol. 37, no. 4, pp. 44:1-44:15, 2011.
- [110] R. B. Gramacy, and M. A. Taddy, "dynaTree: An R package implementing dynamic trees for learning and design," 2010.
- [111] E. C. Capey, "Alleviation of thermal stresses in aircraft structures," Aeronautical Research Council, 1965.
- [112] A. Corrigan, F. F. Camelli, R. Löhner, and J. Wallin, "Running unstructured grid-based CFD solvers on modern graphics hardware," *International Journal for Numerical Methods in Fluids*, vol. 66, no. 2, pp. 221-229, 2010.
- [113] L. A. Schmit, and B. Farsi, "Some approximation concepts for structural synthesis," *AIAA Journal*, vol. 12, no. 5, pp. 692-699, 1974.
- [114] M. S. Eldred, and D. M. Dunlavy, "Formulations for surrogate-based optimization with data fit, multifidelity, and reduced-order models," AIAA Paper 06-7117, 11th AIAA/ISSMO Multidisciplinary Analysis and Optimization Conference, Portsmouth, Virginia, USA, 2006.
- [115] J. Lumley, "The structure of inhomogeneous turbulent flows," *Atmospheric Turbulence and Radio Wave Propagation*, pp. 166-178, 1967.
- [116] J. L. Lumley, *Stochastic tools in turbulence*, New York: Academic Press, 1970.
- [117] K. Karhunen, *Zur spektraltheorie stochastischer prozesse*: Suomalainen tiedeakatemia, 1946.
- [118] D. Kosambi, "Statistics in function space," *J. Indian Math. Soc.*, vol. 7, no. 1, pp. 76-88, 1943.
- [119] M. Loeve, "Functions aleatoire de second ordre," *La Revue Scientifique*, vol. 84, pp. 195-206, 1946.
- [120] A. Obukhov, "Statistical description of continuous fields," *Trudy Geophys. Int. Akad. Nauk. SSSR*, vol. 24, pp. 3-42, 1954.
- [121] V. S. Pugachev, "The general theory of correlation of random functions," *Izvestiya Rossiiskoi Akademii Nauk. Seriya Matematicheskaya*, vol. 17, no. 5, pp. 401-420, 1953.
- [122] L. Sirovich, "Turbulence and the dynamics of coherent structures. part I: coherent structures," *Quarterly of Applied Mathematics*, vol. 45, no. 3, pp. 561-571, 1987.
- [123] M. Fossati, G. Barruzi, and W. G. Habashi, "Simulation of supercooled large droplets impingement via reduced order technology," *Journal of Aircraft*, vol. 49, no. 2, pp. 600-610, 2012.
- [124] P. Holmes, J. L. Lumley, and G. Berkooz, *Turbulence, coherent structures, dynamical systems and symmetry*, Cambridge, England, UK: Cambridge Univ. Press, 1998.
- [125] D. Kbiob, "A statistical approach to some basic mine valuation problems on the Witwatersrand," *Journal of the Chemical, Metallurgical and Mining Engineering Society of South Africa*, vol. 52, no. 6, pp. 119-139, 1951.
- [126] G. Matheron, "Principles of geostatistics," *Economic Geology*, vol. 58, no. 8, pp. 1246-1266, 1963.

- [127] J. Sacks, W. J. Welch, T. J. Mitchell, and H. P. Wynn, "Design and analysis of computer experiments," *Statistical science*, vol. 4, no. 4, pp. 409-423, 1989.
- [128] P. Hemyari, and D. Nofziger, "Analytical solution for punctual kriging in one dimension," *Soil Science Society of America journal*, vol. 51, no. 1, pp. 268-269, 1987.
- [129] M. Li, G. Li, and S. Azarm, "A kriging metamodel assisted multi-objective genetic algorithm for design optimization," *Journal of Mechanical Design*, vol. 130, no. 3, pp. 031401, 2008.
- [130] R. B. Statnikov, and J. B. Matusov, *Multicriteria optimization and engineering*, New York: Chapman & Hall, 1995.
- [131] I. M. Sobol, and R. B. Statnikov, *The choice of optimal parameters in multicriteria problems*, Nauka (in Russian), 1981.
- [132] V. N. Vapnik, and V. Vapnik, *Statistical learning theory*, New York: John Wiley & Sons, 1998.
- [133] D. Amsallem, M. J. Zahr, and C. Farhat, "Nonlinear model order reduction based on local reduced-order bases," *International Journal for Numerical Methods in Engineering*, vol. 92, no. 10, pp. 891-916, 2012.
- [134] A. Faghri, and Y. Zhang, *Transport phenomena in multiphase systems*, New York: Academic Press, 2006.
- [135] D. T. Bowden, *Effect of pneumatic de-icers and ice formations on aerodynamic characteristics of an airfoil*, NACA TN 3564, 1954.
- [136] S. Lee, and M. B. Bragg, "Experimental investigation of simulated large-droplet ice shapes on airfoil aerodynamics," *Journal of Aircraft*, vol. 36, no. 5, pp. 844-850, 1999.
- [137] S. Lee, "Effects of supercolled large-droplet icing on airfoil aerodynamics," Ph.D. Dissertation, University of Illinois at Urbana-Champaign, 2001.
- [138] D. J. Norton, J. M. Macha, and J. C. Young, "Surface temperature effect on subsonic stall," *Journal of Spacecraft and Rockets*, vol. 10, no. 9, pp. 581-587, 1973.
- [139] A. Kazakov, M. Kogan, and V. Kuparev, "Optimization of laminar-turbulent transition delay by means of local heating of the surface," *Fluid dynamics*, vol. 30, no. 4, pp. 563-570, 1995.
- [140] N. Bekka, R. Bessaih, M. Sellam, and A. Chpoun, "Numerical study of heat transfer around the small scale airfoil using various turbulence models," *Numerical Heat Transfer, Part A: Applications*, vol. 56, no. 12, pp. 946-969, 2009.